



University of  
**Leicester**



NEUTRON REFLECTOMETRY STUDIES  
OF CONDUCTING POLYMER FILMS

Thesis submitted for the degree of

Doctor of Philosophy

at the University of Leicester

by

Charlotte Beebee BSc

Department of Chemistry

University of Leicester

January 2015

# Abstract

## Neutron reflectometry studies of conducting polymer films

Charlotte Beebee

Within the field of conducting polymers, it is well understood that the variables in film formation, ranging from the polymerisation and deposition methodologies to the supporting electrolyte in the deposition solution, can produce a wide range of different electrochemical and structural properties for a given polymeric species. For the most part, studies into these effects rely on spectroscopic, electrochemical and surface characterisation techniques. In this work, neutron reflectometry is used to identify the extent of solvent content and spatial distribution within polymer films, providing insight into the internal structure. In conjunction with electrochemical methods, two types of variables are explored: the addition of carbon composites and the electrochemical control function used for polymerisation/deposition. The effect of the incorporation of carbon nanoparticles is explored in the case of composite poly(3,4-ethylenedioxythiophene)-nanodiamond films. These are revealed to be similarly electroactive to pristine poly(3,4-ethylenedioxythiophene) films but present a more ordered internal structure. The effect of the electrodeposition method is investigated by comparing films produced by potentiodynamic, potentiostatic and galvanostatic deposition in the case of two different polymers, polypyrrole and poly(3,4-ethylenedioxythiophene). The results show that the polymerisation efficiency for a given growth protocol differs depending on the polymer species, as do the structural variations, such as porosity or structural stability following charge/discharge processes.

## Acknowledgments

This thesis would not exist without the invaluable help and support of my friends and family, as well as the staff and students of the University of Leicester and of the Institut Laue-Langevin in Grenoble. In particular, I must thank Rob Hillman, Karl Ryder and Bob Cubitt for offering me this incredible opportunity in the first place. I would also like to thank the Institut Laue-Langevin for funding this project.

Without a doubt, the work presented here would not have been possible without my collaborators, trusted sidekicks, teachers, confidantes and most importantly, friends: Rachel Sapstead and Virginia Ferreira. Forming an 'all girl neutron team' with you was an honour and exponentially increased the fun to be had while performing record breaking experiments.

I owe everything I know about neutron reflectometry to Erik Watkins, my supervisor through a simple twist of fate. Thank you for encouraging my perfectionist tendencies and pushing me to always do better. I hope I have 'done you proud'.

Everyone knows that writing a thesis can be a truly unpleasant process. What you really need at that point is a childhood friend with psychic tendencies, able to read your thoughts and detect from hundreds of kilometres away that you need a phone call and a pep talk. Thanks therefore to April Tissier for her timely support, her unquestioning understanding and sympathy. Your encouragement, positivity and unwavering belief in me spurred me on and helped me believe in myself.

Finally, there is one person to whom this thesis is undoubtedly dedicated to: my mother. Thank you doesn't begin to cover the debt of gratitude I feel towards you for pushing me, comforting me, supporting me and loving me. In so many moments when I was prepared to throw in the towel, the only thing that made me bite my tongue and keep going was the picture of you and me at graduation. I wanted to do this for you, for everything you have given me, for every opportunity you created, for every sacrifice you have made, and so that you get to go to another graduation (but can we just have the picture taken and then go for drinks?). I don't expect you to read it but I hope you will like the colourful pictures and that this volume might proudly gather dust on your bookshelf.

# Table of contents

Abstract.....	1
Acknowledgments.....	2
Table of contents.....	3
List of tables.....	7
List of figures.....	10
Abbreviations.....	20
Chapter 1 – Introduction.....	21
1.1    Electroactive polymers.....	22
1.1.1    Polypyrrole.....	24
1.1.2    Poly(3,4-ethylene dioxythiophene).....	27
1.1.3    Polymer-carbon composites.....	30
1.2    Neutron reflectometry.....	33
1.2.1    Studies of conducting polymers.....	33
1.2.2    Combining NR and electrochemical techniques.....	35
1.3    Conclusions.....	38
1.4    Aims and objectives.....	38
1.5    References.....	40
Chapter 2 – Methodology and techniques.....	47
2.1    Neutron reflectometry.....	47
2.1.1    Introduction.....	47
2.1.2    Neutron-nuclei interactions.....	47
2.1.3    Reflectivity theory.....	49
2.1.4    Models and limitations.....	53
2.1.5    Conclusion.....	59
2.2    Electrochemical methods.....	60

2.2.1	Introduction.....	60
2.2.2	Electrochemical cells.....	60
2.2.3	Electrodes .....	62
2.2.4	Electrochemical theory .....	62
2.2.5	Cyclic voltammetry .....	63
2.2.6	Chronoamperometry .....	64
2.2.7	Chronopotentiometry.....	64
2.3	Atomic force microscopy .....	65
2.4	References.....	66
Chapter 3 – Experimental and analysis.....		67
3.1	Neutron reflectometry.....	67
3.1.1	Alignment .....	67
3.1.2	Measurement.....	67
3.1.3	<i>In situ</i> electrochemistry set-up .....	68
3.1.4	Model interpretation and analysis.....	68
3.2	Electrochemical analysis .....	71
3.3	Preparation of gold surface electrodes.....	72
3.4	Atomic force microscopy measurements .....	73
3.5	References.....	74
Chapter 4 – Poly(3,4-ethylenedioxythiophene)-nanodiamond composite films .....		75
4.1	Introduction .....	75
4.2	Experimental .....	76
4.2.1	Potentiostatically deposited PEDOT and PEDOT-ND films.....	76
4.2.2	Potentiodynamically deposited PEDOT and PEDOT-ND films.....	77
4.2.3	PEDOT and PEDOT-ND samples for neutron reflectometry .....	77
4.3	Results.....	79
4.3.1	Potentiostatically deposited PEDOT and PEDOT-ND films.....	79

4.3.2	Potentiodynamically deposited PEDOT and PEDOT-ND films.....	84
4.3.3	PEDOT and PEDOT-ND samples for neutron reflectometry .....	87
4.4	Discussion.....	106
4.5	Conclusions.....	113
4.6	References.....	114
Chapter 5 – Electrodeposition of polypyrrole films.....		117
5.1	Introduction .....	117
5.2	Experimental.....	118
5.2.1	<i>In situ</i> electrochemical growth and NR .....	118
5.2.2	Investigation of variables in galvanostatic deposition protocol.....	120
5.3	Results.....	122
5.3.1	<i>In situ</i> electrochemical growth and NR study .....	122
5.3.2	Investigation of variables in galvanostatic deposition protocol.....	140
5.4	Discussion.....	143
5.4.1	<i>In situ</i> electrochemical growth and NR study .....	143
5.4.2	Investigation of variables in galvanostatic deposition protocol.....	147
5.5	Conclusions.....	150
5.6	References.....	151
Chapter 6 – Electrodeposition of poly(3,4-ethylenedioxythiophene) films .....		153
6.1	Introduction .....	153
6.2	Experimental.....	154
6.2.1	Small scale preliminary deposition experiments.....	154
6.2.2	Scale up deposition experiments .....	155
6.2.3	<i>In situ</i> electrochemical growth and NR .....	155
6.3	Results.....	157
6.3.1	Small scale preliminary deposition experiments.....	157
6.3.2	Scale up deposition experiments .....	159

6.3.3	<i>In situ</i> electrochemical growth and NR .....	161
6.4	Discussion.....	177
6.5	Conclusions.....	187
6.6	References.....	188
Chapter 7 - Conclusions.....		189
Bibliography .....		191

## List of tables

Table 2.1 – Example of the box model with the thickness and SLD parameters for each layer and the roughness value between each layer, e.g. roughness in the row ‘quartz substrate’ is the roughness from the quartz to layer 2; no thickness value is given for the outer materials as they are bulk materials. ....	54
Table 2.2 – Differences between NR/EC cells.....	61
Table 4.1 – Sample summary of potentiostatically grown PEDOT and PEDOT-ND thin films (* indicates that there was no water added to the deposition solution); $Q_g$ and $E_g$ are the growth charge and growth potential respectively .....	76
Table 4.2 – Summary of SLDs used in the analysis of NR results .....	78
Table 4.3 – Comparison of the characteristic Raman bands for PEDOT as found in the literature with the observed spectra for the PEDOT and PEDOT-ND films.....	83
Table 4.4 – Summary of the growth charge and the coulometric estimate of dry film thickness calculated from $Q_g$ for each of the potentiostatically grown samples .....	84
Table 4.5 - Summary of AFM measurements of dry film thickness.....	86
Table 4.6 – Summary of growth charge and estimated dry film thickness calculated from $Q_g$ for PEDOT and PEDOT-ND samples potentiostatically grown for the NR study.....	87
Table 4.7 – Model parameters from fits to the dry film reflectivity measurements; * indicates parameters that were fixed during fitting.....	89
Table 4.8 – Multiple polymer layer model parameters from fits to the dry film reflectivity measurements; * indicates parameters that were fixed during fitting.....	91
Table 4.9 – Fit parameters for the single polymer layer SLD profiles presented in Figure 4.13.....	92
Table 4.10 – Parameters associated with the fits to the solvated PEDOT-ND#15 film data shown in Figure 4.21 .....	100
Table 4.11 – Parameters associated with the fits to the solvated PEDOT-ND#15 film data shown in Figure 4.22.....	103
Table 4.12 – Parameters associated with the fits to the solvated PEDOT-ND#15 film data shown in Figure 4.24.....	105
Table 5.1 – Densities and SLDs of PPy and water in their hydrogenous and deuterated forms .....	118

Table 5.2 – Summary of polypyrrole sample information and deposition conditions, * indicates samples studied on SURF .....	119
Table 5.3 – Summary of galvanostatically grown PPy small sample information and deposition conditions; 15 intervals indicates 2 x 30 s, 1 x 1 min, 5 x 2 min, 1 x 5 min, 1 x 10 min, 5 x 20 min; 7 intervals is 1 x 5 min, 4 x 10 min, 2 x 20 min; 9 intervals is 1 x 5 min, 4 x 10 min, 4 x 20 min.....	120
Table 5.4 – Summary of linear regression analysis results from plots of mass per area as a function of growth charge density.....	131
Table 5.5 – Summary of second order polynomial fits to the mass per area values calculated from the NR data as a function of charge .....	132
Table 5.6 – Summary of the solvent volume fraction values extracted from the fits to the NR data for each stage of growth and redox state; multiple values are associated with multiple layers in the model such that left to right gives values from the electrode to the solution interface .....	135
Table 5.7 – Summary of oxidation charge values from the electrochemical characterisation of NR samples shown in Figure 5.17 .....	138
Table 5.8 – Summary of the thickness and roughness parameters determined by AFM for each film growth protocol .....	139
Table 5.9 – Summary of the growth protocol and characteristics of each sample, including a comparison of the AFM measurement of film thickness with the estimated thickness calculated from the growth charge .....	141
Table 5.10 – Results of the electrochemical characterisation of the galvanostatically grown PPy films; the values are taken from the final (20 <sup>th</sup> ) cycle at each scan rate.....	142
Table 6.1 – Summary of deposition conditions for electrochemically prepared PEDOT films.....	154
Table 6.2 – Summary of deposition conditions for electrochemically prepared PEDOT films on glass substrates.....	155
Table 6.3 – Summary of growth protocols for the <i>in situ</i> deposition of PEDOT films	156
Table 6.4 – Summary of the electrochemical and AFM results of the characterisation of preliminary PEDOT samples.....	157
Table 6.5 – Summary of the electrochemical and AFM results of the characterisation of the scaled up PEDOT samples on glass substrates.....	160

Table 6.6 – Comparison of $\chi^2$ values for single and multi-layered fits to the last three potentiodynamic deposition steps.....	162
Table 6.7 – Comparison of $\chi^2$ values for single and multi-layered fits to the last two potentiostatic deposition steps.....	165
Table 6.8 – Comparison of $\chi^2$ values for single and multi-layered fits to the last three galvanostatic deposition steps.....	168
Table 6.9 – Summary of linear regression analysis results from plots of mass per area as a function of growth charge density.....	170
Table 6.10 – Summary of second order polynomial fits to the mass per area values calculated from the NR data as a function of charge.....	170
Table 6.11 – Summary of solvent volume fractions extracted from single layer fits to the NR data, assuming a PEDOT SLD of $2.25 \times 10^{-6} \text{ \AA}^{-2}$ .....	172
Table 6.12 – Comparison of $\chi^2$ values for single and multi-layered fits to the measurements of the redox states for each deposition method.....	174
Table 6.13 – Summary of solvent volume fractions extracted from multi-layered fits to the NR data, assuming a PEDOT SLD of $2.25 \times 10^{-6} \text{ \AA}^{-2}$ .....	174
Table 6.14 – Summary of the electrochemical characterization of the PEDOT films grown during <i>in situ</i> NR measurements.....	175
Table 6.15 – Summary of AFM characterisation of the PEDOT films grown during <i>in situ</i> NR measurements.....	176

## List of figures

Figure 1.1 – Illustration of delocalisation of electrons in the case of the monomer pyrrole which, once polymerised, leads to conductivity along the polymer chains.....	22
Figure 1.2 – Structures of PEDOT (A), PPy (B), PANI (C).....	23
Figure 1.3 – Schematic of the process of ion incorporation showing a dry film structure (left) and the solvated structure (right) in which ions penetrate the film and cause it to swell.....	23
Figure 1.4 – Conceptual diagram of the role of carbon composites in creating space within the polymer matrix (left) that readily allows the incorporation of ions (right) without resulting in the mechanical strains brought about by swelling .....	24
Figure 1.5 – Schematic of the process of ion exchange in which both anions and cations move in and out of the film to balance charge in response to oxidation (left) and in the case where a large anion is trapped within the polymer matrix such that only the cationic species is mobile (right).....	25
Figure 1.6 – Conceptual illustration of film structure resulting from continuous polymerisation (left) and sequential polymerisation steps (right) which may fill in gaps within previous layers as well as produce distinct interfaces.....	27
Figure 1.7 – Illustration of the boxcar integration method applied to a cyclic voltammogram such that each box shows the section of the cycle during which NR data is acquired.....	34
Figure 2.1 - Bound coherent scattering lengths.....	48
Figure 2.2 – Scattering geometry through layers .....	49
Figure 2.3 – Geometry of the incident and scattered wavevectors and the associated momentum transfer.....	50
Figure 2.4 – Illustration of the roughness parameter in relation to the SLD profile of an interface (blue trace) and the corresponding Gaussian derivative (red trace).....	55
Figure 2.5 – Simulated reflectivity and SLD profiles of 30 nm gold layer on quartz substrate with a 15 Å MPTS layer (blue trace) and without (green trace); roughness is fixed at 5 Å at each interface.....	56
Figure 2.6 – Simulated reflectivity and SLD profiles of a single interface between two bulk materials, the blue trace is a sharp interface with a roughness of 0 Å and the green trace shows the same interface with a roughness of 10 Å .....	56

Figure 2.7 – Simulated reflectivity and SLD profiles of a sample with two distinct interfaces, in the case where both are sharp with 0 Å roughness (blue), where both are diffuse with 10 Å roughness (purple), where the first interface is sharp and the second diffuse (green) and where the first is diffuse and the second is sharp (red).....	57
Figure 2.8 – Simulated reflectivity and SLD profiles of a sample with two distinct interfaces, in the case where both are sharp with 0 Å roughness (blue), where both are diffuse with 20 Å roughness (purple), where the first interface is sharp and the second diffuse (green) and where the first is diffuse and the second is sharp (red).....	58
Figure 2.9 – Simulated reflectivity and SLD profiles of samples with a single 10 nm layer but with SLDs differing by $1 \times 10^{-6} \text{ \AA}^{-2}$ .....	58
Figure 2.10 – Simulated reflectivity and SLD profiles of two-layered samples in which the layers are equally thick (blue trace), in which the lower SLD layer is thinner than the higher SLD layer (green trace) and in which the lower SLD layer is thicker than the higher SLD layer (red trace).....	59
Figure 2.11 – Schematic of the electrochemical cell setup.....	61
Figure 2.12 – Schematic of the neutron reflectometry/electrochemistry cell (NR/EC).....	61
Figure 2.13– Diagrams of the AFM scanning process and the resulting 3D image of the surface.....	65
Figure 4.1– Growth transients for PEDOT (blue) and PEDOT-ND (grey) films grown in organic (A) and aqueous (B) media, full and dashed lines are the current and charge density, respectively, as functions of time.....	79
Figure 4.2 – Optical microscopy images acquired at a magnification of x20 showing a PEDOT-ND film grown in aqueous media (A) and films grown in organic media with (B) and without (C) NDs.....	80
Figure 4.3 – Cyclic voltammograms of films grown in organic (red) and aqueous (blue) media to a growth charge of $60 \text{ mC cm}^{-2}$ and cycled at $50 \text{ mV s}^{-1}$ in $0.1 \text{ M H}_2\text{SO}_4$ (A) and $0.1 \text{ M LiClO}_4$ in MeCN (B and C); full and dashed lines indicate films with and without NDs respectively.....	81
Figure 4.4 – Height profiles from AFM images of a dry pristine PEDOT film deposited with $Q_g = 30 \text{ mC cm}^{-2}$ (light blue), $Q_g = 60 \text{ mC cm}^{-2}$ (dark blue) and of a PEDOT-ND film deposited with $Q_g = 60 \text{ mC cm}^{-2}$ (black); thicknesses quoted are based on three separate section measurements across the scratch.....	82

Figure 4.5 – Raman spectra for the thin films (coloured traces) and ND powder (black trace); inset: shaded area highlights where the characteristic diamond peak should be observed around $1332\text{ cm}^{-1}$ .....	83
Figure 4.6 – First and final cycles of the potentiodynamic growth of PEDOT (1 and 2) and PEDOT-ND (3 and 4) films at a scan rate of $20\text{ mV s}^{-1}$ for 20 cycles with a current cap of $6\text{ mA}$ for an electrode area of $50\text{ cm}^2$ .....	85
Figure 4.7 – Cyclic voltammograms of the PEDOT and PEDOT ND films at $50\text{ mV s}^{-1}$ in $0.1\text{ M H}_2\text{SO}_4$ ; panel A shows the characterisation after growth and panel B the cycles measured following charge (blue) and discharge (red) tests of PEDOT (dashed lines) and PEDOT-ND (full lines) .....	85
Figure 4.8 – AFM images of the PEDOT (1 and 2) and PEDOT-ND (3 and 4) films after deposition; (a) images are $100\text{ }\mu\text{m}^2$ and (b) images are $1\text{ }\mu\text{m}^2$ .....	86
Figure 4.9 – Final cyclic voltammograms from the growth (A) and characterisation (B) of the PEDOT (green), PEDOT-ND#15 (red) and PEDOT-ND#10 (blue) films .....	87
Figure 4.10 – AFM images of the surface of PEDOT (A), PEDOT-ND#15 (B) and PEDOT-ND#10 (C) films.....	88
Figure 4.11 – Reflectivity (left) and SLD (right) profiles of the PEDOT and PEDOT-ND films measured in air; the green traces are the PEDOT data and the red and blue traces are the data for the PEDOT-ND#15 and PEDOT-ND#10 films respectively; $R(Q)$ datasets are offset by increments of 1 for clarity.....	89
Figure 4.12 – Reflectivity (left) and SLD (right) profiles of the PEDOT and PEDOT-ND films measured in air and fitted using a multiple polymer layer model; the green traces are the PEDOT data and the red and blue traces are the data for the PEDOT-ND#15 and PEDOT-ND#10 films respectively; $R(Q)$ datasets are offset by increments of 1 for clarity.....	90
Figure 4.13 – Reflectivity (left) and SLD (right) profiles for the different possible layer fits to the PEDOT-ND#15 data in air: the single layer fit to a thickness of $38\text{ nm}$ (1), the single layer fit to $81\text{ nm}$ (2) and the multilayer fit to $81\text{ nm}$ (3); $R(Q)$ datasets are offset by increments of -2 for clarity .....	92
Figure 4.14 – Reflectivity (left) and SLD (right) profiles for the pristine PEDOT film exposed to $\text{D}_2\text{O}$ , $\text{H}_2\text{O}$ and $\text{H}_2\text{O}/\text{D}_2\text{O}$ mix with an SLD of $2.26 \times 10^{-6}\text{ }\text{\AA}^{-2}$ ; $R(Q)$ datasets are offset by increments of -2 for clarity. Fitted using the Global Reflectometry Analysis tool in Motofit.....	93

Figure 4.15 – Solvent volume fraction profiles for the PEDOT film in H <sub>2</sub> O, D <sub>2</sub> O (overlaid by H <sub>2</sub> O) and H <sub>2</sub> O/D <sub>2</sub> O associated with the fits in Figure 4.14, calculated based on the co-refined PEDOT SLD = $1.21 \times 10^{-6} \text{ \AA}^{-2}$ .....	94
Figure 4.16 – Reflectivity (left) and SLD (right) profiles of the pristine PEDOT film in the three contrasts, fitted using a co-refinement method in which the solvation levels of the MPTS and polymer layers varied independently in each contrast; R(Q) datasets are offset by increments of -2 for clarity .....	95
Figure 4.17 – Reflectivity (right) and SLD (left) profiles of the pristine PEDOT film in the three contrasts obtained by fitting the individual datasets separately; R(Q) datasets are offset by increments of -2 for clarity .....	95
Figure 4.18 – Solvent volume fraction profiles for the PEDOT film in H <sub>2</sub> O and D <sub>2</sub> O associated with the fits in Figure 4.17, calculate based on the single layer fit to the dry PEDOT film so an SLD = $1.825 \times 10^{-6} \text{ \AA}^{-2}$ .....	96
Figure 4.19 – Reflectivity (left) and SLD (right) profiles of the pristine PEDOT film in the three contrasts in which a multiple polymer layer model of the D <sub>2</sub> O data was used to restrict the fitting of the other two contrasts; R(Q) datasets are offset by increments of -2 for clarity .....	97
Figure 4.20 - Solvent volume fraction profiles for the PEDOT film in H <sub>2</sub> O and D <sub>2</sub> O associated with the fits in Figure 4.19, calculated based on the theoretical PEDOT SLD = $2.25 \times 10^{-6} \text{ \AA}^{-2}$ .....	98
Figure 4.21 – Reflectivity (left) and SLD (right) profiles of the PEDOT-ND#15 film in all contrasts: in D <sub>2</sub> O (1), H <sub>2</sub> O (2), H <sub>2</sub> O/D <sub>2</sub> O = $2.26 \times 10^{-6} \text{ \AA}^{-2}$ (3 and 4) and H <sub>2</sub> O/D <sub>2</sub> O = $1.7 \times 10^{-6} \text{ \AA}^{-2}$ (5); R(Q) datasets are offset by increments of -2 for clarity .....	99
Figure 4.22 – Reflectivity (left) and SLD (right) profiles of the PEDOT-ND#15 film in all contrasts: in D <sub>2</sub> O (1), H <sub>2</sub> O (2), H <sub>2</sub> O/D <sub>2</sub> O = $2.26 \times 10^{-6} \text{ \AA}^{-2}$ (3 and 4) and H <sub>2</sub> O/D <sub>2</sub> O = $1.7 \times 10^{-6} \text{ \AA}^{-2}$ (5); R(Q) datasets are offset by increments of -2 for clarity .....	101
Figure 4.23 – Solvent volume fraction profiles for the PEDOT-ND film in H <sub>2</sub> O and D <sub>2</sub> O associated with the fits in Figure 4.22, calculated based on the composite SLD = $2.5 \times 10^{-6} \text{ \AA}^{-2}$ .....	102
Figure 4.24 – Reflectivity (left) and SLD (right) profiles of the PEDOT-ND#15 film in all contrasts: in D <sub>2</sub> O (1), H <sub>2</sub> O (2), H <sub>2</sub> O/D <sub>2</sub> O = $2.26 \times 10^{-6} \text{ \AA}^{-2}$ (3 and 4) and H <sub>2</sub> O/D <sub>2</sub> O = $1.7 \times 10^{-6} \text{ \AA}^{-2}$ (5); R(Q) datasets are offset by increments of -2 for clarity .....	104

Figure 4.25 – Solvent volume fractions for the PEDOT-ND film in D <sub>2</sub> O and H <sub>2</sub> O, associated with the fits in Figure 4.24, calculated based on the composite SLD = 2.5 × 10 <sup>-6</sup> Å <sup>-2</sup> .....	104
Figure 5.1 – NR measurements and fits (left) and corresponding SLD profiles (right) for the potentiodynamic growth of dPPy; the purple trace is the gold measurement prior to deposition. R(Q) datasets are offset by increments of -1 for clarity. Experimental conditions: 0.112 M dPy in 0.1 M NaClO <sub>4</sub> in H <sub>2</sub> O, E : [-0.4 V – E <sub>max</sub> ] vs Ag wire, v = 20 mVs <sup>-1</sup> , i <sub>max</sub> = 3 mA, 30 cycles.....	122
Figure 5.2 – Cyclic voltammograms recorded during the potentiodynamic growth of dPPy. Experimental conditions: 0.112 M dPy in 0.1 M NaClO <sub>4</sub> in H <sub>2</sub> O, E : [-0.4 V – E <sub>max</sub> ] vs Ag wire, v = 20 mVs <sup>-1</sup> , i <sub>max</sub> = 3 mA, 30 cycles.....	123
Figure 5.3 – Plots of film thickness (left) and mass per area (right) as a function of growth charge density as calculated from the electrochemical data (blue) and from the NR data (red) from the potentiodynamic growth of dPPy; the coloured traces are the associated fits to the data, the black dotted trace is the linear fit to the NR data .....	123
Figure 5.4 – NR measurements and fits (left) and corresponding SLD profiles (right) for the potentiostatic growth of dPPy; the purple trace is the gold measurement prior to deposition. R(Q) datasets are offset by increments of -1 for clarity. Experimental conditions: 0.112 M dPy in 0.1 M NaClO <sub>4</sub> in H <sub>2</sub> O, E = 0.3 V vs Ag wire, t <sub>total</sub> = 68 min .....	124
Figure 5.5 – Growth transients from the potentiostatic deposition steps of dPPy. Coloured traces are indicative of the total charge passed following successive deposition intervals. Experimental conditions: 0.112 M dPy in 0.1 M NaClO <sub>4</sub> in H <sub>2</sub> O, E = 0.3 V vs Ag wire, t <sub>total</sub> = 68 min .....	124
Figure 5.6 – Plots of film thickness (left) and mass per area (right) as a function of growth charge density as calculated from the electrochemical data (blue) and from the NR data (red) from the potentiostatic growth of dPPy; the coloured traces are the associated fits to the data, the black dotted trace is the linear fit to the NR data .....	125
Figure 5.7 – NR measurements and fits (left) and corresponding SLD profiles (right) for the galvanostatic growth of dPPy performed on FIGARO; the purple trace is the gold measurement prior to deposition. R(Q) datasets are offset by increments of -1 for clarity. Experimental conditions: 0.065 M dPy in 0.1 M NaClO <sub>4</sub> in H <sub>2</sub> O, i = 2 μA cm <sup>-2</sup> , t <sub>total</sub> = 127 min .....	126

Figure 5.8 – Growth transients from successive intervals during the galvanostatic deposition of dPPy. Coloured traces are indicative of the total charge passed following successive deposition intervals. Experimental conditions: 0.065 M dPy in 0.1 M NaClO <sub>4</sub> in H <sub>2</sub> O, $i = 2 \mu\text{A cm}^{-2}$ , $t_{\text{total}} = 127 \text{ min}$ .....	126
Figure 5.9 – Plots of film thickness (left) and mass per area (right) as a function of growth charge density as calculated from the electrochemical data (blue) and from the NR data (red) from the galvanostatic growth of dPPy in 0.065 M monomer solution; the coloured traces are the associated fits to the data, the black dotted trace is the linear fit to the NR data.....	127
Figure 5.10 – NR measurements and fits (left) and corresponding SLD profiles (right) for the galvanostatic growth of dPPy performed on SURF; the purple trace is the gold measurement prior to deposition. R(Q) datasets are offset by increments of -1 for clarity. Experimental conditions: 0.112 M dPy in 0.1 M NaClO <sub>4</sub> in H <sub>2</sub> O, $i = 2.4 \mu\text{A cm}^{-2}$ , $t_{\text{total}} = 85 \text{ min}$ .....	127
Figure 5.11 – Growth transients from successive intervals during the galvanostatic deposition of dPPy. Coloured traces are indicative of the total charge passed following successive deposition intervals. Experimental conditions: 0.112 M dPy in 0.1 M NaClO <sub>4</sub> in H <sub>2</sub> O, $i = 2.4 \mu\text{A cm}^{-2}$ , $t_{\text{total}} = 85 \text{ min}$ .....	128
Figure 5.12 – Plots of film thickness (left) and mass per area (right) as a function of growth charge density as calculated from the electrochemical data (blue) and from the NR data (red) from the galvanostatic growth of dPPy in 0.112 M monomer solution; the coloured traces are the associated fits to the data, the black dotted trace is the linear fit to the NR data.....	128
Figure 5.13 – NR measurements and fits (left) and corresponding SLD profiles (right) for the galvanostatic growth of hPPy performed on SURF; the purple trace is the gold measurement prior to deposition. R(Q) datasets are offset by increments of -1 for clarity. Experimental conditions: 0.112 M hPy in 0.1 M NaClO <sub>4</sub> in D <sub>2</sub> O, $i = 2.4 \mu\text{A cm}^{-2}$ , $t_{\text{total}} = 35 \text{ min}$ .....	129
Figure 5.14 – Growth transients from successive intervals during the galvanostatic deposition of hPPy. Coloured traces are indicative of the total charge passed following successive deposition intervals. Experimental conditions: 0.112 M hPy in 0.1 M NaClO <sub>4</sub> in D <sub>2</sub> O, $i = 2.4 \mu\text{A cm}^{-2}$ , $t_{\text{total}} = 35 \text{ min}$ .....	130

Figure 5.15 – Plots of film thickness (left) and mass per area (right) as a function of growth charge density as calculated from the electrochemical data (blue) and from the NR data (red) from the galvanostatic growth of hPPy; the coloured traces are the associated fits to the data, the black dotted trace is the linear fit to the NR data.....	130
Figure 5.16 – SLD profiles of the films measured at the open circuit potential following the final growth stage (black), held oxidised at $E = 0.2$ V (blue) and reduced at $E = -0.5$ V (red); insets show the corresponding reflectivity data and fits from which these are derived, offset for clarity .....	134
Figure 5.17 – Cyclic voltammograms of NR samples acquired at $50 \text{ mV s}^{-1}$ in fresh electrolyte solution following film deposition; presented are the traces for dPPy grown potentiodynamically (red), potentiostatically (light blue), galvanostatically (green) from $0.112 \text{ M}$ (full lines) and $0.065 \text{ M}$ (dashed line) monomer solutions, and hPPy grown galvanostatically from $0.112 \text{ M}$ monomer solution (dark blue) .....	136
Figure 5.18 – Cyclic voltammograms of the dPPy films grown potentiostatically (light blue) and galvanostatically from $0.065 \text{ M}$ monomer solution (dashed green) acquired at $50 \text{ mV s}^{-1}$ following the NR measurement in which the films were held in a reduced state at $E = -0.5 \text{ V}$ .....	137
Figure 5.19 – AFM images of the surface of each film produced during the <i>in situ</i> deposition experiments; image labels refer to Table 5.8 .....	139
Figure 5.20 – Transients recorded during the growth of sample I showing a 15 interval growth protocol with a current density of $2 \mu\text{A cm}^{-2}$ ; inset shows a magnification of the transients during earlier stages of growth.....	140
Figure 5.21 – Cyclic voltammograms of the PPy films grown from $0.112 \text{ M}$ (full lines) and $0.065 \text{ M}$ (dashed lines) monomer solutions to a charge density of $12.24 \text{ mC cm}^{-2}$ ; the left panel shows results from cycling at $100 \text{ mV s}^{-1}$ immediately after growth and the right panel shows cycling at the same scan rate following further cycling at slower scan rates.....	141
Figure 6.1 – AFM images of the polymer surface for PEDOT films grown under potentiodynamic (A), potentiostatic (B), and galvanostatic (C) conditions from $0.003 \text{ M}$ EDOT in $0.3 \text{ M LiClO}_4$ ; the images are numbered according to the samples listed in Table 6.4.....	158

Figure 6.2 – AFM images of the polymer surface of PEDOT films grown potentiodynamically (A), potentiostatically (B) and galvanostatically (C) from 0.003 M EDOT in 0.3 M H <sub>2</sub> SO <sub>4</sub> .....	159
Figure 6.3 – AFM images of the polymer surface of the scaled up PEDOT samples on glass substrates.....	160
Figure 6.4 – NR measurements and fits (left) and corresponding SLD profiles (right) for the potentiodynamic growth of PEDOT in which the polymer is modelled as a single layer; the purple trace is the gold measurement prior to deposition. R(Q) datasets are offset by increments of -1.5 for clarity. Experimental conditions: 0.003 M EDOT in 0.3 M LiClO <sub>4</sub> in D <sub>2</sub> O, E : [-0.7 V – E <sub>max</sub> ] vs Ag wire, v = 150 mVs <sup>-1</sup> , i <sub>max</sub> = 0.24 mA cm <sup>-2</sup> , 81 cycles .....	161
Figure 6.5 – NR measurements and fits (left) and corresponding SLD profiles (right) for the final stages (Q <sub>g</sub> = 9.47, 11.73 and 15.16) of the potentiodynamic growth of PEDOT in which the polymer is modelled as two distinct layers; R(Q) datasets are offset by increments of -1.5 for clarity .....	162
Figure 6.6 – Cyclic voltammograms recorded during the potentiodynamic growth of PEDOT. Experimental conditions: 0.003 M EDOT in 0.3 M LiClO <sub>4</sub> in D <sub>2</sub> O, E : [-0.7 V – E <sub>max</sub> ] vs Ag wire, v = 150 mVs <sup>-1</sup> , i <sub>max</sub> = 0.24 mA cm <sup>-2</sup> , 81 cycles .....	163
Figure 6.7 – Plots of film thickness (left) and mass per area (right) as a function of growth charge density as calculated from the electrochemical data (blue) and from the single layer fits to the NR data (red) from the potentiodynamic growth of PEDOT; the coloured traces are the associated fits to the data, the black dotted trace is the linear fit to the NR data .....	163
Figure 6.8 – NR measurements and fits (left) and corresponding SLD profiles (right) for the potentiostatic growth of PEDOT; the purple trace is the gold measurement prior to deposition. R(Q) datasets are offset by increments of -1.5 for clarity. Experimental conditions: 0.003 M EDOT in 0.3 M LiClO <sub>4</sub> in D <sub>2</sub> O, E = 0.55 V vs Ag wire, t <sub>total</sub> = 18 min .....	164
Figure 6.9 – NR measurements and fits (left) and corresponding SLD profiles (right) for the final stages (Q <sub>g</sub> = 11.7 and 15.68) of potentiostatic growth of PEDOT in which the polymer is modelled as two distinct layers; R(Q) datasets are offset by increments of -1.5 for clarity .....	165

Figure 6.10 – Growth transients from successive steps during the potentiostatic growth of PEDOT. Coloured traces indicate the total charge following deposition intervals. Experimental conditions: 0.003 M EDOT in 0.3 M LiClO <sub>4</sub> in D <sub>2</sub> O, E = 0.55 V vs Ag wire, t <sub>total</sub> = 18 min .....	166
Figure 6.11 – Plots of film thickness (left) and mass per area (right) as a function of growth charge density as calculated from the electrochemical data (blue) and from the single layer fits to the NR data (red) from the potentiostatic growth of PEDOT; the coloured traces are the associated fits to the data, the black dotted trace is the linear fit to the NR data .....	166
Figure 6.12 – NR measurements and fits (left) and corresponding SLD profiles (right) for the galvanostatic growth of PEDOT; the purple trace is the gold measurement prior to deposition. R(Q) datasets are offset by increments of -1.5 for clarity. Experimental conditions: 0.003 M EDOT in 0.3 M LiClO <sub>4</sub> in D <sub>2</sub> O, i = 24 μA cm <sup>-2</sup> , t <sub>total</sub> = 12 min .....	167
Figure 6.13 – NR measurements and fits (left) and corresponding SLD profiles (right) for the final stages (Q <sub>g</sub> = 14.52, 15.97 and 17.42) of galvanostatic growth of PEDOT in which the polymer is modelled as two distinct layers; R(Q) datasets are offset by increments of -1.5 for clarity .....	168
Figure 6.14 – Growth transients from successive steps during the galvanostatic growth of PEDOT. Coloured traces indicate the total charge following deposition intervals. Experimental conditions: 0.003 M EDOT in 0.3 M LiClO <sub>4</sub> in D <sub>2</sub> O, i = 24 μA cm <sup>-2</sup> , t <sub>total</sub> = 12 min .....	169
Figure 6.15 – Plots of film thickness (left) and mass per area (right) as a function of growth charge density as calculated from the electrochemical data (blue) and from the single layer fits to the NR data (red) from the galvanostatic growth of PEDOT; the coloured traces are the associated fits to the data, the black dotted trace is the linear fit to the NR data .....	169
Figure 6.16 – SLD profiles of the films produced under potentiodynamic (A), potentiostatic (B) and galvanostatic (C) conditions, measured at the open circuit potential following the final growth stage (black), held oxidized at E = 0.4 V (blue) and reduced at E = -0.5 V (red); insets show the corresponding reflectivity data and fits from which these are derived. The model consisted of a single polymer layer with a rough outer interface. R(Q) datasets are offset by increments of -1 for clarity .....	171

Figure 6.17 – SLD profiles of the potentiodynamic (A), potentiostatic (B) and galvanostatic (C) films measured at the open circuit potential following the final growth stage (black), held oxidized at  $E = 0.4$  V (blue) and reduced at  $E = -0.5$  V (red); insets show the corresponding reflectivity data and fits from which these are derived. The model consisted of the polymer being divided into two distinct layers. R(Q) datasets are offset by increments of -1 for clarity ..... 173

Figure 6.18 – Cyclic voltammograms of PEDOT films grown potentiodynamically (red), potentiostatically (blue) and galvanostatically (green), acquired at  $50 \text{ mV s}^{-1}$  in fresh electrolyte solution following film deposition..... 175

Figure 6.19 – AFM images of the surface of PEDOT films grown potentiodynamically (A), potentiostatically (B) and galvanostatically (C) during *in situ* NR measurements. 176

## Abbreviations

AFM – atomic force microscopy  
CNT – carbon nanotube  
CV – cyclic voltammogram  
dPPy – deuterated polypyrrole  
dPy – deuterated pyrrole  
EC – electrochemical  
EDOT – (3,4-ethylenedioxythiophene)  
EQCM – electrochemical quartz crystal microbalance  
GS – galvanostatic  
hPPy – hydrogenous polypyrrole  
IPA – isopropanol  
MPTS – (3-mercaptopropyl)-trimethoxysilane  
ND – nanodiamond  
NR – neutron reflectometry  
OCP – open circuit potential  
PANI – polyaniline  
PD – potentiodynamic  
PEDOT – poly(3,4-ethylenedioxythiophene)  
PPy - polypyrrole  
PS – potentiostatic  
Py - pyrrole  
SAD – surface area difference  
SDS – sodium dodecyl sulphate  
SLD – scattering length density

## Chapter 1 – Introduction

In a society that is irreversibly reliant on all forms of energy to power transport, appliances and electronic devices of all shapes and sizes, there is substantial research directed at finding novel solutions for how energy is produced, stored and distributed. The field of intrinsically conducting polymers, also known as electroactive polymers, has attracted great interest in the context of batteries<sup>1</sup>, capacitors<sup>2,3</sup> and photovoltaic cells<sup>4</sup>. The versatility of polymers, allowed by their low cost and ease of manufacture, is already recognised but their electrochemical properties still need enhancing and tuning; for this, extensive characterisation and understanding of their structure and the mechanisms by which they transfer charge is indispensable. The following studies will seek to relate the electrochemical and physical behaviour of polymer films and to better understand the properties that make them suitable and desirable for energy storage. Neutron reflectometry (NR) has unique capability in resolving changes in internal structure brought about by the process of solvation<sup>5</sup>, a key determinant of electrochemical behaviour. The overarching aim of the project is therefore to extend and enhance the use of neutron based techniques in the area of electrochemistry generally and more specifically in the context of electroactive polymer films. This research will seek to further develop the field of NR for dynamic studies in conjunction with electrochemical techniques to enable *in situ* and simultaneous measurements that will hopefully lead to more complete characterisation of conducting polymer systems.

This chapter will provide an overview of the work that has already been done in the characterisation of electroactive polymers, focussing on the effects of variables in the deposition method as well as the role of carbon composites. This section will also examine the studies that have previously combined neutron reflectometry and electrochemical techniques.

## 1.1 Electroactive polymers

Electrical conductivity arises from the movement of electrons or ionic charge carriers to produce a flow of charge within a material. The high conductivity of metals is attributed to the delocalisation of electrons around the atoms. Similarly in conducting polymers which are composed of aromatic monomers, the alignment of electrons in the  $p_z$  orbitals resulting from the  $\pi$ -bonding along the polymer backbone, leads to the delocalisation of electrons that facilitates the transfer of charge<sup>6,7</sup>.

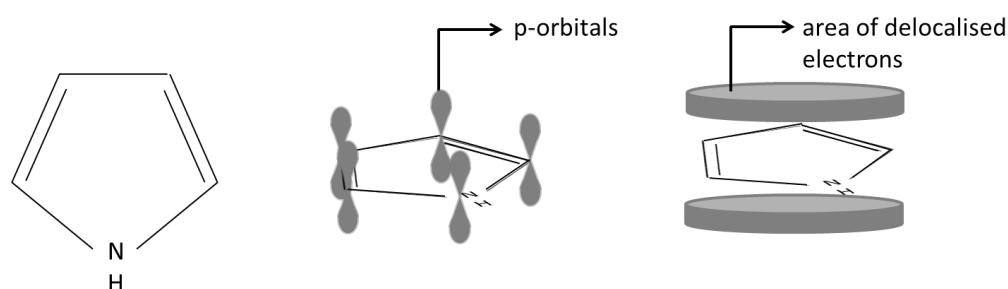


*Figure 1.1 – Illustration of delocalisation of electrons in the case of the monomer pyrrole which, once polymerised, leads to conductivity along the polymer chains*

This natural conductivity has greatly expanded the scope of research into energy storage devices such as batteries and capacitors, as the intrinsic properties of polymer systems make them increasingly desirable over their heavy and expensive metal-based counterpart. Three families of polymer have been of particular interest to researchers in this field, namely those based on polypyrrole (PPy)<sup>8</sup>, polyaniline (PANI)<sup>9</sup> and polythiophenes; a widely studied example of the latter group is poly(3,4-ethylene dioxythiophene) (PEDOT)<sup>10,11</sup>. These have been copolymerised<sup>12,13</sup> and/or combined with various nanoparticles<sup>3</sup> and additives<sup>14</sup> to form composites in order to improve properties such as conductivity, charge density and cycleability.

Several techniques for creating polymer films have been investigated, from the ‘wet chemistry’ methods such as electrodeposition<sup>7</sup>, where the chosen monomer is polymerised electrochemically during the deposition process, to more mechanical methods in which the monomer has already been chemically polymerised prior to deposition such as blade- or spin-coating<sup>15</sup>. The latter are often favoured in industrial applications as they can be easily adapted to large scale production once successful polymer film formulations have been established. However, research suggests that the

method by which a film is produced can affect the morphology of the film<sup>16</sup> and therefore alter its chemical and mechanical properties<sup>17</sup>. Consequently the choice of deposition technique must be considered alongside the choice of additives or chemical and structural modifications to the polymer system when seeking to favour particular characteristics for a specific application.

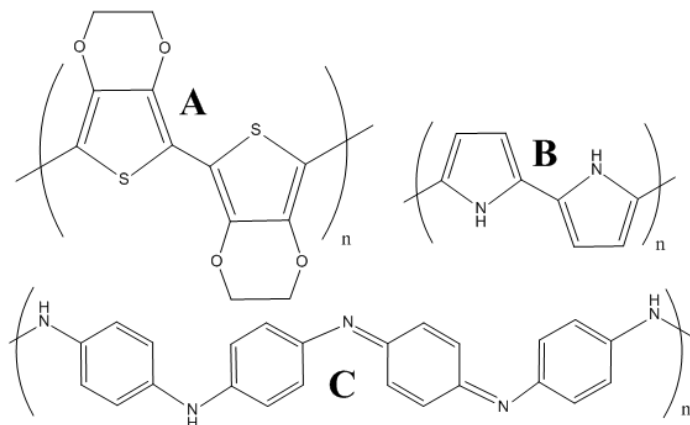


Figure 1.2 – Structures of PEDOT (A), PPy (B), PANI (C)

Snook et al's review of the field of conducting polymers for use in supercapacitors and electrodes highlights the extensive work carried out in this area over the last ten years. The authors conclude that cycle life remains a significant problem in these systems<sup>2</sup>. In the case of PPy and PEDOT, the redox process results in loss or gain of charge from the area of delocalised electrons along the chain; this charge is then compensated by the influx of ions. In the case of PANI there is also an exchange of protons on the nitrogen situated between rings along the chain.

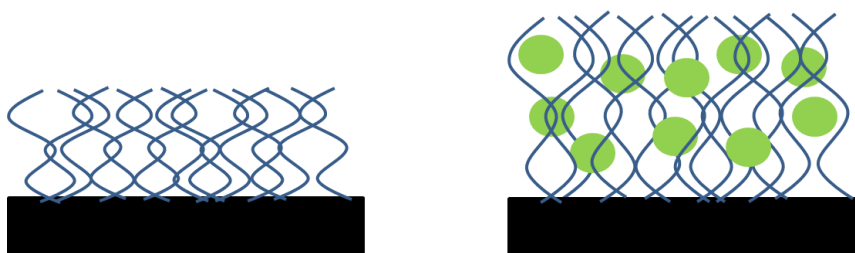
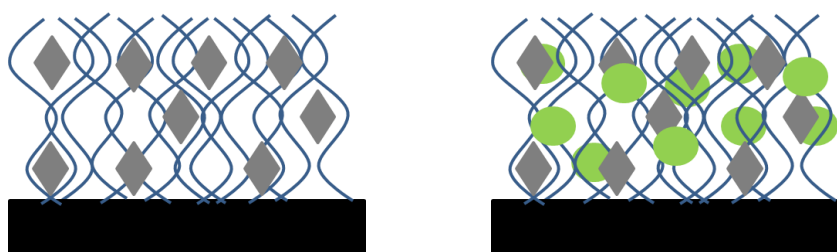


Figure 1.3 – Schematic of the process of ion incorporation showing a dry film structure (left) and the solvated structure (right) in which ions penetrate the film and cause it to swell

The electroactivity of the film will therefore be affected by the facility with which ions can penetrate the film to balance the charge. Given the movement of ions entering and exiting a polymer film during redox cycling, it is recognised that the necessary change

in volume (swelling and shrinking) of the polymer matrix leads to stresses within the films causing structural degradation that subsequently affects the conductivity and mechanical strength of the polymer<sup>2,3</sup>.

In attempts to circumvent this problem, carbon based additives such as carbon nanotubes have been incorporated into films, creating internal space that allows the composite film to adapt to volume changes, and these have demonstrated greater stability and conductivity<sup>2,3,10</sup>. The enhanced porosity brought about by these nanostructures is believed to increase conductivity by increasing the internal surface area available for ion exchange within the polymer film<sup>2,18</sup>. These structural features of porosity and surface area are all related to the spatial distribution of the polymer and additional composites within the film and this makes these systems ideal subjects for studies using neutron reflectivity.



*Figure 1.4 – Conceptual diagram of the role of carbon composites in creating space within the polymer matrix (left) that readily allows the incorporation of ions (right) without resulting in the mechanical strains brought about by swelling*

### 1.1.1 Polypyrrole

Reviewed in 1997 by Vernitskaya and Efimov, PPy was already recognised as a promising material for applications in batteries, capacitors, sensors, biosensors and coatings to name a few<sup>19</sup>. It is no surprise therefore that, more than fifteen years later, the number of publications relating to this polymer is considerable. This section will not be a complete review of the properties and applications of PPy but will seek to discuss the work that has been done with regards to understanding the factors that affect the polymerisation and deposition of these films.

It is widely accepted that a number of variables in the deposition protocol can distinctly affect the electrochemical and structural properties of electroactive polymer

films<sup>7,19</sup>. Substrates<sup>20</sup>, solvents, pH, temperature and, of course, electrochemical control function are just a few of the experimental parameters that have been explored<sup>7</sup>.

The roughness of electrode surfaces is thought to be a determining factor with regards to the stability of PPy films<sup>20</sup>. Li et al suggest that increased roughness promotes better adhesion due to the increased active surface area. In their study, the nature of the electrode itself appeared to have little bearing on the polymer properties, with each sample demonstrating a similar electrochemical response. The effect of roughness had previously been shown to improve conductivity in the case of PPy deposited on gold electrodes, where the electrochemical roughening process produced surface species that subsequently acted in a catalytic manner in the electropolymerisation process<sup>21</sup>.

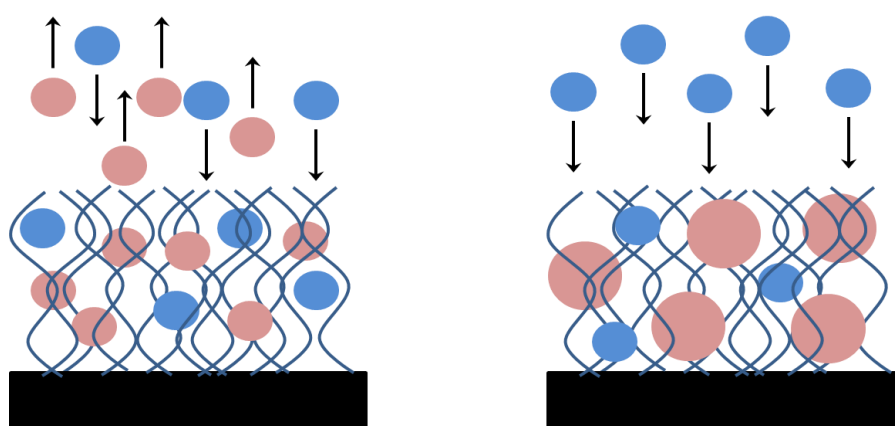


*Figure 1.5 – Schematic of the process of ion exchange in which both anions and cations move in and out of the film to balance charge in response to oxidation (left) and in the case where a large anion is trapped within the polymer matrix such that only the cationic species is mobile (right)*

PPy can be deposited from aqueous or organic solutions. In organic media, a small volume of water is nevertheless required to enable proton elimination. In aqueous solutions there is a risk of nucleophilic attack on intermediates during the polymerisation process<sup>17</sup>. Within the deposition solution, the pH and dopant species can also have an effect on the properties of the film produced. In 1998, Shimoda and Smela explored the effect of pH in the case of PPy doped with a large anionic surfactant, dodecylbenzenesulfonate (DBS)<sup>22</sup>. The use of such a large dopant was designed to limit the movement of ions during charge and discharge of the film since the anion would be trapped within the polymer matrix, leaving only small cations to move between the film and the electrolyte solution. Most work had previously been

done with smaller, more mobile anionic species. They state that these studies had revealed better film conductivities when synthesised in a low pH solution, although it is noted that for dopants such as DBS the pH has little effect on conductivity. In fact, their results confirmed that the electrodeposition was not affected by the pH in the range pH 3 – 10. They attributed this to the immobility of the dopant. The review by Sadki et al also mentions the fact that aromatic surfactant as dopants have been reported to stabilise and improve the mechanical properties of PPy films<sup>7</sup>.

The work by Otero and De Larreta in the late 1980's investigated the morphological differences brought about by the potentiostatic or potentiodynamic deposition of PPy and found that, while the former produced dendrite-like features in the films and poor adhesion, the latter produced smooth, homogeneous and well-adhering films<sup>23</sup>. They comment that the features of the films produced using a constant potential were similar to those reported for films generated galvanostatically. In 1999, Zhou and Heinze reported that the features of the cyclic voltammograms (CVs) of PPy films differed according to whether they were produced by potentiodynamic or galvanostatic deposition<sup>24</sup>. Their work also explored the effect of different potential windows or current densities in the cases of potentiodynamic or galvanostatic growth respectively. The results indicated that subtle variations in the electrodeposition protocol can have a significant impact on the electrochemical response of the films produced, suggesting different structural features within the polymer matrix.

In their work investigating the different electrode substrate materials, Li et al briefly explore the effect of the three different growth protocols<sup>20</sup>. They found that the galvanostatic deposition produced the most electroactive film, whereas the potentiostatic growth resulted in comparatively poor redox capacity. In 2009, Ansari states that the use of constant current is also the most reproducible method for producing PPy films<sup>25</sup>. While these studies all offer some insight into the effects of the electrodeposition method, none of them exclusively compare all three techniques.

In addition to studies investigating the role of the electrochemical control functions, the effect of a pulsed or layer-by-layer deposition has also been explored. Li and Zhitomirsky reported in 2012 that the capacitive behaviour of PPy films grown by continuous galvanostatic polymerisation compared poorly to films produced by an ON/OFF growth protocol<sup>26</sup>. They attributed this increase in specific capacitance to the

smaller size of the granular surface features observed in films grown using the pulse deposition process. This method also resulted in greater polymerisation efficiency and the authors suggest that this may result from the replenishing of monomer and electrolyte at the electrode surface during the OFF periods. In the work by Sangian et al, the layer-by-layer galvanostatic deposition protocol also included a rinsing step between layers<sup>27</sup>. They showed a cross-sectional image of a film produced using their sequential polymerisation (SEP) process which revealed distinct interfaces within the polymer matrix but did not indicate any difference in porosity compared to the continuously deposited films. The films prepared by the SEP method were found to produce films with better mechanical properties and higher conductivity.

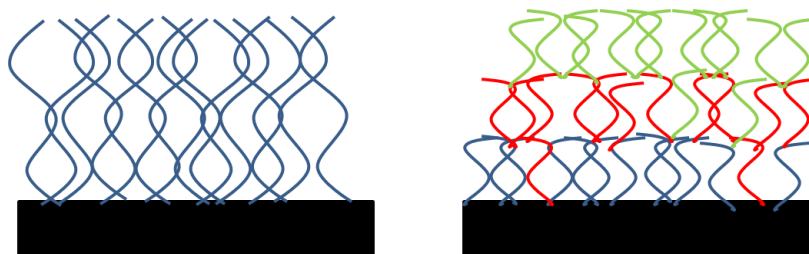


*Figure 1.6 – Conceptual illustration of film structure resulting from continuous polymerisation (left) and sequential polymerisation steps (right) which may fill in gaps within previous layers as well as produce distinct interfaces*

### 1.1.2 Poly(3,4-ethylene dioxythiophene)

PEDOT has been extensively studied for use in energy-storage<sup>28</sup> and photovoltaic<sup>29</sup> devices, as well as in biological applications such as sensors<sup>30</sup> and as coatings for neuroprosthetic electrodes<sup>31,32</sup>. As in the case of PPy mentioned above, there have been numerous studies into the effect on the characteristics of PEDOT films caused by variables in the deposition method. Again, while the choice of current or potential range may be the most obvious culprits in producing different properties, the choice of counter ions<sup>33,34</sup> and deposition medium<sup>35</sup> have all been found to have an effect on film structure or the electrochemical properties.

The monomer, EDOT, has a very low solubility in water and is therefore often polymerised in organic media or in aqueous solutions with added surfactant. Sakmeche et al reported that the use of sodium dodecyl sulphate (SDS) in an aqueous solution for the electrosynthesis of PEDOT produced films with a more compact morphology

and greater electrochemical stability than those prepared in acetonitrile<sup>36</sup>. PEDOT films can however be successfully produced in surfactant-free aqueous media, although ensuring a homogeneous solution requires the use of very low monomer concentrations<sup>37</sup>. Randriamahazaka et al highlighted the importance of the choice of deposition media when they compared electrodeposition processes in acetonitrile and an ionic liquid<sup>38</sup>. They proposed a model which identifies two types of nucleation mechanisms, progressive and instantaneous, which occur according to the deposition medium.

In 2010, Kozak reported the effect of a number of deposition variables, including a series of washing regimes of the electrode surface prior to deposition<sup>39</sup>. He concluded that these cleaning protocols did not affect the electrochemical properties of the PEDOT film but did affect film adhesion which was evaluated with a tape test. Deposition on a silver electrode surface was found to be very poorly adhesive while films formed on indium tin oxide presented the lowest impedance, demonstrating that the nature of the electrode can affect film properties. Two dopant species were investigated, chlorine and polystyrene sulfonate (PSS), with the latter producing more stable films.

The choice of polymerisation potential has also been explored with regards to its effect on morphological and electrochemical features. In 2000, Niu et al investigated the effect of the switching potential in potentiodynamically grown films, revealing that the higher potential limit produced more porous and crystalline films as opposed to the lower potential which resulted in a more compact, amorphous structure<sup>40</sup>. Melato et al also explored the role of polymerisation potential but in the context of potentiostatic deposition<sup>41</sup>. Interestingly, they reported no difference in the electrochemical properties of the films produced at different potentials for the same overall growth charge.

Melato et al extended their study of PEDOT deposition variables to include the effect of scan rate and dopant species<sup>34</sup>. They found that slower scan rates during potentiodynamic deposition resulted in a more crystalline structure and greater film porosity was obtained from faster cycling. The size of the supporting electrolyte also contributed to these structural differences with films produced in LiClO<sub>4</sub> exhibiting greater crystallinity than those deposited from solutions containing TBAPF<sub>6</sub>. They also

reported a shift in polymerisation potential according to the nature of the supporting electrolyte and observed that the polymerisation efficiency was greatest for films deposited from  $\text{LiClO}_4$  solutions. Electrodeposition in the presence of this smaller cation also resulted in more electroactive films. Interestingly, Eliseeva et al reported no significant effect caused by either solvent (acetonitrile and propylene carbonate) or the supporting electrolytes ( $\text{LiClO}_4$ ,  $\text{Bu}_4\text{NBF}_4$  and  $\text{Bu}_4\text{NPF}_6$ ) on the redox capacitance of PEDOT films<sup>42</sup>.

In this work, the effect of different deposition methods on the electrochemical and structural features of PEDOT is examined, focussing on electropolymerisation techniques as opposed to chemical polymerisation and mechanical deposition methods. In a study published in 2008, Patra et al investigated the effect of electrochemical control function on the deposition of PEDOT films on stainless steel using scanning electron microscopy (SEM)<sup>43</sup>. They note that the galvanostatic (GS) and potentiostatic (PS) modes are, by definition, continuous growth mechanisms as they employ constant current and potential respectively. In contrast, the potentiodynamic (PD) mode results in a layer-by-layer growth due to the cycling of the potential in and out of the potential range in which polymerisation occurs. Their results show that at low current densities or potential ranges, the surface morphology is globular. At higher currents or potentials, the globular structure becomes more porous in the case of GS and PS growth, whereas the PD growth exhibits more fibrous surface structures. Ultimately, these differences were dependent on the rate of deposition.

A similar study was undertaken by Melato et al in 2010 using AFM<sup>16</sup>. They observed the same morphological differences between films grown by PS and PD methods. Using *in situ* AFM they were able to examine the evolution of film structure during the deposition process which revealed compact granular clusters in the case of PS growth and the development of fibres during PD growth. They attributed the latter to the reduction of the film occurring between layers of deposition which allows “structural rearrangement”. They note that this reorganisation also occurs in the films grown by the PS method but takes place once the films are cycled in monomer-free electrolyte solutions following deposition.

### 1.1.3 Polymer-carbon composites

The different structures of carbon nanoparticles can be roughly divided into three categories: the fullerenes, the nanotubes and the nanodiamonds, all of which have been used to form composites in polymeric systems. In 2006, Hu et al produced a comprehensive review of the role and properties of carbon nanostructures<sup>44</sup>. They note that a structure of the fullerene variety known as a 'buckyball' can be doped to form conducting material. With regards to carbon nanotubes (CNT), which have been described as ballistic conductors<sup>45</sup>, they explain that the graphite forming the tube is itself a semimetal and that the electronic properties of the nanoparticles "are controlled by the cylindrical symmetry of the structure". The numerous structural properties improved by the incorporation of CNT include increasing the tensile strength, the Young's modulus and the ductility of the composite. Interestingly, the CNT can also alter the electrical properties of the polymer. Finally, the authors describe how the addition of nanodiamonds (ND) is found to increase the mechanical strength of polymer films, possibly through enabling a cross-linking mechanism<sup>44</sup>.

The exceptional electronic properties of CNT have made them a popular composite in the field of electrochemistry, however ND are becoming increasingly studied as they are in fact much less expensive to produce<sup>44</sup>. Furthermore, it has been demonstrated that even low quantities of the particles can dramatically affect the properties of composite materials<sup>46</sup>. A recent review of the role of polymer-ND composites in Li-ion batteries reports that the nanoparticles can be used to improve thermal, electronic and structural properties in composite films and have already been tested as electrodes in battery configurations<sup>1</sup>. The successful functionalization of the ND surface has also been reported<sup>47,48</sup>, providing added versatility in terms of solubility and reactivity.

ND particles present interesting electronic features in part due to their spherical structure which offers a large surface to volume ratio and consists of an  $sp^3$  core and an  $sp^2$  outer shell<sup>47</sup>. The graphitic surface in itself is conductive but also allows the formation of a variety of functional groups which can enhance or inhibit electron transfer reactions<sup>49</sup>. The particles are often hydrophilic<sup>47</sup> due to the electrostatic potential of the surface, which also promotes particle-particle interactions, often leading to agglomeration<sup>50</sup>.

It is generally acknowledged that the electronic properties vary according to the way in which the ND particles are prepared and thus the type of functional groups present and the ratio of graphitic surface carbon. Feoktistov et al examined how boron content and the use of methane in the preparation of boron-doped ND films affected the conductive properties of the samples<sup>51</sup>. Their results indicated that increasing the amount of boron enhanced conductivity however higher concentrations of methane decreased the conductivity for a given level of boron doping. Koroleva et al investigated the effect of different treatments on the conductivity and sedimentation stability of aqueous ND solutions. Their results indicate that exposing the particles to ozone gas produced the most conductive sample, while the largest agglomerate size and greater flocculation was observed for particles that had previously been heated in a dry chlorine atmosphere<sup>49</sup>.

The conductivity of undoped ND is often attributed to the redox activity of the surface bound functional groups, notably the oxygen-containing moieties. Zang et al therefore explored the effect of annealing with regards to modifying the electronic properties<sup>52</sup>. Their work revealed that annealing in vacuum resulted in the removal of oxygen-containing functional groups and produced slower electron transfer kinetics. The surface groups could be reformed by annealing in air. The work by Welch et al in 2014 however suggests that the  $sp^3$  ordered carbon in the core of the ND particles may in fact play a greater role in charge transfer processes<sup>53</sup>.

The electrochemical activity of ND has also been explored for the purposes of producing novel electrode materials. Zang et al used annealed ND powder as an electrode and reported stability in their chosen electrolyte in a potential range spanning 3 V<sup>54</sup>. Holt et al investigated the electrochemical properties ND by creating a ND-modified boron-doped diamond electrode. The purification protocol of the ND particles involved annealing in air. Potential cycling in solutions of differing pH produced different electrochemical responses, indicating that the surface bound functional groups were the source of the electrochemical activity observed<sup>55</sup>.

When forming composites with conducting polymers, ND have been reported to affect the morphology of PANI polymer clusters when included in the deposition solution for potentiostatic and potentiodynamic growth<sup>56</sup>. PANI-ND composites prepared by chemical polymerisation and mixing were found to produce films that

were significantly more stable than pristine PANI films, displaying greater durability when exposed to extensive cycling<sup>57</sup>. The authors suggest this stability is due to the ND providing greater structural strength to the polymer matrix. Gomez et al report that, in the formation of PANI-ND nanocomposites, the individual components retain their properties however the incorporation of ND extends the potential range in which the redox properties can be studied<sup>58</sup>.

Although there have been numerous publications reporting PEDOT-CNT composites, with promising results for applications notably in drug delivery<sup>59</sup>, neurotransmitter sensors<sup>60</sup> and neural stimulation<sup>61</sup>, there has so far been very little work addressing PEDOT-ND composites. Ispas et al deposited such films potentiodynamically and explored the film structure and composition using electrochemical quartz microbalance, scanning electron microscopy and X-ray photoelectron spectroscopy<sup>62</sup>. They reported that the composite film was less porous than the pristine PEDOT film and that the ND also appeared to promote greater film homogeneity. They also observed that the quantity of ND incorporated into the films varied according to the composition of the deposition solution. More recently, Tamburri et al created composite films from the chemical polymerisation of EDOT in the presence of ND<sup>63</sup>. In their work, the ND were found to have a catalytic effect on the polymerisation process and produced longer polymer chains than those found in the pure PEDOT films. They also report enhanced mechanical properties.

## 1.2 Neutron reflectometry

### 1.2.1 Studies of conducting polymers

Over the last two decades, neutron based techniques have been explored as a means of studying electroactive polymer films for the purposes of modifying electrode surfaces. It was demonstrated that neutron reflectivity could be used to study a polymer film at different stages of potentiodynamic deposition as well as in selectively un-doped or p-doped states<sup>5</sup>. The results of these experiments indicated that the gradual thickening of the film during deposition could be observed via neutron reflectivity measurements and highlighted changes in film density as the growth progressed. The effects of doping were also investigated and revealed that the structural changes resulting from this could persist after the film was returned to the undoped state. Another study examined how the polymerisation method used affects the interfacial structure in bilayer systems and the correlation with electrochemical properties<sup>64</sup>. The results showed that electroprecipitation of a polymer onto another to form a bilayer produces segregated layers with a distinct interface whereas electropolymerisation resulted in an entirely composite material with the deposited polymer diffusing into the 'substrate' polymer layer. The study of this buried interface is an ideal example of the benefits of using neutron reflectometry in the characterisation of such systems.

In 1999, Wilson et al published their investigation of the effect of counter ions and redox states on the internal structure of a metallopolymer film<sup>65</sup>. They notably made use of different contrasts in solution to highlight the solvent content within the polymer films. While the results revealed the variations in solvation in internal structure, the reflectivity data also revealed a loose surface structure of diffuse oligomers which had thus far remained undetected by other techniques. Further to this work, in 2003 Glidle et al described the effects of applied potential and electrolyte concentration on the solvation and salt distribution within polyvinylferrocene films. In this case, the use of different contrast solutions allowed the electrolyte to be distinguished from the solvent.

While these initial experiments probed static systems in that the chemistry in the films was unchanging throughout the neutron reflectivity measurements, it is now possible

to dynamically probe electrochemical systems and therefore monitor changes in film composition and structure on a timescale more suited to the rate of these reactions. The first publication to describe this was the work by Cooper et al in 2004 in which they studied the movement of solvent within the film during cycling of the applied potential<sup>66</sup>. In part, the novelty of their work was the approach to the data acquisition. They used a boxcar integration methodology that involved acquiring short ‘windows’ of reflectivity data at successive intervals as the polymer film was cycled linearly between potential limits. With each cycle, more data points were accumulated in each potential window such as to result in a reflectivity profile for the different points in the cycle.

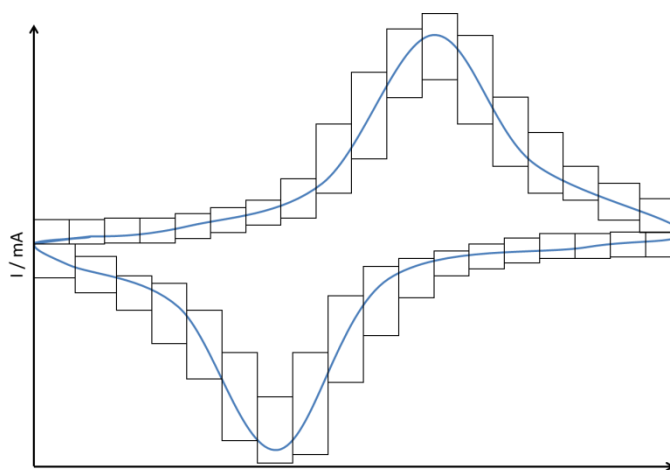


*Figure 1.7 – Illustration of the boxcar integration method applied to a cyclic voltammogram such that each box shows the section of the cycle during which NR data is acquired*

Recent advances in the capabilities of time-of-flight reflectometers mean that fast measurements on the order of 10 s are now achievable. Naturally, the kinetics of the reaction must be such that the sample is not changing significantly during the measurement so for electrochemistry purposes this is still only applicable to slow processes. Furthermore the range of  $Q$  is limited by the restriction to a single angle measurement and the quality of the data is restricted by the flux. There is ongoing research into new instrument components that will address these issues. In particular the work by Cubitt and Stahn has demonstrated that a prism can be used in the place of choppers to ascertain the wavelength range and thereby result in an increase in the flux of neutrons reaching the sample surface<sup>67</sup>.

Further to these instrumental advances, there is increasing interest in using multiple characterisation techniques alongside neutron reflectometry for *in situ* measurements. While this is useful for static, unchanging samples, it is of particular interest to samples required to undergo reactions or transformations during kinetic NR measurements. The simultaneous use of analytical techniques such as cyclic voltammetry and IR or UV-visible spectroscopy<sup>68,69</sup> allows for electrochemical and spectroscopic data to be acquired from the same system during a neutron experiment thus eliminating some of the error associated with characterising a system in different environments at different times.

The fundamental properties of neutrons make them particularly suited to detecting light elements and the study of buried interfaces, allowing structural variations such as thickness, roughness and density, as well as variations in elemental composition to be investigated when studying solvation within thin electroactive polymer films. Not only can the reflectivity profiles of these films provide information on solvation and movement of ions within the system but by the simultaneous use of techniques such as cyclic voltammetry, the electrochemistry within these films can be studied with unprecedented detail. The challenge remains in the design and set up of the experiments that allows for both NR and electrochemical data to be successfully acquired. The facilities providing the neutron beams and instruments will offer advice and assistance in setting up such investigations; however the onus lies with the user to anticipate the material requirements and ensure sufficient forward planning to make the experiments possible and successful.

### 1.2.2 Combining NR and electrochemical techniques

The combination of NR with *in situ* electrochemical techniques has been of great interest to a number of fields of research. The range of techniques made available by the use of a dual purpose cell enables the user to not only perform analytical measurements of their sample but also to drive reactions.

In 2010, Lauw et al described their electrochemical/NR cell designed to allow the study of the electrical double-layer formed at the interface between an ionic liquid and a solid electrode surface<sup>70</sup>. They reported different interfacial structures at different applied potentials. Jerliu et al also developed a cell to perform combined studies of a

silicon electrode in a lithium-ion battery setup<sup>71</sup>. They monitored structural changes in the material during charge and discharge processes and identified the effects of penetration of lithium into the silicon. Veder and co-workers have done extensive work making use of combining electrochemical impedance spectroscopy (EIS) and NR *in situ* to study polymeric systems for use as solid contact ion selective electrodes<sup>72,73,74,75</sup>.

These studies all address fundamental issues relating to applications in energy production or storage, however the advantages of combining electrochemistry with NR is not limited to electroactive systems relating to novel electrode and electrolyte materials. NR has been widely used to study surfactants, proteins and lipid membranes. These types of samples can also benefit from electrochemical characterisation and/or the application of an electric field to drive structural changes. Indeed, Zamlynny et al have published several studies making use of these techniques to investigate surfactant behaviour<sup>76,77,78</sup>. They use electrochemical methods to explore the thermodynamic properties of the system or drive structural reorganisation while using NR to study the interfacial structure. Quite recently, Tronin et al used the combined techniques to explore the effect of a transmembrane electric potential on the structure of a lipid bilayer<sup>79</sup> and Fadda et al studied the effect of voltage on the opening of peptide pores in lipid membrane<sup>80</sup>. Anecdotally, personal discussions with fellow reflectometry users have revealed great interest in using electrochemical methods in their studies of lipid membranes.

Increasingly, neutron instruments have a selection of sample environments available to users such as temperature and pressure controlled environments and sample holders catering to different phases such as liquid or gas containers. What is lacking, however, is equipment that can be adapted to carry out other analytical techniques, such as electrochemistry and spectroscopy, for simultaneous acquisition of data during the neutron experiment. Each neutron facility will engage with the user to integrate additional techniques to neutron experiments, advising on the design and manufacture of custom made cells or devices that can allow connections between instruments for synchronised measurements. Frequently, the problems lie with the instrument to be integrated (potentiostat or spectrometer) as these are not usually designed for use in conjunction with other techniques. As users and facilities continue to innovate and test

these setups, the growing number of publications combining these techniques provides unprecedented insight into these complex systems.

### **1.3 Conclusions**

The substantial number of studies exploring the properties of conducting polymer films has revealed that the electrochemical features are linked to the surface and internal structure of the polymer matrix. While there are numerous factors that affect the polymerisation process, the choice of electrochemical control function has been shown to cause significant differences in the morphology and electrochemical response of polymer films. The effects of the incorporation of carbon nanocomposites have also been explored and found to enhance structural stability resulting in improved electrochemical properties. The penetrating abilities of neutrons and their sensitivity to light elements make NR an ideal tool in the investigation of these systems.

### **1.4 Aims and objectives**

This project contains three distinct studies seeking to further our understanding of the structural features of polymer films that result in different electrochemical behaviours. In a first instance, the subject of carbon additives and their role in modifying the properties of polymer films is explored in the case study of a PEDOT-ND composite. Specifically, the composite films are compared and contrasted with pristine PEDOT samples in order to evaluate the effect of the NDs on the electrochemical response, surface features and internal structure. A complete characterisation is intended to produce not only quantification of the carbon particles present within the film but to understand how they can best be incorporated to improve desirable properties. Thereafter, the effect of the electrodeposition method with regards to variations in structure within the polymer matrix is explored for two of the most studied electroactive polymers: PEDOT and PPy. The aim of these studies is to monitor changes in structure throughout the deposition and following charge/discharge processes by quantifying the solvent content which provides information about accessible sites for charge compensation as well as structural features of porosity and rigidity. The simultaneous use of electrochemical techniques and NR is aimed at providing measurements of structural changes in a sample that may occur as a function of electrochemical control. The results of *in situ* and *ex situ* measurements are then combined to relate structural features to electrochemical properties. In studying the deposition of two different monomers, the resulting structural features, yield efficiency

and charge/discharge properties may be identified as universal for a given electrochemical control function or specific to a polymer type.

The objectives of this work can therefore be summarised as follows:

- Measure the relative solvent content and distribution within a composite film and compare with a pristine film grown from identical conditions
- Identify differences in morphology and electrochemical response brought about by the addition of nanodiamond particles
- Investigate the effect of different electrodeposition protocols on polymerisation efficiency and charge capacity
- Explore the internal structure of films produced by different methods by examining the volume of solvent and its distribution within the films
- Establish whether or not the choice of electrochemical control function for the growth of a polymer produces consistent structural effects for different polymer species.

## 1.5 References

1. Kausar, A., Ashraf, R. & Siddiq, M. Polymer/Nanodiamond Composites in Li-Ion Batteries: A Review. *Polym. Plast. Technol. Eng.* **53**, 550–563 (2014).
2. Snook, G. A., Kao, P. & Best, A. S. Conducting-polymer-based supercapacitor devices and electrodes. *J. Power Sources* **196**, 1–12 (2011).
3. Frackowiak, E., Khomenko, V., Jurewicz, K., Lota, K. & Béguin, F. Supercapacitors based on conducting polymers/nanotubes composites. *J. Power Sources* **153**, 413–418 (2006).
4. Xia, Y. & Ouyang, J. PEDOT-PSS films with significantly enhanced conductivities induced by preferential solvation with cosolvents and their application in polymer photovoltaic cells. *J. Mater. Chem.* **21**, 4927–4936 (2011).
5. Richardson, R. M., Swann, M. J., Hillman, A. R. & Roser, S. J. In situ neutron reflectivity studies of electroactive films. *Faraday Discuss.* **94**, 295–306 (1992).
6. Ferreira, L. F., Souza, L. M., Franco, D. L., Castro, A. C. H., Oliveira, A. A., Boodts, J. F. C., Brito-Madurro, A. G. & Madurro, J. M. Formation of novel polymeric films derived from 4-hydroxybenzoic acid. *Mater. Chem. Phys.* **129**, 46–52 (2011).
7. Sadki, S., Schottland, P., Brodie, N. & Sabouraud, G. The mechanisms of pyrrole electropolymerization. *Chem. Soc. Rev.* **29**, 283–293 (2000).
8. Hojati-Talemi, P. & Simon, G. P. Electropolymerization of Polypyrrole/Carbon Nanotube Nanocomposite Films over an Electrically Nonconductive Membrane. *J. Phys. Chem. C* **114**, 13962–13966 (2010).
9. Hillman, A. R., Dong, Q., Mohamoud, M. A. & Efimov, I. Characterization of viscoelastic properties of composite films involving polyaniline and carbon nanotubes. *Electrochim. Acta* **55**, 8142–8153 (2010).
10. Li, J., Liu, J., Gao, C., Zhang, J. & Sun, H. Influence of MWCNTs doping on the structure and properties of PEDOT:PSS films. *Int. J. Photoenergy* **2009**, 1–5 (2009).
11. Wang, Y. Research progress on a novel conductive polymer–poly(3,4-ethylenedioxythiophene) (PEDOT). *J. Phys. Conf. Ser.* **152**, 012023 (2009).
12. Sönmez, G. & Saraç, A. S. Structural study of pyrrole-EDOT copolymers on carbon fiber micro-electrodes. *Synth. Met.* **135-136**, 459–460 (2003).
13. Tewari, A., Kokil, A., Ravichandran, S., Nagarajan, S., Bouldin, R., Samuelson, L. A., Nagarajan, R. & Kumar, J. Soybean peroxidase catalyzed enzymatic synthesis of pyrrole/EDOT copolymers. *Macromol. Chem. Phys.* **211**, 1610–1617 (2010).

14. Nardes, A. M., Kemerink, M., de Kok, M. M., Vinken, E., Maturova, K. & Janssen, R. A. J. Conductivity, work function, and environmental stability of PEDOT:PSS thin films treated with sorbitol. *Org. Electron.* **9**, 727–734 (2008).
15. Norrman, K., Ghanbari-Siahkali, A. & Larsen, N. B. Studies of spin-coated polymer films. *Annu. Rep. Prog. Chem. Sect. C* **101**, 174 (2005).
16. Melato, A. I., Viana, A. S. & Abrantes, L. M. Influence of the electropolymerisation mode on PEDOT<sub>h</sub> films morphology and redox behaviour — an AFM investigation. *J. Solid State Electrochem.* **14**, 523–530 (2010).
17. Heinze, J., Frontana-Urbe, B. A. & Ludwigs, S. Electrochemistry of conducting polymers - persistent models and new concepts. *Chem. Rev.* **110**, 4724–71 (2010).
18. Liu, R., Duay, J. & Lee, S. B. Heterogeneous nanostructured electrode materials for electrochemical energy storage. *Chem. Commun.* **47**, 1384–404 (2011).
19. Vernitskaya, T. V & Efimov, O. N. Polypyrrole: a conducting polymer; its synthesis, properties and applications. *Russ. Chem. Rev.* **66**, 443 – 457 (1997).
20. Li, C. M., Sun, C. Q., Chen, W. & Pan, L. Electrochemical thin film deposition of polypyrrole on different substrates. *Surf. Coatings Technol.* **198**, 474–477 (2005).
21. Liu, Y.-C., Yang, K.-H. & Wang, C.-C. Enhancements in conductivity and Raman spectroscopy of polypyrrole electropolymerized on electrochemically roughened Au substrates. *J. Electroanal. Chem.* **549**, 151–155 (2003).
22. Shimoda, S. & Smela, E. The effect of pH on polymerization and volume change in PPy(DBS). *Electrochim. Acta* **44**, 219–238 (1998).
23. Otero, T. F. & De Larreta, E. Electrochemical control of the morphology, adherence, appearance and growth of polypyrrole films. *Synth. Met.* **26**, 79–88 (1988).
24. Zhou, M. & Heinze, J. Electropolymerization of pyrrole and electrochemical study of polypyrrole: I . Evidence for structural diversity of polypyrrole. *Electrochim. Acta* **44**, 1733–1748 (1999).
25. Ansari, R. In-situ cyclic voltammetry and cyclic resistometry analyses of conducting electroactive polymer membranes. *Int. J. ChemTech Res.* **1**, 1398–1402 (2009).
26. Li, X. & Zhitomirsky, I. Capacitive behaviour of polypyrrole films prepared on stainless steel substrates by electropolymerization. *Mater. Lett.* **76**, 15–17 (2012).

27. Sangian, D., Zheng, W. & Spinks, G. M. Optimization of the sequential polymerization synthesis method for polypyrrole films. *Synth. Met.* **189**, 53–56 (2014).
28. Liu, R., Cho, S. I. & Lee, S. B. Poly(3,4-ethylenedioxythiophene) nanotubes as electrode materials for a high-powered supercapacitor. *Nanotechnology* **19**, 215710 (2008).
29. Hong, W., Xu, Y., Lu, G., Li, C. & Shi, G. Transparent graphene/PEDOT–PSS composite films as counter electrodes of dye-sensitized solar cells. *Electrochem. Commun.* **10**, 1555–1558 (2008).
30. Xu, G., Li, B., Cui, X. T., Ling, L. & Luo, X. Electrodeposited conducting polymer PEDOT doped with pure carbon nanotubes for the detection of dopamine in the presence of ascorbic acid. *Sensors Actuators B Chem.* **188**, 405–410 (2013).
31. Baek, S., Green, R. A. & Poole-Warren, L. A. The biological and electrical trade-offs related to the thickness of conducting polymers for neural applications. *Acta Biomater.* **10**, 3048–58 (2014).
32. Cui, X. & Martin, D. C. Electrochemical deposition and characterization of poly(3,4-ethylenedioxythiophene) on neural microelectrode arrays. *Sensors Actuators B Chem.* **89**, 92–102 (2003).
33. Blanchard, F., Carré, B., Bonhomme, F., Biensan, P., Pagès, H. & Lemordant, D. Study of poly(3,4-ethylenedioxythiophene) films prepared in propylene carbonate solutions containing different lithium salts. *J. Electroanal. Chem.* **569**, 203–210 (2004).
34. Melato, A. I., Mendonça, M. H. & Abrantes, L. M. Effect of the electropolymerisation conditions on the electrochemical, morphological and structural properties of PEDOT films. *J. Solid State Electrochem.* **13**, 417–426 (2009).
35. Wagner, K., Pringle, J. M., Hall, S. B., Forsyth, M., MacFarlane, D. R. & Officer, D. L. Investigation of the electropolymerisation of EDOT in ionic liquids. *Synth. Met.* **153**, 257–260 (2005).
36. Sakmeche, N., Aeiyaich, S., Aaron, J., Jouini, M., Lacroix, J. C. & Lacaze, P.-C. Improvement of the electrosynthesis and physicochemical properties of poly(3,4-ethylenedioxythiophene) using a sodium dodecyl sulfate micellar aqueous medium. *Langmuir* **15**, 2566–2574 (1999).
37. Pigani, L., Heras, A., Colina, Á., Seeber, R. & López-Palacios, J. Electropolymerisation of 3,4-ethylenedioxythiophene in aqueous solutions. *Electrochem. Commun.* **6**, 1192–1198 (2004).
38. Randriamahazaka, H., Bonnotte, T., Noël, V., Martin, P., Ghilane, J., Asaka, K. & Lacroix, J.-C. Medium effects on the nucleation and growth mechanisms during

- the redox switching dynamics of conducting polymers: case of poly(3,4-ethylenedioxythiophene). *J. Phys. Chem. B* **115**, 205–16 (2011).
39. Kozak, A. Effect of deposition characteristics on electrochemically prepared PEDOT films. *NNIN REU Res. Accompl.* 20–21 (2010).
  40. Niu, L., Kvarnström, C., Fröberg, K. & Ivaska, A. Electrochemically controlled surface morphology and crystallinity in poly (3,4-ethylenedioxythiophene) films. *Synth. Met.* **122**, 425–429 (2001).
  41. Melato, A. I., Viana, A. S. & Abrantes, L. M. Different steps in the electrosynthesis of poly(3,4-ethylenedioxythiophene) on platinum. *Electrochim. Acta* **54**, 590–597 (2008).
  42. Eliseeva, S. N., Spiridonova, D. V., Tolstopyatova, E. G. & Kondratiev, V. V. Redox capacitance of poly-3,4-ethylenedioxythiophene studied by cyclic voltammetry and faradaic impedance spectroscopy. *Russ. J. Electrochem.* **44**, 894–900 (2008).
  43. Patra, S., Barai, K. & Munichandraiah, N. Scanning electron microscopy studies of PEDOT prepared by various electrochemical routes. *Synth. Met.* **158**, 430–435 (2008).
  44. Hu, Y., Shenderova, O. A., Hu, Z., Padgett, C. W. & Brenner, D. W. Carbon nanostructures for advanced composites. *Reports Prog. Phys.* **69**, 1847–1895 (2006).
  45. Todorov, T. N. Carbon nanotubes as long ballistic conductors. **393**, 240–242 (1998).
  46. Dolmatov, V. Y. Polymer-diamond composites based on detonation nanodiamonds. Part I. *J. Superhard Mater.* **29**, 65–75 (2007).
  47. Jee, A.-Y. & Lee, M. Surface functionalization and physicochemical characterization of diamond nanoparticles. *Curr. Appl. Phys.* **9**, e144–e147 (2009).
  48. Krueger, A. New carbon materials: biological applications of functionalized nanodiamond materials. *Chem. Eur. J.* **14**, 1382–90 (2008).
  49. Koroleva, M. Y., Berdnikova, D. V., Spitsyn, B. V. & Yurtov, E. V. Sedimentation stability of aqueous dispersions of nanodiamond agglomerates. *Theor. Found. Chem. Eng.* **43**, 478–481 (2009).
  50. Barnard, A. S. & Sternberg, M. Crystallinity and surface electrostatics of diamond nanocrystals. *J. Mater. Chem.* **17**, 4811 (2007).
  51. Feoktistov, N. A., Grudinkin, S. A., Rybin, M. V., Smirnov, A. N., Aleksenskii, A. E., Vul', A. Y. & Golubev, V. G. Boron-doped transparent conducting nanodiamond films. *Tech. Phys. Lett.* **37**, 322–325 (2011).

52. Zang, J., Wang, Y., Bian, L., Zhang, J., Meng, F., Zhao, Y., Ren, S. & Qu, X. Surface modification and electrochemical behaviour of undoped nanodiamonds. *Electrochim. Acta* **72**, 68–73 (2012).
53. Welch, J. O., Li, P., Chaudhary, A., Edgington, R. & Jackman, R. B. The influence of surface functionalisation on the electrical properties and thermal stability of nanodiamonds. *J. Appl. Phys.* **116**, 133705 (2014).
54. Zang, J. B., Wang, Y. H., Zhao, S. Z., Bian, L. Y. & Lu, J. Electrochemical properties of nanodiamond powder electrodes. *Diam. Relat. Mater.* **16**, 16–20 (2007).
55. Holt, K. B., Caruana, D. J. & Millan-Barrios, E. J. Electrochemistry of undoped diamond nanoparticles: accessing surface redox states. *J. Am. Chem. Soc.* **131**, 11272–11273 (2009).
56. Tamburri, E., Orlanducci, S., Guglielmotti, V., Reina, G., Rossi, M. & Terranova, M. L. Engineering detonation nanodiamond – Polyaniline composites by electrochemical routes: Structural features and functional characterizations. *Polymer (Guildf)*. **52**, 5001–5008 (2011).
57. Kovalenko, I., Bucknall, D. G. & Yushin, G. Detonation nanodiamond and onion-like-carbon-embedded polyaniline for supercapacitors. *Adv. Funct. Mater.* **20**, 3979–3986 (2010).
58. Gomez, H., Ram, M. K., Alvi, F., Stefanakos, E. & Kumar, A. Novel synthesis, characterization, and corrosion inhibition properties of nanodiamond–polyaniline films. *J. Phys. Chem. C* **114**, 18797–18804 (2010).
59. Xiao, Y., Ye, X., He, L. & Che, J. New carbon nanotube-conducting polymer composite electrodes for drug delivery applications. *Polym. Int.* **61**, 190–196 (2012).
60. Samba, R., Fuchsberger, K., Matyichyn, I., Epple, S., Kiesel, L., Stett, A., Schuhmann, W. & Stelzle, M. Application of PEDOT-CNT microelectrodes for neurotransmitter sensing. *Electroanalysis* **26**, 548–555 (2014).
61. Luo, X., Weaver, C. L., Zhou, D. D., Greenberg, R. & Cui, X. T. Highly stable carbon nanotube doped poly(3,4-ethylenedioxythiophene) for chronic neural stimulation. *Biomaterials* **32**, 5551–7 (2011).
62. Ispas, A., Peipmann, R., Adolphi, B., Efimov, I. & Bund, A. Electrodeposition of pristine and composite poly(3,4-ethylenedioxythiophene) layers studied by electro-acoustic impedance measurements. *Electrochim. Acta* **56**, 3500–3506 (2011).
63. Tamburri, E., Guglielmotti, V., Matassa, R., Orlanducci, S., Gay, S., Reina, G., Terranova, M. L., Passeri, D. & Rossi, M. Detonation nanodiamonds tailor the structural order of PEDOT chains in conductive coating layers of hybrid nanoparticles. *J. Mater. Chem. C* **2**, 3703 (2014).

64. Hillman, A. R., Saville, P. M., Glidle, A., Richardson, R. M., Roser, S. J., Swann, M. J. & Webster, J. R. P. Neutron reflectivity determination of buried electroactive interface structure: PBT/PPy and PBT/PXV bilayers. *J. Am. Chem. Soc.* **120**, 12882–12890 (1998).
65. Wilson, R., Cubitt, R., Glidle, A., Hillman, A. R., Saville, P. M. & Vos, J. G. A neutron reflectivity study of [Os(bipy)<sub>2</sub>(PVP)IOCl]<sup>+</sup> polymer film modified electrodes: effect of redox state and counter ion. *Electrochim. Acta* **44**, 3533–3548 (1999).
66. Cooper, J. M., Cubitt, R., Dalgliesh, R. M., Gadegaard, N., Glidle, A., Hillman, A. R., Mortimer, R. J., Ryder, K. S. & Smith, E. L. Dynamic in situ electrochemical neutron reflectivity measurements. *J. Am. Chem. Soc.* **126**, 15362–3 (2004).
67. Cubitt, R. & Stahn, J. Neutron reflectometry by refractive encoding. *Eur. Phys. J. Plus* **126**, 111 (2011).
68. Glidle, A., Hadyoon, C. S., Gadegaard, N., Cooper, J. M., Hillman, A. R., Wilson, R. W., Ryder, K. S., Webster, J. R. P. & Cubitt, R. Evaluating the influence of deposition conditions on solvation of reactive conducting polymers with neutron reflectivity. *J. Phys. Chem. B* **109**, 14335–43 (2005).
69. Glidle, A., Hillman, A. R., Ryder, K. S., Smith, E. L., Cooper, J., Gadegaard, N., Webster, J. R. P., Dalgliesh, R. & Cubitt, R. Use of neutron reflectivity to measure the dynamics of solvation and structural changes in polyvinylferrocene films during electrochemically controlled redox cycling. *Langmuir* **25**, 4093–103 (2009).
70. Lauw, Y., Rodopoulos, T., Gross, M., Nelson, A., Gardner, R. & Horne, M. D. Electrochemical cell for neutron reflectometry studies of the structure of ionic liquids at electrified interface. *Rev. Sci. Instrum.* **81**, 074101 (2010).
71. Jerliu, B., Dörrer, L., Hüger, E., Borchardt, G., Steitz, R., Geckle, U., Oberst, V., Bruns, M., Schneider, O. & Schmidt, H. Neutron reflectometry studies on the lithiation of amorphous silicon electrodes in lithium-ion batteries. *Phys. Chem. Chem. Phys.* **15**, 7777–84 (2013).
72. Veder, J.-P., De Marco, R., Clarke, G., Chester, R., Nelson, A., Prince, K., Pretsch, E. & Bakker, E. Elimination of undesirable water layers in solid-contact polymeric ion-selective electrodes. *Anal. Chem.* **80**, 6731–40 (2008).
73. Veder, J.-P., De Marco, R., Clarke, G., Jiang, S. P., Prince, K., Pretsch, E. & Bakker, E. Water uptake in the hydrophilic poly(3,4-ethylenedioxythiophene):poly(styrene sulfonate) solid-contact of all-solid-state polymeric ion-selective electrodes. *Analyst* **136**, 3252–8 (2011).
74. Veder, J.-P., Patel, K., Sohail, M., Jiang, S. P., James, M. & De Marco, R. An electrochemical impedance spectroscopy/neutron reflectometry study of water uptake in the poly(3,4-ethylenedioxythiophene):poly(styrene

- sulfonate)/polymethyl methacrylate-polydecyl methacrylate copolymer solid-contact ion-selective electrode. *Electroanalysis* **24**, 140–145 (2012).
75. Veder, J.-P., De Marco, R., Patel, K., Si, P., Grygolicz-Pawlak, E., James, M., Alam, M. T., Sohail, M., Lee, J., Pretsch, E. & Bakker, E. Evidence for a surface confined ion-to-electron transduction reaction in solid-contact ion-selective electrodes based on poly(3-octylthiophene). *Anal. Chem.* **85**, 10495–502 (2013).
  76. Zamlynny, V., Burgess, I., Szymanski, G., Lipkowski, J., Majewski, J., Smith, G., Satija, S. & Ivkov, R. Electrochemical and neutron reflectivity studies of spontaneously formed amphiphilic surfactant bilayers at the gold-solution interface. *Langmuir* **16**, 9861–9870 (2000).
  77. Burgess, I., Zamlynny, V., Szymanski, G., Lipkowski, J., Majewski, J., Smith, G., Satija, S. & Ivkov, R. Electrochemical and neutron reflectivity characterization of dodecyl sulfate adsorption and aggregation at the gold-water interface. *Langmuir* **17**, 3355–3367 (2001).
  78. Majewski, J., Smith, G. S., Burgess, I., Zamlynny, V., Szymanski, G., Lipkowski, J. & Satija, S. Neutron reflectivity studies of electric field driven structural transformations of surfactants. *Appl. Phys. A* S364–S367 (2002).
  79. Tronin, A., Chen, C.-H., Gupta, S., Worcester, D., Lauter, V., Strzalka, J., Kuzmenko, I. & Blasie, J. K. Structural changes in single membranes in response to an applied transmembrane electric potential revealed by time-resolved neutron/X-ray interferometry. *Chem. Phys.* **422**, 283–289 (2013).
  80. Fadda, G. C., Lairez, D., Guennouni, Z. & Koutsioubas, A. Peptide pores in lipid bilayers: voltage facilitation pleads for a revised model. *Phys. Rev. Lett.* **111**, 028102 (2013).

## Chapter 2 – Methodology and techniques

### 2.1 Neutron reflectometry

#### 2.1.1 Introduction

Neutron reflectometry and scattering in general are based on the mathematical theory pertinent to optics and the concept of wave-particle duality, although the latter will not be explored here. The purpose of this section is to give the reader a comprehensive and application driven summary of the fundamental principles that underpin the technique, with a particular focus on how this translates into a practical understanding of what can be successfully measured and studied. The basic concepts of neutron interactions with nuclei and the geometry of neutron reflectometry experiments will be outlined, followed by some illustrated examples of the processes of modelling and interpreting data.

#### 2.1.2 Neutron-nuclei interactions

Neutrons are considered ideal probes for a wide range of samples, due to being highly penetrating and sensitive to light elements, unlike analogous X-ray techniques. The ways in which a neutron can interact with an atom include nuclear and magnetic scattering, and absorption<sup>1</sup>. Since neutrons interact with the nuclei of atoms, they can also differentiate between isotopes, allowing for isotopic substitution to be used to highlight features of a sample, a method known as contrast variation<sup>2,3</sup>. When a neutron interacts with a nucleus, the scattered wave is defined as a function of wavelength and scattering angle. With the exception of absorbing elements, however, the interaction cross section tends to be independent of the wavelengths corresponding to the length scales of atomic or molecular spacing, usually in the range  $\lambda = 2 - 30 \text{ \AA}$ . Thus, the probability of scattering for a given atom is defined by the constant known as the scattering length,  $b$ . The magnitude and sign of this constant for a given element is indicative of the scattering strength and whether or not the incident wave phase is affected by the neutron-nuclei interaction. The area in which the neutron-nuclei interaction is likely to occur is known as the cross section,  $\Phi$ , and is related to the scattering length by<sup>4,5</sup>:

$$\Phi = 4\pi|b|^2 \quad (2.1)$$

Neutron cross-sections follow no particular trend in the periodic table as illustrated in Figure 2.1, showing the bound coherent scattering length ( $b_c$ ) of the elements<sup>5</sup>. The values of  $b_c$  for hydrogen and deuterium highlight how different these values can be for isotopes of a single element, a fact that is widely exploited in neutron scattering techniques.

1 H -3.7	2 D 6.7																4.003 He 3.26
6.94 Li -1.9	9.012 Be 7.79	Bound coherent scattering length (fm)										10.81 B 5.3	12.011 C 6.648	14.007 N 9.36	15.999 O 5.805	18.998 F 5.654	20.18 Ne 4.566
22.99 Na 3.63	24.305 Mg 5.375	1.008 ← Atomic Mass ← Atomic Symbol -3.741										26.982 Al 3.449	28.085 Si 4.15	30.974 P 5.13	32.06 S 2.847	35.45 Cl 9.579	39.948 Ar 1.909
39.098 K 3.67	40.078 Ca 4.7	44.956 Sc 12.1	47.867 Ti -3.37	50.942 V -0.443	51.996 Cr 3.635	54.938 Mn -3.75	55.845 Fe 9.45	58.933 Co 2.49	58.693 Ni 10.3	63.546 Cu 7.718	65.546 Zn 5.68	69.723 Ga 7.288	72.63 Ge 8.185	74.922 As 6.58	78.96 Se 7.97	79.904 Br 6.79	83.798 Kr 7.81
85.468 Rb 7.08	87.62 Sr 7.02	88.906 Y 7.75	91.224 Zr 7.16	92.906 Nb 7.054	95.96 Mo 6.715	101.07 Tc 6.8	102.91 Ru 7.02	106.42 Rh 5.9	107.87 Pd 5.91	107.87 Ag 5.922	112.41 Cd 4.83	114.82 In 4.065	118.71 Sn 6.225	121.76 Sb 5.57	127.6 Te 5.68	126.9 I 5.28	131.29 Xe 4.69
132.91 Cs 5.42	137.33 Ba 5.07	La-Lu	178.49 Hf 7.77	180.95 Ta 6.91	183.84 W 4.755	186.21 Re 9.2	190.23 Os 10.7	192.22 Ir 10.6	195.08 Pt 9.6	196.97 Au 7.9	200.59 Hg 12.595	Tl	Pb	Bi	Po	At	Rn
Fr	Ra	Ac-Lr	Rf	Db	Sg	Bh	Hs	Mt	Ds	Rg	Uub	Uut	Uuq	Uup	Uuh	Uus	Uuo
138.91 La 8.24	140.12 Ce 4.84	140.91 Pr 4.58	144.24 Nd 7.69	Pm 12.6	150.36 Sm 0	151.96 Eu 5.3	157.96 Gd 9.5	158.93 Tb 7.34	162.5 Dy 16.9	164.93 Ho 8.44	167.26 Er 7.79	168.93 Tm 7.07	173.05 Yb 12.41	174.97 Lu 7.21			
Ac	Th	Pa	U	Np	Pu	Am	Cm	Bk	Cf	Es	Fm	Md	No	Lr			

Figure 2.1 - Bound coherent scattering lengths

The scattering length density (SLD or  $N_b$ ) of a material is calculated by summing the individual bound coherent scattering lengths of the atoms per unit volume:

$$N_b = \frac{\sum b_c \cdot N_A \cdot \rho}{M} \quad (2.2)$$

where  $\sum b_c$  is the sum of the bound coherent scattering lengths of the atoms in the molecule,  $N_A$  is Avogadro's constant,  $M$  is the molar mass of the molecule and  $\rho$  is the density. The SLD of a compound is therefore related to its composition and density which allows the SLD of mixtures to be easily calculated knowing the SLD of the individual compounds and their volume fractions<sup>3</sup>:

$$N_{b_{AB}} = x N_{b_A} + (1 - x)N_{b_B} \quad (2.3)$$

where  $N_{b(A)}$  and  $N_{b(B)}$  are the SLDs of compounds A and B respectively,  $N_{b(AB)}$  is the SLD of the mixture of compounds A and B, and  $x$  is the volume fraction of compound A within the mixture.

### 2.1.3 Reflectivity theory

The scattering from a flat sample or interface occurs over a wide range of angles so deflected neutrons can be detected by either measuring the scattered intensity at a single angle equal to that of the incident beam, known as specular scattering, or alternatively by measuring the off-specular scattering<sup>1</sup>. The latter can provide information about features in the plane of the sample whereas the former detects features in the axis perpendicular to the surface. In this work, only specular measurements and theory will be discussed since the intention is to study laterally uniform films.

Neutron reflectometry is used to investigate variations in composition and thickness of thin layers as a function of depth averaged over the horizontal plane of the sample. A collimated beam of neutrons is directed at the interface of interest where the neutrons interact with the nuclei of the elements within the sample and are scattered into a detector.

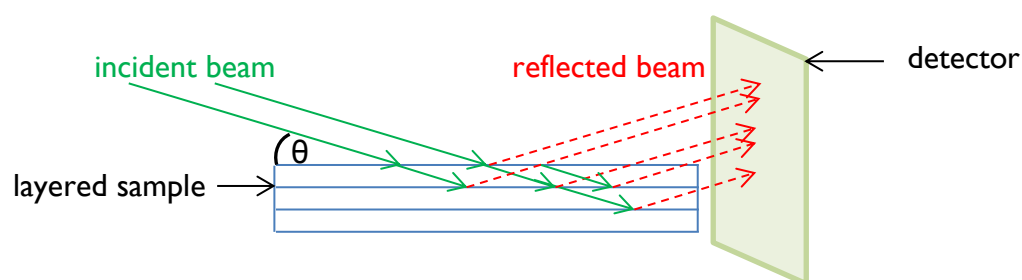


Figure 2.2 – Scattering geometry through layers

As the beam of neutrons travels through a layered sample, it will have distinct interactions with each layer to produce a reflectivity profile which will be a mathematical convolution of the different layer interactions present within the material. The incident beam may transmit through or reflect off each interface such

that the resulting scattered waves are subject to interference, which is manifested by the appearance of fringes in the reflectivity profiles  $R(Q)$  of layered samples.

The reflectivity profile of a sample is the ratio of reflected to incident intensity (known as the reflectivity,  $R$ ) as a function of momentum transfer,  $Q$ , which is related to the incident ( $k_i$ ) and scattered ( $k_s$ ) wavevectors by equation ( 2.4 ) and illustrated in Figure 2.3.

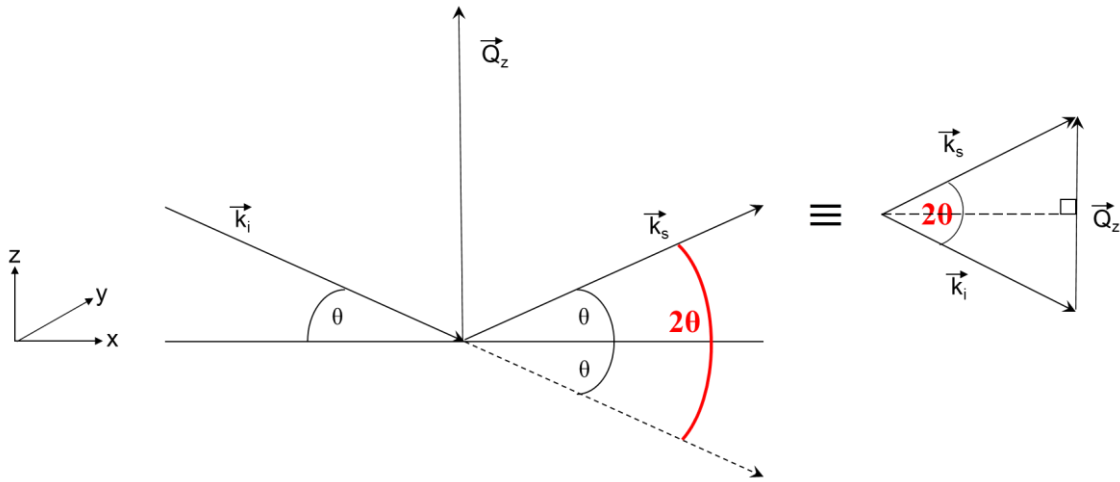


Figure 2.3 – Geometry of the incident and scattered wavevectors and the associated momentum transfer.

$$Q_z = k_s - k_i \quad (2.4)$$

$$k = \frac{2\pi}{\lambda} \quad (2.5)$$

Since the magnitude of the wavevector is defined by equation ( 2.5 ), simple trigonometry allows  $Q$  to be expressed as a function of angle  $\theta$  and wavelength  $\lambda$  in equation ( 2.6 )<sup>1</sup>.

$$Q = \frac{4\pi}{\lambda} \sin \theta \quad (2.6)$$

In an experiment, the range of  $Q$  can be controlled by varying the wavelength of the incident beam of neutrons or changing the incident angle<sup>6</sup>. If the neutron beam contains a range of wavelengths then for a given angle  $\theta$  there will be a range of  $Q$ . In the case of a monochromatic beam, the range of  $Q$  is controlled by adjusting the incident angle. The characteristics of the neutron beam and the wavelength range it provides will be determined by the type of neutron source, nuclear or spallation, by the moderator and thereafter by the design of the instrument.

Since the reflectivity is the ratio of reflected to incident intensity, the definition of total reflection is  $R = 1$ , where the reflected intensity is equal to the incident intensity. The conditions for total reflection stipulate that the bulk substance through which the neutrons travel ( $s_1$ ) before reaching the interface of interest must have a lower SLD than that of the bulk substance from which they reflect ( $s_2$ ).

The position of the critical edge,  $Q_c$ , the point at which the reflectivity drops below  $R=1$ , is determined by the difference between SLDs of the bulk materials according to equation ( 2.7 )<sup>5</sup>.

$$Q_c = 4\sqrt{\pi\Delta N_b} \quad ( 2.7 )$$

where

$$\Delta N_b = SLD s_2 - SLD s_1 \quad ( 2.8 )$$

If the sample comprises materials from which complete reflection occurs, then the angle will be chosen such that the range of  $Q$  will include  $Q_c$  thus resolving the critical edge. The measurement of the critical edge allows the data to be correctly scaled (ensuring the plateau is at  $R = 1$ ) and thus provides an absolute measurement rather than relative intensities. It is also used to check that the position of  $Q_c$  matches the value expected for the materials of the sample, thus avoiding mistakes in the sample, the settings of the instrument or alignment issues.

One of the simplest ways of describing the reflectivity,  $R$ , as a function of  $Q$  is to use the Born approximation as shown in equation ( 2.9 ) In the case of a single interface,

this leads to the relationship defined in equation ( 2.10 ). Although this accurately predicts the reflectivity for higher values of  $Q$ , it does not take into account the requirement that  $R$  must be less than or equal to 1 and therefore does not correctly simulate the area around the critical edge<sup>1</sup>.

$$R(Q) \approx \frac{16\pi^2}{Q^4} \left| \int_{-\infty}^{\infty} \frac{dN_b}{dz} e^{-izQ} dz \right|^2 \quad (2.9)$$

$$R(Q) \approx \frac{16\pi^2 N_b^2}{Q^4} \quad (2.10)$$

In the case of a system with two interfaces, the interference between the waves reflecting and transmitting from these boundaries will produce variations in the intensity known as Kiessig fringes. The distance,  $d$ , between the interfaces in real space will be related to the fringe spacing in  $Q$  space according to equation ( 2.11 ).

$$\Delta Q = \frac{2\pi}{d} \quad (2.11)$$

The situation becomes more complicated with an increasing number of interfaces and is best described by the Parratt recursive formulism. This method uses an iterative procedure to calculate  $R(Q)$  by summing the amplitudes of the reflected and transmitted beams as they travel through the different layers of a sample, iteratively solving the boundary conditions for the transmitted and reflected neutron waves at each interface. It is this method that is used most commonly in the modelling and fitting software available for the analysis of neutron reflectometry data.

The properties of the sample such as repeating layers, overall thickness or the relative thickness of contrasting layers will determine how the instrument should be set up for the measurement, according to the resolution and  $Q$  range requirements needed to clearly resolve the features of the reflectivity. For example, given the reciprocal relationship between  $Q$ -space and real space defined in equation ( 2.11 ), a thick layer

will produce very closely spaced fringes, which will therefore require a higher resolution. A thin layer, on the other hand, would require a measurement to a higher value of  $Q$  in order for the fringe minima to be resolved. For example, in the case of a 30 nm layer of gold, the fringe periodicity or separation in  $Q$  will be in the order of  $0.02 \text{ \AA}^{-1}$ , such that three distinct fringes can be identified in the range up to  $0.06 \text{ \AA}^{-1}$ ; whereas with the addition of a 70 nm polymer film, the fringe minima will fall approximately every  $0.006 \text{ \AA}^{-1}$  therefore there will be almost twice the number of fringes within the same range of  $Q$ .

In this work, the samples are considered thick by neutron reflectometry standards, with an overall sample thickness of between 30 and 100 nm. In these cases, the low  $Q$  area of the reflectivity profile should give sufficient information to measure layer thickness. However, the more subtle changes in SLD and roughness will have an effect at higher  $Q$  so the choice of  $Q$ -range will depend upon the information sought.

#### 2.1.4 Models and limitations

The neutron can be described mathematically by a wavefunction and thus by an amplitude and a phase, but what we measure during scattering experiments is the intensity, the square of the amplitude, such that the phase information is lost<sup>1,2</sup>. In a practical sense, this means that a measured reflectivity could originate from several different sample structures and a single neutron reflectivity experiment alone does not allow differentiation between them. There are a number of methods employed to circumvent this problem but, as a starting point, it is considered good practice to characterise and acquire as much information about a sample prior to the neutron experiment or data fitting. This enables the sample system to be simulated using a model in which one has reasonable estimates of the upper and lower bounds of variables, such as the size of layers and their composition.

A reflectivity profile on its own can only provide a limited amount of information such as the difference in SLD between the bulk outer materials given by the position in  $Q$  of the critical edge, as shown previously in equation ( 2.7 ), and an approximate thickness of the layer with the greatest contrast given by the relationship between reciprocal and real space given in equation ( 2.11 ). For further information to be extracted, it is common to use fitting software that utilizes a box model system which involves

dividing the sample into layers with specific parameters that are variables in the fitting process. Since there may be several possible sample structures that correspond to a single reflectivity, it is preferable to be able to fix parameters to a known value; for example with a solid layer such as gold, the thickness may be measured prior to the experiment and the SLD can be calculated. For other samples where the thickness may not be known and the SLD may vary depending on solvation, the fitting will start from physically plausible values and these parameters will be allowed to vary. A single physical layer of a compound may be modelled as several theoretical layers to allow for subtle differences to be identified, such as spatial variations in density or solvation.

	thickness / Å	SLD $\times 10^{-6}$ Å <sup>-2</sup>	roughness / Å
air or solvent	N/A	0	N/A
layer 1	150	1.5	10
layer 2	150	2.5	10
quartz substrate	N/A	4.18	10

*Table 2.1 – Example of the box model with the thickness and SLD parameters for each layer and the roughness value between each layer, e.g. roughness in the row ‘quartz substrate’ is the roughness from the quartz to layer 2; no thickness value is given for the outer materials as they are bulk materials.*

The three key parameters, as shown in Table 2.1, are the thickness, the SLD and the roughness of each layer. The roughness variable is not in fact a measure of topographical roughness, although it can be affected by the latter. In this case, the roughness  $\sigma$ , is the error function (erf) related to the FWHM of the Gaussian that is the derivative of the SLD profile of an interface by equation ( 2.12 ) as illustrated in Figure 2.4. It therefore provides information about the slope of the SLD profile and allows the interface to be identified as sharp or diffuse.

$$FWHM = 2\sqrt{2 \ln 2} \sigma \quad (2.12)$$

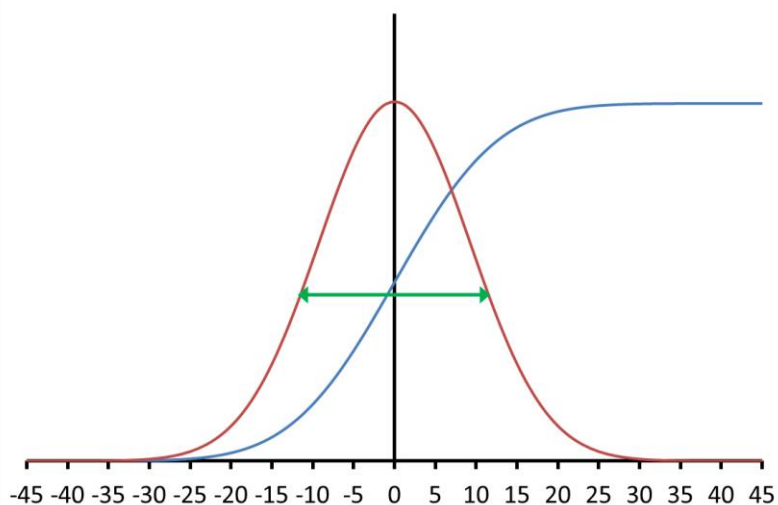


Figure 2.4 – Illustration of the roughness parameter in relation to the SLD profile of an interface (blue trace) and the corresponding Gaussian derivative (red trace)

One method used to aid in selecting the correct structure from different candidates is to manipulate the ‘contrast’. Hydrogen and its isotope, deuterium, have very different scattering lengths which can be used, for example, to highlight particular layers in a sample by modifying their deuterium content. Increasing contrast between layers of a sample can significantly affect a reflectivity profile, for example by adding fringes or increasing the depth of fringe minima which subsequently provides more features to fit. While this can make the fitting process more difficult by increasing the number of variables, it allows structural features to be highlighted and also limits the number of possible corresponding SLD profiles.

In the case of a gold layer deposited on quartz (the substrate used in this work) the binding (3-mercaptopropyl)-trimethoxysilane (MPTS) layer present between the gold and the quartz illustrates well the effect of contrast as shown in Figure 2.5. The simulated reflectivity of a sample without the contrasting MPTS layer shows very weak fringes as the SLD of quartz and gold are not significantly different at  $4.18 \times 10^{-6} \text{ \AA}^{-2}$  and  $4.5 \times 10^{-6} \text{ \AA}^{-2}$  respectively. By adding the MPTS layer, with an SLD of  $0.266 \times 10^{-6} \text{ \AA}^{-2}$ , the fringes of the gold layer are immediately resolved.

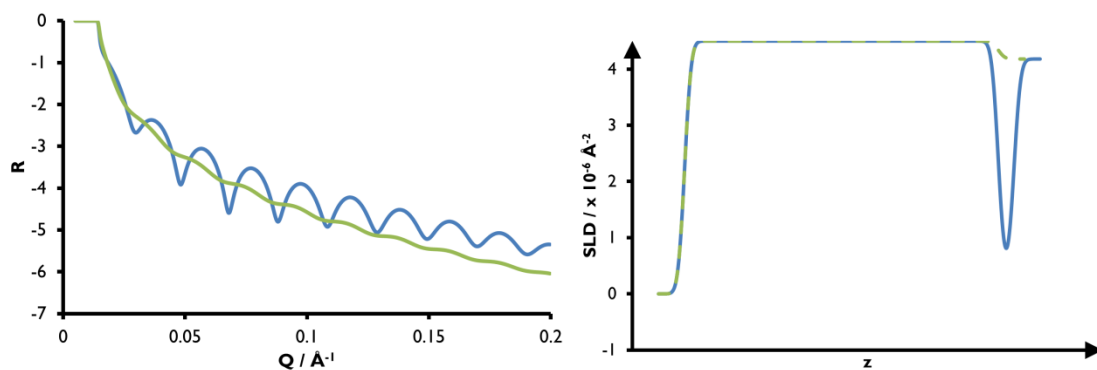


Figure 2.5 – Simulated reflectivity and SLD profiles of 30 nm gold layer on quartz substrate with a 15 Å MPTS layer (blue trace) and without (green trace); roughness is fixed at 5 Å at each interface

‘Contrast matching’ is a further technique used to highlight a particular component of the system and involves creating a mixture of compounds, for example in solution, to achieve an overall SLD that matches the SLD of a particular material in the system. This form of contrast variation enables several reflectivity profiles to be acquired for the same sample in differing solvent environments, such that comparison of the differences in reflectivity profiles can be attributed to the sample environment and the data pertinent to the sample can be extracted.

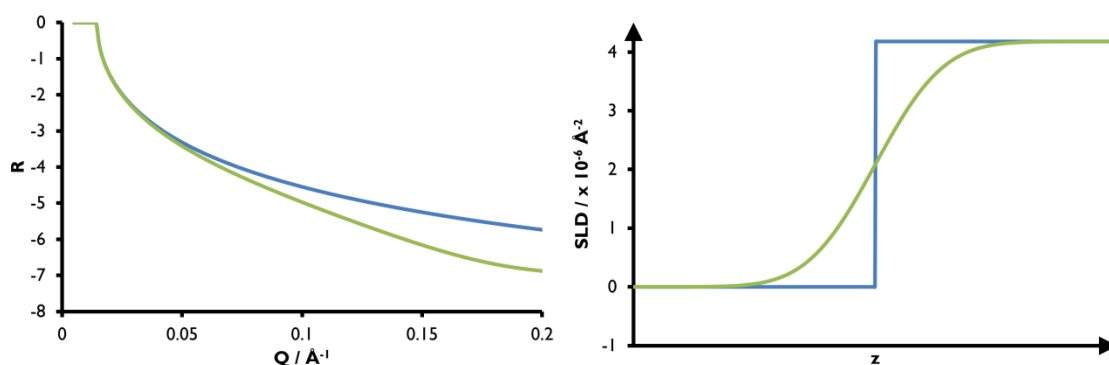


Figure 2.6 – Simulated reflectivity and SLD profiles of a single interface between two bulk materials, the blue trace is a sharp interface with a roughness of 0 Å and the green trace shows the same interface with a roughness of 10 Å

The subtle details of how SLD parameters can affect a reflectivity profile are best explained through illustrative examples. We shall first consider the effect of roughness, starting with the simplest case of a single interface between two bulk materials as shown in Figure 2.6.

As seen previously in equation ( 2.9 ), the Fresnel reflectivity  $R(Q)$  will decrease with increasing  $Q$  by a factor of  $Q^{-4}$ . The roughness parameter however causes a more rapid decay which, in practical terms, could result in a loss of information as the reflectivity may quickly drop below the level of background scattering, which is typically on the order of  $R = 10^{-7}$ .

In cases where there is more than one interface, the different interfacial roughness parameters have a more complicated effect on the reflectivity. This is illustrated in Figure 2.7 which compares the effect of a roughness value of 0 or 10 Å at the various interfaces and Figure 2.8 which shows the same examples but with roughness values of 0 or 20 Å. In the cases where both interfaces are diffuse (purple trace), the reflectivity decays faster than in the case of the sharp interfaces. Furthermore, increasing the roughness to 20 Å results in the reflectivity reaching the background limit and, therefore, a loss of information.

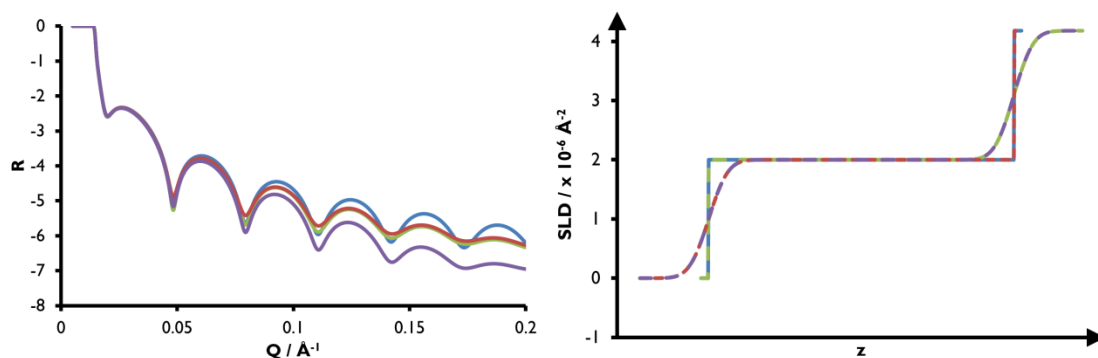


Figure 2.7 – Simulated reflectivity and SLD profiles of a sample with two distinct interfaces, in the case where both are sharp with 0 Å roughness (blue), where both are diffuse with 10 Å roughness (purple), where the first interface is sharp and the second diffuse (green) and where the first is diffuse and the second is sharp (red)

In the cases where one interface is diffuse and the other is sharp, the reflectivity profiles are difficult to distinguish from one another with only slight variations in the depth of the fringe minima. It is clear therefore that, if these were experimental results, identifying which interface was more diffuse could be quite difficult since either model fits the data quite well. The fringes in this case also appear ‘dampened’ compared to the sharp interface model and the reflectivity does not decay as rapidly as in the case of both interfaces being diffuse.

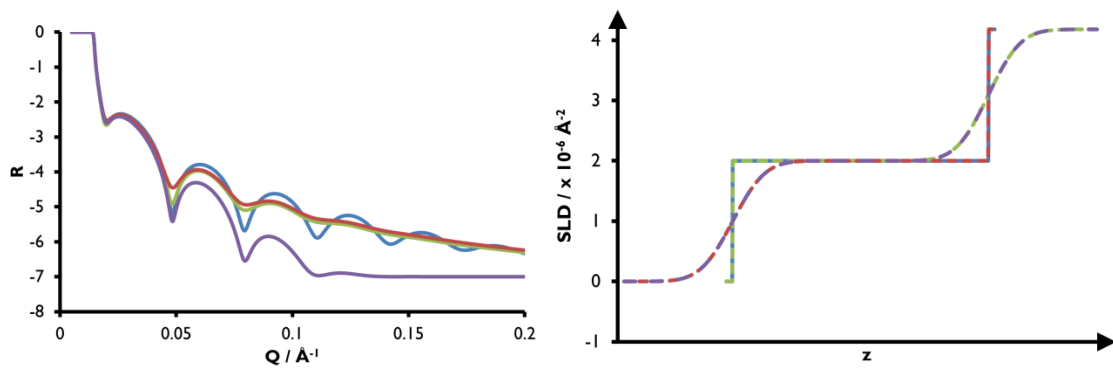


Figure 2.8 – Simulated reflectivity and SLD profiles of a sample with two distinct interfaces, in the case where both are sharp with  $0 \text{ \AA}$  roughness (blue), where both are diffuse with  $20 \text{ \AA}$  roughness (purple), where the first interface is sharp and the second diffuse (green) and where the first is diffuse and the second is sharp (red)

SLD differences in a multi-layered system can also produce similar reflectivity profiles despite significantly different SLD profiles. Figure 2.9 illustrates how two samples with layers of different SLDs can have almost indistinguishable reflectivity profiles. This results from the similar contrast between the layer and the neighbouring layers which, in this example, are the bulk materials air and quartz. In the case of the  $2 \times 10^{-6} \text{ \AA}^{-2}$  layer (blue trace) the difference in SLD between the layer and either of the bulk materials is approximately  $2 \times 10^{-6} \text{ \AA}^{-2}$ . In the other two cases however, the SLD of the layer is closer to one or the other of the bulk materials but both by the same difference in SLD of  $1 \times 10^{-6} \text{ \AA}^{-2}$ . In the reflectivity profile, it is apparent that this results in a very similar reflectivity profile in which the fringes are significantly dampened compared to the layer with an SLD of  $2 \times 10^{-6} \text{ \AA}^{-2}$ .

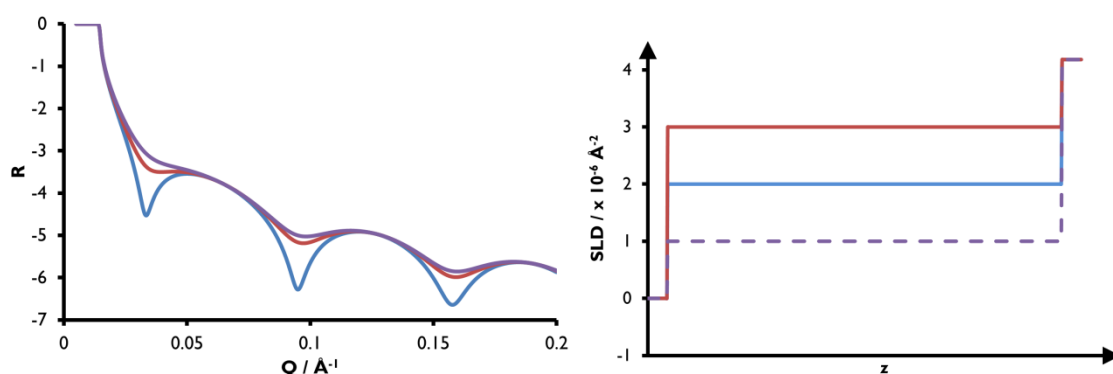
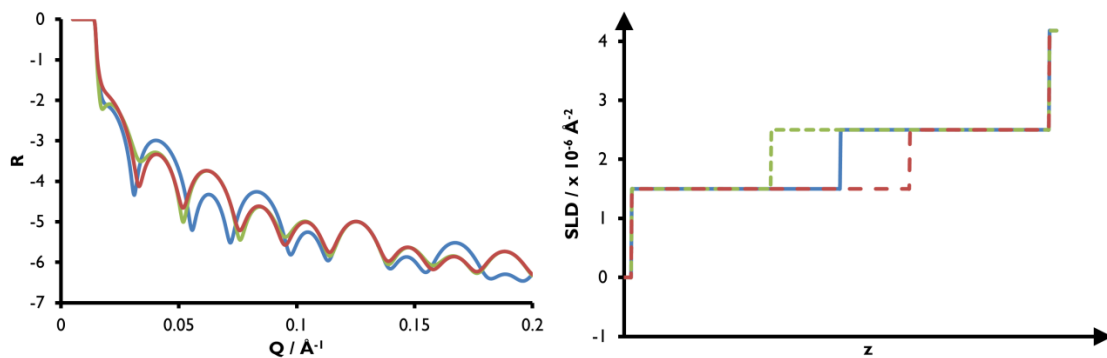


Figure 2.9 – Simulated reflectivity and SLD profiles of samples with a single  $10 \text{ nm}$  layer but with SLDs differing by  $1 \times 10^{-6} \text{ \AA}^{-2}$

Furthermore, differences in thickness combined with a difference in SLD can also produce similar reflectivity profiles. Figure 2.10 illustrates the case of a two layer system in which the thickness of the layers differs. The blue trace is given as a reference in which both layers have the same thickness but an SLD differing by  $1 \times 10^{-6} \text{ \AA}^{-2}$ . What is of interest however is the similarity between the reflectivity profiles of the other two samples (red and green traces) where the plots clearly overlay with the exception of some small differences in the depth of fringe minima. Once again, if this were experimental data, the correct model could be difficult to identify.



*Figure 2.10 – Simulated reflectivity and SLD profiles of two-layered samples in which the layers are equally thick (blue trace), in which the lower SLD layer is thinner than the higher SLD layer (green trace) and in which the lower SLD layer is thicker than the higher SLD layer (red trace)*

### 2.1.5 Conclusion

Neutron reflectometry is a highly sensitive technique that can reveal the structural and compositional detail of surfaces, layers and interfaces. In the context of polymer films, a range of sample thicknesses between 30-100 nm can be reliably explored without posing any considerable challenges with regards to the resolution capabilities of most neutron reflectometers. The quality of the information extracted from an experiment relies strongly on prior characterisation and knowledge of the sample as well as the use of contrast manipulation techniques to complete the use of fitting algorithms.

## 2.2 Electrochemical methods

### 2.2.1 Introduction

The field of electrochemistry encompasses all methods that make use of electric potential or current to drive or analyse chemical reactions. It comprises a considerable number of techniques that can be used in the study of a wide range of samples in all the states of matter. This section will focus on the electrochemical procedures relevant to the formation and study of electroactive polymer films, namely cyclic voltammetry, chronoamperometry and chronopotentiometry. Firstly, the experimental equipment will be described followed by an outline of some of the fundamental concepts of electrochemistry. Thereafter, each technique will be described along with a summary of how it is used in the experiments presented in this work.

### 2.2.2 Electrochemical cells

An electrochemical cell is the vessel in which electrochemical reactions take place or can be manipulated. In its simplest form, it will contain two electrodes, the working electrode at which the reaction occurs and the current or potential is controlled, and the counter electrode that serves to complete the circuit and acts as the anode or cathode according to the reaction taking place at the working electrode<sup>7</sup>. More commonly, the cell comprises a third electrode, known as the reference electrode, which is not involved in the electrochemical reaction but has a stable, known potential against which the potential at the working electrode can be calibrated.

In this work, a glass beaker was predominantly used as an electrochemical cell in which the electrodes were arranged and connected as shown in Figure 2.11. For the purposes of *in situ* neutron reflectometry experiments, custom made cells were developed according to the general design shown in Figure 2.12. These cells contained a compartment to contain the electrolyte solution in contact with the working electrode surface. The latter was the gold coated surface of single crystal quartz block. The reference and counter electrodes were placed along the side and at the back of the solution compartment respectively.

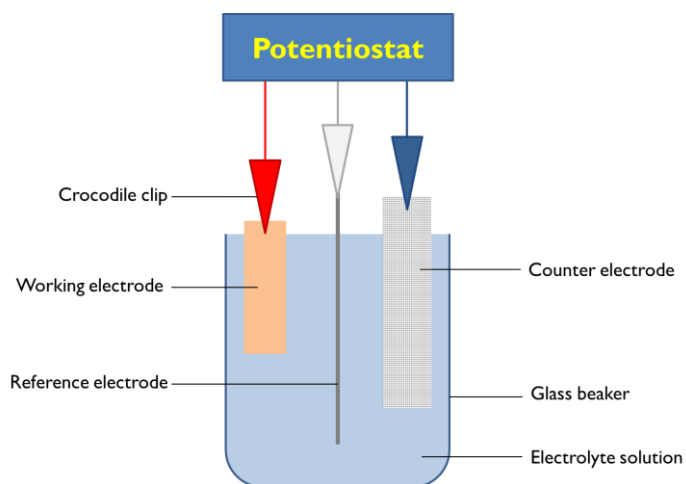


Figure 2.11 – Schematic of the electrochemical cell setup

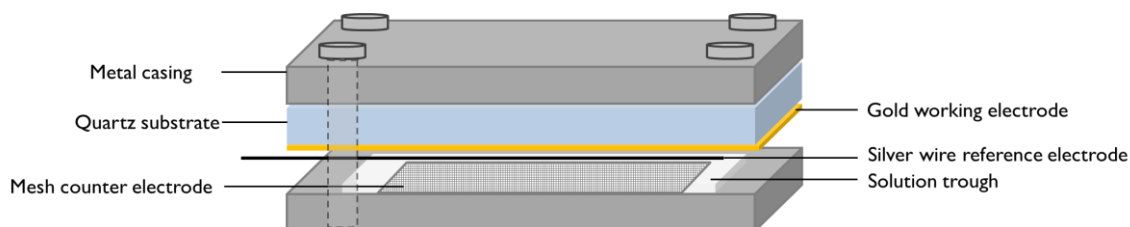


Figure 2.12 – Schematic of the neutron reflectometry/electrochemistry cell (NR/EC)

Two slightly different NR/EC cells were used in this work, one constructed at the University of Leicester (cell A) and the other at the Institut Laue-Langevin (cell B). The main differences are outlined in Table 2.2.

Cell	Seal	Counter electrode	Exposed working electrode area / cm <sup>2</sup>
A	Teflon divider	Platinum mesh	29.4
B	Viton O-ring	Platinum coated titanium grid	24.8

Table 2.2 – Differences between NR/EC cells

### 2.2.3 Electrodes

In this work, unless otherwise stated, the reference electrodes used are Ag wire and AgCl coated Ag wire. The counter electrodes were iridium or platinum coated titanium grids or platinum mesh. The size of the grid was chosen according to the size of the working electrode such that the counter electrode always presented a greater surface area than the working electrode in order to avoid any current limitations.

In all cases the working electrodes were gold coated surfaces. These were prepared on microscope slides, glass blocks or quartz blocks as described in Chapter 3, section 3.3. Gold coated microscope slides with a titanium binding layer were also used, purchased from Platypus Technologies. Depending on the thickness of the substrate, the working electrode was either directly attached to a crocodile clip connecting it to the potentiostat, or connected by means of a copper wire. The wire was connected to the gold surface by conductive silver paint and secured using silicone glue.

### 2.2.4 Electrochemical theory

This study makes use of the principle of electrolysis in which either a potential difference produces a current, or a current is applied to the electrochemical cell, resulting in the transfer of electrons. The latter drives the reaction at the working electrode. The current is related to the reaction rate according to equation ( 2.13 )

$$i = AFj \quad (2.13)$$

where  $i$  is current,  $A$  is the electrode area,  $F$  is Faraday's constant and  $j$  is the flux in units of  $\text{mol cm}^{-2} \text{s}^{-1}$  which can be therefore be considered the rate of the reaction. The yield of the reaction can be determined according to Faraday's laws of electrolysis, summarised by equation ( 2.14 )

$$m = \left(\frac{Q}{F}\right)\left(\frac{M}{z}\right) \quad (2.14)$$

where  $m$  is the mass of substance produced at the electrode,  $Q$  is the charge,  $F$  is Faraday's constant,  $M$  is the molar mass of the substance and  $z$  is the number of

electrons transferred. Hence, the mass of substance produced by the application of potential or current can be predicted according to the molar mass of the substance, the total charge applied to the system and the number of electrons involved in the reaction.

In the case of a redox reaction, the number of electrons involved in the reaction,  $z$ , can be readily determined based on the oxidation state of the molecule. However, the polymerisation process presents a more complex situation due to the chain propagation reaction. Consequently, the number of electrons involved in the polymerisation reaction per monomer unit is determined according to equation ( 2.15 ) adapted from the review by Heinze et al<sup>8</sup>.

$$z = \frac{(2n + 2 + xn)}{(n + 2)} \quad ( 2.15 )$$

In this expression,  $n$  is the number of monomer units per chain and  $x$  indicates the doping level of the polymer, where a charge can be distributed over several monomer units, typically for conducting polymers this lies in the range  $0.25 < x < 0.4$ .

#### 2.2.5 Cyclic voltammetry

This technique involves scanning an applied voltage,  $E$ , linearly with time,  $t$ , at a scan rate,  $\nu$ , and measuring the resulting current,  $I$ . The potential drives reactions at the working electrode interface with the electrolyte solution. The magnitude of peaks in the current as well as the potential at which they occur and the way in which these vary with scan rate, provide information on the kinetics of the reaction<sup>9</sup>. The potential limits are selected according to the potential windows of the electrolyte solution, the electrode material and the reaction of interest at the electrode.

The charge  $Q$  can be calculated by computing the integral of current as a function of time as shown in equation ( 2.16 ).

$$Q = \int i dt \quad ( 2.16 )$$

Knowing the charge and the number of electrons involved in the reaction, the quantity of reacting species can be calculated according to equation ( 2.14 ).

When using cyclic voltammetry to polymerise a monomer, the growth charge can be calculated by integrating the area under the curve in which the current peaks during the polymerisation. The integral of current with respect to time in each cycle is summed to give the total growth charge which can then be used to determine the quantity of monomer consumed in the reaction. In this work, this method is referred to as potentiodynamic deposition in the context of producing a polymer film.

#### 2.2.6 Chronoamperometry

This technique involves the application of a constant potential to a system and measuring the resulting current as a function of time. The potential is selected to drive a reaction at the electrode. In this work chronoamperometry is used either to drive the polymerisation and deposition reactions to produce a polymer film, known as potentiostatic deposition, or to induce oxidation or reduction of the sample. The charge applied can be easily calculated by integrating the resulting current transient over time.

#### 2.2.7 Chronopotentiometry

This technique involves the application of a constant current to a system and measuring the resulting changes in electrode potential as a function of time. Again, the purpose of this technique is to drive a reaction at the electrode however this technique allows greater control over the applied charge by defining the exact amount of time the current is applied. Furthermore, the rate of the reaction is controlled by the choice of current applied. When used to drive a polymerisation reaction this method is referred to as galvanostatic deposition.

### 2.3 Atomic force microscopy

An atomic force microscope (AFM) provides topographical information about a surface by scanning an atomically sharp tip across the desired area and monitoring the forces experienced by the tip as it encounters the surface features. The tip is mounted on a cantilever that reflects a laser, such that the tip and cantilever can move in response to the interatomic forces at the surface and the laser can detect this movement<sup>10</sup>. The forces experienced by the tip are a measure of the tip/surface distance and the resulting displacement of the tip is converted into a three dimensional image of the surface features.

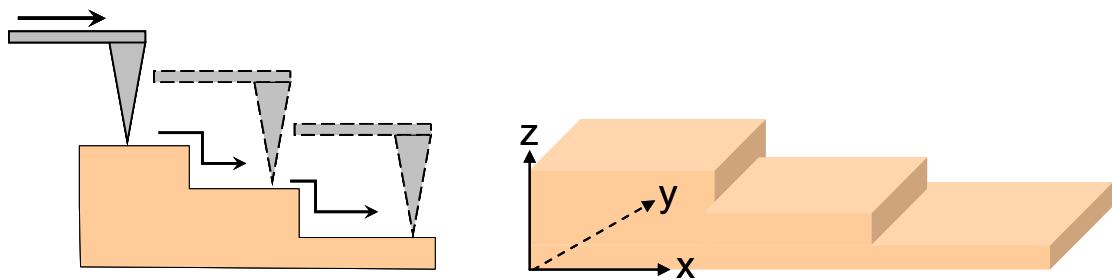


Figure 2.13– Diagrams of the AFM scanning process and the resulting 3D image of the surface.

The AFM has three modes of scanning: contact, non-contact and tapping. ‘Contact’ mode involves scanning the sample at a very small ( $< 1$  nm) sample-tip distance at which the tip/surface interaction is repulsive. This mode is not considered suitable for soft samples such as polymer films due to the possibility of the tip dragging across the sample and damaging the surface layer. The ‘non-contact’ mode involves the tip oscillating above the sample at a resonant frequency of 1-10 nm<sup>11</sup> but this can also incur damage to the surface due to the attractive Van der Waals forces which are particularly strong in this range that can cause the tip to ‘crash’. The ‘tapping’ mode is considered a good compromise in which the tip oscillates at a resonant frequency around 20-100 nm<sup>11</sup>, intermittently ‘tapping’ the surface and encountering the electrostatic forces and resulting in a change in the amplitude of the oscillation<sup>12</sup>.

## 2.4 References

1. Sivia, D. S. *Elementary Scattering Theory For X-ray and Neutron Users*. (Oxford University Press, 2011).
2. Nelson, A. Co-refinement of multiple contrast neutron/X-ray reflectivity data using MOTOFIT. *J. Appl. Crystallogr.* **39**, 273–276 (2006).
3. Richardson, R. M., Swann, M. J., Hillman, A. R. & Roser, S. J. In situ neutron reflectivity studies of electroactive films. *Faraday Discuss.* **94**, 295–306 (1992).
4. Sears, V. F. Neutron scattering lengths and cross sections. *Neutron News* **3**, 26–37 (1992).
5. Dianoux, A.-J. & Lander, G. *Neutron Data Booklet*. (OCP Science, 2003).
6. Penfold, J. *et al.* Recent advances in the study of chemical surfaces and interfaces by specular neutron reflection. *J. Chem. Soc. Faraday Trans.* **93**, 3899–3917 (1997).
7. Faulkner, L. R. Understanding electrochemistry: Some distinctive concepts. *J. Chem. Educ.* **60**, 262 (1983).
8. Heinze, J., Frontana-Uribe, B. A. & Ludwigs, S. Electrochemistry of conducting polymers - persistent models and new concepts. *Chem. Rev.* **110**, 4724–71 (2010).
9. Fisher, A. C. *Electrode Dynamics*. (Oxford University Press, 1996).
10. Attard, G. & Barnes, C. *Surfaces*. (Oxford University Press, 2008).
11. *Scanning Probe Microscopy Training Notebook - Version 3.0*. (Veeco Metrology Group, Digital Instruments, 2000).
12. Zhong, Q., Inniss, D., Kjoller, K. & Elings, V. B. Fractured polymer / silica fiber surface studied by tapping mode atomic force microscopy. *Surf. Sci. Lett.* **290**, L688–L692 (1993).

## Chapter 3 – Experimental and analysis

### 3.1 Neutron reflectometry

#### 3.1.1 Alignment

The alignment protocol varies slightly according to each neutron reflectometry instrument however the basic principles remain the same. The sample is placed on the sample stage of the instrument which can be moved both horizontally and vertically as well as tilted to specific angles. A laser positioned in the neutron guide simulates the trajectory of the neutron beam. The first part of the alignment requires manually adjusting the sample stage such that the laser touches upon the sample's interface of interest. Done 'by eye', this is therefore a very rough approximation of the correct sample position. Following this, the alignment is carried out using the neutron beam itself. The goal is to find the position of the sample at which the incident beam angle is  $0^\circ$ . A series of scans through the sample height and sample angle are carried out, measuring the neutron intensity at each point. The sample position given by the alignment provides the starting point of all the instrument movements that will produce different incident angles throughout the subsequent measurements; it is therefore a calibration specific to each sample.

#### 3.1.2 Measurement

For a given sample, several incident angles may be used to acquire a measurement of  $R$  over the desired  $Q$  range. The settings required to focus the beam onto the interface of interest vary with each angle and affect the incident beam intensity. As described in Chapter 2, the reflectivity is the ratio of the reflected and incident intensities, therefore it is necessary to acquire a measurement of the incident beam; this is known as a direct or transmitted beam measurement. According to the substance through which the incident beam must travel to reach the interface of interest, i.e. air or quartz in this work, a direct beam must be acquired through the same material. The direct beam for each set of instrument settings particular to a given angle will be used to process the reflected data acquired with the equivalent settings; this process is known as the data reduction. For experiments carried out at the ILL, data is reduced using

Cosmos, a program run through LAMP. This software allows the different angles acquired for a single sample measurement to be 'stitched' together to form the final reflectivity profile over the desired range of  $Q$ . It is also used to subtract the background signal from the measured reflectivity. At ISIS, the data is reduced using programs run in Open Genie.

### 3.1.3 In situ electrochemistry set-up

Performing electrochemical experiments on a reflectometer requires not only control of the potentiostat and visualisation of the electrochemical measurements taking place but also the ability to synchronise measurements when necessary. While simple solutions such as using 'remote desktop' software were found to address the first two requirements, ensuring the communication between instruments is more challenging. The Biologic SP-200 was specifically purchased with these experiments in mind and had the advantage of providing a trigger system. The EC-lab software that controls the potentiostat also allows a sequence of measurements and commands to be programmed. Thus the potentiostat was connected to the reflectometer such that it could receive triggers to initiate measurements. This is particularly important for the acquisition of time dependent data in which the two instruments must begin measurements simultaneously.

### 3.1.4 Model interpretation and analysis

In the context of studying polymer films, NR is used to provide information about the internal structure of the films, specifically the solvation, as well as the thickness. It is the SLD of the film that provides information about the solvation of the polymer, as seen in equation ( 2.3 ) in the previous chapter. The thickness of the film may seem easily read from the fitted model however the roughness parameters can affect this value. It is important therefore to consider the SLD profile when examining the model parameters. A large surface roughness may in fact indicate a thicker or thinner film than that indicated by the thickness parameter in the model since the latter represents the average thickness. This can be explored by including additional layers into the model to accommodate for a changing SLD within a physical layer of the polymer, however, in some cases the layer thickness and roughness parameters of a layer can converge to a similar value. In this case, the mathematical description of the roughness

becomes meaningless and often results in a layer that is indistinguishable from neighbouring layers in the SLD profile.

When studying the growth of polymer films, the NR measurements were acquired *in situ* such that the films were in a solvated state. In order to compare the NR fit results to measures of dry thickness, the thickness values from the fits were normalised to account for the volume of solvent. The quantity of polymer is therefore expressed as a mass per area according to equation ( 3.1 ) thereby removing the solvent content contribution to the thickness parameter;  $\rho$  is the density and  $vf$  is the volume fraction.

$$\frac{mass}{area} (g\ cm^{-2}) = thickness\ (cm) \cdot \rho_{polymer}\ (g\ cm^{-3}) \cdot vf_{polymer} \quad (3.1)$$

The quality of the fit is quantified by the  $\chi^2$  value, defined in equation ( 3.2 ) , which is a measure of how well the model fits the data; the lower the value, the better the fit to the data. However, in some cases, a  $\chi^2$  value can be misleading and the way in which the model visually follows the predominant features of the experimental data should also be taken into account.

$$\chi^2 = \frac{1}{number\ of\ data\ points} \sum \frac{(observed\ data - theoretical\ data)^2}{error\ in\ observed\ data^2} \quad (3.2)$$

The  $\chi^2$  value depends largely on the modelled fit being within the error bars of the measured reflectivity data and is weighted according to the number of data points. Consequently, the fit can sometimes produce a lower  $\chi^2$  value, not because the fit follows the features of the data, but because it comes closest to being within the greatest number of error bars. Since  $R$  drops by a factor of  $Q^{-4}$ , the intensity at low  $Q$  is higher, resulting in a greater number of data points and smaller error bars compared to the higher range of  $Q$ . This means that the  $\chi^2$  is in fact weighted to fit the low  $Q$  region preferentially such that the fit with the best  $\chi^2$  value may not adequately fit the data at high  $Q$ ; a visual appraisal of the fit is therefore also required to find the most appropriate model.

In this work, NR data is fitted to models using the Motofit<sup>1</sup> package created by Andrew Nelson within the Igor Pro software.

## 3.2 Electrochemical analysis

The growth charge from the electrochemical deposition of the polymer films allows the thickness of the films to be estimated based on Faraday's laws of electrolysis as expressed in equation ( 2.14 ) in the previous chapter. Using this relationship, the growth charge can be readily converted to a thickness ( 3.3 ), coverage ( 3.4 ) or mass per area ( 3.5 ).

$$thickness (cm) = \frac{Q (C) \cdot M (g mol^{-1})}{z \cdot F (C mol^{-1}) \cdot \rho (g cm^{-3}) \cdot A (cm^2)} \quad (3.3)$$

$$\Gamma (mol cm^{-2}) = \frac{Q (C)}{z \cdot F (C mol^{-1}) \cdot A (cm^2)} \quad (3.4)$$

$$\frac{mass}{area} (g cm^{-2}) = \frac{Q (C) \cdot M (g mol^{-1})}{z \cdot F (C mol^{-1}) \cdot A (cm^2)} \quad (3.5)$$

where  $Q$  is the charge,  $F$  is Faraday's constant,  $M$  is the molar mass,  $\rho$  is the density,  $\Gamma$  is the coverage,  $A$  is the surface area and  $z$  is the number of electrons transferred.

The electrochemical characterisation of a film using cyclic voltammetry provides the value of the charge required to oxidise the film,  $Q_{ox}$ . Since this value is not comparable with the growth charge  $Q_g$ , which includes not only the oxidation charge but also the charge required to polymerise the monomer, these values are converted to coverage values. The calculation thus accounts for the different ways in which the charge was used in these processes.

The oxidation to growth coverage ratio ( $\Gamma_{ox} / \Gamma_g$ ) expressed as a percentage is a quantification of the oxidation charge relative to the growth charge. This allows the electroactivity of films grown from different growth protocols, different electrode areas and with different growth charges to be compared.

### **3.3 Preparation of gold surface electrodes**

The substrates in this work are either microscope slides or blocks of glass or quartz with a gold-coated surface. These were all coated using the same preparation and deposition protocol with the exception of the gold coated microscope slides from Platypus Technologies.

In a first instance, the substrates are cleaned by sonication in Anopol-C solution, a mixture of surfactants and commercial detergents, then rinsed and sonicated in deionised water and dried with compressed air. They are then refluxed for 15 min in a solution containing 3 vol% (3-mercaptopropyl)-trimethoxysilane (MPTS), 3 vol% deionised water and 94 vol% isopropanol (IPA) before being rinsed with IPA and transferred into fresh IPA to sonicate for a further 15 min. The substrates are then dried with compressed air and the process is repeated a further two times. Once coated in MPTS, the substrates are either stored in a container under vacuum to prevent contamination or immediately coated with gold.

The gold coater used in this work is a EMS300R T Triple Target, Large Chamber, Rotary-Pumped Sputter Coater. In order to ensure the most even thickness of gold for NR experiments, the quartz blocks were coated one by one and placed at the centre of the rotating stage in the sputtering chamber. Microscope slides and glass blocks were placed all over the stage and multiple samples were coated at once since the uniform thickness was not required. The coating procedure used a current of 80  $\mu\text{A}$  for 200 s.

### **3.4 Atomic force microscopy measurements**

The AFM measurements were carried out on a Veeco Dimension 3100 Scanning Probe Microscope operated in tapping mode using silicon tips. The measurements of film thickness are achieved by using a scalpel to make a small scratch in the surface of the polymer film, without cutting through the gold surface. An AFM image of the scratch is then acquired and the Nanoscope software, version 6.13R1, was used to evaluate the difference in height across the scratch using the 'section' tool. This gives a height profile of a chosen section of the image.

The surfaces of the polymer films were also studied using AFM to evaluate the surface roughness. The Nanoscope software provides a number of different statistics to express roughness so, for the purposes of studying these films, two measures were selected: the  $R_q$ , the "root mean square average of height deviations taken from the mean data plane", and the surface area difference (SAD) which is the "difference between the image's three-dimensional surface area and two-dimensional projected surface area", as defined in the software manual<sup>2</sup>.

### 3.5 References

1. Nelson, A. Co-refinement of multiple contrast neutron/X-ray reflectivity data using MOTOFIT. *J. Appl. Crystallogr.* **39**, 273–276 (2006).
2. Geschwender, T., Kowalski, C. & Kelley, V. *NanoScope Software 6.13 User Guide*. (2004).

## **Chapter 4 – Poly(3,4-ethylenedioxythiophene)-nanodiamond composite films**

### **4.1 Introduction**

The present interest in nanomaterials has led to substantial research focusing on the combination of conducting polymers with carbon composites, in particular carbon nanotubes<sup>1</sup>, to enhance electronic and structural properties as discussed in Chapter 1. As mentioned previously, the use of nanodiamonds (NDs) as a composite in polymer materials is becoming increasingly common due to their low cost and their ability to modify composite properties at low concentrations<sup>2</sup>. Composite polyaniline(PANI)-ND films displayed improved structural properties and different surface morphology to the pristine PANI films<sup>3,4</sup>. Poly(3,4-ethylenedioxythiophene)(PEDOT)-CNT is another successful composite that has been extensively studied and developed as a promising material for applications<sup>5-7</sup>, therefore it is somewhat surprising that PEDOT-ND has not been more widely investigated to date. This study, inspired by the work of Ispas et al<sup>8</sup>, considers the incorporation of NDs within a PEDOT matrix. The research thus far has examined the physical effect of the presence of nanodiamonds on the composite films, concluding that these particles increase the rigidity of the film while reducing porosity and increasing homogeneity in films containing 2.3 or 3.6 vol% ND.<sup>8</sup>

In this work, the objectives are to a) investigate the effect of deposition protocol on the incorporation of ND; b) identify whether or not the inclusion of ND influences electrochemical behaviour and how this compares to a pristine PEDOT film; c) explore the effect of ND on the internal and surface structure of the films.

## 4.2 Experimental

### 4.2.1 Potentiostatically deposited PEDOT and PEDOT-ND films

All chemicals were used as received from Sigma Aldrich. The working electrodes were gold coated microscope slides cut to form areas between 1.8 and 2.6 cm<sup>2</sup>. The counter and reference electrodes were an iridium coated titanium grid and silver wire respectively. The ND powder used is characterised by spherical particles, < 10 nm in size, with a density of 3.5 g cm<sup>-3</sup> and a bulk density of 0.2 – 0.7 g cm<sup>-3</sup>. A series of solutions were prepared containing 0.01 M EDOT in either 0.1 M LiClO<sub>4</sub> in CH<sub>3</sub>CN or 0.01 M SDS in 0.1 M H<sub>2</sub>SO<sub>4</sub>. Two dispersions of 0.088 wt% and 0.88 wt% NDs were prepared in deionised water. Deposition solutions containing NDs were prepared by combining the chosen monomer solution with the ND dispersion in a ratio of 7.6 : 1 to give concentrations of 0.0085 M and 0.085 M. The concentration of NDs was originally chosen based on the publication by Ispas et al<sup>8</sup>.

Sample	Solvent	ND concentration / M	Working electrode area / cm <sup>2</sup>	Q <sub>g</sub> / mC cm <sup>-2</sup>	E <sub>g</sub> / V vs Ag wire
1	CH <sub>3</sub> CN*	0	1.84	30	1.2
2	CH <sub>3</sub> CN	0.0085	2.295	30	0.9
3	H <sub>2</sub> SO <sub>4</sub>	0	1.955	30	0.9
4	H <sub>2</sub> SO <sub>4</sub>	0.0085	2	30	0.9
5	CH <sub>3</sub> CN	0	1.92	30	1.2
6	H <sub>2</sub> SO <sub>4</sub>	0.085	2.55	30	0.9
7	H <sub>2</sub> SO <sub>4</sub>	0.085	2.145	60	0.9
8	H <sub>2</sub> SO <sub>4</sub>	0	2.04	60	0.9
9	CH <sub>3</sub> CN	0	2.07	60	1.2
10	CH <sub>3</sub> CN	0.085	1.8	60	1.2

Table 4.1 – Sample summary of potentiostatically grown PEDOT and PEDOT-ND thin films (\* indicates that there was no water added to the deposition solution); Q<sub>g</sub> and E<sub>g</sub> are the growth charge and growth potential respectively

To ensure that the deposition solutions were compositionally consistent, deionised water was added in the same ratio when depositing pristine PEDOT. The films were

deposited potentiostatically at either 0.9 V or 1.2 V and limited by a growth charge of 30 or 60 mC cm<sup>-2</sup>. The films were all characterised by cycling between -0.3 and 0.6 V in 0.1 M LiClO<sub>4</sub> in MeCN and those deposited from the aqueous solution were first characterised by cycling in 0.1 M H<sub>2</sub>SO<sub>4</sub>. The details of each sample and the deposition conditions are given in Table 4.1.

#### 4.2.2 Potentiodynamically deposited PEDOT and PEDOT-ND films

The working electrodes were gold coated glass blocks with a surface area of 50 cm<sup>2</sup>. The counter and reference electrodes were an iridium coated titanium grid and a silver wire, respectively. Deposition solutions were prepared containing 0.01 M EDOT in 0.01 M SDS in 0.1 M H<sub>2</sub>SO<sub>4</sub>. The ND dispersion was 0.88 wt% in deionised water. Deposition solutions containing NDs were prepared by combining the monomer solution with the ND dispersion in a ratio of 7.6 : 1 to give a ND concentration of 0.085 M. To ensure that the deposition solutions were compositionally consistent, deionised water was added in the same ratio when depositing pristine PEDOT. The films were deposited potentiodynamically by cycling between -0.3 V and 0.7 V at a scan rate of 20 mV s<sup>-1</sup>, with a current cap of 0.12 mA cm<sup>-2</sup> for 20 cycles.

#### 4.2.3 PEDOT and PEDOT-ND samples for neutron reflectometry

The working electrodes were gold coated quartz blocks with a surface area of 40 cm<sup>2</sup>. All other details of the experimental setup and deposition solutions were as described in section 5.2.2. The films were deposited potentiodynamically by cycling between -0.3 V and 0.8 V at a scan rate of 20 mV s<sup>-1</sup> and with a current cap of 0.12 mA cm<sup>-2</sup>. A pristine PEDOT and a PEDOT-ND film were grown with 15 cycles and a further PEDOT-ND film was made with only 10 cycles to produce a thinner film.

The NR measurements were done on FIGARO and carried out at two angles,  $\theta = 0.624^\circ$  and  $\theta = 2.5^\circ$ , measuring a  $Q$  range of 0.007 – 0.25 Å<sup>-1</sup>.

	H <sub>2</sub> O	D <sub>2</sub> O	ND
$\rho / \text{g cm}^{-3}$	1	1.1	3.5
SLD / $10^{-6} \text{ \AA}^{-2}$	-0.56	6.3	11.7

*Table 4.2 – Summary of SLDs used in the analysis of NR results*

The reflectivity profiles were acquired in air before the samples were transferred to solid/liquid cells and measured in H<sub>2</sub>O, D<sub>2</sub>O and a mixture with an SLD of  $2.26 \times 10^{-6} \text{ \AA}^{-2}$ , the simulated SLD of PEDOT for a density of  $1.34 \text{ g cm}^{-3}$ , the density of the monomer. The PEDOT-ND#15 film was also measured in a mixture contrast matched to  $1.7 \times 10^{-6} \text{ \AA}^{-2}$ , the SLD value for PEDOT with the commonly assumed density<sup>9,10</sup> of  $1 \text{ g cm}^{-3}$ . The pristine PEDOT film was first measured in H<sub>2</sub>O, followed by D<sub>2</sub>O and finally measured in the contrast matched solution. The PEDOT-ND#15 film was measured first in H<sub>2</sub>O, then in the contrast matched solution, followed by D<sub>2</sub>O and then again in the contrast matched solution before the final measurement in the H<sub>2</sub>O/D<sub>2</sub>O mixture with an SLD of  $1.7 \times 10^{-6} \text{ \AA}^{-2}$ . The cell was emptied and rinsed between measurements, but the order in which these were carried out is important as it is recognised that the films may retain solvent which could affect the extent of solvent exchange and therefore affect the measured SLD of the solvated film.

### 4.3 Results

#### 4.3.1 Potentiostatically deposited PEDOT and PEDOT-ND films

A comparative view of how the transients for samples grown in aqueous and organic solvents differed is illustrated in Figure 4.1. The potentiostatic growth transients did not show any significant differences between the pristine PEDOT and PEDOT-ND films. The solvent did, however, affect both the growth and appearance of the films produced.

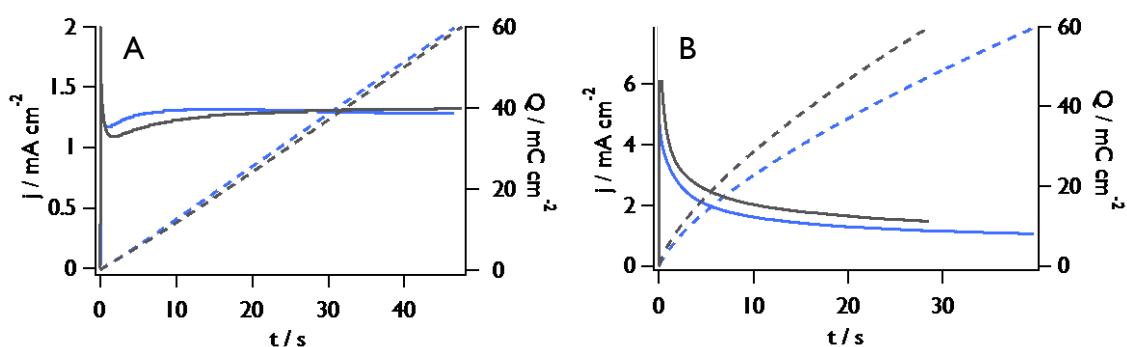


Figure 4.1– Growth transients for PEDOT (blue) and PEDOT-ND (grey) films grown in organic (A) and aqueous (B) media, full and dashed lines are the current and charge density, respectively, as functions of time

In all cases, growth in aqueous media resulted in an initially higher current response therefore the growth was faster to achieve the desired charge density. The PEDOT-ND transient also indicates a faster growth although this was not observed in other samples prepared using the same growth protocol. The initial current peak was found to vary slightly within a given deposition medium therefore this feature is not attributed to the presence of NDs.

The results are consistent with the polymer growth transients presented in the literature and appear to fit with a deposition model of instantaneous nucleation and three-dimensional growth<sup>11,12,13</sup>. In acetonitrile solutions, the initial current peak is followed by a current minimum at which point nucleation begins on the electrode surface and polymerisation is observed via the gradual increase in current to a plateau as the growth progresses<sup>14</sup>. In aqueous solutions the nucleation step is not visible, due

the higher current peak, and therefore higher rate, but the current gradually stabilises to a plateau at a similar current magnitude to that observed in the organic medium.

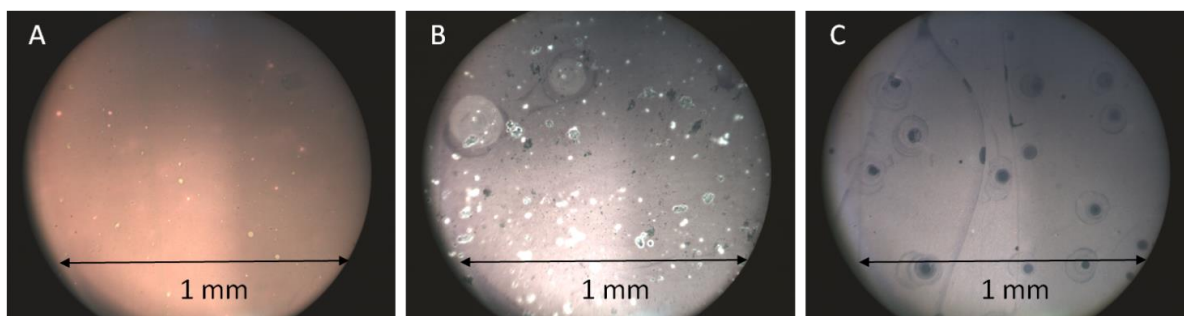


Figure 4.2 – Optical microscopy images acquired at a magnification of  $\times 20$  showing a PEDOT-ND film grown in aqueous media (A) and films grown in organic media with (B) and without (C) NDs

The films prepared from aqueous media were visually more homogeneous than those deposited from organic media. The difference is clear when examining the images in Figure 4.2 which show the optical microscope images of three samples, the first grown from aqueous with NDs and the others grown from acetonitrile with and without NDs. The sample grown from aqueous medium appears to have less surface defects than both films grown in acetonitrile.

The second observation that can be made is that the presence of NDs in the organic solution produced a film containing discernible clusters as well as holes that are identified by the bright spots in the image where the gold substrate is reflecting through. These features can be seen in panel B of Figure 4.2 and panel C shows that they are not present in the pristine PEDOT film grown in acetonitrile.

All films were characterised using cyclic voltammetry. Cycling in organic media produced the box-like shaped voltammograms showing the capacitive behaviour<sup>15</sup> characteristic of PEDOT in this potential range<sup>10,16</sup>, which is in keeping with the data presented by Ispas et al<sup>8</sup>.

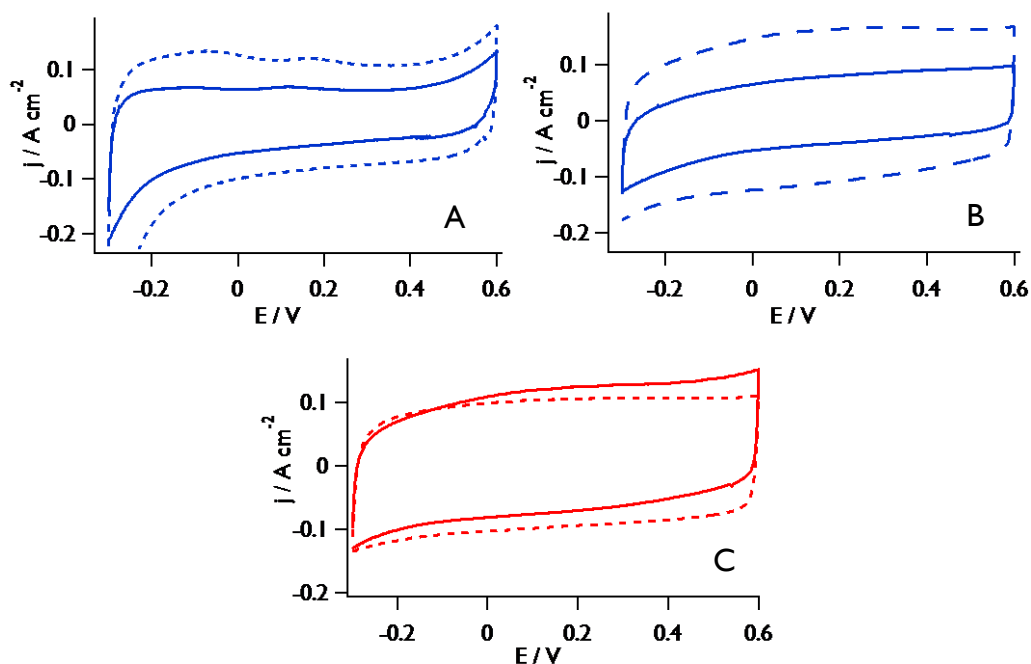


Figure 4.3 – Cyclic voltammograms of films grown in organic (red) and aqueous (blue) media to a growth charge of  $60 \text{ mC cm}^{-2}$  and cycled at  $50 \text{ mV s}^{-1}$  in  $0.1 \text{ M H}_2\text{SO}_4$  (A) and  $0.1 \text{ M LiClO}_4$  in MeCN (B and C); full and dashed lines indicate films with and without NDs respectively

Films produced from aqueous media were also cycled in monomer free sulphuric acid solution and again showed a similar shape with the key difference being a peak and drop in current at the upper and lower potential limits respectively. Figure 4.3 shows a comparison of the voltammograms acquired in both organic and aqueous media for the same samples, as well as that of equivalent films grown from organic media.

In the case of the films grown from the aqueous deposition solutions, the PEDOT-ND sample is less electroactive than the equivalent pristine PEDOT film, presenting a smaller current response, but the opposite is true for these films grown in acetonitrile. This behaviour was not observed in the films grown to a growth charge of  $30 \text{ mC cm}^{-2}$ . The electrochemical characterisation of the films therefore did not indicate any consistent effect produced by the NDs.

AFM was used to evaluate the dry thickness of three films produced by deposition from aqueous media. The inhomogeneity of the samples produced from organic media excluded them from this study.

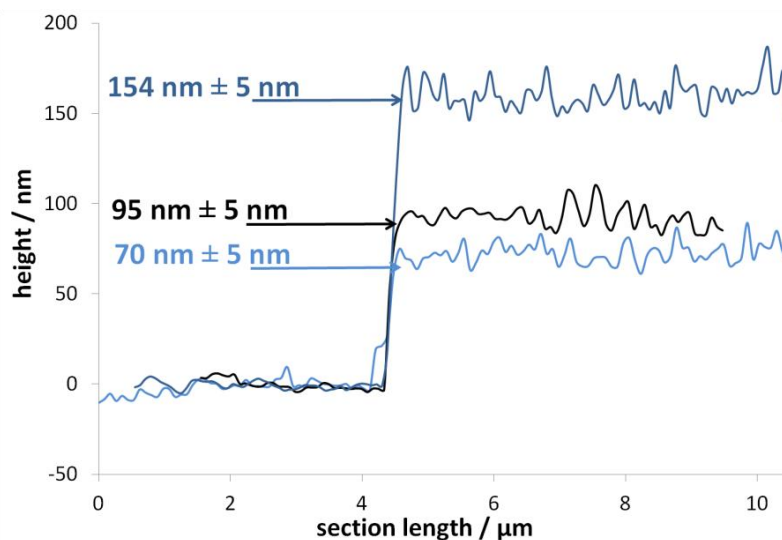


Figure 4.4 – Height profiles from AFM images of a dry pristine PEDOT film deposited with  $Q_g = 30 \text{ mC cm}^{-2}$  (light blue),  $Q_g = 60 \text{ mC cm}^{-2}$  (dark blue) and of a PEDOT-ND film deposited with  $Q_g = 60 \text{ mC cm}^{-2}$  (black); thicknesses quoted are based on three separate section measurements across the scratch

The height profiles shown in Figure 4.4 show that the pristine PEDOT film deposited for a growth charge density  $Q_g = 60 \text{ mC cm}^{-2}$  was twice as thick as the film deposited with half the charge density, as expected. The film grown with NDs, however, was also deposited with  $Q_g = 60 \text{ mC cm}^{-2}$  and yet the thickness is significantly less than the equivalent pristine PEDOT film. This indicates that either the NDs inhibit the polymerisation process or result in a film with a much higher density or conversely a more porous structure that collapses when dried.

Raman spectra were acquired from three samples grown from aqueous media at different points on the film, as well as from a sample of the ND powder. Two of the films were expected to contain NDs and one was a pristine PEDOT film. All the films showed the characteristic PEDOT peaks as illustrated in Figure 4.5. A comparison of the frequencies observed with those in the literature is presented in Table 4.3.

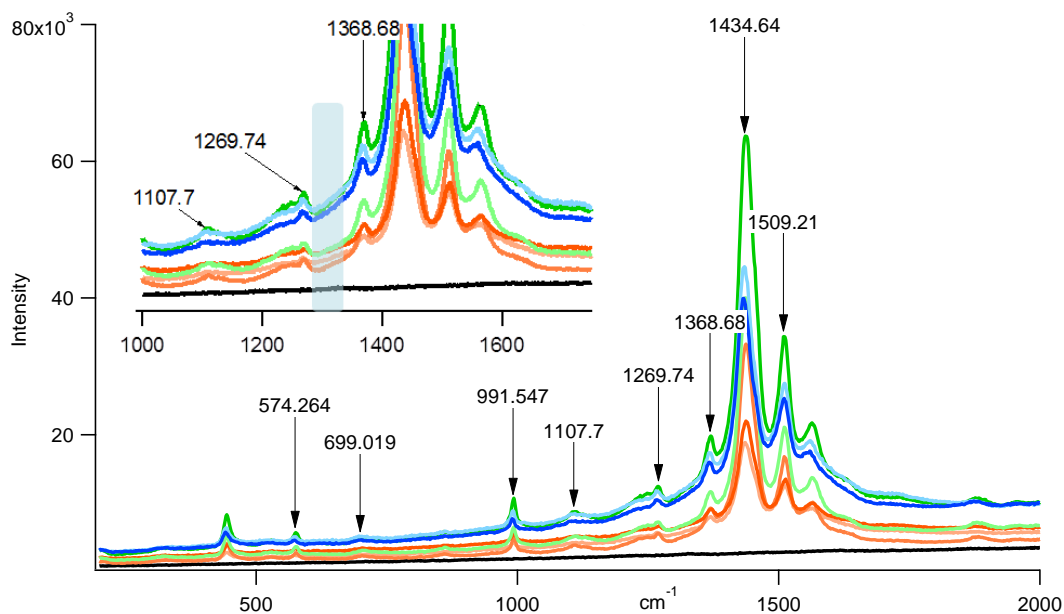


Figure 4.5 – Raman spectra for the thin films (coloured traces) and ND powder (black trace); inset: shaded area highlights where the characteristic diamond peak should be observed around  $1332\text{ cm}^{-1}$

Garreau et al <sup>20</sup>		Gustafsson et al <sup>21</sup>	PEDOT-ND results
theoretical	experimental	experimental	
1509	1518	1515	1509.2
1444	1434	1433	1434.6
1366	1369	1367	1368.7
1267	-	1267	1269.7
1110	-	1109	1107.7
988	991	990	991.5
691	-	697	699
577	-	571	574.3

Table 4.3 – Comparison of the characteristic Raman bands for PEDOT as found in the literature with the observed spectra for the PEDOT and PEDOT-ND films

The spectrum acquired from the ND powder was a flat line, containing no features that would allow identification of the NDs within a polymer matrix. The literature suggested that a characteristic diamond peak should be present around  $1332\text{ cm}^{-1}$ <sup>17</sup> or  $1338\text{ cm}^{-1}$ <sup>18</sup>. It is understood that these particles may present a graphitic or

amorphous structure on the surface which may affect the intensity of the signal from the diamond structure<sup>4,19</sup>.

Complementary EQCM measurements of the potentiostatic deposition of pristine PEDOT and PEDOT-ND films were carried out by Virginia Ferreira. These preliminary experiments indicated a slight increase in mass for films prepared with NDs compared to pristine PEDOT films prepared using an identical deposition protocol. Further samples are needed to confirm these findings.

#### 4.3.2 Potentiodynamically deposited PEDOT and PEDOT-ND films

Pristine PEDOT and PEDOT-ND films grown potentiodynamically in aqueous media showed very few differences in their growth cycles. The first PEDOT film displayed a slightly higher current than the other films as shown in Figure 4.6(A). However, this was not consistent with the second PEDOT film, where the growth was almost identical to that of the PEDOT-ND films. Any differences therefore are not significantly greater than sample variation.

Sample	1	2	3	4
$Q_g / \text{mC cm}^{-2}$	14.4	12.9	12.8	13.4
Calculated dry thickness / nm	67.4	60.4	60	62.8

*Table 4.4 – Summary of the growth charge and the coulometric estimate of dry film thickness calculated from  $Q_g$  for each of the potentiostatically grown samples*

Cyclic voltammetry was used to characterise the films after growth and the second PEDOT film again showed a very similar response to that of the PEDOT-ND films as illustrated in Figure 4.7(A).

The stability of the films was also tested during prolonged charge and discharge. One film of each of type, PEDOT and PEDOT-ND, was held in a reduced state at -0.3 V for 3h, followed by cycling, then 3h in the oxidised state at 0.55 V. Figure 4.7(B) shows how the cyclic voltammograms of these films changed very little during and after these tests, suggesting a good stability of the films.

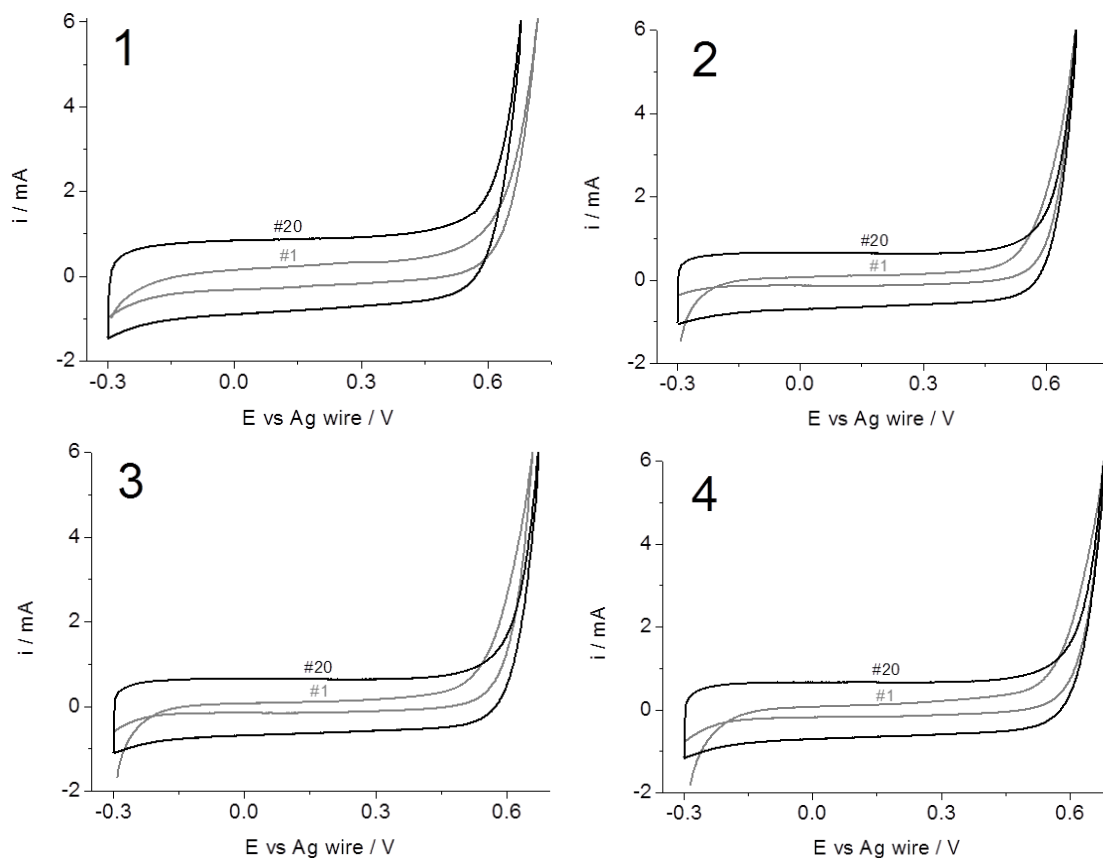


Figure 4.6 – First and final cycles of the potentiodynamic growth of PEDOT (1 and 2) and PEDOT-ND (3 and 4) films at a scan rate of  $20 \text{ mV s}^{-1}$  for 20 cycles with a current cap of 6 mA for an electrode area of  $50 \text{ cm}^2$

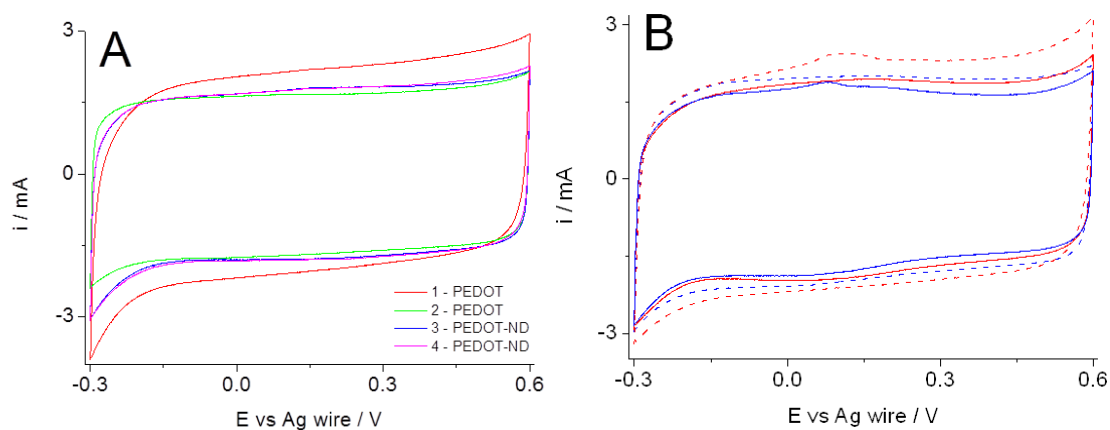


Figure 4.7 – Cyclic voltammograms of the PEDOT and PEDOT ND films at  $50 \text{ mV s}^{-1}$  in  $0.1 \text{ M H}_2\text{SO}_4$ ; panel A shows the characterisation after growth and panel B the cycles measured following charge (blue) and discharge (red) tests of PEDOT (dashed lines) and PEDOT-ND (full lines)

AFM images in Figure 4.8 illustrate how, in small areas of  $1 \mu\text{m}^2$ , the films displayed similar globular features on the surface (3(b) and 4(b)) but when considered over a larger area the PEDOT-ND films appear to have large ‘lumps’ in heights exceeding 100 nm and in sizes up to  $2 \mu\text{m}$  (3(a) and 4(a)). These could therefore be clusters of NDs on the surface of the films.

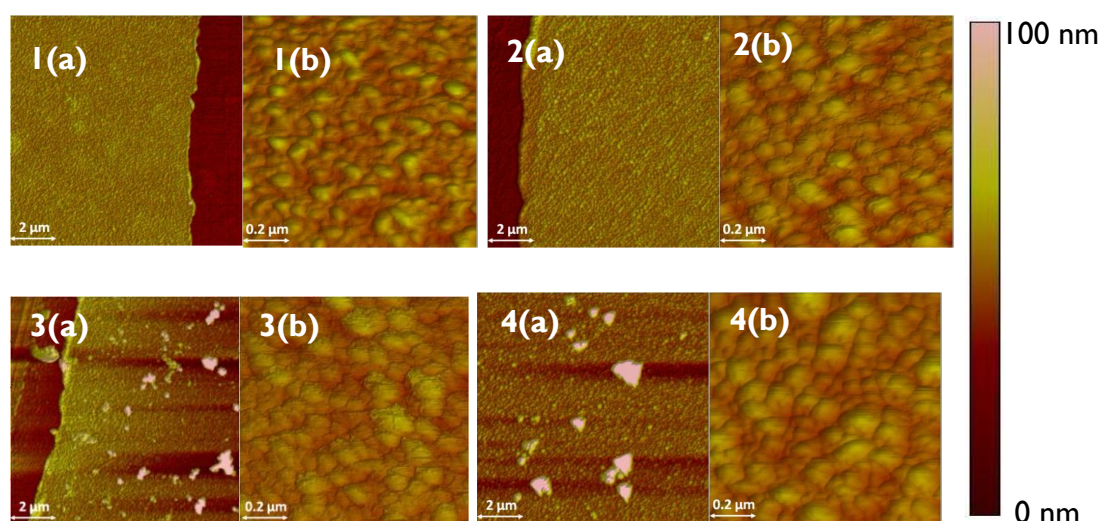


Figure 4.8 – AFM images of the PEDOT (1 and 2) and PEDOT-ND (3 and 4) films after deposition; (a) images are  $100 \mu\text{m}^2$  and (b) images are  $1 \mu\text{m}^2$

Thickness measurements of the dry films from AFM image profiles are summarised in Table 4.5 and show that there were slight variations between the films but in an inconsistent manner, such that no particular trend emerges. Comparison of these values with the estimates of dry thickness calculated from the growth charge, presented in Table 4.4, shows that the AFM measurements are close to the predicted values.

Sample	Composition	Dry thickness / nm
1	PEDOT	$55 \pm 5$
2	PEDOT	$65 \pm 10$
3	PEDOT-ND	$55 \pm 7$
4	PEDOT-ND	$75 \pm 10$

Table 4.5 - Summary of AFM measurements of dry film thickness

### 4.3.3 PEDOT and PEDOT-ND samples for neutron reflectometry

The growth of the PEDOT-ND#15 film exhibited a higher current than the PEDOT film grown with the same growth protocol, i.e. identical scan rate, number of cycles and current cap. Furthermore, the electrochemical characterisation indicated greater electroactivity whereas the PEDOT-ND#10 film resulted in a similar CV to that of the pristine PEDOT despite the former being grown with fewer cycles. Figure 4.9 shows the CVs from both the growth and characterisation of the films in which the effect of the NDs in the deposition solution appears to result in an over-potential in the growth as well as a greater redox charge.

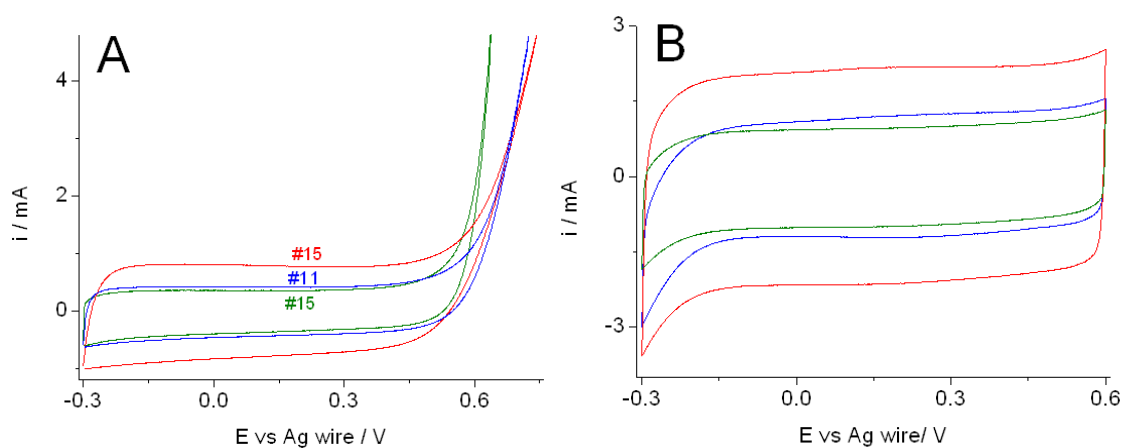


Figure 4.9 – Final cyclic voltammograms from the growth (A) and characterisation (B) of the PEDOT (green), PEDOT-ND#15 (red) and PEDOT-ND#10 (blue) films

Sample	PEDOT 15 cycles	PEDOT-ND 10 cycles	PEDOT-ND 15 cycles
$Q_g / \text{mC cm}^{-2}$	7.12	8.61	16.9
Calculated dry thickness / nm	33.4	40.4	79.2

Table 4.6 – Summary of growth charge and estimated dry film thickness calculated from  $Q_g$  for PEDOT and PEDOT-ND samples potentiostatically grown for the NR study

AFM measurements were used to determine the thickness of the dried films and revealed that the PEDOT-ND film grown with 15 cycles was  $80 \pm 5$  nm which was twice as thick as the equivalent PEDOT film at  $40 \pm 5$  nm. The PEDOT-ND grown with 10 cycles was  $30 \pm 5$  nm. The difference in thickness between the PEDOT and

PEDOT-ND#15 films is in fact accounted for by the difference in growth charge as shown in Table 4.6. Comparison of the measured and estimated dry thickness values reveals that the PEDOT film was 20% thicker than the calculated estimate, whereas the PEDOT-ND#10 film was 25% thinner. This clearly is not consistent with the potentiodynamically grown films presented previously, in which there was no significant difference between the PEDOT and PEDOT-ND films in terms of the growth charge density achieved for the same deposition protocol. The only difference in the setup would be the size of the electrode area however this was accounted for by limiting the maximum current density.

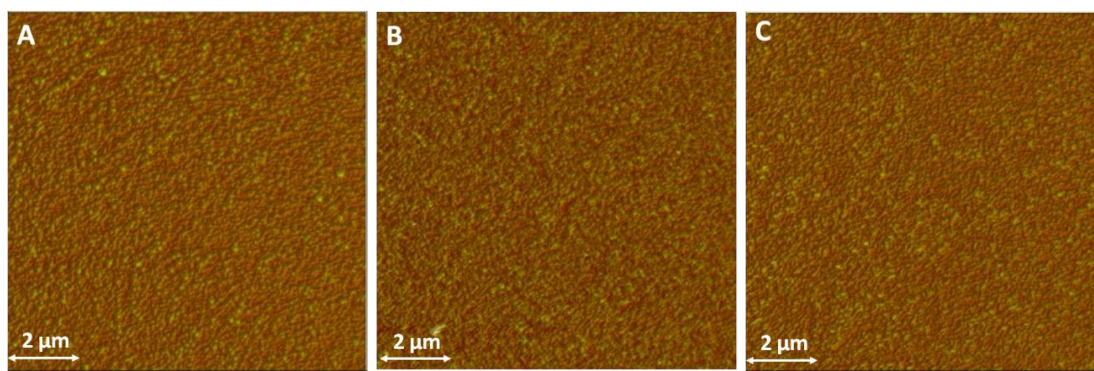


*Figure 4.10 – AFM images of the surface of PEDOT (A), PEDOT-ND#15 (B) and PEDOT-ND#10 (C) films*

Figure 4.10 shows that the 10 x 10 μm images did not reveal the same ‘lumps’ on the surface of the PEDOT-ND films as seen in Figure 4.8 in section 4.3.2.

The NR measurements in air, using the AFM results as starting points for the fits, confirmed the substantial difference in film thickness between the PEDOT and PEDOT-ND films grown to 15 cycles. The single polymer layer model fits to the data are shown in Figure 4.11. It is also noticeable that the PEDOT-ND films have a bulk SLD that is slightly higher than that of the pristine PEDOT film.

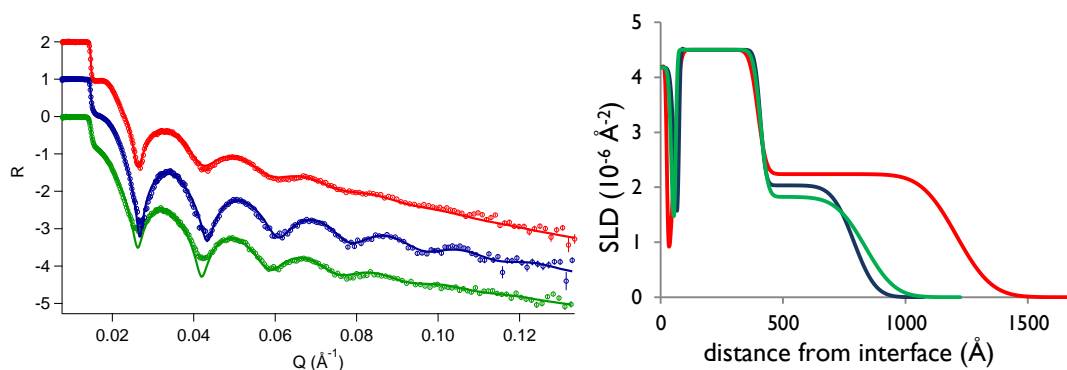


Figure 4.11 – Reflectivity (left) and SLD (right) profiles of the PEDOT and PEDOT-ND films measured in air; the green traces are the PEDOT data and the red and blue traces are the data for the PEDOT-ND#15 and PEDOT-ND#10 films respectively;  $R(Q)$  datasets are offset by increments of 1 for clarity

		PEDOT	PEDOT/ND#15	PEDOT/ND#10
	$\chi^2$	19.1	9.5	4.1
Air	SLD / $10^{-6} \text{ \AA}^{-2}$	0*	0*	0*
Polymer	Thickness / $\text{\AA}$	428.2	813.8	382
	SLD / $10^{-6} \text{ \AA}^{-2}$	1.825	2.3	2.034
	Roughness / $\text{\AA}$	95.5	115.5	70.3
Gold	Thickness / $\text{\AA}$	347	333*	332.7
	SLD / $10^{-6} \text{ \AA}^{-2}$	4.5*	4.5*	4.5*
	Roughness / $\text{\AA}$	23.6	26.1	18
MPTS	Thickness / $\text{\AA}$	16	29.6	16.6
	SLD / $10^{-6} \text{ \AA}^{-2}$	0.266*	0.266*	0.266*
	Roughness / $\text{\AA}$	5.8	5.3	5.4
Quartz	SLD / $10^{-6} \text{ \AA}^{-2}$	4.18*	4.18*	4.18*
	Roughness / $\text{\AA}$	10	20.8	13.2

Table 4.7 – Model parameters from fits to the dry film reflectivity measurements; \* indicates parameters that were fixed during fitting

The complete model parameters and  $\chi^2$  values associated with the fits are given in Table 4.7. The binding silane layer was found to be between 1.5 and 3 nm and the gold layer between 33 and 35 nm. The fit to the dry PEDOT film measurement could not

be improved to better fit the fringe minima around 0.025 and 0.04  $\text{\AA}^{-1}$  resulting in a higher  $\chi^2$ .

Fitting using a multiple polymer layer model improves the  $\chi^2$  of the fits. Figure 4.12 shows the reflectivity and SLD profiles of the multi-layered models in which the variations in SLD within the polymer matrix are visible. The PEDOT-ND films exhibit an area of lower SLD between the gold and bulk polymer layers, whereas the pristine PEDOT film shows a consistently decreasing SLD from the gold/polymer interface to the surface of the polymer. Again, the PEDOT-ND films present an overall higher SLD. The slightly lower value at the electrode interface could indicate that there are few or no NDs close to the gold surface but rather that they are distributed throughout the bulk of the film.

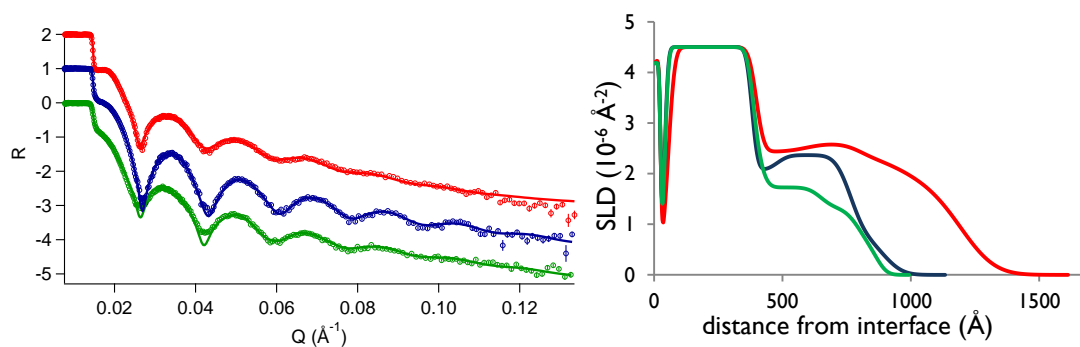


Figure 4.12 – Reflectivity (left) and SLD (right) profiles of the PEDOT and PEDOT-ND films measured in air and fitted using a multiple polymer layer model; the green traces are the PEDOT data and the red and blue traces are the data for the PEDOT-ND#15 and PEDOT-ND#10 films respectively;  $R(Q)$  datasets are offset by increments of 1 for clarity

The parameters of the fits are presented in Table 4.8. The polymer layer was divided into four sections except in the case of the PEDOT-ND#10 film, where the four layer model did not improve the  $\chi^2$  over the three layer model. The model for the PEDOT-ND#15 data was divided into four even layers to maintain physically reasonable values for the interfacial roughness. The thickness of the layers in this case was therefore restricted based on the thickness found using AFM and the single polymer layer model.

		PEDOT	PEDOT-ND#15	PEDOT-ND#10	
	$\chi^2$	14.8	7.9	2.9	
Air	SLD / $10^{-6} \text{ \AA}^{-2}$	0*	0*	0*	
Polymer	Thickness / $\text{\AA}$	72.35	210*	N/A	
	SLD / $10^{-6} \text{ \AA}^{-2}$	0.42	1.57	N/A	
	Roughness / $\text{\AA}$	28.7	100.3	N/A	
	Thickness / $\text{\AA}$	152.3	200*	130.5	
	SLD / $10^{-6} \text{ \AA}^{-2}$	1.34	2.5	0.78	
	Roughness / $\text{\AA}$	49	148.5	58.6	
	Thickness / $\text{\AA}$	236.9	200*	283.9	
	SLD / $10^{-6} \text{ \AA}^{-2}$	1.73	2.69	2.37	
	Roughness / $\text{\AA}$	39.3	52.5	46.9	
	Thickness / $\text{\AA}$	27.9	200*	99	
	SLD / $10^{-6} \text{ \AA}^{-2}$	2.64	2.45	2.06	
	Roughness / $\text{\AA}$	26.4	83	35.5	
	Gold	Thickness / $\text{\AA}$	339	331.6	340
		SLD / $10^{-6} \text{ \AA}^{-2}$	4.5*	4.5*	4.5*
Roughness / $\text{\AA}$		20.8	23.6	18	
MPTS	Thickness / $\text{\AA}$	16.4	29.1	16.1	
	SLD / $10^{-6} \text{ \AA}^{-2}$	0.266*	0.266*	0.266*	
	Roughness / $\text{\AA}$	6.5	5*	10.8	
Quartz	SLD / $10^{-6} \text{ \AA}^{-2}$	4.18*	4.18*	4.18*	
	Roughness / $\text{\AA}$	10*	20.7	5*	

*Table 4.8 – Multiple polymer layer model parameters from fits to the dry film reflectivity measurements; \* indicates parameters that were fixed during fitting*

The PEDOT-ND#15 film presents a peculiar case in that the data can be fitted to two different film thicknesses. Although the results presented above agree with growth charge estimate and the AFM measurement of thickness for the film, this was achieved by using the assumption that the film was approximately 80 nm and fixing the thickness parameter accordingly whereas, when allowed to fit freely, the fits indicate a much thinner film as shown in Figure 4.13.

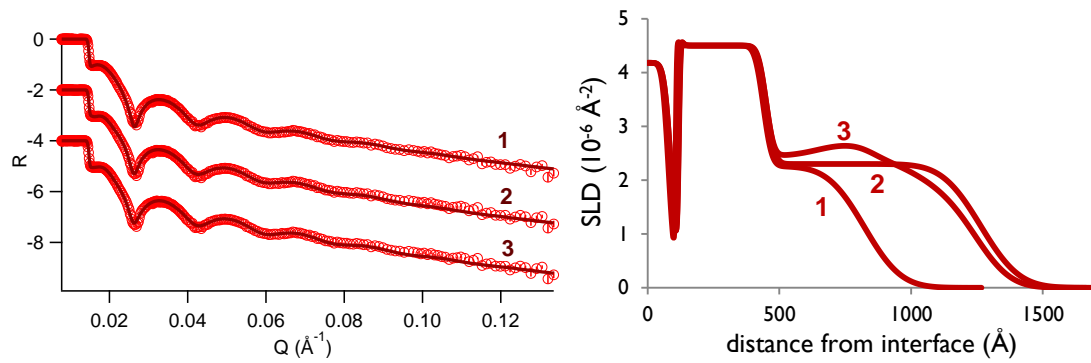


Figure 4.13 – Reflectivity (left) and SLD (right) profiles for the different possible layer fits to the PEDOT-ND#15 data in air: the single layer fit to a thickness of 38 nm (1), the single layer fit to 81 nm (2) and the multilayer fit to 81 nm (3);  $R(Q)$  datasets are offset by increments of -2 for clarity

The fits are visibly very similar. However, the disparity between the polymer thicknesses is significant, with one fit indicating the film to be half the thickness of the others. Table 4.9 indicates the fit parameters and associated  $\chi^2$  which highlights how both single layer models provide good fits to the data. The multilayer fit parameters are those presented in Table 4.8. Not only do the fits present different thickness values but they also indicate different SLD values for the dry film which is of particular significance in the quantification of NDs present in the film.

	$\chi^2$	9.7	9.5
Air	SLD / $10^{-6} \text{ \AA}^{-2}$	0*	0*
Polymer	Thickness / $\text{\AA}$	383.5	813.8
	SLD / $10^{-6} \text{ \AA}^{-2}$	2.26	2.3
	Roughness / $\text{\AA}$	110	115.5
Gold	Thickness / $\text{\AA}$	333*	333*
	SLD / $10^{-6} \text{ \AA}^{-2}$	4.5*	4.5*
	Roughness / $\text{\AA}$	25.5	26.1
MPTS	Thickness / $\text{\AA}$	27.4	29.6
	SLD / $10^{-6} \text{ \AA}^{-2}$	0.266*	0.266*
	Roughness / $\text{\AA}$	3.8	5.3
Quartz	SLD / $10^{-6} \text{ \AA}^{-2}$	4.18*	4.18*
	Roughness / $\text{\AA}$	18.4	20.8

Table 4.9 – Fit parameters for the single polymer layer SLD profiles presented in Figure 4.13

The data can also be fitted to a multilayer model in which the polymer layer fits to a thickness of approximately 47 nm although the final 9 nm have a very low SLD such that the SLD profile looks to have a significant roughness at the polymer/air interface. This fit has a similar  $\chi^2$  to that of the multilayer model shown in Figure 4.12 of 8.87. It is worth noting that the previous model required the polymer layers to be fixed during fitting whereas fitting to a smaller thickness occurs without restraining the parameters for the polymer layer. Nevertheless, the multi-layered fit to a thickness of 81 nm is considered to be the most reasonable model since it agrees with the AFM measure of the dry thickness as well as the coulometric estimate.

The solvated PEDOT film data was particularly difficult to fit therefore the following figures will illustrate the possible approaches to identifying a suitable model and the results that can be derived.

The three datasets from the film measured in  $D_2O$ ,  $H_2O$  and a mixture matching an SLD of  $2.26 \times 10^{-6} \text{ \AA}^{-2}$  were initially fitted simultaneously, using a co-refinement tool, Global Reflectometry Analysis tool, in the Motofit software<sup>22</sup>. All the layers of the model were linked to the equivalent layers in each contrast, with the exception of the polymer/solution roughness parameter which was allowed to fit independently. The polymer layer was modelled as four layers to allow flexibility in adapting to differences in solvation throughout the film. The overall  $\chi^2$  of the co-refined fit was 29.67 and Figure 4.14 illustrates how the fits follow the data.

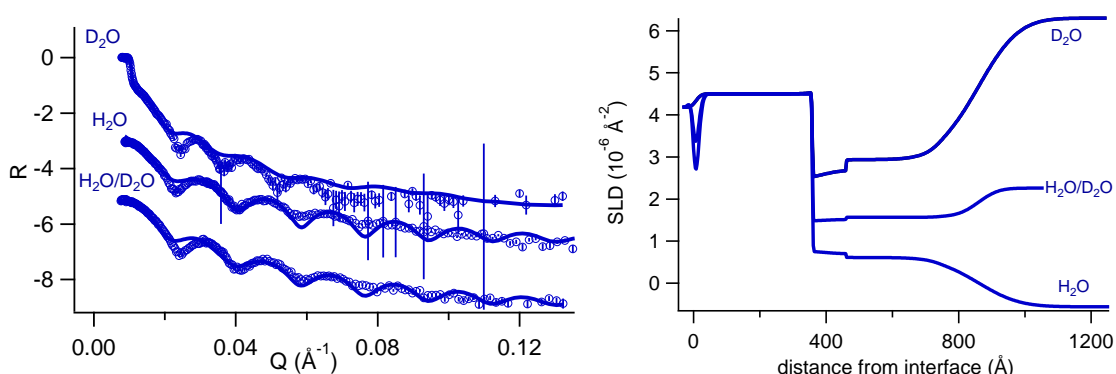


Figure 4.14 – Reflectivity (left) and SLD (right) profiles for the pristine PEDOT film exposed to  $D_2O$ ,  $H_2O$  and  $H_2O/D_2O$  mix with an SLD of  $2.26 \times 10^{-6} \text{ \AA}^{-2}$ ;  $R(Q)$  datasets are offset by increments of -2 for clarity. Fitted using the Global Reflectometry Analysis tool in Motofit

The results indicate a film approximately 46.5 nm thick with a dry polymer SLD of  $1.21 \times 10^{-6} \text{ \AA}^{-2}$  and a graduated level of solvation from 25% nearest the gold interface to 36% at the solution interface. On average, therefore, the films are 31% solvated however the extent of the swelling does not support this since the thickness is not significantly greater than the AFM and NR measurements of thickness of the film in the dry state. The large roughness at the film/solution interface nevertheless suggests a diffuse area of polymer which could indicate that the bulk of the film may not collapse upon drying but that these additional surface chains settle on the surface to form a more diffuse layer. Figure 4.15 shows how the SLDs extracted from the fits convert to a solvent volume fraction profile as a function of depth. The profiles of the film exposed to  $\text{H}_2\text{O}$  and  $\text{D}_2\text{O}$  overlay as, by definition, the co-refinement resulted in an identical solvation profile. The profile of the film in the  $\text{H}_2\text{O}/\text{D}_2\text{O}$  mixture displays a different roughness at the solution interface which can be considered an artefact of the fit since the step in SLD values between the film and the solution is much smaller.

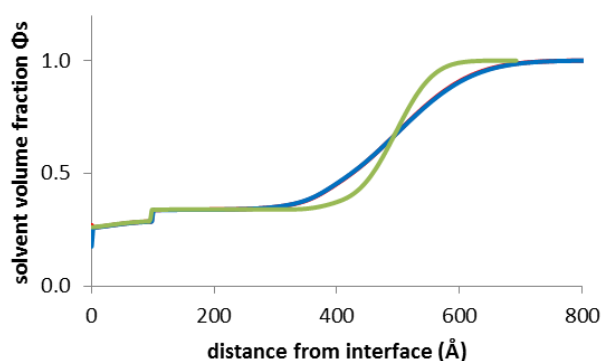


Figure 4.15 – Solvent volume fraction profiles for the PEDOT film in  $\text{H}_2\text{O}$ ,  $\text{D}_2\text{O}$  (overlayed by  $\text{H}_2\text{O}$ ) and  $\text{H}_2\text{O}/\text{D}_2\text{O}$  associated with the fits in Figure 4.14, calculated based on the co-refined PEDOT SLD =  $1.21 \times 10^{-6} \text{ \AA}^{-2}$

In order to allow even greater flexibility in the fitting, the solvation of the MPTS and polymer layers was allowed to vary independently in each contrast to allow for the possibility of poor solvent exchange. Figure 4.16 illustrates how this produced in a slightly better fit with a  $\chi^2$  of 25.86 however the result indicates a polymer thickness of only approximately 10 nm which is about a quarter of the dry thickness measured both by AFM and NR. It was therefore concluded that the thickness of the film could not be co-refined in the three contrasts, perhaps due to a complex solvation profile.

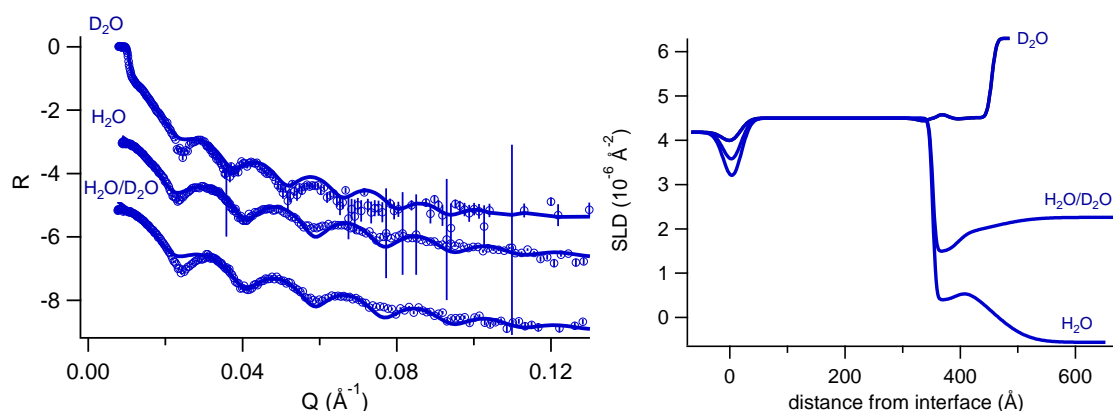


Figure 4.16 – Reflectivity (left) and SLD (right) profiles of the pristine PEDOT film in the three contrasts, fitted using a co-refinement method in which the solvation levels of the MPTS and polymer layers varied independently in each contrast;  $R(Q)$  datasets are offset by increments of -2 for clarity

If the reflectivity profiles of the different contrasts are fitted separately, the thickness of the film is found to fall between 50 and 55 nm with varying levels of solvation. Figure 4.17 shows how the resulting fit parameters are, however, not entirely reasonable with most notably a peak in SLD at the gold/polymer interface brought about by a large roughness parameter. Fixing this particular parameter does not allow the fit to converge. These fits were modelled using four layers to represent the polymer.

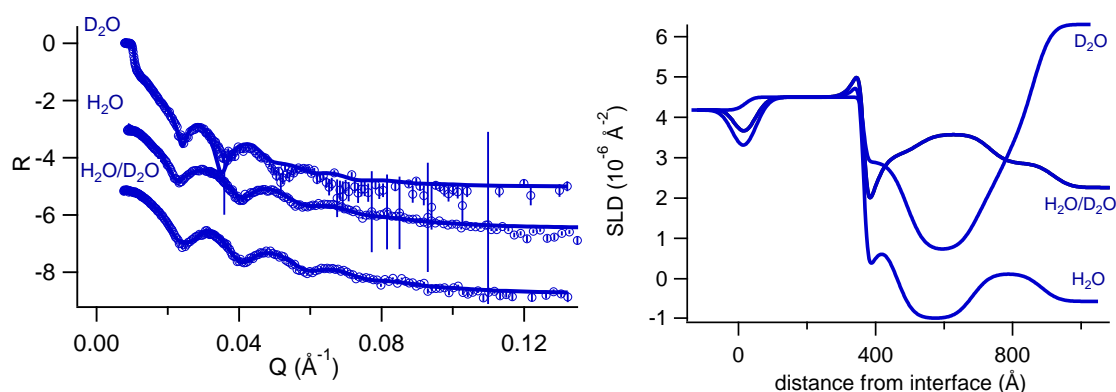


Figure 4.17 – Reflectivity (right) and SLD (left) profiles of the pristine PEDOT film in the three contrasts obtained by fitting the individual datasets separately;  $R(Q)$  datasets are offset by increments of -2 for clarity

The film was first measured in  $H_2O$ , then  $D_2O$  and finally the mixed contrast. What we see is an inhomogeneous solvation profile suggesting pockets of solvent trapped within

the film. The reflectivity data acquired in the H<sub>2</sub>O contrast indicates an overall lower SLD than that of the dry polymer however there is also an area of significantly lower SLD which is in fact lower than the SLD of the solvent; therefore the model is physically impossible. Nevertheless, when the solution is changed to D<sub>2</sub>O, this area of lower SLD is similarly placed suggesting a poor exchange of solvent within the film. Finally the last contrast has an area of higher SLD in the same area where the other two showed a lower SLD. Since this contrast was measured after the measurement in D<sub>2</sub>O, it is suggested that the film continued to exchange solvent during the measurement. This could explain the difficulty fitting the data since the SLD profile would have been changing during the measurement and D<sub>2</sub>O would have been trapped within the film when the final contrast was measured. These results could indicate that the film has varying levels of polymer chain density resulting in pockets of lower density, in which the solution can move and become trapped, surrounded by areas of greater film density through which the solution diffuses more slowly.

The solvent volume fraction profiles extracted from these fits are presented in Figure 4.18. The data for the film exposed to the H<sub>2</sub>O/D<sub>2</sub>O solution is not presented as the values distort the y-axis scale, indicating a maximum solvent volume fraction of 4.0. This peak in solvation is also present in the case of the film exposed to H<sub>2</sub>O, suggesting a volume fraction greater than 1.0, whereas in the same area, the data acquired in D<sub>2</sub>O reveals a negative solvation.

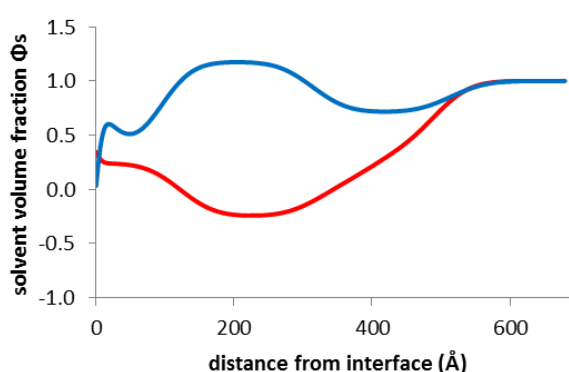


Figure 4.18 – Solvent volume fraction profiles for the PEDOT film in H<sub>2</sub>O and D<sub>2</sub>O associated with the fits in Figure 4.17, calculate based on the single layer fit to the dry PEDOT film so an SLD =  $1.825 \times 10^{-6} \text{ \AA}^{-2}$

Finally, using a fit to the PEDOT film in D<sub>2</sub>O data, the H<sub>2</sub>O and H<sub>2</sub>O/D<sub>2</sub>O data were restricted to fit using the same thicknesses found in the D<sub>2</sub>O fit but allowing the SLD and roughness of the polymer layers to change. The results are presented in Figure 4.19 and correspond to a solvated film thickness of approximately 61 nm, a 42% increase in thickness compared to the dry film fits. The modelled reflectivity in each case does not fit the data as closely as in Figure 4.17 however the parameters of the model are theoretically more reasonable in terms of the thickness of the film.

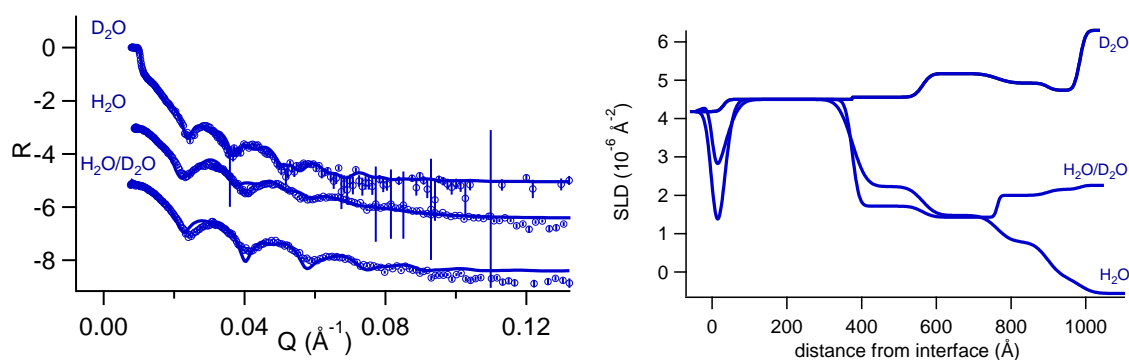


Figure 4.19 – Reflectivity (left) and SLD (right) profiles of the pristine PEDOT film in the three contrasts in which a multiple polymer layer model of the D<sub>2</sub>O data was used to restrict the fitting of the other two contrasts;  $R(Q)$  datasets are offset by increments of -2 for clarity

The SLD profile shows the polymer being incrementally more solvated from 0 - 85% in H<sub>2</sub>O from the gold/polymer interface to the solution, assuming the SLD of PEDOT to be the theoretical value of  $2.25 \times 10^{-6} \text{\AA}^{-2}$ . The layer of polymer at the gold/polymer interface fits to an SLD of  $2.23 \times 10^{-6} \text{\AA}^{-2}$  which is higher than the value found in the fits to the dry film measurements. The dry PEDOT film data can however be fitted with an SLD value of  $2.23 \times 10^{-6} \text{\AA}^{-2}$  for a thickness of 46 nm, although this causes the  $\chi^2$  value to increase to 36. Consequently, this higher SLD in the solvated film measurements could in fact be correct.

Although the data acquired for the sample exposed to H<sub>2</sub>O is more in keeping with expectations with regards to the levels of solvation throughout the film, the other two contrasts do not display the same solvation profile. In D<sub>2</sub>O, the film appears to have an area of greater solvent content in the centre of the film, whereas in the H<sub>2</sub>O/D<sub>2</sub>O mixture it presents an area with an SLD value lower than that of the pure polymer. Given the order in which the solution environment was changed, this last feature

cannot be attributed to trapped solvent from the previous measurement as this would have resulted in an increase in SLD, not a decrease.

Figure 4.20 shows the volume fraction profiles associated with the fits in Figure 4.19. The data acquired for the film in the H<sub>2</sub>O/D<sub>2</sub>O solution is once again not presented as, in this case, the very small difference between the SLD value for the dry film ( $2.25 \times 10^{-6} \text{ \AA}^{-2}$ ) and that of the solution ( $2.26 \times 10^{-6} \text{ \AA}^{-2}$ ) mean that any small shift in SLD represents a large change in the calculated volume fraction. The contrast in this solution is therefore inadequate with regards to accurately quantifying the level of solvation. In the case of the film exposed to H<sub>2</sub>O, the solvent content gradually increases from the electrode to the solution interface. In D<sub>2</sub>O, the film appears to have a relatively homogeneous solvent volume fraction, with a slight increase in the centre of the film, between 200 – 400 Å from the electrode interface.

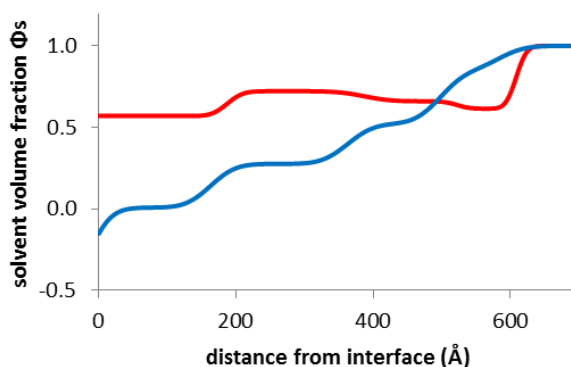


Figure 4.20 - Solvent volume fraction profiles for the PEDOT film in H<sub>2</sub>O and D<sub>2</sub>O associated with the fits in Figure 4.19, calculated based on the theoretical PEDOT SLD =  $2.25 \times 10^{-6} \text{ \AA}^{-2}$

The NR data for this film does not present a clear picture of the solvation profile in the different contrasts but in considering the different fits together it is possible to speculate what structural features may be present. The dry fit indicated a film with a lower SLD than the theoretical value which suggested a more porous film. Such a film may therefore solvate without presenting significant swelling. Furthermore, if the pores penetrate the full depth of the polymer matrix it is conceivable that rinsing may not have been sufficient to allow a full solvent exchange throughout the film. As a result, a mixing of solvent within the film may have occurred during the NR measurements resulting in the situation where no single model can adequately simulate the measured reflectivity.

The PEDOT-ND#15 film was also measured in the three contrasts and the co-refinement method similarly was not successful in converging upon a reasonable fit therefore these will not be presented. Each dataset could however be fitted individually but offered several possible fits.

The polymer layer could not be freely fitted to a thickness greater than 80 nm. In fact, as shown in Table 4.10, the fit converges to a solvated film thickness between 41 and 56 nm. This is an acceptable solvated thickness if the fit to the dry film data, indicating a thickness of 39 nm, is considered to be correct as it indicates a 5 - 44% increase due to solvation. Despite some disparity between the thicknesses of the polymer in each contrast, the SLD profile in Figure 4.21 clearly shows that the film thickness is in fact very similar in each case.

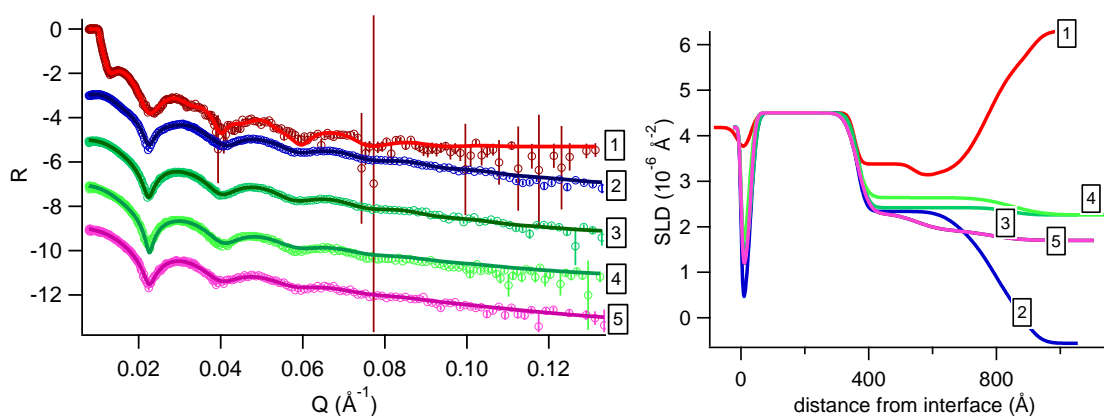


Figure 4.21 – Reflectivity (left) and SLD (right) profiles of the PEDOT-ND#15 film in all contrasts: in  $D_2O$  (1),  $H_2O$  (2),  $H_2O/D_2O = 2.26 \times 10^{-6} \text{ \AA}^{-2}$  (3 and 4) and  $H_2O/D_2O = 1.7 \times 10^{-6} \text{ \AA}^{-2}$  (5);  $R(Q)$  datasets are offset by increments of -2 for clarity

The thickness difference can in fact be attributed to the way in which the polymer/solution interface is modelled in the fits. In the case of the film measured in  $H_2O$  or  $D_2O$ , the increasingly solvated interface is modelled by more highly solvated polymer layers combined with a large roughness. In the case of the measurements of the film in the  $H_2O/D_2O$  mixtures, the fit converges to a greater roughness parameter at this interface. It is clear therefore that while these fits are numerically different in their parameters, the film appears to have a consistent thickness in each contrast.

Contrast		1	2	3	4	5
Solution		D <sub>2</sub> O	H <sub>2</sub> O	H <sub>2</sub> O/D <sub>2</sub> O = 2.26 × 10 <sup>-6</sup> Å <sup>-2</sup>	Repeated H <sub>2</sub> O/D <sub>2</sub> O = 2.26 × 10 <sup>-6</sup> Å <sup>-2</sup>	H <sub>2</sub> O/D <sub>2</sub> O = 1.7 × 10 <sup>-6</sup> Å <sup>-2</sup>
	χ <sup>2</sup>	1.83	4.25	2.23	4.7	1.7
Quartz	SLD / 10 <sup>-6</sup> Å <sup>-2</sup>	4.18*	4.18*	4.18*	4.18*	4.18*
	Thickness / Å	22.6	29.6	35.2	26.4	30.9
MPTS	SLD / 10 <sup>-6</sup> Å <sup>-2</sup>	0.266*	0.266*	0.266*	0.266*	0.266*
	Solvation / %	45.9	50*	50*	50*	50*
	Roughness / Å	20*	5*	5*	5*	5*
Gold	Thickness / Å	333*	333*	333*	333*	333*
	SLD / 10 <sup>-6</sup> Å <sup>-2</sup>	4.5*	4.5*	4.5*	4.5*	4.5*
	Roughness / Å	20*	16.1	14.2	14	12
	Thickness / Å	184.5	313.9	264.8	490*	185.1
	SLD / 10 <sup>-6</sup> Å <sup>-2</sup>	3.38	2.34	2.42	2.64	2.3
	Roughness / Å	15*	21.9	23.9	27.8	30*
	Thickness / Å	65.7	121.7	206.9		230.8
	SLD / 10 <sup>-6</sup> Å <sup>-2</sup>	3.12	1.79	2.42		1.93
	Roughness / Å	21.9	52.6	48.2		59.7
Polymer	Thickness / Å	169	101.5			
	SLD / 10 <sup>-6</sup> Å <sup>-2</sup>	3.14	0.04		N/A	
	Roughness / Å	5*	62.6			
	Thickness / Å	140.6		N/A		N/A
	SLD / 10 <sup>-6</sup> Å <sup>-2</sup>	5.8	N/A			
	Roughness / Å	74.6				
Solution	SLD / 10 <sup>-6</sup> Å <sup>-2</sup>	6.3*	-0.56*	2.26*	2.26*	1.7*
	Roughness / Å	32.1	37.5	52.5	80*	80*

Table 4.10 – Parameters associated with the fits to the solvated PEDOT-ND#15 film data shown in Figure 4.21

Although the measurements in D<sub>2</sub>O and H<sub>2</sub>O present a similar profile at the polymer/solution interface with a gradually increasing level of solvation, the bulk of the

film in each case appears to be solvated to a different extent. In  $D_2O$ , the film displays a bulk film SLD between  $3.12 \times 10^{-6} \text{ \AA}^{-2}$  and  $3.38 \times 10^{-6} \text{ \AA}^{-2}$  which would indicate a solvent volume fraction between 0.21 and 0.27 for a dry SLD of  $2.3 \times 10^{-6} \text{ \AA}^{-2}$ , the value found from the single layer fit to the dry film data. In  $H_2O$  however, the film presents a bulk film SLD of  $2.34 \times 10^{-6} \text{ \AA}^{-2}$ , higher than either the dry film SLD or that of the solvent. It does nevertheless show an increasingly solvated outer layer of the polymer film. When exposed to the other solutions, the film also exhibits a higher SLD than the dry film. This could be due to the movement of the NDs creating an area within the polymer with a higher volume fraction of NDs. However, the higher SLD is consistent throughout the polymer layer and not confined to a particular region, which would suggest a higher volume fraction of NDs throughout the film which is impossible. The fact that the film appears to present a more conventional solvation profile in both  $D_2O$  and  $H_2O$ , showing an increasing volume fraction of solvent from the gold/polymer interface to the polymer/solution interface, also contradicts this theory. Only in the case of the contrast solution '4' could the increase in SLD be caused by trapped solvent, since this measurement was performed after the film had been measured in  $D_2O$ .

The data could be forced to fit to a thickness exceeding 100 nm, although the  $\chi^2$  values, indicative of the quality of the fit, were generally not as good. The results are presented in Figure 4.22 and the associated fit parameters in Table 4.11.

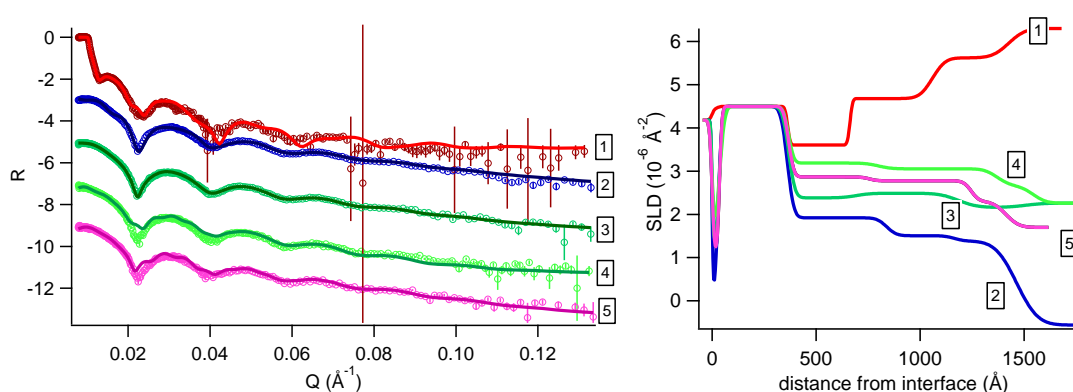


Figure 4.22 – Reflectivity (left) and SLD (right) profiles of the PEDOT-ND#15 film in all contrasts: in  $D_2O$  (1),  $H_2O$  (2),  $H_2O/D_2O = 2.26 \times 10^{-6} \text{ \AA}^{-2}$  (3 and 4) and  $H_2O/D_2O = 1.7 \times 10^{-6} \text{ \AA}^{-2}$  (5);  $R(Q)$  datasets are offset by increments of -2 for clarity

The thickness in these fits was found to fall between 104 and 118 nm, indicating an increase of between 28 – 46% on the dry film thickness of 81 nm. Based on the dry film SLDs, the fits show the solvent volume fractions in D<sub>2</sub>O and H<sub>2</sub>O to be consistent with this degree of swelling. The solvent volume fraction profiles for the film in H<sub>2</sub>O and D<sub>2</sub>O are presented in Figure 4.23, assuming that the PEDOT-ND form a composite with an SLD of  $2.5 \times 10^{-6} \text{ \AA}^{-2}$ , based on the fits to the dry film. They reveal a sharper increase in solvation when exposed to the D<sub>2</sub>O solution as opposed to the more gradual increase in solvent content displayed by the film in H<sub>2</sub>O.

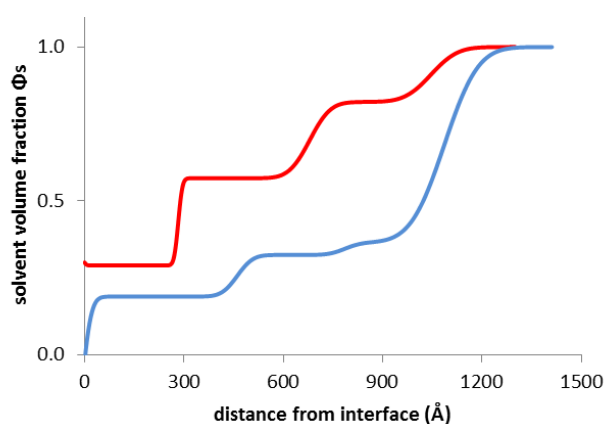


Figure 4.23 – Solvent volume fraction profiles for the PEDOT-ND film in H<sub>2</sub>O and D<sub>2</sub>O associated with the fits in Figure 4.22, calculated based on the composite SLD =  $2.5 \times 10^{-6} \text{ \AA}^{-2}$

Once again the polymer layer in the H<sub>2</sub>O/D<sub>2</sub>O solutions fits to a higher SLD than expected. In this case however, the multi-layered fit to the dry film measurement is used as the starting point therefore the PEDOT-ND film is considered to have a higher SLD of between  $2.45 \times 10^{-6} \text{ \AA}^{-2}$  and  $2.7 \times 10^{-6} \text{ \AA}^{-2}$ . Nevertheless, when exposed to the contrast solutions '4' and '5', the film exhibits an SLD higher than both that of the dry film and the solution. It is possible that this could be caused by trapped D<sub>2</sub>O from the earlier measurement however it is unlikely that this would persist to such a degree through to the final measurement. Since the entire film presents the increased SLD and not just a section of the film, it cannot be attributed to the formation of a cluster of NDs within the polymer matrix.

Contrast		1	2	3	4	5
Solution		D <sub>2</sub> O	H <sub>2</sub> O	H <sub>2</sub> O/D <sub>2</sub> O = 2.26 × 10 <sup>-6</sup> Å <sup>-2</sup>	Repeated H <sub>2</sub> O/D <sub>2</sub> O = 2.26 × 10 <sup>-6</sup> Å <sup>-2</sup>	H <sub>2</sub> O/D <sub>2</sub> O = 1.7 × 10 <sup>-6</sup> Å <sup>-2</sup>
	χ <sup>2</sup>	3.7	12.4	1.63	7.47	5.57
Quartz	SLD / 10 <sup>-6</sup> Å <sup>-2</sup>	4.18*	4.18*	4.18*	4.18*	4.18*
	Thickness / Å	30*	28.7	35.2	35.2	35.2
MPTS	SLD / 10 <sup>-6</sup> Å <sup>-2</sup>	0.266*	0.266*	0.266*	0.266*	0.266*
	Solvation / %	69.4	50*	50*	50*	50*
	Roughness / Å	10*	5*	5*	10*	10*
	Thickness / Å	333*	333*	333*	333*	333*
Gold	SLD / 10 <sup>-6</sup> Å <sup>-2</sup>	4.5*	4.5*	4.5*	4.5*	4.5*
	Roughness / Å	10*	15*	14.1	20*	10*
	Thickness / Å	300*	477.84	326.6	432.1*	387.7
Polymer	SLD / 10 <sup>-6</sup> Å <sup>-2</sup>	3.6	1.92	2.38	3.19	2.87
	Roughness / Å	10*	25*	24.4	20*	20*
	Thickness / Å	398.8	324.9	489.6	571.3	490.2
	SLD / 10 <sup>-6</sup> Å <sup>-2</sup>	4.68	1.51	2.49	3.05	2.78
	Roughness / Å	10*	37.1	54.3	50*	30*
	Thickness / Å	366.4	300*	322.7	172.4	166.5
	SLD / 10 <sup>-6</sup> Å <sup>-2</sup>	5.62	1.38	2.16	2.66	2.3
	Roughness / Å	49.2	38.4	71.1	50*	30*
Solution	SLD / 10 <sup>-6</sup> Å <sup>-2</sup>	6.3*	-0.56*	2.26*	2.26*	1.7*
	Roughness / Å	62.4	80*	70*	50*	50*

Table 4.11 – Parameters associated with the fits to the solvated PEDOT-ND#15 film data shown in Figure 4.22

Finally, in Figure 4.24, the fits to contrasts '3', '4' and '5' were forced to a more appropriate SLD between  $2 \times 10^{-6} \text{ \AA}^{-2}$  and  $2.5 \times 10^{-6} \text{ \AA}^{-2}$ . Where possible, the data was freely fitted within parameter limits. In the case of contrast '4' allowing it to converge freely resulted in an SLD of  $2.8 \times 10^{-6} \text{ \AA}^{-2}$  or  $2.9 \times 10^{-6} \text{ \AA}^{-2}$ . The best fit was found by fixing the layer at the gold/polymer interface to an SLD of  $2.5 \times 10^{-6} \text{ \AA}^{-2}$  and allowing the outer layer to fit freely. The parameters of all these fits are presents in Table 4.12.

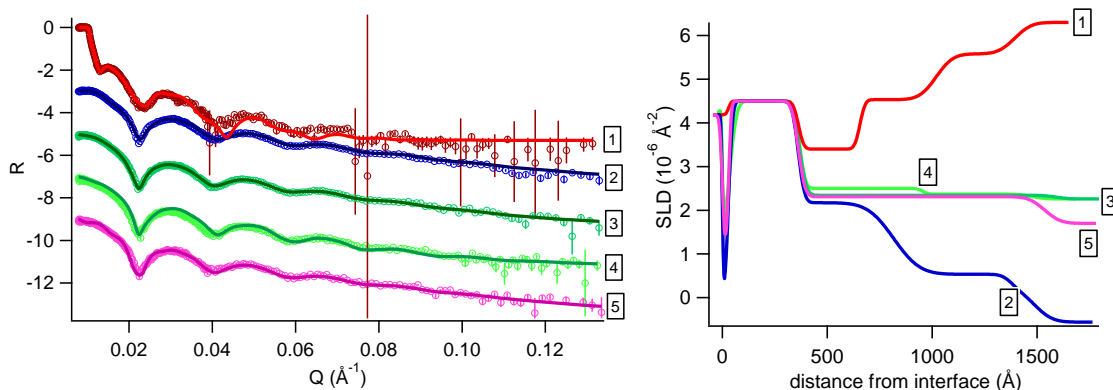


Figure 4.24 – Reflectivity (left) and SLD (right) profiles of the PEDOT-ND#15 film in all contrasts: in  $D_2O$  (1),  $H_2O$  (2),  $H_2O/D_2O = 2.26 \times 10^{-6} \text{ \AA}^{-2}$  (3 and 4) and  $H_2O/D_2O = 1.7 \times 10^{-6} \text{ \AA}^{-2}$  (5);  $R(Q)$  datasets are offset by increments of -2 for clarity

The thickness parameter of the models was fixed or converged to a similar degree of swelling as found in the fits of Figure 4.22. This is also consistent with the solvation of the film according to the SLD profiles of the film exposed to  $D_2O$  and  $H_2O$ . The solutions with an SLD of  $2.26 \times 10^{-6} \text{ \AA}^{-2}$  and  $1.7 \times 10^{-6} \text{ \AA}^{-2}$  are not considered ideal for evaluating solvent content as the value of the SLD is too close to that of the polymer matrix. Consequently, a very small change in SLD represents a very large change in solvation and, since the films have already been seen to fit to several possible models, extracting solvent volume fractions from the fitted SLD values is considered unreliable in these contrasts.

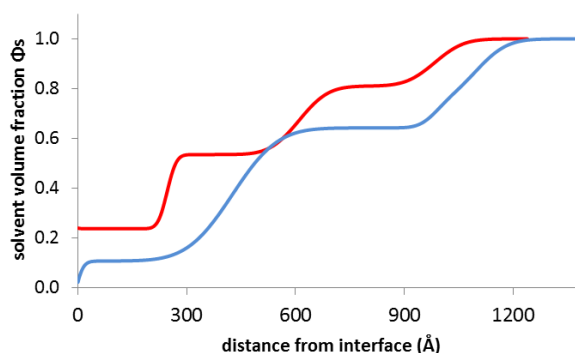


Figure 4.25 – Solvent volume fractions for the PEDOT-ND film in  $D_2O$  and  $H_2O$ , associated with the fits in Figure 4.24, calculated based on the composite  $SLD = 2.5 \times 10^{-6} \text{ \AA}^{-2}$

The solvent volume fraction profiles for the film exposed to H<sub>2</sub>O and D<sub>2</sub>O are presented in Figure 4.25 for a composite PEDOT-ND SLD = 2.5 × 10<sup>-6</sup> Å<sup>-2</sup>. They show the gradually increasing level of solvation throughout the film in both contrasts.

Contrast		1	2	3	4	5
Solution		D <sub>2</sub> O	H <sub>2</sub> O	H <sub>2</sub> O/D <sub>2</sub> O = 2.26 × 10 <sup>-6</sup> Å <sup>-2</sup>	Repeated H <sub>2</sub> O/D <sub>2</sub> O = 2.26 × 10 <sup>-6</sup> Å <sup>-2</sup>	H <sub>2</sub> O/D <sub>2</sub> O = 1.7 × 10 <sup>-6</sup> Å <sup>-2</sup>
	χ <sup>2</sup>	5.16	4.5	3.18	22.7	4.85
Quartz	SLD / 10 <sup>-6</sup> Å <sup>-2</sup>	4.18*	4.18*	4.18*	4.18*	4.18*
	Thickness / Å	30*	29.1	35.2*	35.2*	30
MPTS	SLD / 10 <sup>-6</sup> Å <sup>-2</sup>	0.266*	0.266*	0.266*	0.266*	0.266*
	Solvation / %	65*	50*	50*	50*	50*
	Roughness / Å	10*	5*	5*	4.6	10*
Gold	Thickness / Å	333*	333*	333*	333*	333*
	SLD / 10 <sup>-6</sup> Å <sup>-2</sup>	4.5*	4.5*	4.5*	4.5*	4.5*
	Roughness / Å	10*	15*	14.2*	26.3	10*
	Thickness / Å	293	454.7	1100*	588.2	1181.4
	SLD / 10 <sup>-6</sup> Å <sup>-2</sup>	3.4	2.17	2.32	2.5*	2.31
	Roughness / Å	20*	23.7	26.1	21.6	25*
Polymer	Thickness / Å	363.9	557.5		522	
	SLD / 10 <sup>-6</sup> Å <sup>-2</sup>	4.53	0.535		2.37	
	Roughness / Å	20*	97.9		20*	
	Thickness / Å	374.4	113	N/A		N/A
	SLD / 10 <sup>-6</sup> Å <sup>-2</sup>	5.58	0.24		N/A	
	Roughness / Å	63.1	36			
Solution	SLD / 10 <sup>-6</sup> Å <sup>-2</sup>	6.3*	-0.56*	2.26*	2.26*	1.7*
	Roughness / Å	62.6	68	50*	50*	60*

Table 4.12 – Parameters associated with the fits to the solvated PEDOT-ND#15 film data shown in Figure 4.24

#### 4.4 Discussion

Only very minor, inconsistent differences were noticeable between the growth of PEDOT and PEDOT-ND films, regardless of the chosen deposition control function. The magnitude of current response for the potentiostatic growth to a specific charge density varied slightly irrespective of whether or not there were NDs in the films. While in some cases, during the potentiodynamic growth, the NDs appeared to result in an over-potential and an increased charge, in others the growth was identical to that of PEDOT as illustrated in Figure 4.6. These small differences are therefore not sufficient to either confirm or deny the effect or even the presence of NDs in the films.

One of the key issues in this work was ensuring the homogeneity of the NDs suspension as the particles are known to form aggregates<sup>8,19</sup>. Although measures were taken to thoroughly mix the solutions using stirring and sonication, when left undisturbed the NDs would eventually aggregate and drop out of suspension. It is therefore possible that in each solution the ND concentration gradient at the electrode interface was different thus producing different effects.

The electrochemical characterisation of the films did not indicate any significant differences brought about by the presence of ND in the deposition medium. The potentiostatically grown films showed some effect from the NDs, however these effects were inconsistent with some ND films displaying a lower redox charge than their pristine PEDOT equivalent yet others exhibiting slightly greater electroactivity. The potentiodynamically grown films on glass substrates displayed very similar, almost indistinguishable cyclic voltammograms whereas the films prepared on quartz suggested that the presence of NDs produced films with significantly greater redox charge as shown in Figure 4.9(B).

The optical microscopy results in Figure 4.2 from the potentiostatic growth gave compelling evidence in showing the effect of the NDs in producing a film with a different structure to the pristine PEDOT. Not only do the images indicate clusters of material but they also showed a more porous structure evidenced by the gold visible through the film in places. Although the films grown in acetonitrile showed the most distinctive effect from the NDs, the smoother films produced from aqueous media

were preferable for the purposes of studying these films using NR. The latter were examined further using AFM. The surface of the films revealed little or no difference between films grown with and without NDs. The height profiles shown in Figure 4.4, however, indicated that the NDs either inhibited the growth of the film or produced a film with a greater density. In their work, Ispas et al stated that the incorporation of NDs had produced a composite film that was less porous than the pristine PEDOT sample<sup>8</sup>. Another study in which PANI-ND films were formed, the authors described the composite fibres as being more closely packed<sup>3</sup>, so an increased density is a reasonable hypothesis.

It is nonetheless counter-intuitive that the film should be so much thinner than its pristine PEDOT equivalent since the NDs, with an average diameter of 5 to 10 nm, would be expected to take up space within the polymer matrix. The question arises therefore as to whether or not this structural effect is caused by the incorporation of NDs or simply by their presence in the deposition solution interfering with the deposition process. With regards to their composite PANI-ND films, Tamburri et al discussed the fact that the nucleation process was affected by the presence of NDs which present additional surfaces to which monomers and oligomers may adsorb<sup>3</sup>. As such, either the NDs were incorporated but subsequently inhibited growth of the polymer film such that overall the film was thinner than the PEDOT film, or the NDs were not incorporated but affected the growth such that the film produced had a greater density than the pristine PEDOT.

AFM measurements of the films potentiodynamically grown on Au/glass revealed that the pristine PEDOT films were more structurally homogeneous on the surface of the film as seen in Figure 4.8. The globular structure of the films over small surface areas was similar. However, the PEDOT-ND films exhibited large structures on the surface in clusters. Since the films were made using the same growth protocol and this feature was exclusively seen in the PEDOT-ND films, this strongly indicates that these 'lumps' may have been incorporated NDs. The films grown for the NR study however did not show these same structures on the surface. In fact, the films were indistinguishable from one another, as illustrated in Figure 4.10. The morphological effect of the NDs is still debated since previous work has revealed a rough surface on globular fibres of

PANI-ND<sup>3</sup> but in the case of PEDOT, the formation of a ND composite was found to produce films with improved homogeneity<sup>8</sup>.

Raman spectroscopy of the potentiostatically grown films and the ND powder could not confirm that the films were composite materials. The ND powder appeared to have no signal, producing an essentially flat line which can be seen in Figure 4.5. All the polymer samples measured invariably showed the distinctive features of the PEDOT structure, with no differences between the pristine PEDOT films and those supposedly containing NDs. Virginia Ferreira's measurement of ND powder revealed broad peaks around 1335 cm<sup>-1</sup> and 1595 cm<sup>-1</sup>. However, these had a very low intensity and were unlikely to present a detectable contribution to the PEDOT spectra. Since ND is meant to have quite a distinctive spectrum, these results are particularly disappointing. The literature does suggest however that ND particles can be coated with amorphous or graphitic carbon<sup>4,19</sup> which would substantially reduce the Raman signal from the diamond structure since the technique is significantly more sensitive to sp<sup>2</sup> carbon bonding<sup>18,23</sup>. Furthermore, in the work by Tamburri et al in which they chemically polymerised PEDOT in the presence of ND, their Raman spectra showed only a very slightly visible band associated with ND<sup>24</sup>. It should be noted that NR does not distinguish between the different types of carbon bonding therefore the NDs should still be detectable using reflectometry.

The single layer model fits to the dry film NR measurements in Figure 4.11 confirmed the surprisingly large difference in thickness between pristine PEDOT and the equivalent PEDOT-ND film. The fits also reveal that the average SLD of the PEDOT-ND films is slightly higher than that of the PEDOT. The PEDOT film itself presented an SLD that was lower than expected. The theoretical SLD had been calculated assuming a film density similar to the monomer density of 1.33 g cm<sup>-3</sup> which gives an SLD of  $2.25 \times 10^{-6} \text{ \AA}^{-2}$ . However, the fitted SLD indicates a density closer to 1 g cm<sup>-3</sup> which is nevertheless in keeping with the PEDOT density assumed by other authors<sup>9,16</sup>.

In the multilayered model, the PEDOT film also seems to have a thin (3 nm) layer with a higher SLD of  $2.6 \times 10^{-6} \text{ \AA}^{-2}$ . The roughness parameter associated with this layer is as big as the layer itself indicating that this is in fact a representation of the roughness at the gold/polymer interface. This model shows that the SLD of the film decreases from the gold interface to the surface of the film, suggesting that the film may have areas of

differing density throughout its thickness, going from a greater packing density at the electrode surface to a more porous structure at the film surface.

The single layer model fits to the PEDOT-ND dry film data indicated SLDs of  $2.3 \times 10^{-6} \text{ \AA}^{-2}$  and  $2.03 \times 10^{-6} \text{ \AA}^{-2}$  for the films grown by 15 and 10 cycles respectively. On the one hand these values are within a reasonable range for a PEDOT only film assuming the density is between  $1.2$  and  $1.36 \text{ g cm}^{-3}$ . However, if we consider the lower SLD value of the pristine PEDOT film and consider that to be a normal value for PEDOT when it is prepared in this way, we see that these SLDs could indicate an incorporation of NDs between 2 and 5 % by volume as the SLD of ND is calculated to be  $11.7 \times 10^{-6} \text{ \AA}^{-2}$  for a particle density of  $3.5 \text{ g cm}^{-3}$ .

The multi-layered model fits in Figure 4.12 indicate a higher SLD for inner parts of the film, descending to significantly lower SLDs at the polymer/air interface. In the case of the PEDOT-ND#15 film the highest SLD reaches  $2.6 \times 10^{-6} \text{ \AA}^{-2}$  which, if it were only PEDOT, would suggest a film density of  $1.5 \text{ g cm}^{-3}$ . Assuming therefore that the SLD of pure PEDOT is between  $1.7 \times 10^{-6} \text{ \AA}^{-2}$  and  $1.85 \times 10^{-6} \text{ \AA}^{-2}$  we can calculate percentage of NDs by volume to be between 7.5 and 9 vol%. In the other areas of the PEDOT-ND#15 film the SLD is around  $2.4 \times 10^{-6} \text{ \AA}^{-2}$  which would be equivalent to 5.5 – 7 vol% ND and the outer layer, approximately 20 nm has an SLD of  $1.5 \times 10^{-6} \text{ \AA}^{-2}$ , suggesting that this area is a particularly porous area containing only the polymer with a density of  $0.89 \text{ g cm}^{-3}$ .

The same approach is taken when considering the PEDOT-ND#10 film which shows a small layer at the gold/polymer interface, approximately 10 nm in which the SLD is slightly lower at  $2.06 \times 10^{-6} \text{ \AA}^{-2}$  than the bulk which fits to  $2.37 \times 10^{-6} \text{ \AA}^{-2}$ . This could either be an area of polymer with an increased density of  $1.2 \text{ g cm}^{-3}$  or could indicate a lower percentage of NDs present. This would mean that the ND content would be 2 – 3.5 vol% near the gold interface, 5 – 6.5 vol% in the bulk and none in the final 13 nm of the film in which the SLD drops to  $0.78 \times 10^{-6} \text{ \AA}^{-2}$  probably due to this area being a more porous structure of PEDOT.

It is important to note that, while this analysis is based on the SLD value of the pristine PEDOT film made for this experiment, different values have been found for PEDOT in other NR studies. The work of Rachel M. Sapstead (née Brown) with PEDOT films

grown from organic media indicated a much higher film density with the SLD reaching  $2.6 \times 10^{-6} \text{ \AA}^{-2}$ . In the literature, the density of PEDOT is reported to be between  $1.45 - 1.65 \text{ g cm}^{-3}$ <sup>25,16,26</sup>, which would result in an SLD range of  $2.45 - 2.79 \times 10^{-6} \text{ \AA}^{-2}$ . Since it is known that different deposition conditions can change the properties of polymer films, we are assuming that the pristine PEDOT in this work may be less dense and that the properties of the solution and deposition protocol that produced this effect would have the same effect on polymer growth when grown with NDs.

The pristine PEDOT solvated film data is difficult to interpret due to the poor fits to the data. By considering the overall results of the different methods employed to address the fitting however, it seems reasonable to conclude that the film presented a very porous structure that may have resulted in 'pockets' of solvent within the film. These areas may therefore have resulted in a poor exchange of solvent within the film such that during the NR measurement the new contrast solvent continued to mix with the trapped solvent from the previous contrast within the film, resulting in a changing reflectivity during the measurement. The formation of 'pockets' of solvent throughout the film may also have occurred in the plane of the film. Since the neutron interactions are averaged over the area of the beam footprint, any detail of variations or lack of homogeneity in this plane is averaged in the resulting reflectivity.

The fitting of the PEDOT-ND solvated film data was, on the other hand, more successful but the polymer layer could not be freely fitted to a thickness greater than 80 nm suggesting that the correct model for the dry data for this film could in fact be a polymer layer of approximately 39 nm. Although this does not agree with the AFM data, it is possible that the scratch applied to the film in order to measure the height profile may have in fact also cut through the gold layer beneath the polymer. The consistent convergence of the fits producing results confirming this thinner polymer film are convincing evidence against the AFM measurement. However, the growth charge estimate of thickness agrees with the latter therefore further models were explored.

The first models presented in Figure 4.2I show the free fitting results which indicate a thinner film than that measured by AFM. The SLDs of the polymer layers in these fits are also higher than expected based on the SLD values from the dry measurements. Assuming that the film will present the same volume fraction of solvent in each

solution, the SLD values of the polymer layer at the gold interface, when exposed to D<sub>2</sub>O and H<sub>2</sub>O, were used to calculate the fitted SLD of the polymer. In this case it fits to  $2.86 \times 10^{-6} \text{ \AA}^{-2}$  for a solvent content of 15%. This would represent a volume fraction of NDs of 0.105. This is significantly different from the dry film results which indicated a 39 nm film with a ND volume fraction of 0.05.

In Figure 4.22, the fits were forced towards a film thickness greater than 81 nm. The results were in keeping with the expected extent of swelling due to solvation, between 30 and 40%. The SLDs of the polymer layers were still higher than the single layered model to the dry measurements suggested but closer to the values found in the multi-layered fit to the dry data in Figure 4.12. The fitted value of the film SLD was calculated to be  $2.72 \times 10^{-6} \text{ \AA}^{-2}$  for a solvent content of 24.5%. While this value represents a ND volume fraction of approximately 0.09 and therefore in agreement with the dry film measurement, the fits in the other contrast solutions presented unrealistically high SLDs.

In order to find a more realistic model, the fits in Figure 4.24 were achieved by limiting the range of the SLD parameter in the case of the H<sub>2</sub>O/D<sub>2</sub>O mixed solutions. The fitted SLD of the polymer was found to be  $2.77 \times 10^{-6} \text{ \AA}^{-2}$  for a solvent content of 18% in D<sub>2</sub>O and H<sub>2</sub>O. As has been mentioned previously, the SLDs of the other solutions are too close to that of the polymer matrix for that the exact volume fractions to be reliably calculated therefore they shall not be discussed. However, these fits do present more reasonable SLD values for the polymer film in these media.

These subtle variations in SLD do not allow for the presence of NDs to be confirmed beyond reasonable doubt however they do suggest the presence and/or effect of the NDs within the film since the SLD and behaviour of the film in solution is markedly different to that of the pristine PEDOT film. Since the PEDOT presented such complex solvation behaviour with what appeared to be a disordered structure, the NDs could be responsible for the PEDOT-ND film presenting a more structured layer. It has been previously reported that the incorporation of ND could promote cross-linking which enhances film stability and strength<sup>27</sup>. This indirect evidence would suggest that there could be a very small volume of ND within the film.

The tendency for the film to fit to a higher SLD than deemed reasonable, according to the dry film measurements and the choice of solvent, could in fact indicate that the NDs may move slightly within the polymer matrix. From the first fits to the dry data, it is clear that the film presents a higher SLD closest to the gold interface, with a rough interface at the surface of the film. When transferred into solution, the film again displays higher SLDs, and therefore ND volume fractions, at the gold interface. As the film swells to accommodate solvent, it is possible that the NDs could shift accordingly, resulting in areas with slightly greater concentrations.

It is clear that the quantity of NDs incorporated into these films was not sufficient to fully differentiate them from a pristine PEDOT film with a greater density. They do not form a layer or cluster since if they did, they would be immediately identifiable due to their very high SLD. Quite simply, the PEDOT and NDs form a matrix that is subsequently treated as a single compound with a given SLD. In order to differentiate between such a mixture and a pure PEDOT film, the overall SLD must be significantly greater than the possible SLD values of PEDOT. Incorporating a ND volume fraction of 0.12 should be sufficient as this would give the PEDOT-ND film an overall SLD over  $3 \times 10^{-6} \text{ \AA}^{-2}$ .

## 4.5 Conclusions

The deposition of PEDOT-ND composite films was investigated by potentiostatic and potentiodynamic deposition. It was observed that smoother and more homogeneous films were produced when using an aqueous deposition solution as opposed to working in organic medium. The potentiodynamic deposition resulted in PEDOT films with a globular topography, including large surface structures when NDs were present during deposition.

The observed differences in electrochemical behaviour that may possibly be connected to the incorporation of NDs in the PEDOT films were not sufficiently reproducible to ascertain a direct causal link. Further work is required to investigate how the presence of NDs affects the electroactivity of the polymer matrix although the results presented here do suggest an increase in redox charge compared to a pristine PEDOT equivalent film. Perhaps most importantly, the NDs did not appear to have a detrimental effect on the electrochemical properties of the polymer.

Finally, whether the NDs are incorporated in the films or affecting the deposition process in solution, this work strongly indicates that there is an effect on the structure of the resulting films. The small scale PEDOT-ND samples clearly showed greater porosity in the case of the potentiostatically grown films and displayed large surface features when grown potentiodynamically. The samples potentiodynamically grown for the NR study revealed a more stable and homogeneous internal structure compared to a pristine PEDOT film.

Looking forward, it is clear that the properties of the NDs in solution need to be more specifically addressed to ensure a well dispersed deposition solution and rule out effects caused by agglomerating particles. Once this has been achieved, the reproducibility of the deposition protocols will not be compromised by the uncontrolled behavior of the particles in solution and will allow the assumption that the effect of the concentration at the electrode interface is negligible. It is expected that this will allow composite films to be produced with more consistent results and therefore more general conclusions to be drawn as to the electrochemical and structural effects of these particles on a polymer matrix.

## 4.6 References

1. Snook, G. A., Kao, P. & Best, A. S. Conducting-polymer-based supercapacitor devices and electrodes. *J. Power Sources* **196**, 1–12 (2011).
2. Dolmatov, V. Y. Polymer-diamond composites based on detonation nanodiamonds. Part I. *J. Superhard Mater.* **29**, 65–75 (2007).
3. Tamburri, E., Orlanducci, S., Guglielmotti, V., Reina, G., Rossi, M. & Terranova, M. L. Engineering detonation nanodiamond – Polyaniline composites by electrochemical routes: Structural features and functional characterizations. *Polymer (Guildf)*. **52**, 5001–5008 (2011).
4. Kovalenko, I., Bucknall, D. G. & Yushin, G. Detonation nanodiamond and onion-like-carbon-embedded polyaniline for supercapacitors. *Adv. Funct. Mater.* **20**, 3979–3986 (2010).
5. Xiao, Y., Ye, X., He, L. & Che, J. New carbon nanotube-conducting polymer composite electrodes for drug delivery applications. *Polym. Int.* **61**, 190–196 (2012).
6. Samba, R., Fuchsberger, K., Matychyn, I., Epple, S., Kiesel, L., Stett, A., Schuhmann, W. & Stelzle, M. Application of PEDOT-CNT microelectrodes for neurotransmitter sensing. *Electroanalysis* **26**, 548–555 (2014).
7. Luo, X., Weaver, C. L., Zhou, D. D., Greenberg, R. & Cui, X. T. Highly stable carbon nanotube doped poly(3,4-ethylenedioxythiophene) for chronic neural stimulation. *Biomaterials* **32**, 5551–7 (2011).
8. Ispas, A., Peipmann, R., Adolphi, B., Efimov, I. & Bund, A. Electrodeposition of pristine and composite poly(3,4-ethylenedioxythiophene) layers studied by electro-acoustic impedance measurements. *Electrochim. Acta* **56**, 3500–3506 (2011).
9. Eliseeva, S. N., Spiridonova, D. V., Tolstopyatova, E. G. & Kondratiev, V. V. Redox capacitance of poly-3,4-ethylenedioxythiophene studied by cyclic voltammetry and faradaic impedance spectroscopy. *Russ. J. Electrochem.* **44**, 894–900 (2008).
10. Bobacka, J., Lewenstam, A., Ivaska, A. & Fin, A. Electrochemical impedance spectroscopy of oxidized poly ( 3 , 4-ethylenedioxythiophene ) film electrodes in aqueous solutions. **489**, 17–27 (2000).
11. Asavapiriyant, S., Chandler, G. K., Gunawardena, G. A. & Pletcher, D. The electrodeposition of polypyrrole films from aqueous solutions. *J. Electroanal. Chem.* **117**, 229–244 (1984).

12. Downard, A. J. & Pletcher, D. A study of the conditions for the electrodeposition of polythiophene in acetonitrile. *J. Electroanal. Chem.* **206**, 147–152 (1986).
13. Otero, T. F. & De Larreta, E. Electrochemical control of the morphology, adherence, appearance and growth of polypyrrole films. *Synth. Met.* **26**, 79–88 (1988).
14. Pigani, L., Heras, A., Colina, Á., Seeber, R. & López-Palacios, J. Electropolymerisation of 3,4-ethylenedioxythiophene in aqueous solutions. *Electrochem. Commun.* **6**, 1192–1198 (2004).
15. Liu, R., Cho, S. I. & Lee, S. B. Poly(3,4-ethylenedioxythiophene) nanotubes as electrode materials for a high-powered supercapacitor. *Nanotechnology* **19**, 215710 (2008).
16. Baek, S., Green, R. A. & Poole-Warren, L. A. The biological and electrical trade-offs related to the thickness of conducting polymers for neural applications. *Acta Biomater.* **10**, 3048–58 (2014).
17. Schwan, J., Ulrich, S., Batori, V., Ehrhardt, H. & Silva, S. R. P. Raman spectroscopy on amorphous carbon films. *J. Appl. Phys.* **80**, 440 (1996).
18. Gomez, H., Ram, M. K., Alvi, F., Stefanakos, E. & Kumar, A. Novel Synthesis, Characterization, and Corrosion Inhibition Properties of Nanodiamond–Polyaniline Films. *J. Phys. Chem. C* **114**, 18797–18804 (2010).
19. Barnard, A. S. & Sternberg, M. Crystallinity and surface electrostatics of diamond nanocrystals. *J. Mater. Chem.* **17**, 4811 (2007).
20. Garreau, S., Louarn, G., Buisson, J. P., Froyer, G. & Lefrant, S. In situ spectroelectrochemical raman studies of poly(3,4-ethylenedioxythiophene) (PEDT). *Macromolecules* **32**, 6807–6812 (1999).
21. Gustafsson, H., Kvarnström, C. & Ivaska, A. Comparative study of n-doping and p-doping of poly(3,4-ethylenedioxythiophene) electrosynthesised on aluminium. *Thin Solid Films* **517**, 474–478 (2008).
22. Nelson, A. Co-refinement of multiple contrast neutron/X-ray reflectivity data using MOTOFIT. *J. Appl. Crystallogr.* **39**, 273–276 (2006).
23. Osswald, S., Yushin, G., Mochalin, V., Kucheyev, S. O. & Gogotsi, Y. Control of sp<sup>2</sup>/sp<sup>3</sup> carbon ratio and surface chemistry of nanodiamond powders by selective oxidation in air. *J. Am. Chem. Soc.* **128**, 11635–42 (2006).
24. Tamburri, E., Guglielmotti, V., Matassa, R., Orlanducci, S., Gay, S., Reina, G., Terranova, M. L., Passeri, D. & Rossi, M. Detonation nanodiamonds tailor the structural order of PEDOT chains in conductive coating layers of hybrid nanoparticles. *J. Mater. Chem. C* **2**, 3703 (2014).

25. Niu, L., Kvarnström, C., Fröberg, K. & Ivaska, A. Electrochemically controlled surface morphology and crystallinity in poly (3,4-ethylenedioxythiophene) films. *Synth. Met.* **122**, 425–429 (2001).
26. Ocampo, C., Oliver, R., Armelin, E., Alemán, C. & Estrany, F. Electrochemical synthesis of poly(3,4-ethylenedioxythiophene) on steel electrodes: properties and characterization. *J. Polym. Res.* **13**, 193–200 (2005).
27. Hu, Y., Shenderova, O. A., Hu, Z., Padgett, C. W. & Brenner, D. W. Carbon nanostructures for advanced composites. *Reports Prog. Phys.* **69**, 1847–1895 (2006).

## **Chapter 5 – Electrodeposition of polypyrrole films**

### **5.1 Introduction**

It has been observed that the choice of electrodeposition method<sup>1,2</sup> as well as other elements of the deposition protocol, such as supporting electrolyte<sup>3</sup> or monomer concentration<sup>4</sup>, can affect the electrochemical and structural properties of polymer films. The following study explores the effect of the electrochemical control function employed in the deposition of polypyrrole (PPy) films. In particular, the surface morphology and redox behaviour will be examined using AFM and cyclic voltammetry, respectively. Neutron reflectometry (NR) is used to evaluate how the deposition method affects the internal composition of these films. This particular aspect of film structure is still poorly understood since very few techniques can explore the depths of the polymer matrix in a solvated state. NR can exclusively provide spatially resolved compositional information which can be used to further understanding of the solvation effects within the films.

The thickness and solvation levels of films in progressive stages of growth are presented for different deposition protocols. The results indicate that the electrochemical control function affects both the polymerisation efficiency and the porosity of the films. Despite this, no significant differences in the electroactivity of the films were observed. The effect of monomer concentration in the deposition solution is investigated and a higher concentration is found to produce films with initially greater redox capacity which diminishes following prolonged cycling.

## 5.2 Experimental

### 5.2.1 *In situ* electrochemical growth and NR

All chemicals were used as received from Sigma Aldrich. Deposition solutions were prepared containing 0.065 M or 0.112 M hydrogenous or deuterated pyrrole in 0.1 M NaClO<sub>4</sub> in D<sub>2</sub>O or H<sub>2</sub>O, respectively. The working electrodes were gold coated quartz blocks. NR measurements of the gold surface in the deposition solution were carried out prior to starting the deposition process. Following polymer deposition, the cells were emptied and rinsed before being refilled with the monomer-free electrolyte solution, 0.1 M NaClO<sub>4</sub> in H<sub>2</sub>O or D<sub>2</sub>O. The characterisation solution was always consistent with the deposition solution with regards to the choice of solvent contrast, i.e. if the film was deposited from a solution of the electrolyte in D<sub>2</sub>O containing hydrogenous monomer then the film produced was also characterised in a deuterated solution. Each film was cycled in monomer-free electrolyte after deposition then held at a reducing potential of -0.5 V and at an oxidising potential of 0.2 V.

NR measurements were carried out using a 'stop/start' methodology such that the growth was intermittently paused, during which time the film remained at the open circuit potential and therefore was not subject to change during the data acquisition time. Measurements on FIGARO were carried out at one or two angles with a low angle of 0.7° and a high angle of 3.5°, to give a *Q* range of 0.008 – 0.35 Å<sup>-1</sup>. Measurements on SURF were done using three angles: 0.35°, 0.7° and 1.5°. A fourth angle of 0.25° was used when measuring in deuterated media in order to fully resolve the critical edge, thus a total *Q* range of 0.008 – 0.6 Å<sup>-1</sup>.

	C <sub>4</sub> D <sub>3</sub> N	C <sub>4</sub> H <sub>3</sub> N	H <sub>2</sub> O	D <sub>2</sub> O
$\rho / \text{g cm}^{-3}$	1.4	1.4	1	1.1
$N_b / \times 10^{-6} \text{ \AA}^{-2}$	6.93	3.2	-0.56	6.3

Table 5.1 – Densities and SLDs of PPy and water in their hydrogenous and deuterated forms

The SLDs and the densities associated with the different components involved in the NR experiments are listed in Table 5.1. These values are used in the subsequent fitting, interpretation and analysis of the data. The concentrations of the monomer and

electrolyte in solution are so low that they do not change the overall SLD from that of pure water.

Table 5.2 summarises the conditions and details of each of the samples prepared during *in situ* NR measurements. All films were deposited and measured in the NR/EC cell B except for the dPPy film grown with 0.065 M monomer solution in cell A, details of the cells are outlined previously in Chapter 2. For potentiostatic and galvanostatic growth,  $t_{\text{total}}$  indicates the total deposition time, the growth intervals between NR measurements varied and are presented in section 5.3. The first three films, measured on FIGARO, were intended to be a similar thickness. This was evaluated by continuous monitoring and fitting of the reflectivity measurements rather than aiming for a particular charge density as it is known that a portion of the charge supplied is used to oxidise polymer present rather than contribute to polymerisation processes.

Electrochemical control function	Deposition conditions	Solution	Exposed electrode area / cm <sup>2</sup>
Potentiodynamic	E : [-0.4 V – E <sub>max</sub> ] vs Ag wire v = 20 mVs <sup>-1</sup> i <sub>max</sub> = 3 mA 30 cycles	0.112 M dPy in 0.1 M NaClO <sub>4</sub> in H <sub>2</sub> O	24.8
Potentiostatic	E = 0.3 V vs Ag wire t <sub>total</sub> = 68 min	0.112 M dPy in 0.1 M NaClO <sub>4</sub> in H <sub>2</sub> O	24.8
Galvanostatic	i = 2 μA cm <sup>-2</sup> t <sub>total</sub> = 127 min	0.065 M dPy in 0.1 M NaClO <sub>4</sub> in H <sub>2</sub> O	29.4
Galvanostatic*	i = 2.4 μA cm <sup>-2</sup> t <sub>total</sub> = 85 min	0.112 M dPy in 0.1 M NaClO <sub>4</sub> in H <sub>2</sub> O	24.8
Galvanostatic*	i = 2.4 μA cm <sup>-2</sup> t <sub>total</sub> = 35 min	0.112 M hPy in 0.1 M NaClO <sub>4</sub> in D <sub>2</sub> O	24.8

Table 5.2 – Summary of polypyrrole sample information and deposition conditions, \* indicates samples studied on SURF

In some cases, the gold electrode presented with a thin surface layer with a lower SLD. Where present, this was maintained as a layer with fixed parameters in the subsequent fits to the polymer growth measurements. The fitting routines can also result in unreasonably large roughness parameters; in such cases the roughness of the

layer was modified manually to a good fit to the features of the data, and then fixed before other parameters were allowed to converge.

### 5.2.2 Investigation of variables in galvanostatic deposition protocol

Deposition solutions were prepared containing 0.065 M or 0.112 M pyrrole in 0.1 M NaClO<sub>4</sub>. The working electrodes from Platypus Technologies were gold coated aluminosilicate glass slides with a titanium underlayer. The exposed surface area was delimited to 1 cm<sup>2</sup> using teflon tape. The reference and counter electrodes were a silver chloride coated silver wire and platinum coated titanium mesh, respectively. The samples were galvanostatically deposited with a current density of 2 or 2.4 μA cm<sup>-2</sup> in a series of growth intervals.

Sample	Monomer concentration / M	Intervals	Current density / μA cm <sup>-2</sup>	Q <sub>g</sub> / mC cm <sup>-2</sup>
1	0.112	15	2	15.24
2	0.065	15	2	15.24
3	0.112	7	2	10.2
4	0.065	7	2	10.2
5	0.112	7	2.4	12.24
6	0.065	7	2.4	12.24
7	0.112	7	2.4	12.24
8	0.065	7	2.4	12.24
9	0.112	9	2	15
10	0.065	9	2	15

*Table 5.3 – Summary of galvanostatically grown PPy small sample information and deposition conditions; 15 intervals indicates 2 x 30 s, 1 x 1 min, 5 x 2 min, 1 x 5 min, 1 x 10 min, 5 x 20 min; 7 intervals is 1 x 5 min, 4 x 10 min, 2 x 20 min; 9 intervals is 1 x 5 min, 4 x 10 min, 4 x 20 min*

The deposition conditions and protocol for each sample are listed in Table 5.3 which shows that each set of parameters was tested for both monomer concentrations and

the time intervals were selected based on the growth protocols used for the NR experiments in section 5.2.1. Film growth was paused for 1 min between each interval. The electrochemical characterisation of the films was carried out in fresh 0.1 M NaClO<sub>4</sub> solution and each film was cycled for 20 cycles at successive scan rates of 100 mV s<sup>-1</sup>, 50 mV s<sup>-1</sup>, 20 mV s<sup>-1</sup> and finally at 100 mV s<sup>-1</sup> again.

## 5.3 Results

### 5.3.1 *In situ* electrochemical growth and NR study

The *in situ* measurements of the potentiodynamic growth of dPPy were achieved by pausing the deposition every six cycles to measure the reflectivity at the open circuit potential (OCP) where the polymer was in the neutral state, stabilising to a potential around 0 V. Figure 5.1 shows the reflectivity measurements in which the increasing frequency of Kiessig fringes indicates the growth of the film, and the associated SLD profiles where the fits clearly show a regular increase in film thickness corresponding to each growth interval.

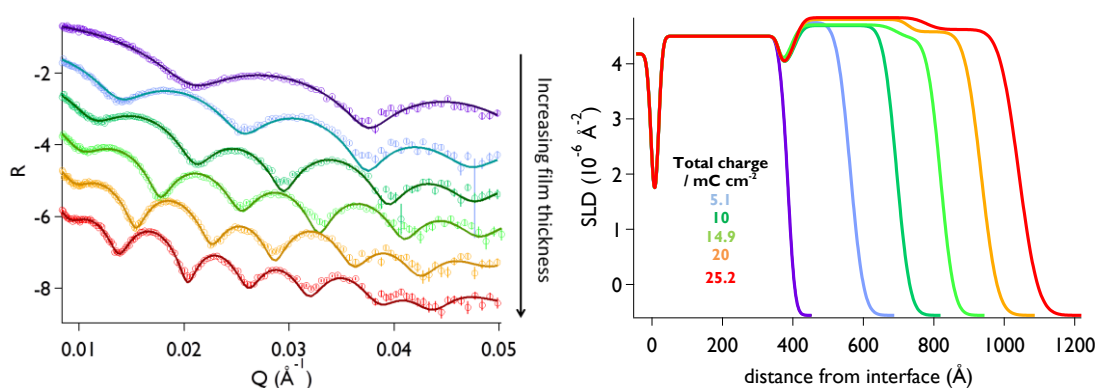


Figure 5.1 – NR measurements and fits (left) and corresponding SLD profiles (right) for the potentiodynamic growth of dPPy; the purple trace is the gold measurement prior to deposition.  $R(Q)$  datasets are offset by increments of -1 for clarity. Experimental conditions: 0.1 l 2 M dPy in 0.1 M  $\text{NaClO}_4$  in  $\text{H}_2\text{O}$ ,  $E$ :  $[-0.4 \text{ V} - E_{\text{max}}]$  vs Ag wire,  $v = 20 \text{ mVs}^{-1}$ ,  $i_{\text{max}} = 3 \text{ mA}$ , 30 cycles

The cyclic voltammograms during film deposition showed the usual characteristics such as a nucleation loop during the first cycle and a progressively increasing current magnitude with each cycle. These features can be seen in Figure 5.2. Comparisons of thickness and mass of deposited polymer per area as calculated from the growth charge density and the NR fits are presented in Figure 5.3. The thickness of the film extracted from the NR data is consistently greater than that predicted by the electrochemical data as it includes the volume of solvent in the film. The plot shows the film to be quite consistently solvated throughout the deposition process. The mass per area plots suggest that the efficiency of growth could diminish slightly as the growth of the film progresses, since the mass per area calculated from the fits to the NR data begins to fall beneath the values predicted from the electrochemical data. This

can also be observed in the SLD profile in Figure 5.1, where the film thickness difference between intervals decreases as the deposition proceeds. While the electrochemical data is, by definition, a linear relationship between mass deposited and the number of growth cycles, the fits to the NR data suggest that there may be less material deposited per cycle in the later stages of growth, with the rate of growth dropping slightly towards the final cycles. Evaluation of the charge of the oxidation peak of each cycle indicates that the growth charge density  $Q_g$  was approximately  $0.84 \pm 0.05 \text{ mC cm}^{-2}$  every cycle.

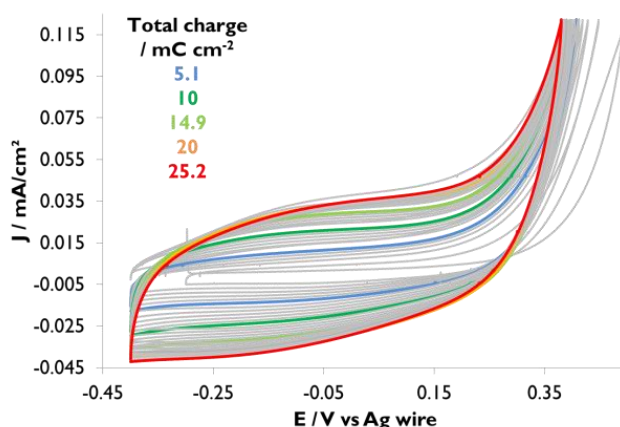


Figure 5.2 – Cyclic voltammograms recorded during the potentiodynamic growth of dPPy. Experimental conditions:  $0.112 \text{ M dPy}$  in  $0.1 \text{ M NaClO}_4$  in  $\text{H}_2\text{O}$ ,  $E : [-0.4 \text{ V} - E_{max}]$  vs Ag wire,  $v = 20 \text{ mVs}^{-1}$ ,  $i_{max} = 3 \text{ mA}$ , 30 cycles.

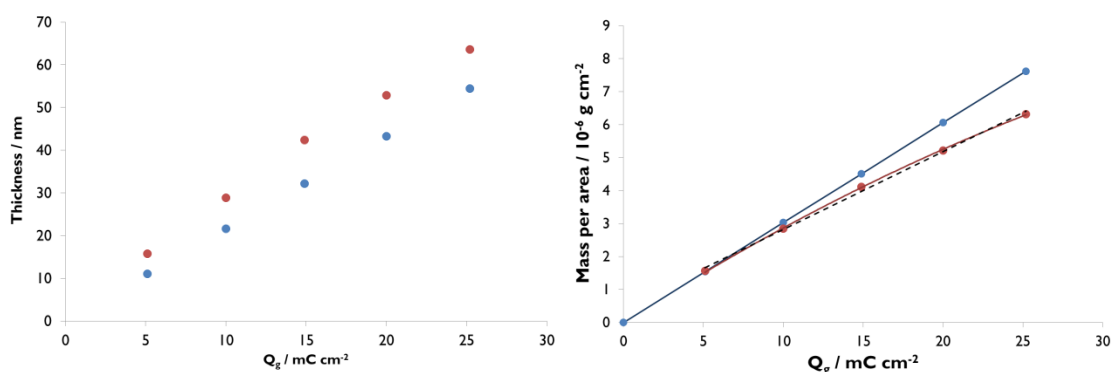


Figure 5.3 – Plots of film thickness (left) and mass per area (right) as a function of growth charge density as calculated from the electrochemical data (blue) and from the NR data (red) from the potentiodynamic growth of dPPy; the coloured traces are the associated fits to the data, the black dotted trace is the linear fit to the NR data

The fitted reflectometry data acquired for five growth stages during the potentiostatic growth of dPPy is presented in Figure 5.4. Each stage corresponds to the equivalent colour in the transients presented in Figure 5.5.

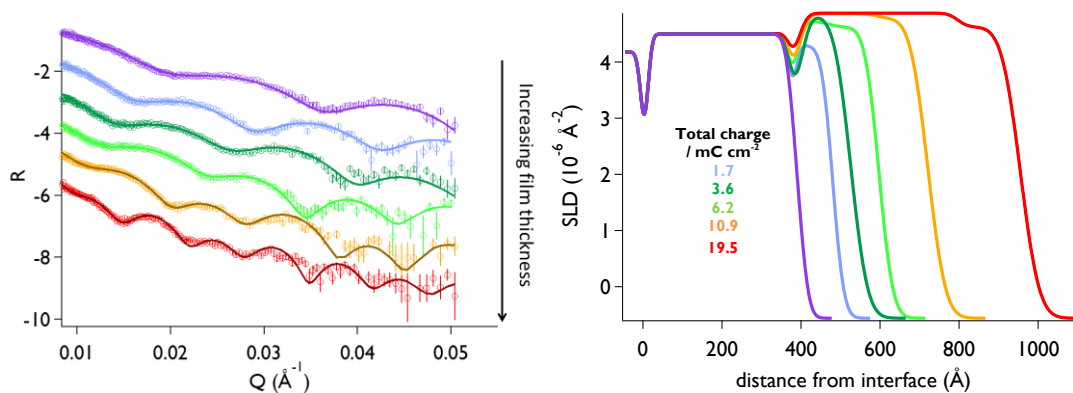


Figure 5.4 – NR measurements and fits (left) and corresponding SLD profiles (right) for the potentiostatic growth of dPPy; the purple trace is the gold measurement prior to deposition.  $R(Q)$  datasets are offset by increments of  $-1$  for clarity. Experimental conditions:  $0.112\text{ M dPPy}$  in  $0.1\text{ M NaClO}_4$  in  $\text{H}_2\text{O}$ ,  $E = 0.3\text{ V vs Ag wire}$ ,  $t_{\text{total}} = 68\text{ min}$

The SLD profiles suggest that the earlier growth stages result in a film that is more solvated with a solvent volume fraction of approximately  $\Phi_s \sim 0.35$  but that the growing film eventually stabilises to a homogeneous solvent volume fraction of around  $\Phi_s \sim 0.28$  with an outer layer slightly more solvated to  $\Phi_s \sim 0.3$ . The potentiodynamic growth fits also indicated a more solvated outer polymer layer, however the initial growth stages immediately reached a stable level of solvation of  $\Phi_s \sim 0.3$ .

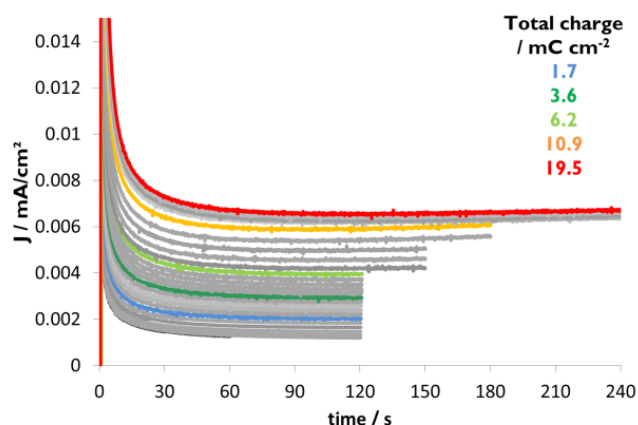


Figure 5.5 – Growth transients from the potentiostatic deposition steps of dPPy. Coloured traces are indicative of the total charge passed following successive deposition intervals. Experimental conditions:  $0.112\text{ M dPPy}$  in  $0.1\text{ M NaClO}_4$  in  $\text{H}_2\text{O}$ ,  $E = 0.3\text{ V vs Ag wire}$ ,  $t_{\text{total}} = 68\text{ min}$

Unlike the potentiodynamic growth, in this case, the amount of polymer deposited as calculated from the electrochemical data coincides closely with the results of the fits to the NR data as shown in Figure 5.6. This suggests polymerisation efficiency close to 100 % although the NR data for the final growth stage begins to fall beneath the trend predicted by the coulometric data. The plots of thickness as a function of growth charge density show once again that the thickness from the NR fits is greater than the coulometric estimates and that the gap between the values increases with each growth step showing the increased solvation of the film as the deposition progresses.

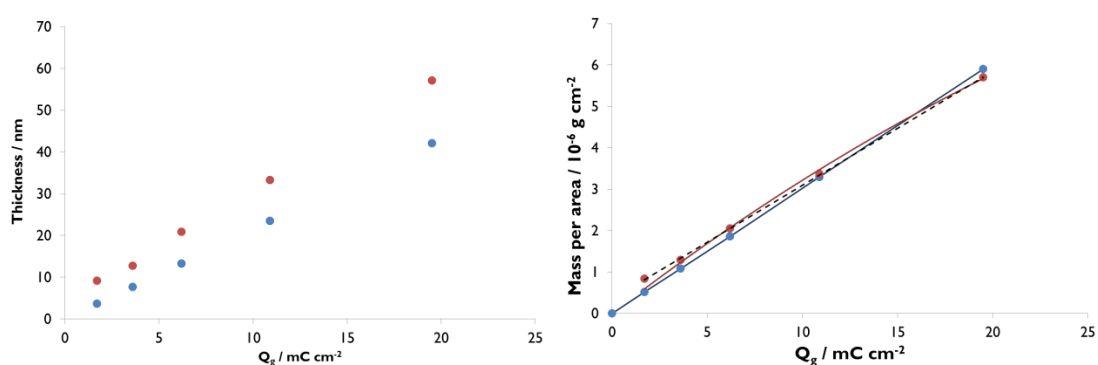


Figure 5.6 – Plots of film thickness (left) and mass per area (right) as a function of growth charge density as calculated from the electrochemical data (blue) and from the NR data (red) from the potentiostatic growth of dPPy; the coloured traces are the associated fits to the data, the black dotted trace is the linear fit to the NR data

The galvanostatic growth of dPPy, grown from a monomer concentration that was approximately half that used to grow the potentiodynamic and potentiostatic films, presented the most significantly different growth profile. As shown in Figure 5.7, the SLD profiles indicate a significantly more solvated film since the bulk of the polymer film has a significantly lower SLD than those produced by potentiodynamic or potentiostatic growth. Once again the film presents a more solvated outer layer with  $\Phi_s > 0.54$  in the last three growth steps.

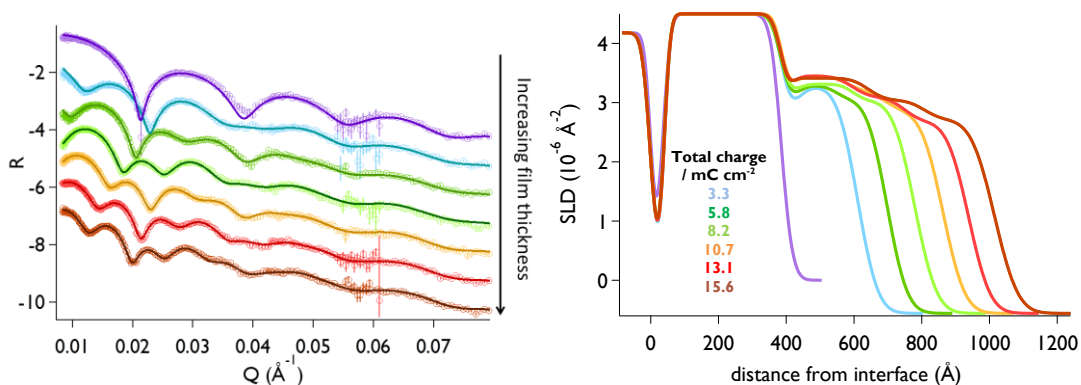


Figure 5.7 – NR measurements and fits (left) and corresponding SLD profiles (right) for the galvanostatic growth of dPPy performed on FIGARO; the purple trace is the gold measurement prior to deposition.  $R(Q)$  datasets are offset by increments of  $-1$  for clarity. Experimental conditions:  $0.065\text{ M dPy}$  in  $0.1\text{ M NaClO}_4$  in  $\text{H}_2\text{O}$ ,  $i = 2\ \mu\text{A cm}^{-2}$ ,  $t_{\text{total}} = 127\text{ min}$

However, the solvent volume fraction in this case appears to increase more gradually from the electrode to the polymer/solution interface, which can be observed in the slope of the polymer layer in the SLD profile in Figure 5.7. The associated growth transients are presented in Figure 5.8.

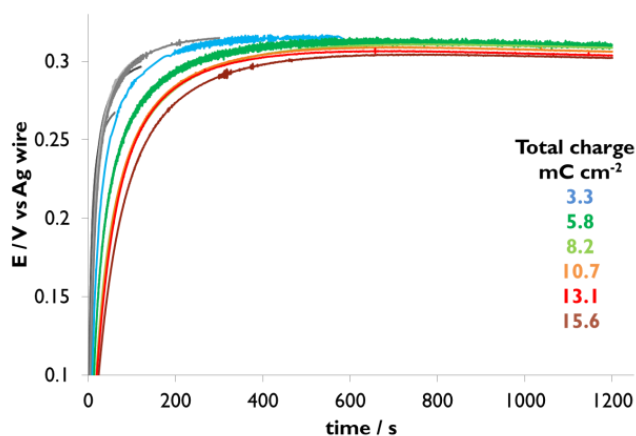


Figure 5.8 – Growth transients from successive intervals during the galvanostatic deposition of dPPy. Coloured traces are indicative of the total charge passed following successive deposition intervals. Experimental conditions:  $0.065\text{ M dPy}$  in  $0.1\text{ M NaClO}_4$  in  $\text{H}_2\text{O}$ ,  $i = 2\ \mu\text{A cm}^{-2}$ ,  $t_{\text{total}} = 127\text{ min}$

The plots of thickness as a function of growth charge density presented in Figure 5.9 clearly show that the thickness from the NR fits is substantially greater than the predicted value from the electrochemical data. Furthermore the increasing difference

between these values as the growth progresses highlights the increasing volume of solvent within the polymer film.

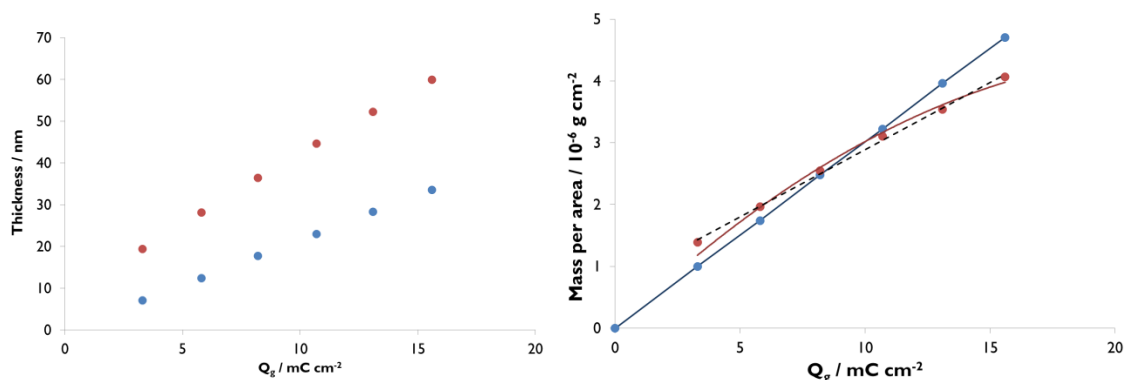


Figure 5.9 – Plots of film thickness (left) and mass per area (right) as a function of growth charge density as calculated from the electrochemical data (blue) and from the NR data (red) from the galvanostatic growth of dPPy in 0.065 M monomer solution; the coloured traces are the associated fits to the data, the black dotted trace is the linear fit to the NR data

The mass per area comparison plot shows that while the values calculated from the electrochemical and NR data are close, the linear trend in the electrochemical estimate of growth is not quite replicated by the values extracted from the SLD profiles. As previously seen in the case of the potentiodynamic growth, the values calculated from the electrochemical data appear to overestimate the deposited mass.

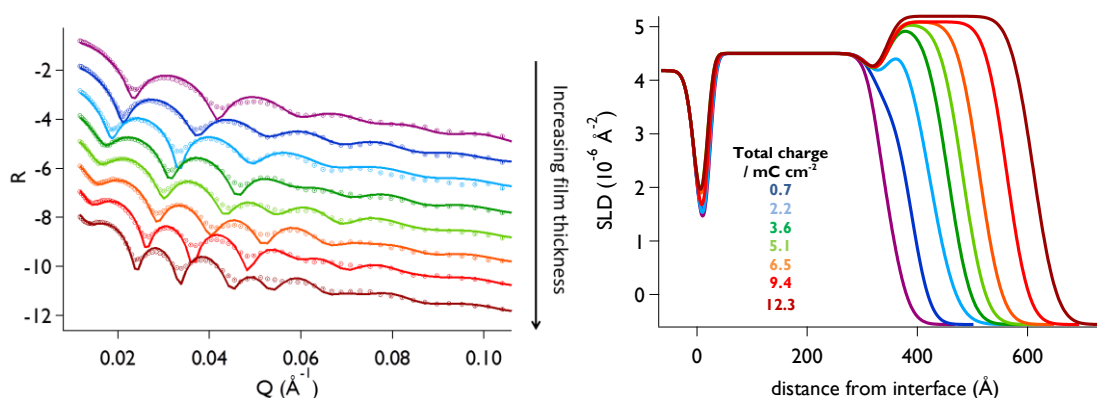


Figure 5.10 – NR measurements and fits (left) and corresponding SLD profiles (right) for the galvanostatic growth of dPPy performed on SURF; the purple trace is the gold measurement prior to deposition.  $R(Q)$  datasets are offset by increments of  $-1$  for clarity. Experimental conditions: 0.112 M dPPy in 0.1 M  $\text{NaClO}_4$  in  $\text{H}_2\text{O}$ ,  $i = 2.4 \mu\text{A cm}^{-2}$ ,  $t_{\text{total}} = 85 \text{ min}$

The galvanostatic growth of dPPy was repeated on SURF with different growth interval times and the monomer concentration in this case matched that used in the potentiodynamic and potentiostatic deposition experiments. Figure 5.10 shows the NR data and corresponding fits which clearly show a polymer film with a similar solvation profile to that seen in the case of the potentiostatic deposition. The early stages of film growth suggest a slightly more solvated film which stabilises to an overall solvation of approximately  $\Phi_s \sim 0.24$ .

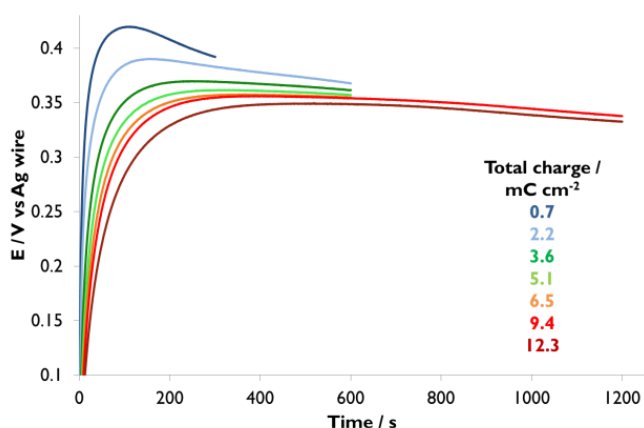


Figure 5.11 – Growth transients from successive intervals during the galvanostatic deposition of dPPy. Coloured traces are indicative of the total charge passed following successive deposition intervals. Experimental conditions: 0.112 M dPy in 0.1 M NaClO<sub>4</sub> in H<sub>2</sub>O,  $i = 2.4 \mu\text{A cm}^{-2}$ ,  $t_{\text{total}} = 85 \text{ min}$

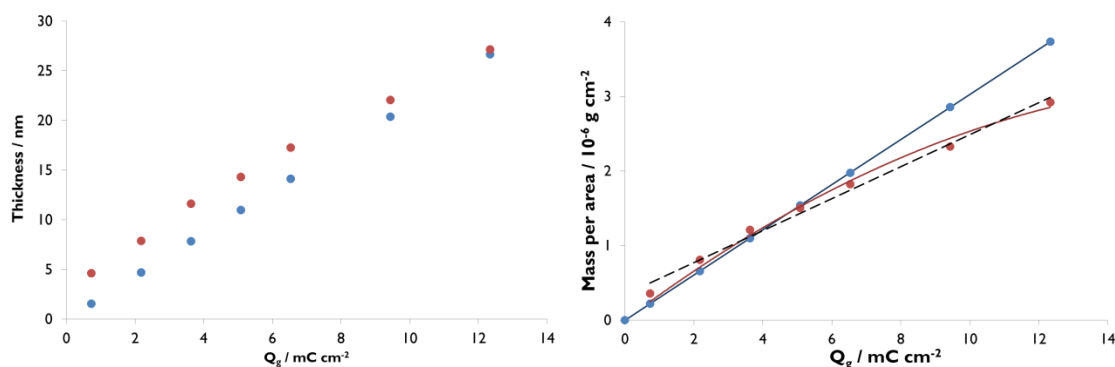


Figure 5.12 – Plots of film thickness (left) and mass per area (right) as a function of growth charge density as calculated from the electrochemical data (blue) and from the NR data (red) from the galvanostatic growth of dPPy in 0.112 M monomer solution; the coloured traces are the associated fits to the data, the black dotted trace is the linear fit to the NR data

Figure 5.11 shows how the growth transients in this case presented a higher peak potential during the initial deposition interval compared to that shown in Figure 5.8. Unlike the previous film growth, longer intervals of applied current were used from the start. In Figure 5.12, the plot of mass per area as a function of growth charge density indicates once again that the electrochemical estimate of mass is more than that calculated from the fits to the NR data. The plot of thickness however shows a different trend than seen previously whereby the film thickness from the NR data does not maintain a steady increase but in the final growth state appears to be equal to that calculated from the coulometric data. Since the film was measured in a solvated state, this would indicate that the dry thickness of the film is now significantly less than the predicted value.

The galvanostatic growth of hPPy was carried out with the same current density and time intervals as the previous film, although the desired growth charge density was not achieved. Figure 5.13 shows the data acquired and the SLD profiles resulting from the fits.

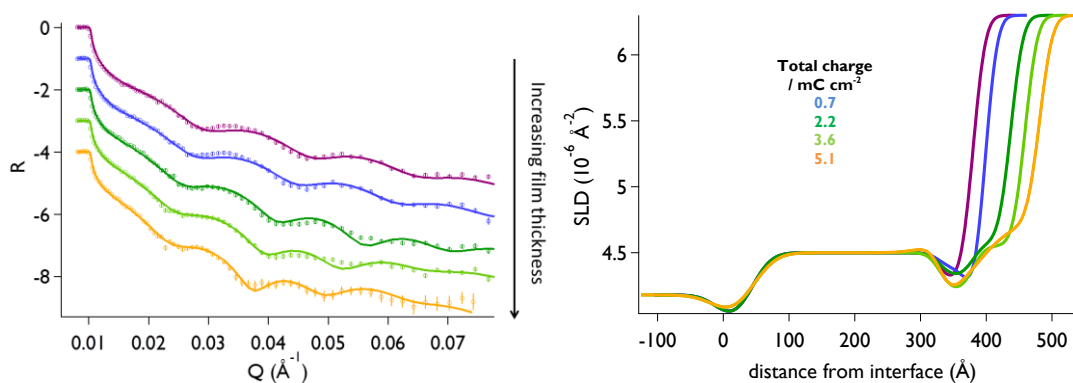


Figure 5.13 – NR measurements and fits (left) and corresponding SLD profiles (right) for the galvanostatic growth of hPPy performed on SURF; the purple trace is the gold measurement prior to deposition.  $R(Q)$  datasets are offset by increments of -1 for clarity. Experimental conditions: 0.112 M hPPy in 0.1 M  $\text{NaClO}_4$  in  $\text{D}_2\text{O}$ ,  $i = 2.4 \mu\text{A cm}^{-2}$ ,  $t_{\text{total}} = 35 \text{ min}$

In this case, the fringes of the reflectivity curves are noticeably less defined compared with those seen in the data presented for the other films. This is due to the fact that the solvated film SLD is very close to that of the gold resulting in very poor contrast between these layers. In terms of its SLD, the polymer layer becomes almost an extension of the gold layer and variations in the solvation of the film translate to a

large roughness at the solution interface. Consequently, the details of the polymer layer were more difficult to ascertain since the fit tended towards large roughness parameters at both the gold/polymer and polymer/solvent interfaces.

As shown in Figure 5.14, the potential as a function of time transients for this film were similar to those recorded during the growth of dPPy from the 0.065 M monomer solution and therefore differ from the growth of dPPy from the 0.112 M monomer solution in that there is no potential peak during the early growth stages.

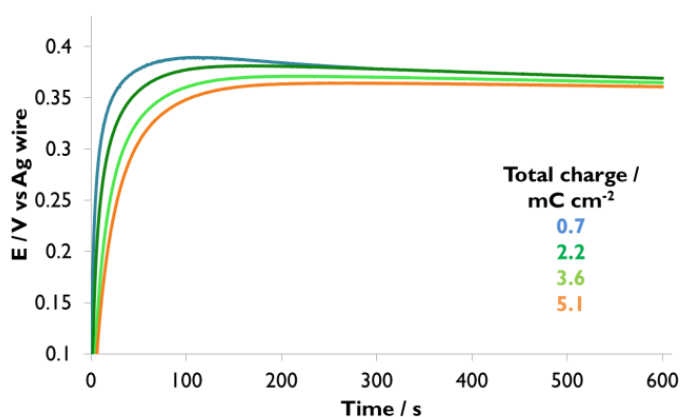


Figure 5.14 – Growth transients from successive intervals during the galvanostatic deposition of hPPy. Coloured traces are indicative of the total charge passed following successive deposition intervals. Experimental conditions: 0.112 M hPy in 0.1 M NaClO<sub>4</sub> in D<sub>2</sub>O,  $i = 2.4 \mu\text{A cm}^{-2}$ ,  $t_{\text{total}} = 35 \text{ min}$

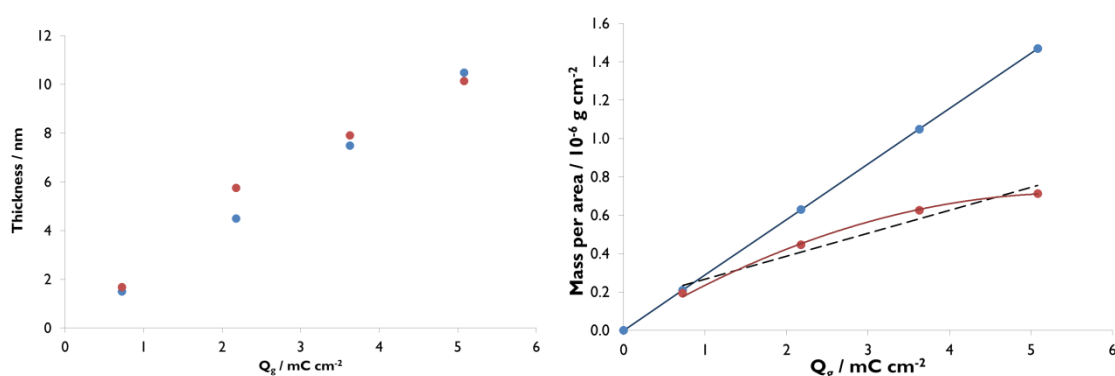


Figure 5.15 – Plots of film thickness (left) and mass per area (right) as a function of growth charge density as calculated from the electrochemical data (blue) and from the NR data (red) from the galvanostatic growth of hPPy; the coloured traces are the associated fits to the data, the black dotted trace is the linear fit to the NR data

Figure 5.15 shows the plot of film thickness as a function of the growth charge density in which the values from the NR data show a similar trend to those in Figure 5.12 whereby, in the final stage of growth, the solvated thickness from the NR measurement is commensurate with the dry thickness from the coulometric estimate. The plot of mass per area as a function of growth charge density indicates that the values calculated from the fits to the NR data are significantly lower than those calculated from the electrochemical data. While this has been seen previously in the case of the other films, the lack of contrast presented by this system may play a role in affecting the accuracy of the parameter values extracted from the fits.

			Intercept	Gradient	R	e <sup>-</sup> per monomer (z)	polymerisation efficiency / %
Figure 5.3	PD	EC data	0	0.30	1	2.33	
		NR data	0.45	0.24	0.9987	2.98	78.29
Figure 5.6	PS	EC data	0	0.30	1	2.33	
		NR data	0.35	0.28	0.9999	2.56	90.96
Figure 5.9	GS	EC data	0	0.30	1	2.33	
		NR data	0.72	0.22	0.9989	3.24	71.85
Figure 5.12	GS	EC data	0	0.30	1	2.33	
		NR data	0.34	0.21	0.9952	3.29	70.78
Figure 5.15	GS	EC data	0	0.29	1	2.33	
		NR data	0.15	0.12	0.9783	5.62	41.47

Table 5.4 – Summary of linear regression analysis results from plots of mass per area as a function of growth charge density

$$\frac{\text{mass}}{\text{area}} (g \text{ cm}^{-2}) = \frac{M (g \text{ mol}^{-1})}{z \cdot F (C \text{ mol}^{-1}) \cdot 1000} \cdot Q_g (mC \text{ cm}^{-2}) \quad (5.1)$$

The results of the linear fits to the mass per area data are presented in Table 5.4. The relationship between the growth charge and the mass per area was defined in Chapter 3, equation ( 3.4 ), and can be rearranged to form the linear correlation shown in equation ( 5.1 ). As such,  $\frac{M (g \text{ mol}^{-1})}{z \cdot F (C \text{ mol}^{-1}) \cdot 1000}$  is the gradient of the linear plot and since the molar mass is known, the value of z can be extracted from the linear regression analysis of the NR data. In all cases, the fits reveal a greater value of z, indicating that

more electrons were consumed per monomer unit in the reaction. Assuming  $z = 2.33$  for the polymerisation process and a doping level of one charge per three monomer units, the excess can be used to calculate the percentage of charge that was 'lost', for example in the formation of oligomers that did not form part of the final film. Hence an approximation of the average polymerisation efficiency for a given growth protocol can be determined. An error propagation analysis of the thickness and SLD parameters in the NR fits was performed and the errors associated with the mass per area values were found to be no larger than the data point markers therefore these are not shown.

While the linear fits produce a good estimate of the average number of electrons consumed per monomer unit for a given system, they do not correctly describe the higher polymerisation efficiency at the start of the deposition process and the subsequent decay in efficiency as the growth progresses. The data correlates better to a second order polynomial equation of the form  $y = Ax + Bx^2$  where  $y$  is the mass per area and  $x$  is the growth charge. The gradient, indicative of the polymerisation rate, then becomes a linear equation as a function of  $Q$  such that  $\frac{dy}{dx} = A + 2Bx$ . Hence the polymerisation rate is seen to change as a function of the growth charge. The results of the polynomial fits to the mass per area data from the NR fits is presented in Table 5.5. The linear coefficient  $A$  is the gradient for  $Q = 0$  and the quadratic coefficient  $2B$  becomes the rate at which this gradient changes as a function of  $Q$ .

	Polynomial fit coefficients		Initial polymerisation efficiency / %	loss of polymerisation efficiency / %	R
	A	B			
PD	0.3105	-0.0024	102.65	-1.59	0.9998
PS	0.3542	-0.0032	117.10	-2.12	0.9975
GS	0.3842	-0.0084	127.01	-5.55	0.9937
GS SURF	0.3458	-0.0094	114.32	-6.22	0.9950
GS H	0.2583	-0.0233	89.33	-16.12	0.9987

*Table 5.5 – Summary of second order polynomial fits to the mass per area values calculated from the NR data as a function of charge*

In some cases, such as the plot shown in Figure 5.12, it could be argued that the initial stages of growth could present a linear trend with a greater gradient than that of the subsequent growth steps. This would indicate that the charge is more efficiently used in the nucleation process and initial deposition layers. The polymerisation efficiency appears to decrease with increasing film thickness. The second order polynomial fits to the data confirm this, modelling a high initial polymerisation efficiency that subsequently decreases as a function of the growth charge. Since all the films were produced by a layer-by-layer methodology due to the necessity to stop and start the growth to acquire NR measurements, the films were returned to a neutral state between each deposition stage. It is therefore suggested that, as the growth progressed, the charge was increasingly consumed by the oxidation of the existing film and possibly producing oligomers in solution before the deposition process resumed.

The mass per area values were also used as a means of verifying that fits to the NR data of the films held oxidised and reduced were consistent with the equivalent final growth stage. Since differences in solvation could occur due to the movement of ions within the films, a comparison of the quantity of polymer irrespective of the volume of solvent was required. Fits were considered within the margins of error if the mass per area value differed by no more than  $\pm 5\%$  from the final growth state. This value was selected to allow for the possible dissolution of surface oligomers during cycling prior to measurement of the redox states, as well as to compensate for possible changes in roughness at the polymer/solution interface which would affect the thickness parameters in the fits.

Figure 5.16 shows the SLD profiles of the films held in an oxidised and reduced state, compared with the final growth state where they were measured in the neutral state at the open circuit potential. In each case, following cycling and holding in doped states, the films presented a more solvated structure than as measured after the final stage of growth. This increase in solvation was usually on the order of 10 - 20 %. In most cases the oxidised and reduced states appear to show very little variation with only very slight changes in SLD and thickness. The most notable difference is in the case of the galvanostatically grown film, measured on FIGARO, in which the oxidised state is 4% less solvated than the reduced state but without any significant difference in thickness.

The hPPy film presents the opposite case whereby the oxidised state is seen to be 4% more solvated than the reduced state.

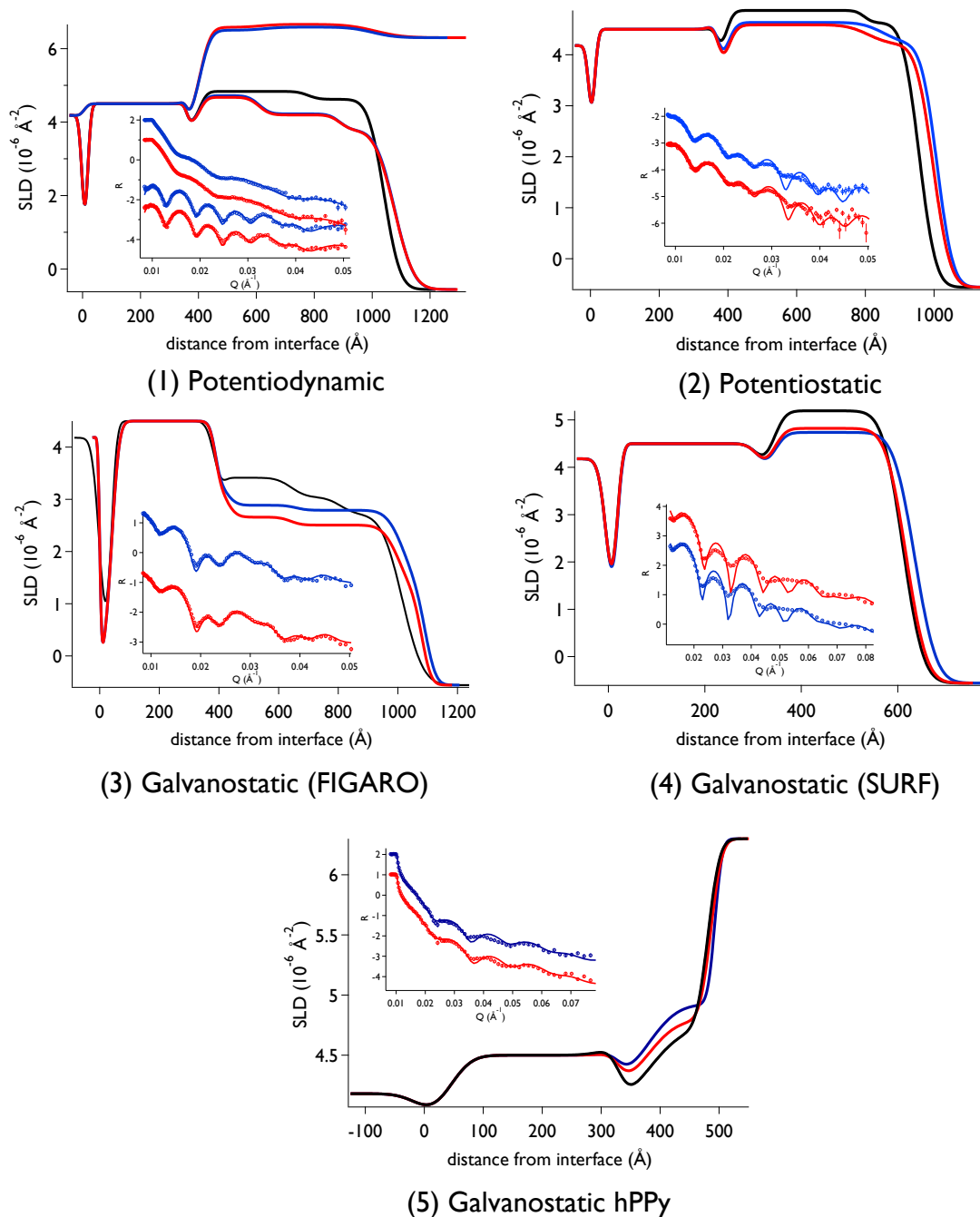


Figure 5.16 – SLD profiles of the films measured at the open circuit potential following the final growth stage (black), held oxidised at  $E = 0.2$  V (blue) and reduced at  $E = -0.5$  V (red); insets show the corresponding reflectivity data and fits from which these are derived, offset for clarity

Figure 5.1		Figure 5.4		Figure 5.10	
Potentiodynamic dPPy		Potentiostatic dPPy		Galvanostatic dPPy	
$Q_g$ / mC cm <sup>-2</sup>	$\Phi_s$	$Q_g$ / mC cm <sup>-2</sup>	$\Phi_s$	$Q_g$ / mC cm <sup>-2</sup>	$\Phi_s$
5.1	0.29	1.7	0.35	0.7	0.45
10.0	0.3 - 0.28	3.6	0.28	2.2	0.27
14.9	0.3 - 0.33	6.2	0.3 - 0.31	3.6	0.26
20.0	0.28 - 0.31	10.9	0.28 - 0.29	5.1	0.25
25.2	0.28 - 0.31	19.5	0.28 - 0.31	6.5	0.25
				9.4	0.25
				12.3	0.23
Figure 5.16 (1)		Figure 5.16 (2)		Figure 5.16 (4)	
E / V	$\Phi_s$	E / V	$\Phi_s$	E / V	$\Phi_s$
0.2	0.3 - 0.36 - 0.42	0.2	0.31 - 0.36	0.2	0.29
-0.5	0.3 - 0.37 - 0.42	-0.5	0.31 - 0.36	-0.5	0.28
Figure 5.7			Figure 5.10		
Galvanostatic dPPy			Galvanostatic hPPy		
$Q_g$ / mC cm <sup>-2</sup>	$\Phi_s$	$Q_g$ / mC cm <sup>-2</sup>	$\Phi_s$	$Q_g$ / mC cm <sup>-2</sup>	$\Phi_s$
3.3	0.49	0.7	0.18		
5.8	0.49 - 0.52	2.2	0.45		
8.2	0.48 - 0.52	3.6	0.44		
10.7	0.47 - 0.50 - 0.54	5.1	0.50		
13.1	0.47 - 0.51 - 0.57				
15.6	0.47 - 0.52 - 0.56				
Figure 5.16 (3)			Figure 5.16 (4)		
E / V	$\Phi_s$	E / V	$\Phi_s$	E / V	$\Phi_s$
0.2	0.54 - 0.55 - 0.78	0.2	0.56		
-0.5	0.57 - 0.59 - 0.79	-0.5	0.52		

Table 5.6 – Summary of the solvent volume fraction values extracted from the fits to the NR data for each stage of growth and redox state; multiple values are associated with multiple layers in the model such that left to right gives values from the electrode to the solution interface

The potentiodynamically grown film was exceptionally also measured in an electrolyte solution prepared with D<sub>2</sub>O. The results of the fits to this data do not fall within the acceptable 5% of the mass per area value of the final growth state but are shown nevertheless to demonstrate how the choice of contrast can affect the level of detail accessible through neutron measurements. While, numerically, the fits make little

sense since the lack of contrast does not allow sufficient distinction between subtle variations in solvation, visually the data reveals a high SLD layer of approximately the same thickness as that of the final growth state and the redox states measured in homogeneous electrolyte solutions.

In some cases, the SLD profiles also show how the internal structure of the films, in terms of the variation of solvent volume fraction as a function of depth, changed following the characterisation using cyclic voltammetry. The potentiodynamically grown film was relatively homogeneously solvated in the final growth state but presents three distinct areas of different solvation when held at an oxidising or reducing potential, as well as being overall more solvated. On the other hand, the galvanostatically deposited film measured on FIGARO presented an increasing solvation profile from the gold to the solution interface in the final growth state. In the redox states, however, it appears more homogeneously solvated presenting a bulk solvent volume fraction between  $\Phi_s \sim 0.54 - 0.55$  in the oxidised state and between  $\Phi_s \sim 0.57 - 0.59$  in the reduced state. The roughness at the polymer/solution interface was best modelled using a third layer in which the solvation was almost  $\Phi_s \sim 0.8$ . Table 5.6 summarises the solvent volume fractions from all the fits to the NR data acquired at the different stages of film deposition and in the redox states.

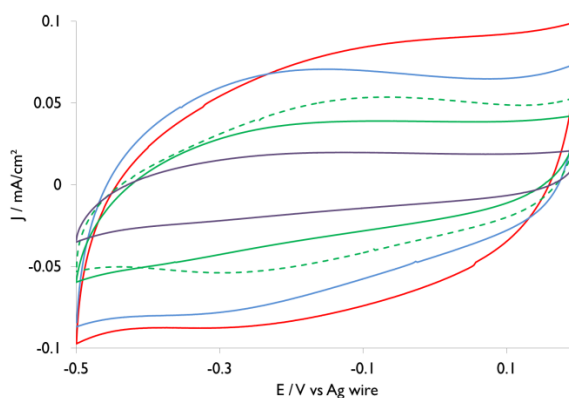


Figure 5.17 – Cyclic voltammograms of NR samples acquired at  $50 \text{ mV s}^{-1}$  in fresh electrolyte solution following film deposition; presented are the traces for dPPy grown potentiodynamically (red), potentiostatically (light blue), galvanostatically (green) from 0.112 M (full lines) and 0.065 M (dashed line) monomer solutions, and hPPy grown galvanostatically from 0.112 M monomer solution (dark blue)

The cyclic voltammograms used to characterise the films following deposition are presented in Figure 5.17. The most notable feature is a predominant lack of distinct redox peaks. The potentiostatically grown film presents a broad current peak around -0.25 V. The galvanostatically grown film deposited from the 0.065 M monomer solution also presents broad peaks at an oxidation potential of approximately -0.15 V and at a reduction potential of -0.25 V.

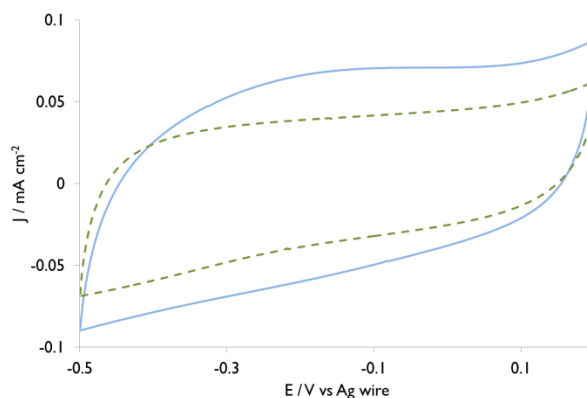


Figure 5.18 – Cyclic voltammograms of the dPPy films grown potentiostatically (light blue) and galvanostatically from 0.065 M monomer solution (dashed green) acquired at  $50 \text{ mV s}^{-1}$  following the NR measurement in which the films were held in a reduced state at  $E = -0.5 \text{ V}$

All the films exhibited a loss of electroactivity in their cyclic voltammograms following the NR measurements in which they were held at oxidising and reducing potentials. The two films previously presenting broad redox peaks lost these features as illustrated in Figure 5.18 which shows the cyclic voltammograms of the films after they were maintained in a reduced state during the acquisition of the reflectivity measurement.

The redox charge of the different films is presented in Table 5.7. Based on the results of the cyclic voltammograms recorded after deposition, the coverage calculated from the oxidation charge is also presented as a percentage of the coverage calculated from the growth charge for ease of comparison of the electroactivity of the different films. In all cases, the doping level is assumed to be  $x = 0.33$ .

Electrochemical control function	Monomer conc / M	$Q_g$ / mC cm <sup>-2</sup>	$Q_{ox}$ / mC cm <sup>-2</sup>	$\Gamma_{ox} / \Gamma_g$ / %
Potentiodynamic	0.112	25.2	0.99	32.05
Potentiostatic	0.112	19.5	0.8	33.47
Galvanostatic	0.065	15.6	0.54	28.24
Galvanostatic	0.112	12.3	0.42	27.85
Galvanostatic	0.112	5.1	0.21	33.59

*Table 5.7 – Summary of oxidation charge values from the electrochemical characterisation of NR samples shown in Figure 5.17*

The results of the AFM measurements are presented in Table 5.8 alongside the deposition protocol details and the estimated thickness calculated from the growth charge density,  $Q_g$ . It can be observed that the measured thickness of the dried films was greater than the calculated estimate from  $Q_g$ . However it was in some cases significantly greater than the fitted thickness of the solvated films, suggesting that the AFM measurements may have been inaccurate. The process of scratching the film is a delicate one in which the gold electrode layer can also be scratched. Since this layer is known to be on the order of 30 nm, this could explain the significant thickness difference, particularly in the case of the potentiodynamically and potentiostatically grown films. The other AFM measurements of thickness are quite close to the fitted values suggesting that the films may be quite rigid and do not collapse when dried.

Films A and C were found to have the highest roughness parameter, a feature that is well illustrated in Figure 5.19 where the images clearly show light spots indicating peaks in the surface topography.

	Electrochemical control function	Solvated thickness from NR / nm	Total charge density / mC cm <sup>-2</sup>	Thickness from Qg / nm	AFM thickness / nm	Roughness Rq / nm	SAD / %
A	Potentiodynamic	65 ± 2	25.2	54.4	80 ± 5	13.5	3.36
B	Potentiostatic	60 ± 3	19.5	42.2	100 ± 5	7.56	1.42
C	Galvanostatic	64 ± 4	15.6	33.6	60 ± 5	9.01	0.5
D	Galvanostatic	28 ± 1	12.3	26.7	35 ± 5	3.19	0.73
E	Galvanostatic	10 ± 1	5.1	10.5	12 ± 3	2.85	0.59

Table 5.8 – Summary of the thickness and roughness parameters determined by AFM for each film growth protocol

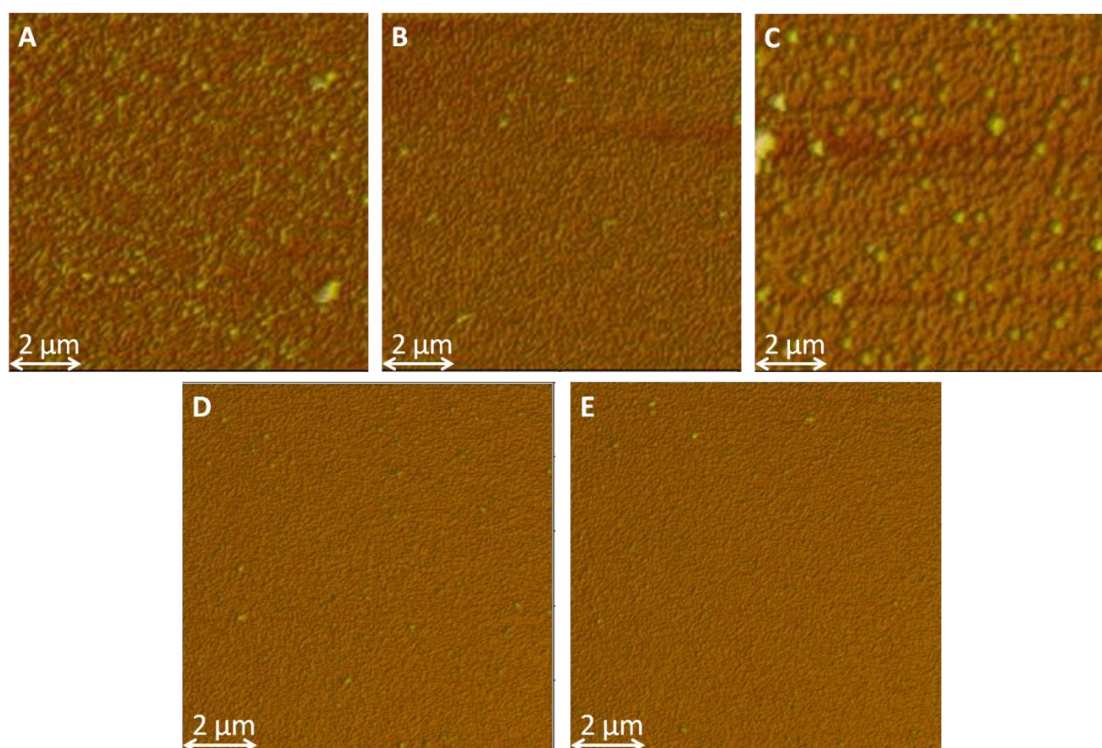
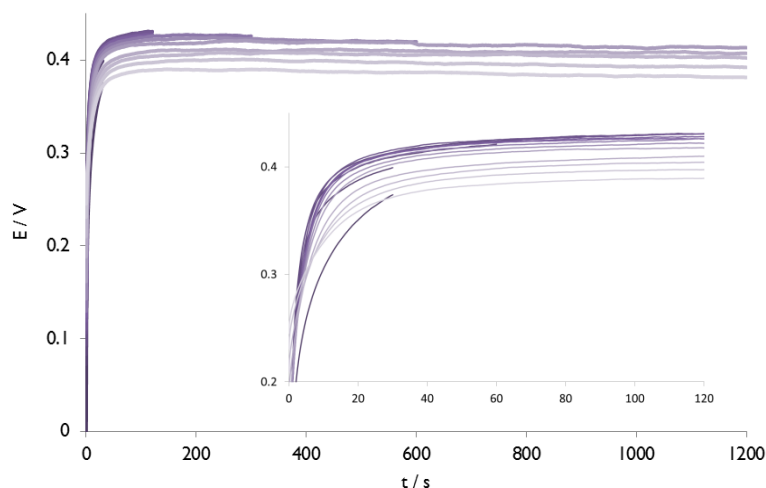


Figure 5.19 – AFM images of the surface of each film produced during the in situ deposition experiments; image labels refer to Table 5.8

### 5.3.2 Investigation of variables in galvanostatic deposition protocol

All the growth transients of these samples presented similar features. Figure 5.20 shows the transients recorded for sample 1, deposited with a 15 interval protocol. The inset shows the shorter intervals in the earlier stages of growth. In all cases, the shorter intervals did not allow the transient to reach the maximum potential. Once the interval is sufficiently long for the maximum to be reached, the current is observed to plateau, before gradually falling to a lower potential. Table 5.9 shows the details of the growth protocol of each sample along with the AFM measurements of film thickness.

A set of samples, '5' and '6', were repeated to evaluate the reproducibility of the films. These films were all grown to the same final charge density using identical growth steps and both monomer concentrations were tested. The only significant difference in the growth transients was with regards to the maximum potential ( $E_{\max}$ ) reached during growth which was 0.43 V except in the case of one sample which reached 0.493 V. During the growth of other samples in this study, the  $E_{\max}$  was found to vary in the range of 0.41 – 0.49 V therefore this discrepancy is thought to be due to shifting of the pseudo-reference electrode.



*Figure 5.20 – Transients recorded during the growth of sample 1 showing a 15 interval growth protocol with a current density of  $2 \mu\text{A cm}^{-2}$ ; inset shows a magnification of the transients during earlier stages of growth*

Sample	Monomer concentration / M	Intervals	Current density / $\mu\text{A cm}^{-2}$	Max $E_g$ / V	$Q_g$ / $\text{mC cm}^{-2}$	Thickness from $Q_g$ / nm	AFM thickness / nm
1	0.112	15	2	0.43	15.24	31.47	$30 \pm 5$
2	0.065	15	2	0.446	15.24	31.47	$30 \pm 5$
3	0.112	7	2	0.413	10.2	21.07	$23 \pm 5$
4	0.065	7	2	0.467	10.2	21.07	$23 \pm 5$
5	0.112	7	2.4	0.43	12.24	25.28	$30 \pm 3$
6	0.065	7	2.4	0.493	12.24	25.28	$30 \pm 3$
7	0.112	7	2.4	0.43	12.24	25.28	$27 \pm 3$
8	0.065	7	2.4	0.43	12.24	25.28	$27 \pm 3$
9	0.112	9	2	0.457	15	30.98	$36 \pm 3$
10	0.065	9	2	0.446	15	30.98	$33 \pm 3$

Table 5.9 – Summary of the growth protocol and characteristics of each sample, including a comparison of the AFM measurement of film thickness with the estimated thickness calculated from the growth charge

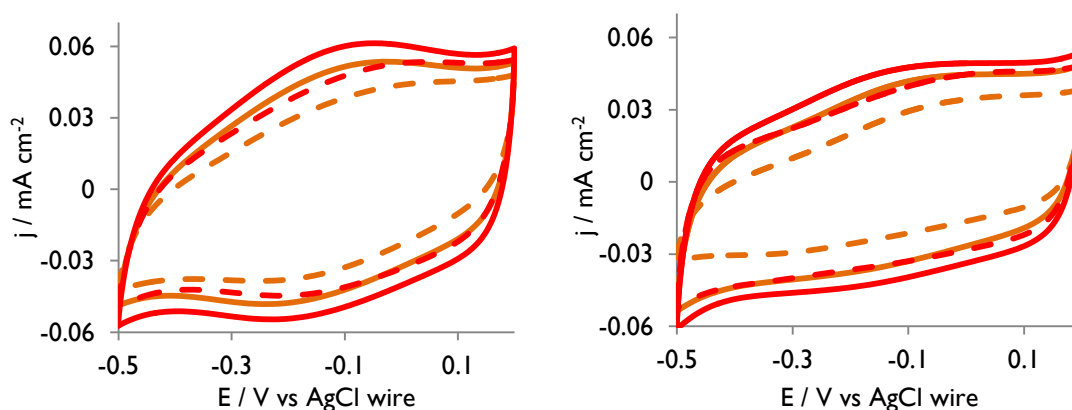


Figure 5.21 – Cyclic voltammograms of the PPy films grown from 0.112 M (full lines) and 0.065 M (dashed lines) monomer solutions to a charge density of  $12.24 \text{ mC cm}^{-2}$ ; the left panel shows results from cycling at  $100 \text{ mV s}^{-1}$  immediately after growth and the right panel shows cycling at the same scan rate following further cycling at slower scan rates

The reproducibility tests indicated that films deposited from the higher concentration exhibited a greater electroactivity with a more distinct oxidative peak, as shown in

Figure 5.21. This peak becomes less substantial and to some extent disappears after prolonged cycling. Furthermore, between 10 and 25 % of the oxidative charge is lost between the initial and repeated cyclic voltammograms at  $100 \text{ mV s}^{-1}$ , following cycling at  $50 \text{ mV s}^{-1}$  and  $20 \text{ mV s}^{-1}$ , so after a total of 80 cycles.

The full details of the cyclic voltammetry characterisation of the samples are presented in Table 5.10. The samples produced from the lower monomer concentration consistently present no distinctive oxidation peak. In the case of the samples produced from the higher monomer concentration, the oxidation peak is broad and tends to disappear over the course of extended cycling. The peak potential for these samples is seen to shift slightly between 0 and  $-0.1 \text{ V}$ , however it is important to note that increasing breadth of the peak as it becomes less distinct makes it difficult to identify the maximum. Consequently, this feature was not considered reliable in the characterisation of these samples.

Sample	$Q_g / \text{mC cm}^{-2}$	$100 \text{ mV s}^{-1}$		$50 \text{ mV s}^{-1}$		$20 \text{ mV s}^{-1}$		100 $\text{mV s}^{-1}$ repeated	
		$E_p^{\text{ox}} / \text{V}$	$Q_{\text{ox}} / \text{mC cm}^{-2}$	$E_p^{\text{ox}} / \text{V}$	$Q_{\text{ox}} / \text{mC cm}^{-2}$	$E_p^{\text{ox}} / \text{V}$	$Q_{\text{ox}} / \text{mC cm}^{-2}$	$E_p^{\text{ox}} / \text{V}$	$Q_{\text{ox}} / \text{mC cm}^{-2}$
1	15.24	0.01	0.29	-0.06	0.30	-0.11	0.30	0.01	0.25
2	15.24		0.16		0.19	0.00	0.21		0.15
3	10.2	-0.03	0.20	-0.06	0.19	-0.10	0.19	-0.03	0.15
4	10.2		0.16		0.18		0.19		0.14
5	12.24	-0.03	0.26	-0.06	0.27	-0.09	0.27		0.22
6	12.24		0.20		0.20		0.21		0.15
7	12.24	-0.05	0.30	-0.09	0.31	-0.11	0.30		0.26
8	12.24		0.25		0.26		0.26		0.22
9	15	-0.01	0.35	-0.06	0.36	-0.11	0.36		0.30
10	15		0.25		0.30		0.32		0.24

Table 5.10 – Results of the electrochemical characterisation of the galvanostatically grown PPy films; the values are taken from the final (20<sup>th</sup>) cycle at each scan rate

## 5.4 Discussion

### 5.4.1 *In situ* electrochemical growth and NR study

NR measurements of the growth of dPPy revealed that the electrochemical control function used to grow the films results in different growth stages that are evidenced by the changes in solvation level of the film at different points in the deposition process. The growth protocols were tested using the same monomer and electrolyte concentrations and the same working electrode surface area.

The potentiodynamic growth resulted in a film that was evenly solvated at every stage as shown in Figure 5.1. The SLD profile of the film following the first growth step indicates that the film has an SLD of  $4.75 \times 10^{-6} \text{ \AA}^{-2}$  which suggests a solvent volume fraction of  $\Phi_s \sim 0.29$ . Each of the subsequent growth steps produced a further layer of polymer with the same SLD and therefore the same level of solvation. Although this growth mechanism produced a consistently solvated film at each deposition interval, the cycling of the film requires each new 'layer' to be oxidised prior to the continued growth such that the polymerisation efficiency drops as the reaction progresses. This is seen in the mass per area plot in Figure 5.3 as well as in the SLD profile of Figure 5.1 where the thickness difference between growth intervals decreases slightly for the final two growth steps.

On the other hand, the potentiostatic growth yields a more solvated film in the first stages of growth but quickly reaches a homogeneous level of solvation as the deposition progresses as illustrated in Figure 5.4. In this case the film reaches a 'bulk' solvation state after the fifteenth deposition step and a total charge density of  $3.6 \text{ mC cm}^{-2}$ . The solvent volume fraction was  $\Phi_s \sim 0.28$  in the bulk, increasing slightly to  $\Phi_s \sim 0.31$  at the polymer/solution interface in the final growth stage. This method produced the highest average polymerisation efficiency, around 90 %, as shown in Figure 5.6. The polynomial fit indicates a polymerisation efficiency greater than 100 % that decreases by 2 % as a function of  $Q$ . Since the stop/start protocol results in the film returning to the neutral state between each deposition step, the applied potential also oxidises the existing film when the growth resumes. In a continuous deposition methodology, the film would be oxidised continuously throughout the reaction, therefore it is possible

that potentiostatic deposition could be 100 % efficient under these experimental conditions.

The galvanostatic growth, from the same monomer concentration, displayed a similar growth to the potentiostatic method, with the SLD profiles showing a more solvated film in the early stages of growth. Figure 5.10 shows the progression to a more homogeneous film was more gradual in this case, only reaching a 'bulk' solvent content at the fourth growth step after a charge density of  $5.08 \text{ mC cm}^{-2}$ . The overall SLD of the film was higher than both the potentiodynamic and potentiostatically grown films, suggesting that the galvanostatic growth results in a more compact film since it displays a slightly lower solvent volume fraction of between  $\Phi_s \sim 0.23 - 0.26$ .

All these films resulted in a homogeneously solvated bulk with the potentiodynamic and potentiostatically grown films presenting a more solvated outer layer. As the bulk region is 'filled in' during the growth, the outer region is more diffuse with the end of the polymer chains more loosely packed at the solution interface. This is not apparent in the galvanostatic data; however, the quality of the fits in this case is not quite as good since the modelled reflectivity does not closely fit to the fringe minima. The latter are in fact quite dampened which would suggest a greater roughness.

The film grown galvanostatically from a solution containing approximately half the monomer concentration ( $0.065 \text{ M}$ ) displayed a significantly more solvated film throughout the growth as illustrated in Figure 5.7, with a solvent volume fraction around  $\Phi_s \sim 0.5$ . AFM measurements indicated that the film was almost 50% thicker than the dry thickness estimated from the growth charge density. In the case of the other films produced using the galvanostatic method, the coulometric estimate was usually 70-80% of the thickness measured by AFM. This suggests that this growth protocol resulted in a significantly more porous structure than the other films. The concentration was not, however, the only difference. The current steps were initially applied in much shorter intervals and the current density differed by  $0.4 \mu\text{A cm}^{-2}$ . The effect of this difference in growth protocol was therefore explored in a series of small scale experiments.

In general, the results of the mass per area analysis revealed that the average polymerisation efficiency for the deposition of the dPPy films was 70 - 90 % according

to the linear fit. It would seem that the efficiency decreases as the growth of the film progresses. The polynomial fits to the data indicate initial polymerisation efficiency, greater than 100 % that decreases by 1.6 – 6.2 % depending on the deposition method. This is thought to be due to charge being lost to the oxidation of the existing polymer film and to side-reactions such as the formation of short oligomers. In 1997, the review of polypyrrole by Vernitskaya and Efimov, they state that electrochemical polymerisation has the advantage of producing a yield close to 100 % in terms of applied charge<sup>5</sup>. It may be that the stop/start mechanism employed in this study was in part responsible for this lower efficiency. Since all the films were nevertheless produced in this layer-by-layer fashion, they can be compared relative to one another. Under these conditions therefore, the potentiostatic growth protocol would seem to be the most efficient method with the highest average polymerisation efficiency. The potentiostatic also presents high initial polymerisation efficiency with a low rate of decay at 2 %. The potentiodynamic deposition displays a lower loss of polymerisation efficiency but also presents a lower initial rate which results in a lower average.

The choice of an aqueous solution for the deposition process may also affect the polymerisation efficiency. Polypyrrole is often polymerised in organic solvents such as acetonitrile and it has been suggested that, while a small amount of water is necessary to enable proton elimination, the radical intermediates of the polymerisation reaction may be subject to nucleophilic attack in aqueous media<sup>6,7</sup>. Ko et al reported that polypyrrole films prepared in non-aqueous solutions presented a higher conductivity but that those deposited from aqueous media were more porous and displayed greater capacitance<sup>8</sup>.

Overall, the results from the films grown from 0.112 M monomer solutions indicate that the electrochemical control function results in a different internal structure such that, in order of decreasing density and thus increasing porosity the methods can be organised as follows: galvanostatic < potentiostatic < potentiodynamic. If we consider that an increased porosity would result in a more diffuse surface that would translate visually as a roughness then the AFM images of these films, presented in Figure 5.19, certainly seem to confirm these findings. The potentiodynamically grown film shows more clusters of material on the surface, whereas the film produced using the potentiostatic method appears to have only a few imperfections. Finally, the films

grown galvanostatically are noticeably smoother, with the exception of the film produced with the different growth protocol Figure 5.19(C). The latter does not fit with the trend in density in relation to the other methods, however, the NR results indicated a significantly greater solvation and therefore porosity and, again, this is apparent in the more globular surface structure visible in the AFM image.

Following deposition, the films are transferred to fresh electrolyte and cycled prior to being measured in the redox states. This means that any oligomers trapped within the polymer matrix could become free during cycling, allowing solvent to more fully permeate the film. The NR measurements of the films in the oxidised and reduced states revealed increased solvation following cycling which can be seen in the SLD profiles in Figure 5.16. Interestingly, there was little or no difference between the solvent content brought about by the change in redox state, both presented a similar degree of solvation. This contrasts with the work done by Cascales et al who stated that oxidation would result in greater intake of solvent and thus swelling of the film, whereas in the reduced state the polymer chain interactions dominate, caused by the hydrophobicity that expulses the electrolyte solution<sup>9</sup>. However, an earlier review of the electropolymerisation of polypyrrole noted that the size of the cation in solution had been shown to have an effect on the conductivity of the films produced<sup>7</sup>, thus suggesting that the reduction process involves the movement of cations into the film accompanied by an ingress of solvent.

Although the cyclic voltammograms of the films following the NR measurements showed a decreasing oxidation charge with increasing charge and discharge cycles, the SLD profiles do not suggest that any loss of material occurred as the films present a thickness in keeping with the deposited mass per area. This could therefore indicate a loss of electroactivity following repetitive cycling.

The different electrochemical control functions did not appear to produce significantly different films in terms of their electroactivity. All the samples presented an oxidation to growth coverage ratio ( $\Gamma_{ox} / \Gamma_g$ ) of  $30 \pm 3$  %. The galvanostatically grown film was slightly less electroactive than those grown under potentiostatic or potentiodynamic control. This contrasts with the findings by Li et al in which their deposition of PPy on glassy carbon electrodes resulted in galvanostatic deposition producing the most electroactive films<sup>10</sup>. Their results revealed that potentiostatic deposition produced the

least electroactive films; however, the use of the stop/start methodology has also been shown to affect the electroactivity of PPy. In a study published in 2012, the pulsed galvanostatic deposition was found to produce films with greater redox capacity than those produced by continuous growth<sup>11</sup>. More recently, a layer-by-layer approach, in which the films were rinsed between deposition steps, also produced films with greater electroactivity and conductivity<sup>12</sup>.

#### 5.4.2 Investigation of variables in galvanostatic deposition protocol

In the experiments used to investigate the galvanostatic growth of PPy, AFM measurements of film thickness indicated that there may be a slight difference of approximately 3 nm between the nominally identical films. Nevertheless the films were all between 27 and 30 nm thick  $\pm$  10%. This is slightly higher than the calculated value of thickness from the growth charge which indicated a thickness of 25 nm, assuming a doping level of  $x = 0.33$ . This could either be due to trapped solvent and electrolyte adding to the bulk of the film or because the density of the film does not match the value used in the calculation of thickness from the oxidative charge. The films had been thoroughly rinsed with deionised water before being exposed to ambient temperatures and dried for several days. Therefore it is assumed that the solvent (water) had sufficient time to evaporate and that the electrolyte would not be present in sufficient quantities to affect the thickness by 5 nm and the value of the density is examined. The value used in the calculations is the density of the monomer solution,  $1.4 \text{ g cm}^{-3}$ . To give a thickness between 27 and 30 nm, the density would have to be between  $1.3$  and  $1.15 \text{ g cm}^{-3}$ , whereas the literature indicates that PPy has a density of between  $1.47 - 1.52 \text{ g cm}^{-3}$ <sup>5,9</sup>. The difference in thickness is therefore likely to be the result of increased porosity. As seen in the case of the films prepared in the NR study, the greater thickness measured by AFM could in fact indicate that the films do not entirely collapse upon drying.

Finally, the differences between the films made using the same monomer concentration and deposition protocol could also be attributed to slight variations in the electrode area. The electrodes were gold coated microscope slides with a titanium binding layer. The area was delimited with Teflon insulating tape to give an exposed area of  $1 \text{ cm}^2$ . This was however determined by eye and, although care was taken to ensure that the tape was securely adhered to the electrode surface, it is possible that electrolyte

penetrated beneath the tape and polymerisation occurred outside the delimited area. A more controlled electrode area would be needed to repeat these experiments to ascertain the reproducibility more accurately. Nevertheless, for the purposes of these experiments, the reproducibility seems sufficient and allows a comparison to be drawn with the other deposition protocols explored here.

As mentioned above, the effect of the monomer concentration appears to be that the higher concentration produces films that are more electroactive than films produced from a lower monomer concentration solution with the same growth protocol. This is seen in the shape of the cyclic voltammograms, such as in Figure 5.21, where more distinct oxidation and reduction peaks are observed. It is noted, however, that following further cycling the amplitude of the peaks diminishes and in some cases these features disappear entirely.

The AFM measurements revealed that, for a given growth protocol, there was little or no difference between the thicknesses of films grown from different monomer concentrations. The concentration of the monomer in solution should only become an issue if there is a significant depletion of the monomer available to polymerize at the working electrode/solution interface. This result therefore confirms that even the lower concentration contained a sufficient quantity of monomer to preserve a consistent concentration gradient at the electrode throughout the deposition process.

In order to evaluate the effect of the growth steps samples were prepared with the same monomer concentration and the same current density but with different growth intervals designed to reach the same overall  $Q_g$ . Once again, films produced from the more concentrated monomer solution exhibited greater electroactivity. Interestingly, while the films made with the 9 interval growth protocol technically have a very slightly lower deposition charge ( $15 \text{ mC cm}^{-2}$  versus  $15.24 \text{ mC cm}^{-2}$  in the 15 interval protocol), the AFM results indicated that the films were thicker than those made using the 15 interval growth protocol. The cyclic voltammograms support this in that the 9 interval samples display a greater redox charge than their 15 interval equivalents, suggesting more material available to undergo redox reactions.

The small scale tests reveal that there is no evidence of the thickness being affected by the monomer concentration of the deposition solution since there were no significant

differences in thickness between films made using the same deposition protocol and differing monomer solutions. The only noticeable effect was in the cyclic voltammograms, where the higher concentration of monomer seemed to result in films that were more electroactive and displayed a more distinct oxidation peak. This was *not* the case for the NR samples where in fact the opposite behaviour was observed. Only the film grown from the lower monomer concentration produced a cyclic voltammogram that showed distinctive redox peaks. In the literature, monomer concentration has been found to affect the degree of crystallinity<sup>13</sup> and the rate of polymerisation during potentiostatic deposition<sup>14</sup>, therefore further work should be done to explore this variable.

The small scale tests also suggested that a greater number of growth intervals results in slightly thinner film than the equivalent film made with less intervals. Theoretically this result could be explained through the loss of oligomers at the surface of the film during the pause between growth intervals. However, this does not support our findings during the NR experiment in which the 15 interval growth protocol resulted in a film that was almost twice as thick as the coulometric estimate.

It should be noted that the volume of the deposition solution relative to the size of the working electrode area was significantly greater in the case of these samples compared to those prepared in the NR investigation. While the experiments were designed to be scaled such as to replicate the conditions used in the case of the larger samples, it is nevertheless possible that monomer depletion at the electrode interface may have caused the differences observed in the NR samples produced using the galvanostatic growth protocol.

## 5.5 Conclusions

This study has shown structural differences occurring within the polymer film during the deposition process according to the choice of growth protocol. These differences were mostly observed in the degree of solvation at the different stages of film growth.

In the case of growth controlled by the potential at the electrode, the films presented a similar solvation profile but differed in the subsequent electrochemical characterisation and in the film behaviour following extended cycling. Potentiostatic deposition was found to result in greater average polymerisation efficiency than the potentiodynamic method.

Controlling the current (and thus the rate of the reaction) produced a film that presented a more compact structure, evidenced by a lesser degree of solvation, as well as being slightly less electroactive.

The role of monomer concentration, current density and growth intervals was explored in the case of galvanostatic deposition. The results indicate that the higher monomer concentration results in a more electroactive film, however the redox charge is found to decrease over the course of cycling for all films.

These results are only a starting point with regards to understanding how the growth protocol affects the electrochemical polymerisation and deposition of thin films. Further work is required to investigate the other variables in the deposition process such as monomer concentration, species of supporting electrolyte and choice of potential or current limits. Nevertheless, gaining insight into the solvation profile of these films during and after the deposition process is a promising step towards understanding how the internal structure is related to stability and electrochemical behaviour.

## 5.6 References

1. Otero, T. F. & De Larreta, E. Electrochemical control of the morphology, adherence, appearance and growth of polypyrrole films. *Synth. Met.* **26**, 79–88 (1988).
2. Zhou, M. & Heinze, J. Electropolymerization of pyrrole and electrochemical study of polypyrrole: I . Evidence for structural diversity of polypyrrole. *Electrochim. Acta* **44**, 1733–1748 (1999).
3. Shimoda, S. & Smela, E. The effect of pH on polymerization and volume change in PPy(DBS). *Electrochim. Acta* **44**, 219–238 (1998).
4. Villarreal, I., Morales, E., Otero, T. F. & Acosta, J. L. Electropolymerization kinetics of pyrrole in aqueous solution on graphite felt electrodes. *Synth. Met.* **123**, 487–492 (2001).
5. Vernitskaya, T. V & Efimov, O. N. Polypyrrole: a conducting polymer; its synthesis, properties and applications. *Russ. Chem. Rev.* **66**, 443 – 457 (1997).
6. Heinze, J., Frontana-Urbe, B. A. & Ludwigs, S. Electrochemistry of conducting polymers - persistent models and new concepts. *Chem. Rev.* **110**, 4724–71 (2010).
7. Sadki, S., Schottland, P., Brodie, N. & Sabouraud, G. The mechanisms of pyrrole electropolymerization. *Chem. Soc. Rev.* **29**, 283–293 (2000).
8. Ko, J. M., Rhee, H. W., Park, S.-M. & Kim, C. Y. Morphology and electrochemical properties of polypyrrole films prepared in aqueous and nonaqueous solvents. *J. Electrochem. Soc.* **137**, 905–909 (1990).
9. López Cascales, J. J., Fernández, A. J. & Otero, T. F. Characterization of the reduced and oxidized polypyrrole/water interface: a molecular dynamics simulation study. *J. Phys. Chem. B* **107**, 9339–9343 (2003).
10. Li, C. M., Sun, C. Q., Chen, W. & Pan, L. Electrochemical thin film deposition of polypyrrole on different substrates. *Surf. Coatings Technol.* **198**, 474–477 (2005).
11. Li, X. & Zhitomirsky, I. Capacitive behaviour of polypyrrole films prepared on stainless steel substrates by electropolymerization. *Mater. Lett.* **76**, 15–17 (2012).
12. Sangian, D., Zheng, W. & Spinks, G. M. Optimization of the sequential polymerization synthesis method for polypyrrole films. *Synth. Met.* **189**, 53–56 (2014).
13. Thombare, J. V., Rath, M. C., Han, S. H. & Fulari, V. J. The influence of monomer concentration on the optical properties of electrochemically synthesized polypyrrole thin films. *J. Semicond.* **34**, 1674–4926 (2013).

14. Demoustier-Champagne, S., Ferain, E., Jérôme, C., Jérôme, R. & Legras, R. Electrochemically synthesized polypyrrole nanotubules: effects of different experimental conditions. *Eur. Polym. J.* **34**, 1767–1774 (1998).

## **Chapter 6 – Electrodeposition of poly(3,4-ethylenedioxythiophene) films**

### **6.1 Introduction**

In a further investigation of the effect of deposition protocol on the structure of polymer films, this study will examine the effect of the electrochemical control function on the structural and electrochemical properties of poly(3,4-ethylenedioxythiophene) (PEDOT) films. Cyclic voltammetry is used to characterise the films and allow a comparison of their electroactivity according to the growth protocol employed. AFM is used to obtain further measurements of film thickness and to explore differences in surface morphology related to the deposition method. Neutron reflectometry is used to monitor the changes in the internal structure of the films as the growth progresses and to evaluate how the films respond to charge/discharge processes. Specifically, the spatial distribution of solvent within the films at different stages of growth is examined.

The results show that reducing the rate of deposition increases electroactivity and produces smoother films. Potentiodynamic growth produces a consistent structure throughout deposition that is resilient to charge/discharge processes. Potentiostatic and galvanostatic growth protocols produce a more flexible structure in which the solvent volume fraction changes and the films collapse when dried. Overall, the films present similar electroactivity despite the different deposition methods.

## 6.2 Experimental

### 6.2.1 Small scale preliminary deposition experiments

All chemicals were used as received from Sigma Aldrich. Aqueous deposition solutions were prepared containing 0.003 M 3,4-ethylenedioxythiophene (EDOT) in either 0.3 M LiClO<sub>4</sub> or 0.3 M H<sub>2</sub>SO<sub>4</sub>. The deposition conditions and protocol for each sample are listed in

Table 6.1. The films were characterised in 0.3 M LiClO<sub>4</sub> or 0.3 M H<sub>2</sub>SO<sub>4</sub> according to the solution in which they were grown.

0.003 M EDOT 0.3 M LiClO <sub>4</sub>				
Potentiodynamic	Area / cm <sup>2</sup>	E / V vs Ag/AgCl	rate / mVs <sup>-1</sup>	cycles
PD01	1.54	[-0.1 - 1.3]	50	5
PD02	1.5	[-1 - 1.3]	100	10
Potentiostatic	Area / cm <sup>2</sup>	E / V vs Ag/AgCl	time / s	
PS01	1.8	0.85	60	
PS02	1.68	0.8	60	
Galvanostatic	Area / cm <sup>2</sup>	I / mA	time / s	
GS01	1.26	0.6	60	
GS02	1.16	0.2	60	
0.003 M EDOT 0.3 M H <sub>2</sub> SO <sub>4</sub>				
Potentiodynamic	Area / cm <sup>2</sup>	E / V vs	rate / mVs <sup>-1</sup>	cycles
SPD01	1.65	[-1 - 1.3]	100	3
		[-0.7 - 1.3]	100	13
Potentiostatic	Area / cm <sup>2</sup>	E / V vs	time / s	
SPS01	1.45	0.8	60	
Galvanostatic	Area / cm <sup>2</sup>	I / mA	time / s	
SGS01	1.49	0.2	60	

Table 6.1 – Summary of deposition conditions for electrochemically prepared PEDOT films

The working electrodes from Platypus Technologies were gold coated aluminosilicate glass slides with a titanium underlayer. The exposed surface area was delimited using

Teflon tape. The reference and counter electrodes were a silver chloride coated silver wire and platinum coated titanium mesh respectively.

### 6.2.2 Scale up deposition experiments

These films were deposited from 0.003 M EDOT in 0.3 M LiClO<sub>4</sub> and the substrates were gold coated glass blocks. Samples were prepared in the NR/EC cell B, details of which are outlined in Chapter 2. The reference and counter electrodes were, therefore, a platinum coated titanium grid and a silver wire, respectively, and the exposed working electrode area was 24.8 cm<sup>2</sup>. The full details of the deposition protocol for each sample are summarised in Table 6.2. Following deposition the films were characterised in aqueous 0.3 M LiClO<sub>4</sub>.

Potentiodynamic		Area / cm <sup>2</sup>	E / V vs Ag/AgCl	rate / mV s <sup>-1</sup>	cycles
	PDG01	24.8	[-1 - 1.3]	100	20
	PDG02	24.8	[-0.7 - 0.7]	100	20
Potentiostatic		Area / cm <sup>2</sup>	E / V vs Ag/AgCl	time / s	
	PSG01	24.8	0.65	300	
	PSG02	24.8	0.6	300	
Galvanostatic		Area / cm <sup>2</sup>	I / mA	time / s	
	GSG01	24.8	0.6	300	

Table 6.2 – Summary of deposition conditions for electrochemically prepared PEDOT films on glass substrates

### 6.2.3 In situ electrochemical growth and NR

Deposition solutions were 0.003 M EDOT in 0.3 M LiClO<sub>4</sub> in D<sub>2</sub>O. The working electrodes were gold coated quartz blocks. Deposition was carried out in the NR/EC cell B, described in Chapter 2, section 2.2.2. NR measurements of the gold surface in the deposition solution were carried out prior to starting the deposition process. Following deposition the cells were emptied and rinsed before being refilled with the monomer-free electrolyte solution, 0.3 M LiClO<sub>4</sub> in D<sub>2</sub>O. Each film was cycled in monomer free electrolyte after deposition then held reduced (-0.5 V) and oxidised

(0.4 V). NR measurements were carried out on FIGARO with a low angle of  $0.7^\circ$  and a high angle of  $3.5^\circ$  to give a  $Q$  range of  $0.008 - 0.35 \text{ \AA}^{-1}$ .

Table 6.3 summarises the conditions and details of each of the samples prepared during *in situ* NR measurements. For potentiostatic and galvanostatic growth,  $t_{\text{total}}$  indicates the total deposition time, the growth intervals between NR measurements varied and are presented in section 6.3. The final films were intended to be of similar thickness, which was achieved by continuous monitoring and fitting of the reflectivity measurements.

Electrochemical control function	Deposition conditions
Potentiodynamic	$E : [-0.7 \text{ V} - E_{\text{max}}] \text{ vs Ag wire}$ $v = 150 \text{ mV s}^{-1}$ $i_{\text{max}} = 0.24 \text{ mA cm}^{-2}$ 81 cycles
Potentiostatic	$E = 0.55 \text{ V vs Ag wire}$ $t_{\text{total}} = 18 \text{ min}$
Galvanostatic	$i = 24 \text{ \mu A cm}^{-2}$ $t_{\text{total}} = 12 \text{ min}$

Table 6.3 – Summary of growth protocols for the *in situ* deposition of PEDOT films

Analysis of the NR data, such as the calculation of solvent content from fitted SLD values, was carried out assuming a PEDOT SLD of  $2.25 \times 10^{-6} \text{ \AA}^{-2}$  and  $\rho = 1.33 \text{ g cm}^{-3}$ . The SLDs of  $\text{H}_2\text{O}$  and  $\text{D}_2\text{O}$  are  $-0.56 \times 10^{-6} \text{ \AA}^{-2}$  and  $6.3 \times 10^{-6} \text{ \AA}^{-2}$  respectively.

## 6.3 Results

### 6.3.1 Small scale preliminary deposition experiments

The electrochemical results and AFM measurements of thickness of the preliminary samples are presented in Table 6.4.

0.003 M EDOT 0.3 M LiClO <sub>4</sub>					
		$Q_g$ / mC cm <sup>-2</sup>	$\Gamma_{ox} / \Gamma_g$ / %	Thickness from $Q_g$ / nm	Thickness from AFM / nm
Potentiodynamic	PD01	60.3	5.97	283	35 ± 5
	PD02	93.6	10.96	439	55 ± 5
Potentiostatic	PS01	24.9	28.07	117	60 ± 5
	PS02	20.8	45.70	98	75 ± 10
Galvanostatic	GS01	28.6	25.66	134	65 ± 5
	GS02	10.3	56.18	48	50 ± 5
0.003 M EDOT 0.3 M H <sub>2</sub> SO <sub>4</sub>					
		$Q_g$ / mC cm <sup>-2</sup>	$\Gamma_{ox} / \Gamma_g$ / %	Thickness from $Q_g$ / nm	Thickness from AFM / nm
Potentiodynamic	SPD01	185.8	2.33	871	
Potentiostatic	SPS01	20.3	37.87	95	55 ± 5
Galvanostatic	SGS01	8	48.92	38	40 ± 5

*Table 6.4 – Summary of the electrochemical and AFM results of the characterisation of preliminary PEDOT samples*

The potentiodynamic deposition resulted in a very high growth charge density due to the wide potential range, high current and small electrode surface area. The thickness as measured by AFM was approximately 12% of the estimated thickness, however the surface images showed large fibrous structures as illustrated in Figure 6.1 A(1) and A(2). These fibres emerged from the bulk of the polymer films to heights exceeding 200 nm in the case of sample PD01, and in excess of 2 μm in the case of sample PD02.

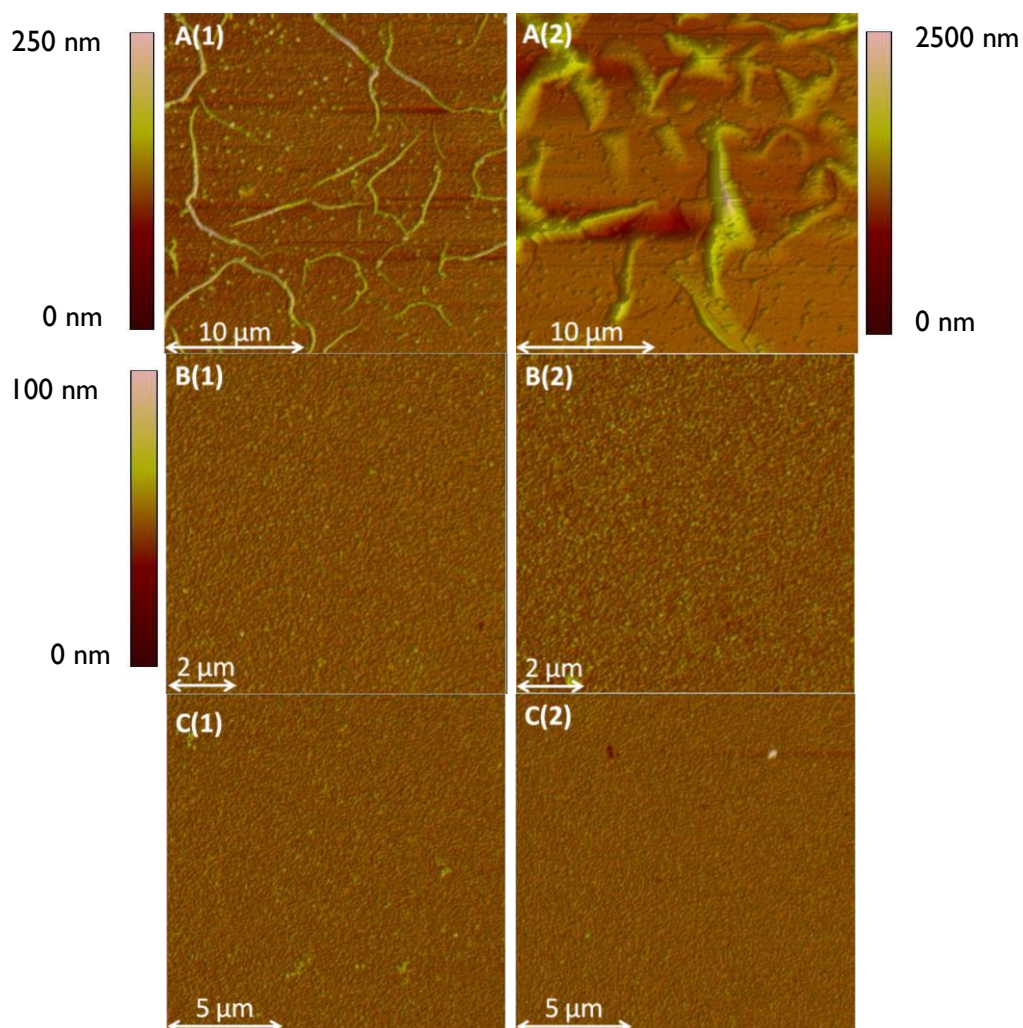


Figure 6.1 – AFM images of the polymer surface for PEDOT films grown under potentiodynamic (A), potentiostatic (B), and galvanostatic (C) conditions from 0.003 M EDOT in 0.3 M LiClO<sub>4</sub>; the images are numbered according to the samples listed in Table 6.4

The potentiodynamic deposition carried out in H<sub>2</sub>SO<sub>4</sub> did not result in the same fibrous structures but presented a very rough surface including large clusters of material as shown in Figure 6.2 A. The thickness of the film could not be measured by AFM due to this significant roughness. The oxidation to growth coverage ratio was particularly low suggesting that the polymerisation process was very inefficient. Given the large quantity of polymer in the form of clusters reaching heights of between 100 – 200 nm on the surface, this does not seem a likely explanation. The polymer did not appear to have formed a condensed film but rather isolated masses of material. This lack of connection between parts of the film could be responsible for the low redox capacity relative to the growth charge. The polymerisation in this case may also have

resulted in oligomers that never deposited but diffused into the solution during cycling to the reducing potential.

The potentiostatic deposition in  $\text{LiClO}_4$ , produced a much smoother film as shown in Figure 6.1 B(1) and B(2). Lowering the growth potential was found to produce a film with a significantly higher oxidation to growth coverage ratio. The AFM measurement of thickness was also found to be closer to the estimate calculated from the growth charge. The lower potential may therefore result in a more efficient use of charge during the polymerisation process. The potentiostatic growth in  $\text{H}_2\text{SO}_4$  once again produced a film with significantly greater surface roughness, visible in Figure 6.2 B.

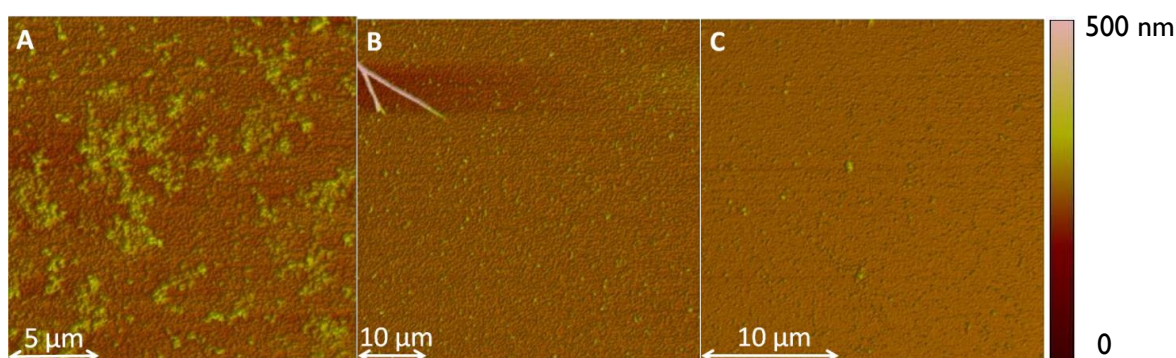


Figure 6.2 – AFM images of the polymer surface of PEDOT films grown potentiodynamically (A), potentiostatically (B) and galvanostatically (C) from 0.003 M EDOT in 0.3 M  $\text{H}_2\text{SO}_4$

The galvanostatic growth with the lower current density, produced a smooth film with an improved oxidation to growth coverage ratio and an AFM measurement of thickness in keeping with the estimated value calculated from the growth charge.

### 6.3.2 Scale up deposition experiments

The electrochemical results and AFM measurements of thickness for the samples deposited onto gold/glass substrates are presented in Table 6.5. The potentiodynamic growth revealed that a smoother film with a better oxidation to growth coverage ratio could be achieved by restricting both the cathodic and anodic potential limits of the cycles. The surface images are presented in Figure 6.3.

		$Q_g$ / mC cm <sup>-2</sup>	$\Gamma_{ox} / \Gamma_g$ / %	Thickness from $Q_g$ / nm	Thickness from AFM / nm
Potentiodynamic	PDG01	15.88	27.55	74	55 ± 5
	PDG02	8.35	38.33	39	20 ± 5
Potentiostatic	PSG01	17.9	32.02	84	50 ± 5
	PSG02	7.8	41.22	37	40 ± 5
Galvanostatic	GSG01	7.26	69.12	34	50 ± 5

Table 6.5 – Summary of the electrochemical and AFM results of the characterisation of the scaled up PEDOT samples on glass substrates

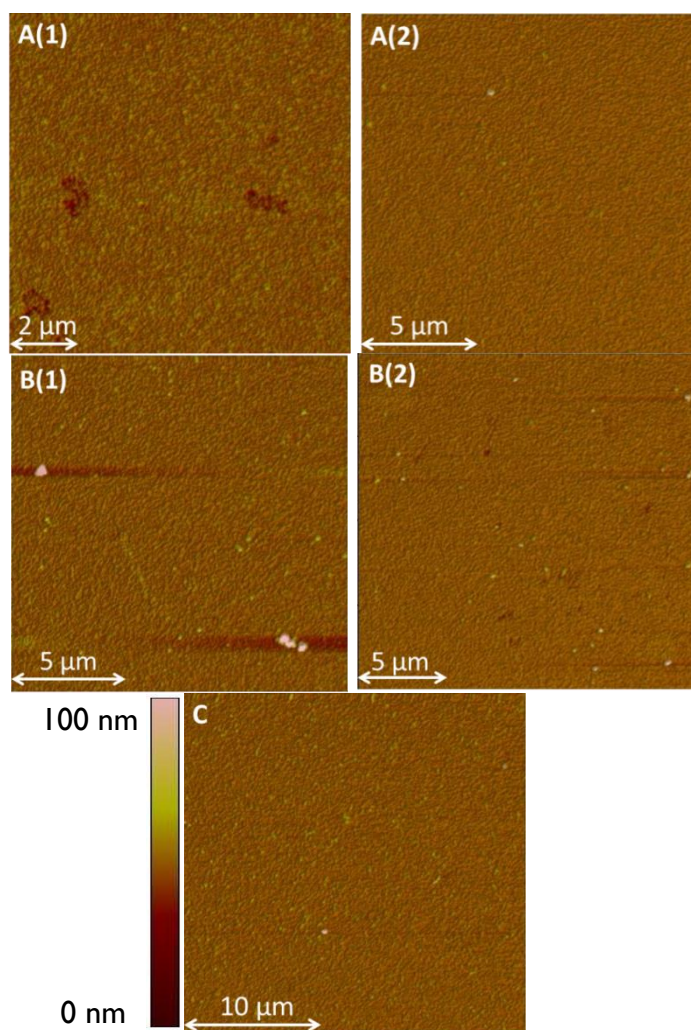


Figure 6.3 – AFM images of the polymer surface of the scaled up PEDOT samples on glass substrates

Similarly to the small scale samples presented in section 6.3.1, the potentiostatic growth at a slightly lower potential produced a smoother film with a greater electroactivity and a measured thickness closest to the estimated value from the coulometric data. The galvanostatic growth produced a film with a similar growth charge to the potentiostatic sample, PSG02. However it presented a significantly greater oxidation to growth coverage ratio and the AFM measurement of thickness was greater than the predicted value. This suggests possibly greater polymerisation efficiency as well as a more porous internal structure.

### 6.3.3 *In situ* electrochemical growth and NR

The NR measurements of the potentiodynamic growth of PEDOT reveal, at a first glance, a film deposition with regular growth intervals as shown in Figure 6.4.

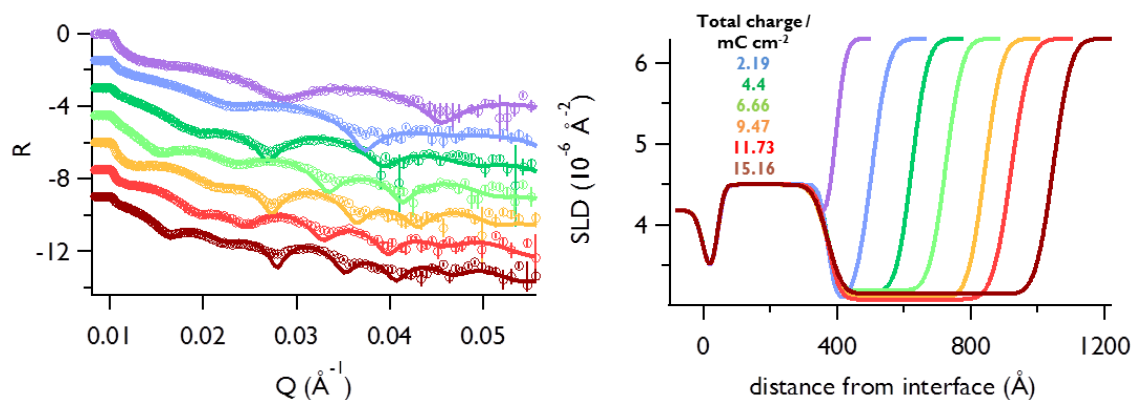


Figure 6.4 – NR measurements and fits (left) and corresponding SLD profiles (right) for the potentiodynamic growth of PEDOT in which the polymer is modelled as a single layer; the purple trace is the gold measurement prior to deposition.  $R(Q)$  datasets are offset by increments of  $-1.5$  for clarity. Experimental conditions:  $0.003\text{ M EDOT}$  in  $0.3\text{ M LiClO}_4$  in  $D_2O$ ,  $E : [-0.7\text{ V} - E_{max}]$  vs Ag wire,  $v = 150\text{ mVs}^{-1}$ ,  $i_{max} = 0.24\text{ mA cm}^{-2}$ , 81 cycles

Evaluation of the SLD of the polymer layer in these fits indicate a consistently solvated state with a solvent volume fraction of between  $\Phi_s \sim 0.2 - 0.23$ . The final three growth stages can, however, be fitted with a model that divides the polymer layer into two layers that can fit independently. The other stages of growth do not fit with such a model and converge to a single layer therefore it can be concluded that these early stages produce a homogeneously solvated film. On the other hand, the later stages of growth reveal a divide between the polymer layer at the gold/polymer interface and

the outer layer at the polymer/solution interface. The latter become progressively more solvated as the growth progresses while the former retains a slightly lower volume fraction of solvent. These models can be seen in Figure 6.5. The orange trace, after a growth charge density of  $9.47 \text{ mC cm}^{-2}$ , shows the film presenting a very low volume fraction of solvent of  $\Phi_s \sim 0.13$  throughout the bulk of the film with the polymer/solvent interface modelled using an additional layer and significant roughness parameter.

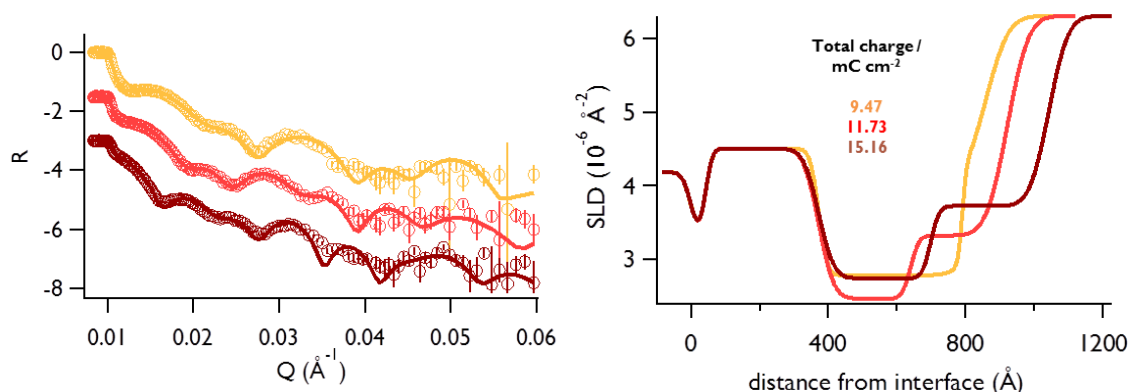


Figure 6.5 – NR measurements and fits (left) and corresponding SLD profiles (right) for the final stages ( $Q_g = 9.47$ ,  $11.73$  and  $15.16$ ) of the potentiodynamic growth of PEDOT in which the polymer is modelled as two distinct layers;  $R(Q)$  datasets are offset by increments of  $-1.5$  for clarity

The red trace shows the film, after further growth cycles, now presenting very distinct inner and outer layers with significantly different levels of solvation. The layer at the gold/polymer interface has an SLD indicating a solvent volume fraction of just  $\Phi_s \sim 0.05$ , whereas the outer layer has a volume fraction of  $\Phi_s \sim 0.26$ . Finally, the last growth stage has an inner and outer layer solvation of  $\Phi_s \sim 0.12$  and  $\Phi_s \sim 0.36$  respectively.

$Q_g / \text{mC cm}^{-2}$		9.47	11.73	15.16
$\chi^2$	Single layer fit	7.4	4.7	15.1
	Two layer fit	5.92	2	8.4

Table 6.6 – Comparison of  $\chi^2$  values for single and multi-layered fits to the last three potentiodynamic deposition steps

The  $\chi^2$  values for the different fits are presented in Table 6.6. Although the multi-layered models do improve these values, the way in which the fits follow the features of the reflectivity data is not necessarily improved. The differences between the types of model used are predominantly at the higher end of the Q range where the reflectivity data presents the largest error bars. The improvement in  $\chi^2$  values may therefore be an artefact of the manner in which they are calculated.

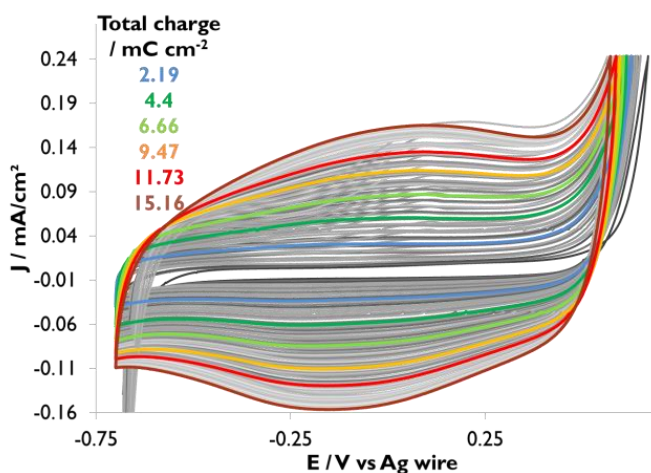


Figure 6.6 – Cyclic voltammograms recorded during the potentiodynamic growth of PEDOT. Experimental conditions: 0.003 M EDOT in 0.3 M LiClO<sub>4</sub> in D<sub>2</sub>O, E : [-0.7 V – E<sub>max</sub>] vs Ag wire,  $v = 150 \text{ mVs}^{-1}$ ,  $i_{\text{max}} = 0.24 \text{ mA cm}^{-2}$ , 81 cycles

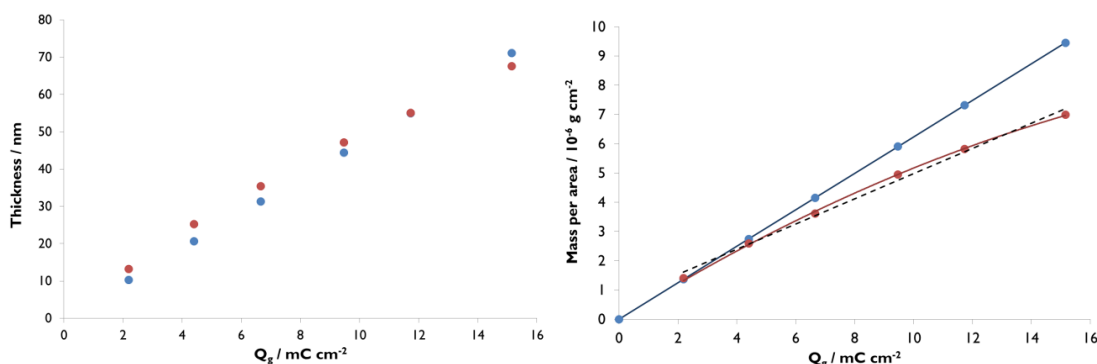


Figure 6.7 – Plots of film thickness (left) and mass per area (right) as a function of growth charge density as calculated from the electrochemical data (blue) and from the single layer fits to the NR data (red) from the potentiodynamic growth of PEDOT; the coloured traces are the associated fits to the data, the black dotted trace is the linear fit to the NR data

The plot of thickness as a function of growth charge presented in Figure 6.6 reveals the difference between the coulometric estimate and the measured thickness from the single layer fits, highlighting the additional volume of solvent. The data for the early stages of growth confirms the consistent level of solvation observed in the SLD profiles. In the later stages, however, the solvated thickness measured by NR becomes less than the predicted thickness for the dry film. Since the SLD profiles clearly indicate that the film is still solvated at this stage, this would suggest that the polymerisation efficiency drops as the growth progresses.

This is more clearly seen in the mass per area plot where the gradient of the single layer fit results falls beneath the values calculated from the growth charge density, indicating a slower rate of deposition than that predicted by the electrochemical data. Since this could be due to the constraint of modelling the polymer as a single layer, the results of the multi-layer fits are examined. These were expected to provide a greater level of detail by allowing greater flexibility in the model parameters. The results, however, indicate lower mass per area values than those provided by the single layer fits. This would therefore suggest that the measured growth rate diverges further from that predicted by the growth charge.

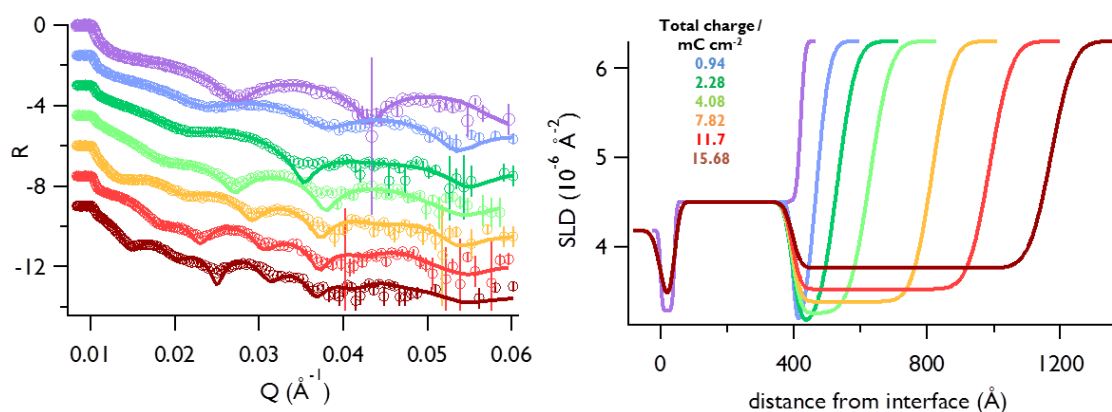


Figure 6.8 – NR measurements and fits (left) and corresponding SLD profiles (right) for the potentiostatic growth of PEDOT; the purple trace is the gold measurement prior to deposition.  $R(Q)$  datasets are offset by increments of -1.5 for clarity. Experimental conditions: 0.003 M EDOT in 0.3 M  $\text{LiClO}_4$  in  $\text{D}_2\text{O}$ ,  $E = 0.55 \text{ V}$  vs Ag wire,  $t_{\text{total}} = 18 \text{ min}$

The potentiostatic growth of PEDOT presented a slightly different growth pattern with regards to solvation throughout the growth stages. As shown in Figure 6.8, the early deposition intervals present a polymer layer with a low SLD which gradually

increases with each deposition step. In terms of solvation, this translates to an initial solvated state of approximately  $\Phi_s \sim 0.2$  which progresses to  $\Phi_s \sim 0.3$  and eventually  $\Phi_s \sim 0.37$  in the final growth stage.

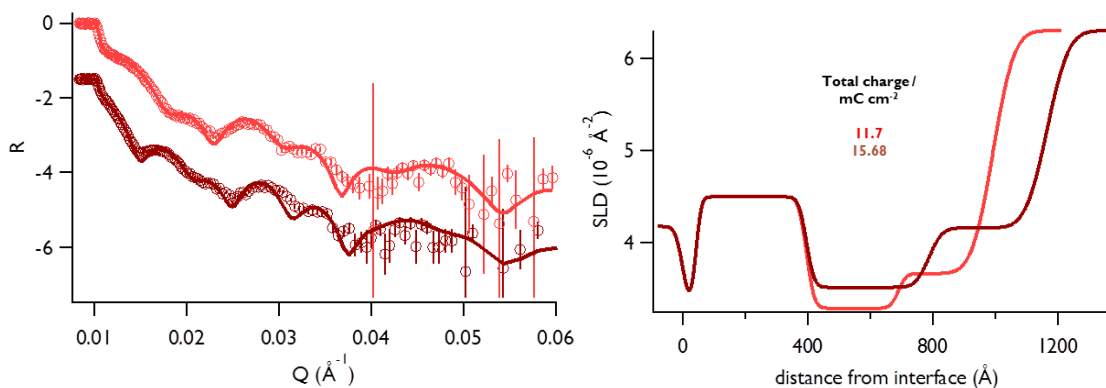


Figure 6.9 – NR measurements and fits (left) and corresponding SLD profiles (right) for the final stages ( $Q_g = 11.7$  and  $15.68$ ) of potentiostatic growth of PEDOT in which the polymer is modelled as two distinct layers;  $R(Q)$  datasets are offset by increments of  $-1.5$  for clarity

$Q_g / \text{mC cm}^{-2}$		<b>11.7</b>	<b>15.68</b>
$\chi^2$	Single layer fit	5.3	13
	Two layer fit	4.2	9.3

Table 6.7 – Comparison of  $\chi^2$  values for single and multi-layered fits to the last two potentiostatic deposition steps

Once again, a multi-layered model can be used to fit the later stages of growth as shown in Figure 6.9. In this case, the penultimate growth step presents distinct inner and outer layers with solvent volume fractions of  $\Phi_s \sim 0.26$  and  $\Phi_s \sim 0.35$  respectively. The final growth stage also shows a solvation profile with a step in solvent volume fraction from  $\Phi_s \sim 0.31 - 0.47$ .

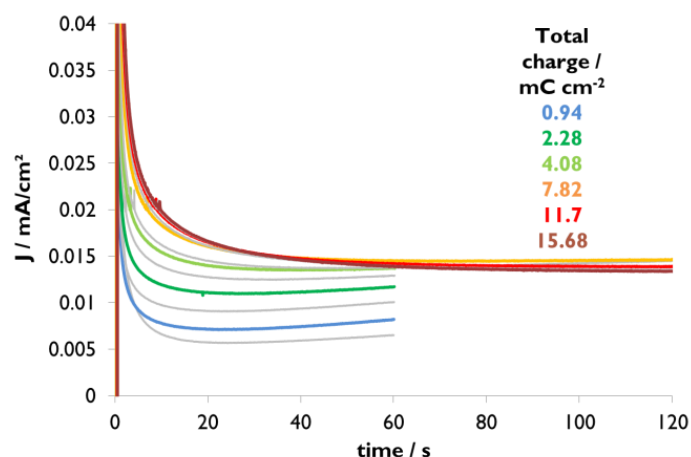


Figure 6.10 – Growth transients from successive steps during the potentiostatic growth of PEDOT. Coloured traces indicate the total charge following deposition intervals. Experimental conditions: 0.003 M EDOT in 0.3 M LiClO<sub>4</sub> in D<sub>2</sub>O, E = 0.55 V vs Ag wire, t<sub>total</sub> = 18 min

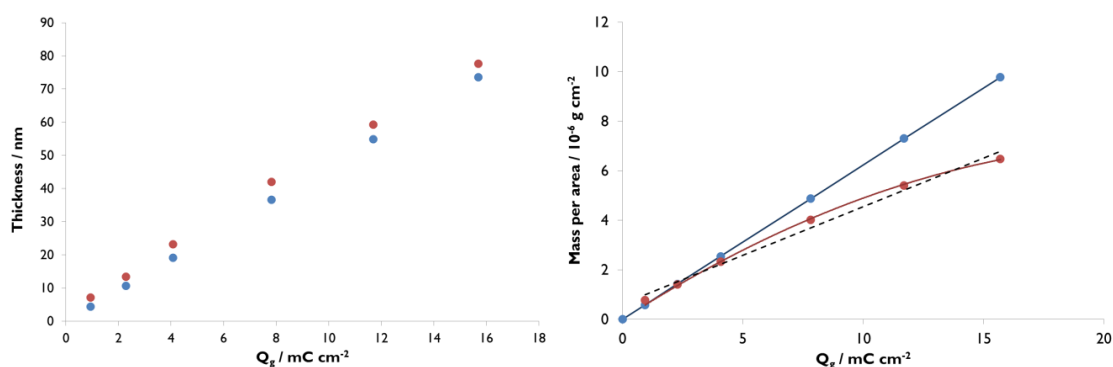


Figure 6.11 – Plots of film thickness (left) and mass per area (right) as a function of growth charge density as calculated from the electrochemical data (blue) and from the single layer fits to the NR data (red) from the potentiostatic growth of PEDOT; the coloured traces are the associated fits to the data, the black dotted trace is the linear fit to the NR data

Figure 6.11 shows the plots of thickness as a function of charge in which the solvated thickness of the films is consistently higher than that of the dry film estimate. This is consistent with the SLD profiles that indicate a solvated film throughout the growth, however there is no sign of an increasing degree of solvation as the deposition progresses. As in the case of the potentiodynamic growth, this would suggest that the polymerisation efficiency decreases with successive growth steps. The mass per area plot confirms this hypothesis in that the final growth stages are seen to diverge from the growth trend established by the electrochemical data.

The NR measurements of the galvanostatic growth of PEDOT reveal a very slight increase in the degree of solvation as the growth progresses. This can be observed in the SLD profiles presented in Figure 6.12, where the SLD remains unchanging in the early stages of growth before increasing slightly in the last two growth intervals. The volume fraction of solvent in the first three growth steps is consistently  $\Phi_s \sim 0.33$ , before increasing to  $\Phi_s \sim 0.35$  and  $\Phi_s \sim 0.38$  in the penultimate and final stages respectively.

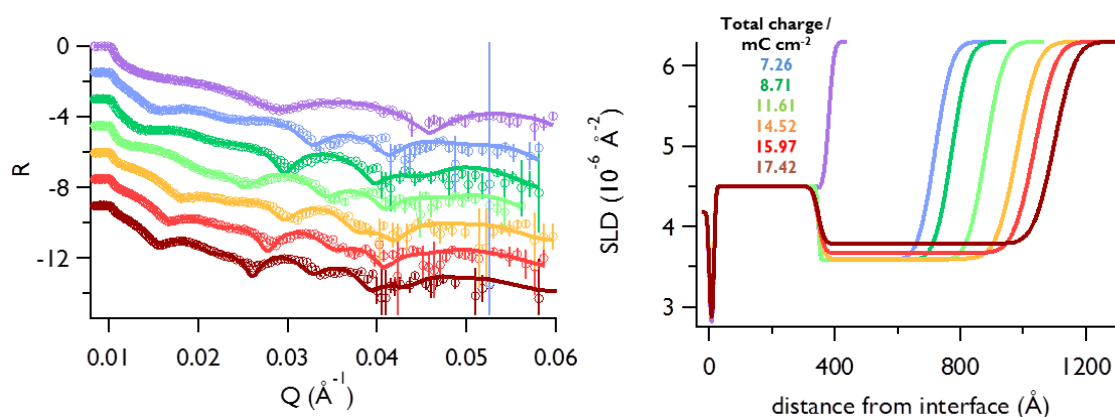


Figure 6.12 – NR measurements and fits (left) and corresponding SLD profiles (right) for the galvanostatic growth of PEDOT; the purple trace is the gold measurement prior to deposition.  $R(Q)$  datasets are offset by increments of  $-1.5$  for clarity. Experimental conditions:  $0.003\text{ M EDOT}$  in  $0.3\text{ M LiClO}_4$  in  $D_2O$ ,  $i = 24\ \mu\text{A cm}^{-2}$ ,  $t_{\text{total}} = 12\text{ min}$

Although the last three growth stages can be fitted to a multi-layered polymer model, the fit converges to an SLD profile in which the film is homogeneously solvated, with a volume fraction of  $\Phi_s \sim 0.35 - 0.37$ , but presents a large roughness at the polymer/solution interface as shown in Figure 6.13. Thus the solvation level of the film does not change significantly from the single layer models. This would suggest that the galvanostatic film presents a more consistent structure throughout the growth.

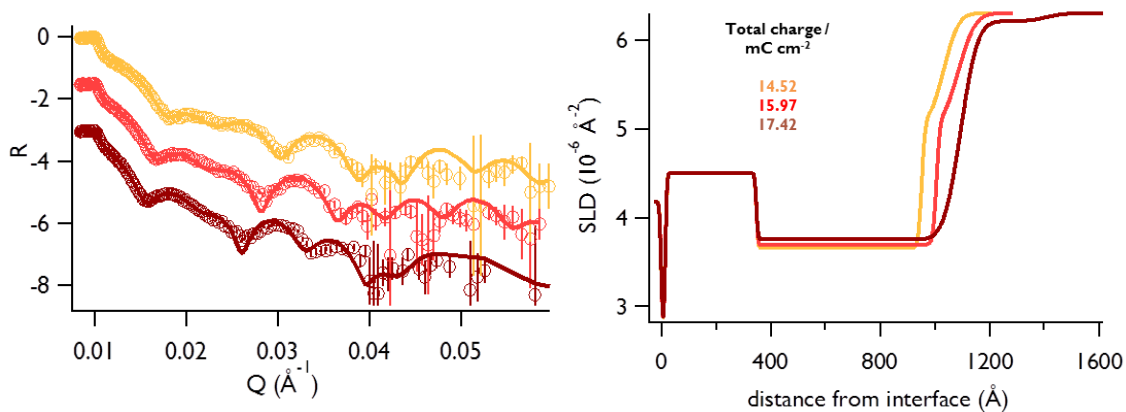


Figure 6.13 – NR measurements and fits (left) and corresponding SLD profiles (right) for the final stages ( $Q_g = 14.52, 15.97$  and  $17.42$ ) of galvanostatic growth of PEDOT in which the polymer is modelled as two distinct layers;  $R(Q)$  datasets are offset by increments of  $-1.5$  for clarity

$Q_g / \text{mC cm}^{-2}$		14.52	15.97	17.42
$\chi^2$	Single layer fit	5.7	7.8	9.5
	Two layer fit	3.8	4.7	5.2

Table 6.8 – Comparison of  $\chi^2$  values for single and multi-layered fits to the last three galvanostatic deposition steps

The plot of thickness as a function of growth charge density presented in Figure 6.15 shows a similar trend to those seen previously for the films produced by potentiodynamic and potentiostatic control functions. Similarly, the mass per area plot indicates that the growth of the film as measured by NR was not as efficient as the growth predicted by the electrochemical data. This suggests that the applied charge in this case is not entirely consumed by the polymerisation process or is used to produce oligomers that do not form part of the final film.

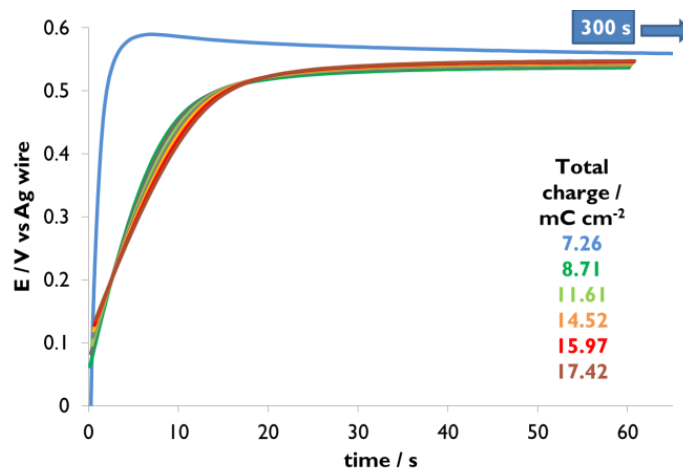


Figure 6.14 – Growth transients from successive steps during the galvanostatic growth of PEDOT. Coloured traces indicate the total charge following deposition intervals. Experimental conditions: 0.003 M EDOT in 0.3 M LiClO<sub>4</sub> in D<sub>2</sub>O,  $i = 24 \mu\text{A cm}^{-2}$ ,  $t_{\text{total}} = 12 \text{ min}$

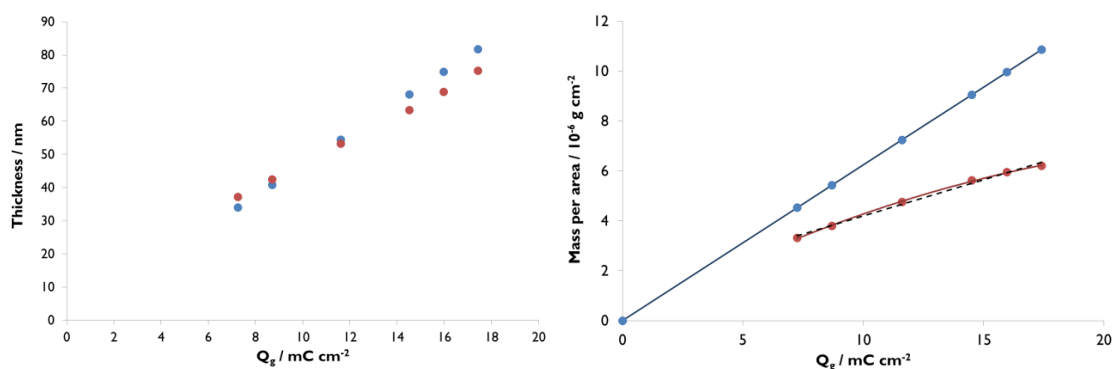


Figure 6.15 – Plots of film thickness (left) and mass per area (right) as a function of growth charge density as calculated from the electrochemical data (blue) and from the single layer fits to the NR data (red) from the galvanostatic growth of PEDOT; the coloured traces are the associated fits to the data, the black dotted trace is the linear fit to the NR data

The results of the linear fits to the mass per area plots are presented in Table 6.9. Following the same methodology as that described in Chapter 5, the gradient of the line is used to calculate the number of electrons per monomer unit consumed on average in the polymerisation process which, compared with the theoretical value, permits a quantification of the average polymerisation efficiency.

			Intercept	Gradient	R	e <sup>-</sup> per monomer (z)	polymerisation efficiency / %
Figure 6.7	PD	EC data	0	0.62	1	2.33	
		NR data	0.66	0.43	0.9967	3.37	69.20
Figure 6.11	PS	EC data	0	0.62	1	2.33	
		NR data	0.62	0.39	0.9940	3.70	63.00
Figure 6.15	GS	EC data	0	0.62	1	2.33	
		NR data	1.29	0.29	0.9964	5.01	46.55

Table 6.9 – Summary of linear regression analysis results from plots of mass per area as a function of growth charge density

The potentiodynamic and potentiostatic growth protocols both produced early stages of film growth that correspond quite closely to the coulometric estimates of growth, such that the first 2 – 3 data points fall along the predicted trend. The plots subsequently diverge suggesting that the polymerisation efficiency diminishes as the deposition proceeds. In the case of the galvanostatic growth, the film presents a consistently lower rate of deposition than that predicted by the electrochemical data. The polymerisation efficiency is calculated to be less than 50%.

	Polynomial fit coefficients		Initial polymerisation efficiency / %	loss of polymerisation efficiency / %	R
	A	B			
PD	0.6270	-0.0111	100.54	-3.56	0.9996
PS	0.6270	-0.0138	100.54	-4.43	0.9991
GS	0.5212	-0.0094	83.58	-3.01	0.9996

Table 6.10 – Summary of second order polynomial fits to the mass per area values calculated from the NR data as a function of charge

In all cases, the linear fits to the mass per area values calculated from the NR data do not pass through the origin and therefore indicate that the linear trend is not a realistic model of growth. A second order polynomial fit best describes the data as discussed

previously in Chapter 5. The results of these fits are presented in Table 6.10. The potentiodynamic and potentiostatic methods display a similar trend with 100 % initial polymerisation efficiency that drops by 3.6 % and 4.4 % respectively. In the case of the galvanostatic deposition, the lower average polymerisation efficiency is shown to be due to the initial stages of growth being less efficient but displays a lower decay in polymerisation efficiency as a function of charge.

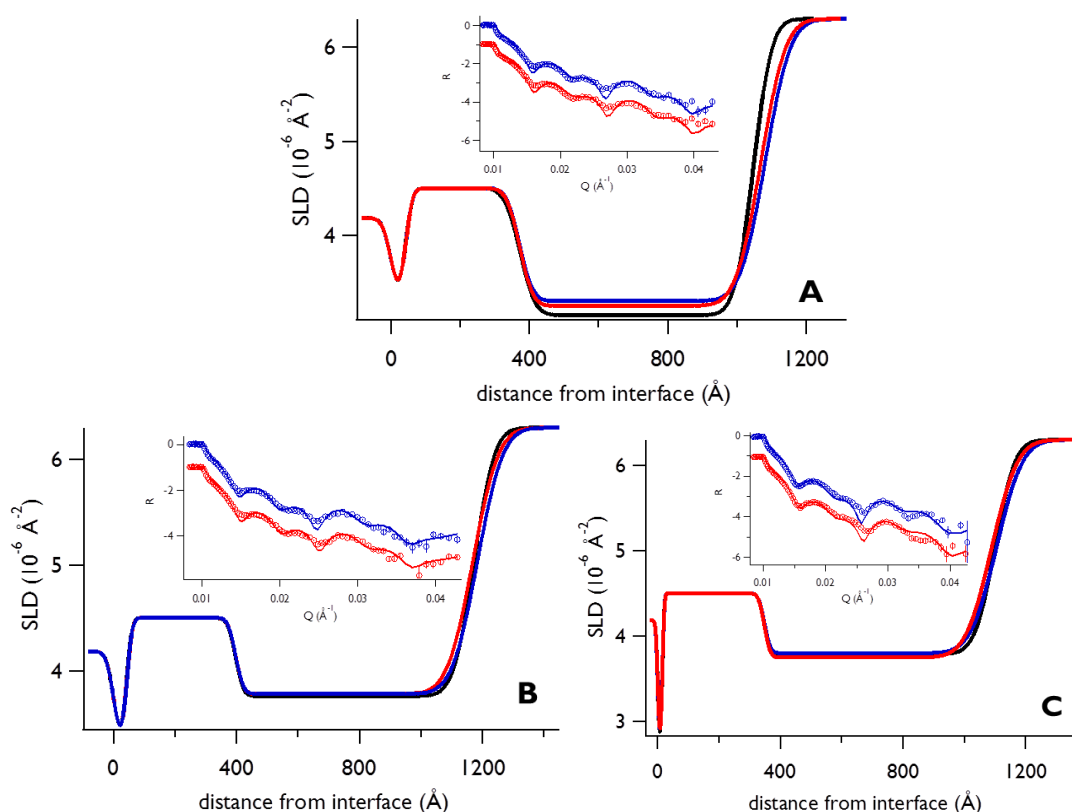


Figure 6.16 – SLD profiles of the films produced under potentiodynamic (A), potentiostatic (B) and galvanostatic (C) conditions, measured at the open circuit potential following the final growth stage (black), held oxidized at  $E = 0.4 \text{ V}$  (blue) and reduced at  $E = -0.5 \text{ V}$  (red); insets show the corresponding reflectivity data and fits from which these are derived. The model consisted of a single polymer layer with a rough outer interface.  $R(Q)$  datasets are offset by increments of  $-1$  for clarity

Each film was cycled in fresh electrolyte following deposition then held in an oxidised and reduced state to examine the effect of charging and discharging on the internal structure of the film. Once again, the NR data could be fitted using a single layer to model the polymer film and the results are presented in Figure 6.16 alongside the SLD profiles of the final growth stage for each electrochemical control function.

Overall, the films presented no significant structural changes and, in fact, showed almost identical SLD profiles to those of the final growth stages. Only the potentiodynamically grown film exhibited a slight increase in the level of solvation of the film from a solvent volume fraction of  $\Phi_s \sim 0.22$  after growth to between  $\Phi_s \sim 0.24 - 0.26$  in the redox states. This film also presented a slightly rougher interface at the boundary between the polymer and the solution. The solvent volume fractions associated with the single layer fits to the data are presented in Table 6.11 for ease of comparison.

Potentiodynamic		Potentiostatic		Galvanostatic	
$Q_g / \text{mC cm}^{-2}$	$\Phi_s$	$Q_g / \text{mC cm}^{-2}$	$\Phi_s$	$Q_g / \text{mC cm}^{-2}$	$\Phi_s$
2.2	0.20	0.9	0.19	7.3	0.33
4.4	0.23	2.3	0.21	8.7	0.33
6.7	0.23	4.1	0.25	11.6	0.33
9.5	0.21	7.8	0.28	14.5	0.33
11.7	0.20	11.7	0.31	16.0	0.35
15.2	0.22	15.7	0.37	17.4	0.38
E / V	$\Phi_s$	E / V	$\Phi_s$	E / V	$\Phi_s$
0.4	0.25	0.4	0.38	0.4	0.38
-0.5	0.26	-0.5	0.38	-0.5	0.37

Table 6.11 – Summary of solvent volume fractions extracted from single layer fits to the NR data, assuming a PEDOT SLD of  $2.25 \times 10^{-6} \text{ \AA}^{-2}$

As in the case of the NR data from the growth, the redox data can also be fitted using a model in which the polymer is divided into two layers. The results are presented in Figure 6.17 although it must be noted that the mass per area values extracted from these fits are not as close to the final growth stage values as in the case of the single layer models. These values differ most significantly in the case of the potentiodynamic data where they suggest a 23% difference in the amount of polymer. The fit indicates a polymer film that is more solvated to a volume fraction of  $\Phi_s \sim 0.43 - 0.47$  and in which the polymer does not present such a large difference in solvation between the inner and outer layers.

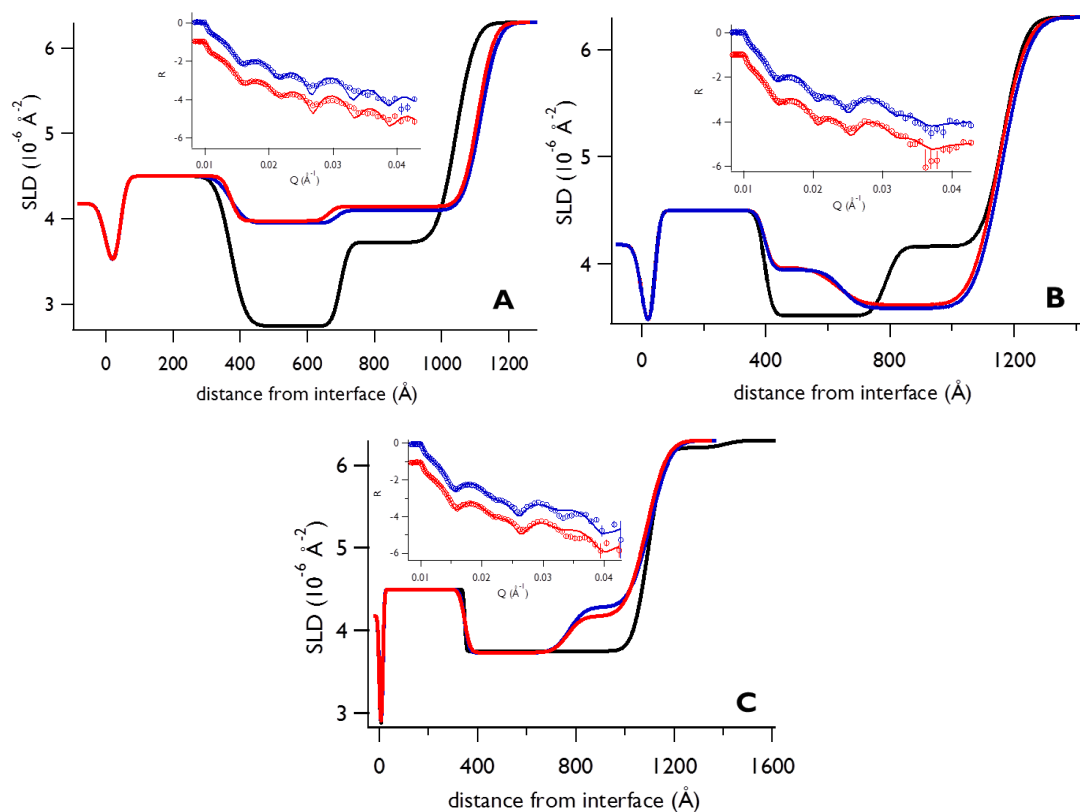


Figure 6.17 – SLD profiles of the potentiodynamic (A), potentiostatic (B) and galvanostatic (C) films measured at the open circuit potential following the final growth stage (black), held oxidized at  $E = 0.4$  V (blue) and reduced at  $E = -0.5$  V (red); insets show the corresponding reflectivity data and fits from which these are derived. The model consisted of the polymer being divided into two distinct layers.  $R(Q)$  datasets are offset by increments of  $-1$  for clarity

In the case of the potentiostatically grown film, the mass per area values derived from the fit differed from the final growth stage by less than 5% which is considered within the margins of error. However, the fit presents an unusual SLD profile in which the outer layer of the polymer is less solvated than the inner layer. This is not only the opposite of the multi-layered fit to the measurement of the final growth stage but also counter intuitive. It suggests that the inner layer could form a porous area in which the solvent collects to a volume fraction of  $\Phi_s \sim 0.42$ . The remainder of the film has a solvation of  $\Phi_s \sim 0.33 - 0.34$ .

The galvanostatic redox data presents a more common SLD profile in which the inner layer is similarly solvated to the film in the final growth state but presents a more solvated outer layer with a volume fraction of  $\Phi_s \sim 0.47 - 0.5$ . The mass per area values are within 10% of those calculated from the fit to the final growth state.

A comparison of  $\chi^2$  values obtained for the different models fitted to the NR data of the films in the different redox states is presented in Table 6.12. The solvent volume fraction data from the multi-layered models is presented in Table 6.13.

E / V		PD		PS		GS	
		0.4	-0.5	0.4	-0.5	0.4	-0.5
$\chi^2$	Single layer fit	16.4	18.8	16.5	16.1	37.5	31.5
	Two layer fit	15.2	16.8	12.1	12.9	10.6	9.4

Table 6.12 – Comparison of  $\chi^2$  values for single and multi-layered fits to the measurements of the redox states for each deposition method

Potentiodynamic		Potentiostatic		Galvanostatic	
$Q_g / \text{mC cm}^{-2}$	$\Phi_s$	$Q_g / \text{mC cm}^{-2}$	$\Phi_s$	$Q_g / \text{mC cm}^{-2}$	$\Phi_s$
9.5	0.13 - 0.44	7.8	N/A	14.5	0.35 - 0.69
11.7	0.05 - 0.26	11.7	0.26 - 0.35	16.0	0.36 - 0.68
15.2	0.12 - 0.36	15.7	0.31 - 0.47	17.4	0.37 - 0.98
E / V	$\Phi_s$	E / V	$\Phi_s$	E / V	$\Phi_s$
0.4	0.43 - 0.46	0.4	0.42 - 0.33	0.4	0.37 - 0.50
-0.5	0.42 - 0.47	-0.5	0.42 - 0.34	-0.5	0.37 - 0.47

Table 6.13 – Summary of solvent volume fractions extracted from multi-layered fits to the NR data, assuming a PEDOT SLD of  $2.25 \times 10^{-6} \text{ \AA}^{-2}$

The electrochemical characterisation of the films following deposition showed very similar CVs for all three films as shown in Figure 6.18. The films were also cycled between the NR measurements of the films in oxidised and reduced states as well as following these measurements. The CVs remained unchanged with the films exhibiting a loss of oxidation charge of less than 5% over the course of cycling.

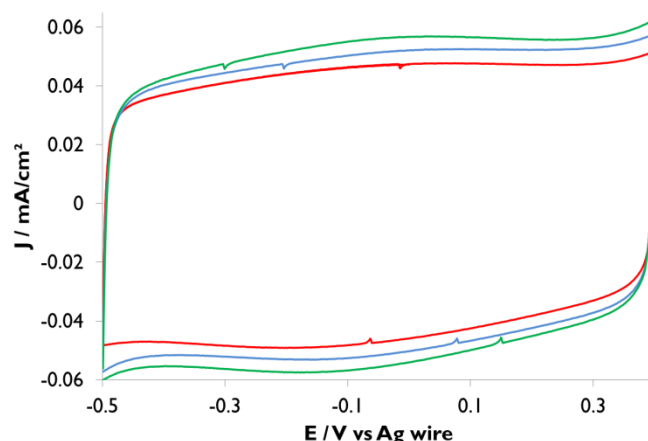


Figure 6.18 – Cyclic voltammograms of PEDOT films grown potentiodynamically (red), potentiostatically (blue) and galvanostatically (green), acquired at  $50 \text{ mV s}^{-1}$  in fresh electrolyte solution following film deposition

The electrochemical data from the characterisation is presented in Table 6.14 alongside the growth data. The oxidation to growth coverage ratio indicates that the films presented similar electroactivity.

Sample	Potentiodynamic	Potentiostatic	Galvanostatic
$Q_{\text{ox}} / \text{mC cm}^{-2}$	0.80	0.86	0.92
$\Gamma_{\text{ox}} / \times 10^{-8} \text{ mol cm}^{-2}$	2.49	2.67	2.86
$Q_{\text{g}} / \text{mC cm}^{-2}$	15.16	15.68	17.42
$\Gamma_{\text{g}} / \times 10^{-8} \text{ mol cm}^{-2}$	6.75	6.98	7.75
$\Gamma_{\text{ox}} / \Gamma_{\text{g}} \%$	36.88	38.33	36.91

Table 6.14 – Summary of the electrochemical characterization of the PEDOT films grown during in situ NR measurements

The thickness results from the growth charge estimates, the AFM measurements and the NR fits are presented in Table 6.15. They reveal disparities between the estimated and measured values, as well as between the films grown using the different electrochemical control functions. The potentiodynamically grown film presents the most consistent results. The AFM measurement of thickness is only 6% less than the solvated thickness measured by NR, suggesting that there is little or no collapsing of the film when it is removed from the electrolyte solution.

	$Q_g$ / mC cm <sup>-2</sup>	Thickness from $Q_g$ / nm	Thickness from AFM / nm	Roughness Rq / nm	SAD / %	Solvated thickness from NR fits / nm
Potentiodynamic	15.16	71	65 ± 5	4.8	0.5	69 ± 2
Potentiostatic	15.68	73.5	54 ± 5	6.34	0.74	77 ± 1
Galvanostatic	17.42	81.7	53 ± 10	7.74	0.92	75 ± 1

Table 6.15 – Summary of AFM characterisation of the PEDOT films grown during in situ NR measurements

The AFM measurement of the potentiostatically grown film reveals that the film was swollen by the solvent during the NR measurements and subsequently collapsed after drying. The solvated thickness is 43% greater than the dry thickness. The latter is however significantly less than the estimated value, suggesting that the polymerisation process was not as efficient as in the case of the potentiodynamic growth. The galvanostatically grown film presented a similar case to that of the potentiostatic growth in which the dry film measurement indicates a collapse of the film when it is dried. All the films displayed rather globular surface features as shown in Figure 6.19.

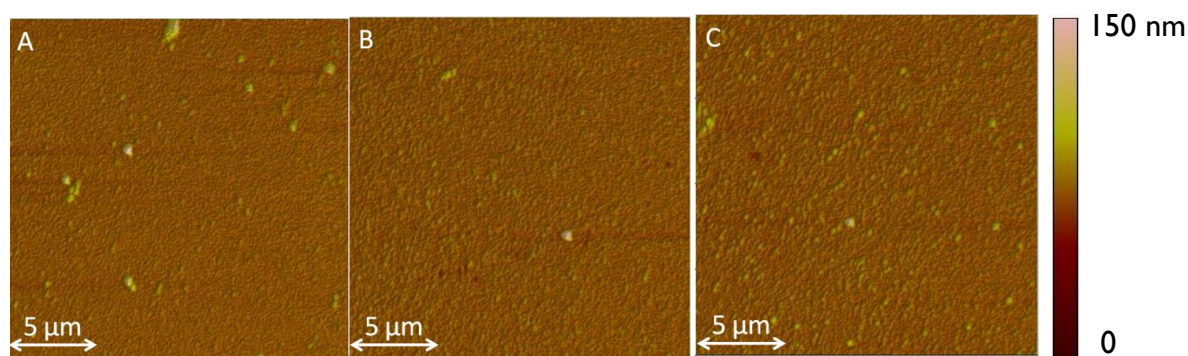


Figure 6.19 – AFM images of the surface of PEDOT films grown potentiodynamically (A), potentiostatically (B) and galvanostatically (C) during in situ NR measurements

## 6.4 Discussion

Overall, the small scale deposition samples indicated that faster growth, whether using, potentiodynamic, potentiostatic or galvanostatic methods, resulted in relatively poor electroactivity as summarised in Table 6.4, which is likely to be indicative of low polymerisation/deposition efficiency. The speed of the deposition process, controlled by the choice of potential or current density was adjusted in the scaled up experiments. The aim was not only to produce films with as smooth a surface as possible and good electroactivity but also to slow the growth to a pace in which NR measurements could capture any important structural changes in the early stages of the deposition process.

Both the small scale samples and the experiments on glass substrates indicated that in the case of potentiostatic growth, lower potentials were conducive to greater electroactivity of the resulting film. Furthermore, the use of a lower deposition potential produced films for which the estimated thickness from the growth charge and the thickness measured by AFM were more comparable, suggesting that the charge applied was more efficiently used in the growth process. This is in keeping with the work by Pigani et al who have also reported that higher potentials result in a lower polymerisation efficiency<sup>1</sup>. The small scale galvanostatic samples displayed the same benefits brought about by using lower current densities. Additionally, reducing the growth charge density was found to reduce the surface roughness which is supported by the findings Baek et al<sup>2</sup>.

In the case of the potentiodynamically grown films, limiting the potential range, the maximum current density and increasing the scan rate, such that the potential window for deposition was reduced, were all used to limit the rate of growth. These variables also played a role in controlling the surface roughness. In the study by Patra et al, which used scanning electron microscopy to examine the role of electrochemical control function in determining the morphology of PEDOT films, higher potential ranges were found to produce a more fibrous structure as opposed to lower current densities and potentials that resulted in a globular morphology<sup>3</sup>. The choice of potential range has also been shown to influence the degree of crystallinity of the deposited films<sup>4</sup>. AFM images of the small scale PEDOT samples grown from lithium perchlorate monomer solutions revealed that the potentiodynamic growth resulted in

large fibrous structures on the surface of the films, as shown in Figure 6.1. Using the same growth protocol and a greater number of cycles but on a substantially larger working electrode area, thus reducing the total growth charge density, resulted in a film that did not present such large surface features, illustrated by the AFM images in Figure 6.3. Thus the large surface area necessary for the NR experiments proved to be an advantage in producing the low surface roughness that would allow successful NR measurements of the sample. Films grown from the sulphuric acid solutions presented significantly greater roughness and inhomogeneities compared to the films prepared from lithium perchlorate therefore the latter was selected as the growth medium for the NR experiments.

The surprising feature of the potentiodynamically grown films with large growth charge densities was their apparently low electroactivity. The charge density not only predicted very thick films but the AFM revealed the large amount of polymer fibres on the surface, distinct from the bulk of the film. Melato et al have previously reported that PEDOT has a fibrous morphology when prepared potentiodynamically, as opposed to a granular structure when deposited under constant potential<sup>5</sup> therefore the topographical features are not unusual. However, it is generally considered that increased porosity results in greater electroactivity, as well as stability during cycling, since it allows greater solvent penetration to the active sites within the film<sup>6</sup>. This is evidenced by studies that have explored the role of the counter ions and found that the molar mass of the ions has an effect the electroactive response of the polymer films<sup>7</sup>; notably, smaller ionic species will have greater ease in penetrating the polymer matrix resulting in faster ion transport<sup>8</sup>. Theoretically, therefore, it could be assumed that these fibrous structures would increase the active surface area of the film, creating greater accessibility to the redox active sites in the polymer chains and thus increasing the electroactivity of the film. Since this was not observed, it raises the question as to whether these surface structures are sufficiently connected to the bulk of the film covering the electrode. Perhaps the connection to the surface bound film becomes strained as these fibres increase in size, or maybe the greater electroactivity results from a polymer matrix and not from large, separate clusters. The parameters of the growth protocols employed in this case were quite different therefore these samples do not provide sufficient information to explore these theories since a number of factors could be responsible for these features.

In the deposition experiments conducted on glass substrates, one of the potentiostatic samples and the galvanostatic samples were deposited to a similar growth charge density yet presented differences with regards to electroactivity and thickness as measured by AFM. The details are summarised in Table 6.5. The galvanostatic film presented a greater oxidation to growth coverage ratio and the thickness measured was greater than the estimate from the growth charge density, suggesting greater polymerisation efficiency as well as possibly a different internal structure. In the case of samples produced during the NR measurements, however, these differences were not apparent between the potentiostatically and galvanostatically grown films. Both films presented a similar electroactivity, as summarised in Table 6.14 and, in both cases, the AFM measurements of thickness were less than the estimates from the growth charge, although the solvated thickness was in keeping with the predicted value as shown in Table 6.15. Furthermore, the analysis of the plots of mass per area as a function of growth charge revealed that the galvanostatic deposition resulted in the lowest average polymerisation efficiency at 47 %.

In terms of structural differences, the single layer fits to the NR data do not reveal significant differences although the potentiostatic growth presented a film that was increasingly solvated as the growth progressed whereas the galvanostatically grown film remained largely at the same level of solvation throughout the deposition process. The multi-layered fits, on the other hand, indicate significant differences in solvation within the potentiostatically grown film, with a more solvated layer at the polymer/solution interface that is not so distinct in the case of the film grown galvanostatically. The more homogeneous solvation of the latter could indicate a more consistent porosity throughout the film. In the case of the potentiostatically grown film, perhaps areas of the films present different degrees of porosity which inhibit the movement of ions in solution thus affecting the overall redox capabilities of the film. Such a difference in electroactivity was not, however, observed in the characterisation of the films using cyclic voltammetry.

When comparing the electroactivity of the samples on glass substrates, it was observed that a decrease in the growth charge density produced films with greater redox capacity. This coincided with decreasing the potential limits in the potentiodynamic growth and the lowering of the deposition potential in the case of the

potentiostatic growth. However, the galvanostatically grown film from the NR experiment was grown with exactly the same current density as the sample on glass but to a greater growth charge density and presented a lower oxidation to growth coverage ratio. It is therefore suggested that a greater growth charge density, which ultimately translates to a greater thickness, could result in a less electroactive film. This could be explained by a loss of accessibility to the more 'buried' redox sites as the film becomes thicker. Furthermore, the mass per area plots associated with the samples studied using NR revealed that the polymerisation efficiency decreases as the growth progresses. As a result, the formation of oligomers that do not form part of the deposited film may increase with increasing growth charge which would also explain a decrease in relative redox capacity. More experiments are needed to explore this hypothesis and further NR measurements during growth to lesser and greater growth charge densities could help identify these possible structural variations. It should be noted that the NR measurements required the growth to be interrupted which may also have affected the structure and therefore electroactivity of the sample, as it has been reported that a layer-by-layer approach to deposition may indeed reduce the redox capacity of the film produced<sup>9</sup>.

The NR data was fitted to two types of models, one in which the polymer layer was modelled as a single layer and another in which the layer was divided in two. Dividing the polymer into further layers was not found to improve the fits. The fits only converged successfully to multi-layered models for the measurements of the final growth steps and of the film held in oxidised and reduced states. When modelled using a two-layered system, the other stages of growth resulted in a fit in which only one layer modelled the polymer film and the other layer converged to a thickness of 0; these datasets therefore fitted best to the single polymer layer model.

In the case of the potentiodynamic and potentiostatic growth, the multi-layered fits to the final stages of the deposition revealed a split solvation with a significant difference between the inner layer, at the polymer/electrode interface, and the outer layer, at the polymer/solution interface. While it is conceivable that there be distinct areas of differing solvent content, and particularly an increasing degree of solvation from the electrode to the solution interface, the extent to which the polymers porosity appears to change between the earlier and later stages of growth is unexpected. When the

multi-layered fits to the redox data are examined, they present further changes that seem unrealistic, particularly in the case of the potentiostatically grown film where the solvation profile becomes inverted as shown in Figure 6.17. Melato et al have reported that the potentiostatic deposition of PEDOT can result in a two layered system in which the first layer on the electrode surface is more compact and the outer layer consists of polymer clusters<sup>10</sup>. These features were, however, observed only for films with a growth charge density  $> 20 \text{ mC cm}^{-2}$  and the deposition was carried out in acetonitrile as opposed to aqueous solutions.

The multi-layered fits to the galvanostatically grown film, on the other hand, simply present a rougher interface between the polymer and the solution. The NR measurements of the redox states reveal a slight increase in solvation at the polymer/solution interface, with a bulk solvent content in keeping with that observed during the growth. These differences between the films suggest that the galvanostatic growth produced a polymer film structure that is more homogeneous throughout the film.

It is important to note, that the reflectivity data acquired for these samples only extends to  $Q = 0.06 \text{ \AA}^{-1}$  and that any improvements to the fits, brought about by the additional layer to model the polymer, usually occurred in the range of  $Q = 0.04 - 0.06 \text{ \AA}^{-1}$ . The errors in this area are greater than in the rest of the reflectivity data so, while the multi-layered fits suggest that there may be further information to be extracted, these fits are less reliable in terms of the accuracy of the information they provide. To improve the statistics in the higher range of  $Q$ , the reflectivity would have to be measured using an additional incident beam angle.

The single layer fits to the data acquired during the potentiodynamic growth of PEDOT reveal that the film grows with a consistent volume fraction of solvent between  $\Phi_s \sim 0.2 - 0.23$  as shown in Figure 6.4 and Table 6.11. The final growth stage was the only dataset in which the SLD parameter had to be restrained as it would freely fit to a higher SLD. Although this produced a lower  $\chi^2$  value, the model did not fit the prominent features of the reflectivity data in the higher  $Q$  range. The single layer fits to the redox data indicate a slightly increased solvation of  $\Phi_s \sim 0.24 - 0.26$ . These fits do not suggest any significant differences in terms of structure, surface roughness or loss of material as a result of cycling and charging/discharging of the film.

This is supported by the fact that the cyclic voltammograms revealed only a small, less than 5%, decrease in oxidation charge following cycling and redox measurements. This is consistent with the study by Aradilla et al in which the layer-by-layer deposition protocol produced PEDOT films that were less electroactive but more stable than those grown by continuous deposition<sup>9</sup>.

The AFM results presented in Table 6.15 indicate that the potentiodynamically grown film thickness was in keeping with the growth charge estimate and the NR fits to the solvated film. This suggests an efficient use of the charge in the polymerisation process and a stable, robust film that did not collapse upon drying. This polymerisation efficiency is supported by the mass per area analysis of the data, presented in Figure 6.7, which reveals a good correlation between the mass per area values calculated from the growth charge and the values extracted from the fits to the NR data, in the early stages of growth. However, the two datasets begin to diverge as the growth progresses, suggesting that the efficiency diminishes as the quantity of surface bound polymer increases. This is likely to be because more charge is required to oxidise the polymer film before further polymerisation can occur. There may also be the formation of oligomers during the oxidising potential sweep which do not deposit and diffuse into the bulk of the solution during the reduction of the film. Nevertheless, the potentiodynamic growth appears to be the most efficient according to the fits to the mass per area data, resulting in an average polymerisation efficiency of 69 % and a decay in efficiency of 3.5 % as a function of charge.

The potentiostatically grown film presented an interesting case in which the polymer film was incrementally more solvated as the growth progressed, as shown in Figure 6.8. The early stages of growth presented a solvent volume fraction of approximately  $\Phi_s \sim 0.2$  and the following steps increased to a final solvation of  $\Phi_s \sim 0.37$ . This would suggest that the initial polymer layers are more compact and the continued polymerisation renders the film more porous. Surprisingly, it does not appear that these early growth steps form a 'base' layer with a lower level of solvation that persists in the structure of the film following further deposition, but rather that the film maintains a homogeneous degree of solvation throughout its thickness. This is counter-intuitive since it could be assumed that the initial polymer layer becomes less porous as it is gradually filled in by the nucleation of additional oligomers. However, if

it is considered that each chain is extended with subsequent growth steps, then it is conceivable that the lengthening of the polymer strands could result in a more disordered and porous structure.

The redox measurements revealed very little change from the final growth stage and the cyclic voltammograms remained consistent following cycling and the charge/discharge measurements. This suggests a stable film in terms of its electrochemical behaviour however the AFM measurements of thickness revealed that the film may not have been as structurally robust. The thickness was substantially lower than both the estimated thickness from the growth charge and the solvated thickness from the fits to the NR data. This indicates a collapse of the film from the solvated to dry state of around 30 %.

The combination of these results appears to indicate that the potentiostatic growth produced a film that was more porous than the film grown potentiodynamically. Although the electrochemical characterisation of the films was very similar as seen in Figure 6.18, the films reveal a different internal structure with the potentiostatic growth resulting in a higher volume fraction of solvent penetrating the film. While the potentiodynamic growth displayed a consistent level of solvation during the deposition process, the potentiostatic growth suggested a changing structure throughout the growth.

The galvanostatically grown film displayed features present in both the potentiodynamic and potentiostatic growth. In the early stages of growth, the solvent volume fraction remained stable around  $\Phi_s \sim 0.33$ . In the final stages, however, this increased to  $\Phi_s \sim 0.35$  then  $\Phi_s \sim 0.38$ . This increase in solvation is not as significant as that observed during the potentiostatic growth but suggests nevertheless a less consistent growth than the potentiodynamic deposition. Once again, the redox data indicates that there is very little change between the measurement of the final growth stage and the measurements following cycling and charge/discharge of the film, and the cyclic voltammograms present consistent electrochemical behaviour suggesting good stability.

The AFM measurements of thickness reveal similar results to those found in the case of the potentiostatically grown film, indicating a collapse of the film after drying. The

solvated measurement of thickness from the NR fits differs significantly from the dry measurement although it is comparable to the growth charge estimate. The comparison of the mass per area values derived from the growth charge and NR data, presented in Figure 6.15, also reveal that the galvanostatic growth was less efficient than the deposition using the other control functions. In both the potentiodynamic and potentiostatic growth, the mass per area values in the early stages of growth extracted from the NR data matched those calculated from the growth charge. It was only as the growth progressed that the two datasets diverged. In this case however, the mass per area values for the very first growth step differ significantly and the rate of the deposition as measured by the NR data is clearly not as fast as that predicted by the growth charge. This suggests a much less efficient use of charge in the polymerisation process than observed for the other two growth protocols.

Expressing the quantity of polymer in the form of mass per area as opposed to thickness or moles is important as it allows the thickness measurements from the fits to the NR data to be converted to a quantity that represents solely the polymer and not the solvent content. Consequently, these values can also be converted into an estimate of the dry thickness, in which it is assumed all solvent has been removed, along with the volume it occupies, and is thus comparable to the AFM measurements of the films in the dry state. Accordingly, the potentiodynamically grown film has a calculated dry thickness of 53 nm and the potentiostatic and galvanostatic growth protocols should result in a dry thickness of 49 and 47 nm respectively. This demonstrates that the AFM measurements of thickness are in keeping with the fits to the NR data, although the potentiodynamic growth appears to produce a more porous film.

A value of the polymerisation efficiency was derived from the linear fits to the plots of mass per area as a function of growth charge and allowed a comparison of the different methods used. Accordingly, the electrochemical control functions, under the conditions used here, can be ranked in order of polymerisation efficiency as follows: potentiodynamic > potentiostatic > galvanostatic. Interestingly, the electrochemical characterisation indicated little to no differences between these films, the features that differentiate them are observed in the structural characterisation using NR and AFM. The electroactivity of the films was very similar with regards to the oxidation to

growth coverage ratio, as summarised in Table 6.14. This is somewhat surprising since it could be assumed that a film in which the growth charge did not produce the maximum amount of polymer would therefore not exhibit as great an electroactivity as a more efficiently polymerised film. It seems clear that the differences in internal structure observed in the variations in solvent content throughout the growth indicate differences in porosity that also contribute to the redox capacity of these films.

Finally, it is important to note that the deposition process was frequently paused to allow for the NR measurements. While the use of NR allows measurements *in situ* which could not be achieved by any other technique, interrupting the growth may also have had an effect on the resulting films. For instance, during the data acquisition, the films were at the open circuit potential since any current or potential would have continued the polymerisation process. Consequently, when the deposition was restarted, a proportion of the charge supplied would have been used to oxidise the film before polymerisation progressed. In the case of the potentiodynamic deposition, this is probably not an important factor since the NR measurements were carried out following full cycles such that the film would have already been at a reducing potential and the deposition would have been continued from this same potential. In the case of the potentiostatic and galvanostatic growth, however, the film would be progressively oxidised throughout the growth if the deposition were continuous. The lower efficiency may therefore be related to this stop/start mechanism.

Ideally, the growth of these films would be slowed down such that NR measurements could be acquired in real time. However, this poses several problems: firstly, the range of  $Q$  would remain limited by the use of a single angle as changing angles requires several minutes for the instrument to adopt the correct configuration, a timescale that is not appropriate for these kinetic measurements; secondly, the growth of films at such a reduced rate may not be representative of faster growth mechanisms. While this would be a valid and certainly interesting experiment, it would not be sufficient in fully understanding the structural implications of the choice of electrochemical control function.

To complement these experiments, further measurements are needed to explore the effect of the stop/start mechanism as well as the role of the total growth charge density. This could be easily achieved by growing films *in situ*, without interruption of

the deposition process, with the same growth protocol and growth charge density. These could then be compared to films with the same growth protocol but lower growth charge density.

## 6.5 Conclusions

In this study, the role of the deposition protocol has been explored in terms of its effect on the electrochemical behaviour, internal structure and solvation properties of PEDOT films. The small scale experiments revealed that decreasing the rate of deposition by using faster potential scan rates, lower current densities and lower potentials increases the relative electroactivity of the films as well as producing a smoother surface morphology. Increasing the electrode surface area was also found to facilitate this.

NR measurements revealed that the potentiodynamic growth results in a more consistent deposition, producing a homogeneously solvated film that retains this structure when subjected to charge and discharge processes. This film also presented a robust, porous structure evidenced by only a 6 % reduction in thickness from the solvated to the dry state. The potentiostatic and galvanostatic growth protocols resulted in films that were more solvated and that presented an increasing degree solvation during the deposition process. Furthermore, the films were more flexible as demonstrated by shrinking of the films when dried, resulting in a dry thickness that was 30 % less than that of the solvated film. These three films displayed similar electrochemical behaviour and were found to be comparably electroactive despite different polymerisation efficiencies.

The potentiodynamic growth was found to be the most efficient in terms of the growth charge resulting in polymerisation. This finding may however be related to the way in which NR data was acquired by pausing the film growth which is unlikely to have affected the potentiodynamic deposition but may have had an adverse effect on the films grown using the other two control functions. Consequently, further work is needed to confirm or eliminate the impact of the stop/start methodology on the polymerisation efficiency during potentiostatic and galvanostatic deposition.

## 6.6 References

1. Pigani, L., Heras, A., Colina, Á., Seeber, R. & López-Palacios, J. Electropolymerisation of 3,4-ethylenedioxythiophene in aqueous solutions. *Electrochem. Commun.* **6**, 1192–1198 (2004).
2. Baek, S., Green, R. A. & Poole-Warren, L. A. The biological and electrical trade-offs related to the thickness of conducting polymers for neural applications. *Acta Biomater.* **10**, 3048–58 (2014).
3. Patra, S., Barai, K. & Munichandraiah, N. Scanning electron microscopy studies of PEDOT prepared by various electrochemical routes. *Synth. Met.* **158**, 430–435 (2008).
4. Niu, L., Kvarnström, C., Fröberg, K. & Ivaska, A. Electrochemically controlled surface morphology and crystallinity in poly (3,4-ethylenedioxythiophene) films. *Synth. Met.* **122**, 425–429 (2001).
5. Melato, A. I., Viana, A. S. & Abrantes, L. M. Influence of the electropolymerisation mode on PEDOT films morphology and redox behaviour — an AFM investigation. *J. Solid State Electrochem.* **14**, 523–530 (2010).
6. Snook, G. A., Kao, P. & Best, A. S. Conducting-polymer-based supercapacitor devices and electrodes. *J. Power Sources* **196**, 1–12 (2011).
7. Balint, R., Cassidy, N. J. & Cartmell, S. H. Conductive polymers: towards a smart biomaterial for tissue engineering. *Acta Biomater.* **10**, 2341–53 (2014).
8. Melato, A. I., Mendonça, M. H. & Abrantes, L. M. Effect of the electropolymerisation conditions on the electrochemical, morphological and structural properties of PEDOT films. *J. Solid State Electrochem.* **13**, 417–426 (2009).
9. Aradilla, D., Estrany, F. & Aleman, C. Different properties for poly (3, 4-ethylenedioxythiophene) films derived from single or multiple polymerization steps. *J. Appl. Polym. Sci.* **121**, 1982–1991 (2011).
10. Melato, A. I., Viana, A. S. & Abrantes, L. M. Different steps in the electrosynthesis of poly(3,4-ethylenedioxythiophene) on platinum. *Electrochim. Acta* **54**, 590–597 (2008).

## Chapter 7 - Conclusions

The body of work on the study of conducting polymer films is substantial and one of the prevalent features of these systems is the wide range of electrochemical and structural properties that can be manipulated according to the parameters of the deposition protocol. The research presented here therefore contributes to a much wider investigation of such variables and focusses particularly on the internal structure of the polymer matrix. In part, the novelty of this work is the use of neutron reflectometry as the predominant technique, allowing unique insight into the spatial distribution of solvent species within the films. The results are analysed in conjunction with electrochemical and surface characterisation techniques.

In a first instance, the incorporation of NDs in a PEDOT film was explored with respect to the influence afforded by the particles on the electrochemical response and the structural changes they produce in the polymer matrix. A comparison of pristine and composite films produced by potentiostatic and potentiodynamic methodologies revealed no consistent differences in electroactivity. Under a constant potential growth protocol, the presence of NDs in the deposition solution produced a more porous film. Composite films grown potentiostatically displayed a greater surface roughness than the pristine PEDOT films. The NR investigation revealed that the NDs produced films with greater thickness and a more ordered internal structure which is in keeping with previous studies indicating that the incorporation of carbon nanoparticles affords greater structural stability.

In the subsequent studies, the role of the electrochemical control function in affecting film structure and the charge/discharge processes was examined in the case of PPy and PEDOT films. The former presented a similar solvation profile, and therefore porosity, when deposited using potentiodynamic and potentiostatic methods but displayed structural differences following electrochemical characterisation, indicating a greater re-ordering of the polymer matrix in the case of the film grown potentiodynamically. The galvanostatic deposition resulted in more compact and less electroactive film. All the films presented a decrease in polymerisation efficiency as

the growth progressed, with the potentiostatic growth presenting the most efficient use of charge overall.

This contrasts with the case of PEDOT for which the potentiodynamic deposition was found to be the most efficient method, as well as producing the most consistent and stable structure throughout the growth and following charge/discharge processes. Both the potentiostatic and galvanostatic methods resulted in porous films and an evolving structure throughout the growth. These films were also less robust, appearing to collapse once dried.

These results suggest that the effect of the electrochemical control function may differ for each polymer species. The role of the other variables should not however be overlooked; due to the poor solubility of the EDOT monomer, the concentration used in deposition of PEDOT was very low compared to that used in the case of PPy. The molecular structure of these two species is also markedly different therefore it would be interesting to investigate whether or not trends in structural features result from the deposition method for polymers with similar composition and/or bonding structure.

Looking ahead, proposals have already been submitted to neutron facilities requesting beam time on NR instruments to further investigate the structural differences afforded by the growth protocol. In particular, these studies would explore whether or not the features of the internal structure such as greater density, or conversely porosity, are maintained following extended charge/discharge processes, or whether the polymer films eventually adopt a common structure regardless of the deposition method used. Additionally, a comparison of films grown continuously and those deposited using the stop/start protocol would be advisable in order to establish the effect of the layer-by-layer approach.

NR is undoubtedly a powerful tool in elucidating the structural features of these films. These studies have shown how the combination of this technique with electrochemical methods can provide unprecedented insight into the structural features that directly impact on the electroactivity and stability of these films.

## Bibliography

Ansari, R. In-situ cyclic voltammetry and cyclic resistometry analyses of conducting electroactive polymer membranes. *Int. J. ChemTech Res.* **1**, 1398–1402 (2009).

Aradilla, D., Estrany, F. & Aleman, C. Different properties for poly (3, 4-ethylenedioxythiophene) films derived from single or multiple polymerization steps. *J. Appl. Polym. Sci.* **121**, 1982–1991 (2011).

Asavapiriyant, S., Chandler, G. K., Gunawardena, G. A. & Pletcher, D. The electrodeposition of polypyrrole films from aqueous solutions. *J. Electroanal. Chem.* **117**, 229–244 (1984).

Attard, G. & Barnes, C. *Surfaces*. (Oxford University Press, 2008).

Baek, S., Green, R. A. & Poole-Warren, L. A. The biological and electrical trade-offs related to the thickness of conducting polymers for neural applications. *Acta Biomater.* **10**, 3048–58 (2014).

Balint, R., Cassidy, N. J. & Cartmell, S. H. Conductive polymers: towards a smart biomaterial for tissue engineering. *Acta Biomater.* **10**, 2341–53 (2014).

Barnard, A. S. & Sternberg, M. Crystallinity and surface electrostatics of diamond nanocrystals. *J. Mater. Chem.* **17**, 4811 (2007).

Blanchard, F., Carré, B., Bonhomme, F., Biensan, P., Pagès, H. & Lemordant, D. Study of poly(3,4-ethylenedioxythiophene) films prepared in propylene carbonate solutions containing different lithium salts. *J. Electroanal. Chem.* **569**, 203–210 (2004).

Bobacka, J., Lewenstam, A., Ivaska, A. & Fin, A. Electrochemical impedance spectroscopy of oxidized poly ( 3 , 4-ethylenedioxythiophene ) film electrodes in aqueous solutions. **489**, 17–27 (2000).

Burgess, I., Zamlynny, V., Szymanski, G., Lipkowski, J., Majewski, J., Smith, G., Satija, S. & Ivkov, R. Electrochemical and neutron reflectivity characterization of dodecyl sulfate adsorption and aggregation at the gold-water interface. *Langmuir* **17**, 3355–3367 (2001).

Cooper, J. M., Cubitt, R., Dalgliesh, R. M., Gadegaard, N., Glidle, A., Hillman, A. R., Mortimer, R. J., Ryder, K. S. & Smith, E. L. Dynamic in situ electrochemical neutron reflectivity measurements. *J. Am. Chem. Soc.* **126**, 15362–3 (2004).

Cubitt, R. & Stahn, J. Neutron reflectometry by refractive encoding. *Eur. Phys. J. Plus* **126**, 111 (2011).

- Cui, X. & Martin, D. C. Electrochemical deposition and characterization of poly(3,4-ethylenedioxythiophene) on neural microelectrode arrays. *Sensors Actuators B Chem.* **89**, 92–102 (2003).
- Demoustier-Champagne, S., Ferain, E., Jérôme, C., Jérôme, R. & Legras, R. Electrochemically synthesized polypyrrole nanotubules: effects of different experimental conditions. *Eur. Polym. J.* **34**, 1767–1774 (1998).
- Dianoux, A.-J. & Lander, G. *Neutron Data Booklet*. (OCP Science, 2003).
- Dolmatov, V. Y. Polymer-diamond composites based on detonation nanodiamonds. Part I. *J. Superhard Mater.* **29**, 65–75 (2007).
- Downard, A. J. & Pletcher, D. A study of the conditions for the electrodeposition of polythiophene in acetonitrile. *J. Electroanal. Chem.* **206**, 147–152 (1986).
- Eliseeva, S. N., Spiridonova, D. V., Tolstopyatova, E. G. & Kondratiev, V. V. Redox capacitance of poly-3,4-ethylenedioxythiophene studied by cyclic voltammetry and faradaic impedance spectroscopy. *Russ. J. Electrochem.* **44**, 894–900 (2008).
- Fadda, G. C., Lairez, D., Guennouni, Z. & Koutsioubas, A. Peptide pores in lipid bilayers: voltage facilitation pleads for a revised model. *Phys. Rev. Lett.* **111**, 028102 (2013).
- Faulkner, L. R. Understanding electrochemistry: Some distinctive concepts. *J. Chem. Educ.* **60**, 262 (1983).
- Feoktistov, N. A., Grudinkin, S. A., Rybin, M. V., Smirnov, A. N., Aleksenskii, A. E., Vul', A. Y. & Golubev, V. G. Boron-doped transparent conducting nanodiamond films. *Tech. Phys. Lett.* **37**, 322–325 (2011).
- Ferreira, L. F., Souza, L. M., Franco, D. L., Castro, A. C. H., Oliveira, A. A., Boodts, J. F. C., Brito-Madurro, A. G. & Madurro, J. M. Formation of novel polymeric films derived from 4-hydroxybenzoic acid. *Mater. Chem. Phys.* **129**, 46–52 (2011).
- Fisher, A. C. *Electrode Dynamics*. (Oxford University Press, 1996).
- Frackowiak, E., Khomenko, V., Jurewicz, K., Lota, K. & Béguin, F. Supercapacitors based on conducting polymers/nanotubes composites. *J. Power Sources* **153**, 413–418 (2006).
- Garreau, S., Louarn, G., Buisson, J. P., Froyer, G. & Lefrant, S. In situ spectroelectrochemical raman studies of poly(3,4-ethylenedioxythiophene) (PEDT). *Macromolecules* **32**, 6807–6812 (1999).
- Geschwender, T., Kowalski, C. & Kelley, V. *NanoScope Software 6.13 User Guide*. (2004).
- Glidle, A., Hadyoon, C. S., Gadegaard, N., Cooper, J. M., Hillman, A. R., Wilson, R. W., Ryder, K. S., Webster, J. R. P. & Cubitt, R. Evaluating the influence of deposition

conditions on solvation of reactive conducting polymers with neutron reflectivity. *J. Phys. Chem. B* **109**, 14335–43 (2005).

Glidle, A., Hillman, A. R., Ryder, K. S., Smith, E. L., Cooper, J., Gadegaard, N., Webster, J. R. P., Dalgliesh, R. & Cubitt, R. Use of neutron reflectivity to measure the dynamics of solvation and structural changes in polyvinylferrocene films during electrochemically controlled redox cycling. *Langmuir* **25**, 4093–103 (2009).

Gomez, H., Ram, M. K., Alvi, F., Stefanakos, E. & Kumar, A. Novel synthesis, characterization, and corrosion inhibition properties of nanodiamond–polyaniline films. *J. Phys. Chem. C* **114**, 18797–18804 (2010).

Gustafsson, H., Kvarnström, C. & Ivaska, A. Comparative study of n-doping and p-doping of poly(3,4-ethylenedioxythiophene) electrosynthesised on aluminium. *Thin Solid Films* **517**, 474–478 (2008).

Heinze, J., Frontana-Uribe, B. A. & Ludwigs, S. Electrochemistry of conducting polymers - persistent models and new concepts. *Chem. Rev.* **110**, 4724–71 (2010).

Hillman, A. R., Dong, Q., Mohamoud, M. A. & Efimov, I. Characterization of viscoelastic properties of composite films involving polyaniline and carbon nanotubes. *Electrochim. Acta* **55**, 8142–8153 (2010).

Hillman, A. R., Saville, P. M., Glidle, A., Richardson, R. M., Roser, S. J., Swann, M. J. & Webster, J. R. P. Neutron reflectivity determination of buried electroactive interface structure: PBT/PPy and PBT/PXV bilayers. *J. Am. Chem. Soc.* **120**, 12882–12890 (1998).

Hojati-Talemi, P. & Simon, G. P. Electropolymerization of Polypyrrole/Carbon Nanotube Nanocomposite Films over an Electrically Nonconductive Membrane. *J. Phys. Chem. C* **114**, 13962–13966 (2010).

Holt, K. B., Caruana, D. J. & Millan-Barrios, E. J. Electrochemistry of undoped diamond nanoparticles: accessing surface redox states. *J. Am. Chem. Soc.* **131**, 11272–11273 (2009).

Hong, W., Xu, Y., Lu, G., Li, C. & Shi, G. Transparent graphene/PEDOT–PSS composite films as counter electrodes of dye-sensitized solar cells. *Electrochem. Commun.* **10**, 1555–1558 (2008).

Hu, Y., Shenderova, O. A., Hu, Z., Padgett, C. W. & Brenner, D. W. Carbon nanostructures for advanced composites. *Reports Prog. Phys.* **69**, 1847–1895 (2006).

Ispas, A., Peipmann, R., Adolphi, B., Efimov, I. & Bund, A. Electrodeposition of pristine and composite poly(3,4-ethylenedioxythiophene) layers studied by electro-acoustic impedance measurements. *Electrochim. Acta* **56**, 3500–3506 (2011).

Jee, A.-Y. & Lee, M. Surface functionalization and physicochemical characterization of diamond nanoparticles. *Curr. Appl. Phys.* **9**, e144–e147 (2009).

- Jerliu, B., Dörrer, L., Hüger, E., Borchardt, G., Steitz, R., Geckle, U., Oberst, V., Bruns, M., Schneider, O. & Schmidt, H. Neutron reflectometry studies on the lithiation of amorphous silicon electrodes in lithium-ion batteries. *Phys. Chem. Chem. Phys.* **15**, 7777–84 (2013).
- Kausar, A., Ashraf, R. & Siddiq, M. Polymer/Nanodiamond Composites in Li-Ion Batteries: A Review. *Polym. Plast. Technol. Eng.* **53**, 550–563 (2014).
- Ko, J. M., Rhee, H. W., Park, S.-M. & Kim, C. Y. Morphology and electrochemical properties of polypyrrole films prepared in aqueous and nonaqueous solvents. *J. Electrochem. Soc.* **137**, 905–909 (1990).
- Koroleva, M. Y., Berdnikova, D. V., Spitsyn, B. V. & Yurtov, E. V. Sedimentation stability of aqueous dispersions of nanodiamond agglomerates. *Theor. Found. Chem. Eng.* **43**, 478–481 (2009).
- Kovalenko, I., Bucknall, D. G. & Yushin, G. Detonation nanodiamond and onion-like-carbon-embedded polyaniline for supercapacitors. *Adv. Funct. Mater.* **20**, 3979–3986 (2010).
- Kozak, A. Effect of deposition characteristics on electrochemically prepared PEDOT films. *NNIN REU Res. Accompl.* 20–21 (2010).
- Krueger, A. New carbon materials: biological applications of functionalized nanodiamond materials. *Chem. Eur. J.* **14**, 1382–90 (2008).
- Lauw, Y., Rodopoulos, T., Gross, M., Nelson, A., Gardner, R. & Horne, M. D. Electrochemical cell for neutron reflectometry studies of the structure of ionic liquids at electrified interface. *Rev. Sci. Instrum.* **81**, 074101 (2010).
- Li, C. M., Sun, C. Q., Chen, W. & Pan, L. Electrochemical thin film deposition of polypyrrole on different substrates. *Surf. Coatings Technol.* **198**, 474–477 (2005).
- Li, J., Liu, J., Gao, C., Zhang, J. & Sun, H. Influence of MWCNTs doping on the structure and properties of PEDOT:PSS films. *Int. J. Photoenergy* **2009**, 1–5 (2009).
- Li, X. & Zhitomirsky, I. Capacitive behaviour of polypyrrole films prepared on stainless steel substrates by electropolymerization. *Mater. Lett.* **76**, 15–17 (2012).
- Liu, R., Cho, S. I. & Lee, S. B. Poly(3,4-ethylenedioxythiophene) nanotubes as electrode materials for a high-powered supercapacitor. *Nanotechnology* **19**, 215710 (2008).
- Liu, R., Duay, J. & Lee, S. B. Heterogeneous nanostructured electrode materials for electrochemical energy storage. *Chem. Commun.* **47**, 1384–404 (2011).
- Liu, Y.-C., Yang, K.-H. & Wang, C.-C. Enhancements in conductivity and Raman spectroscopy of polypyrrole electropolymerized on electrochemically roughened Au substrates. *J. Electroanal. Chem.* **549**, 151–155 (2003).

- López Cascales, J. J., Fernández, A. J. & Otero, T. F. Characterization of the reduced and oxidized polypyrrole/water interface: a molecular dynamics simulation study. *J. Phys. Chem. B* **107**, 9339–9343 (2003).
- Luo, X., Weaver, C. L., Zhou, D. D., Greenberg, R. & Cui, X. T. Highly stable carbon nanotube doped poly(3,4-ethylenedioxythiophene) for chronic neural stimulation. *Biomaterials* **32**, 5551–7 (2011).
- Majewski, J., Smith, G. S., Burgess, I., Zamlynny, V., Szymanski, G., Lipkowski, J. & Satija, S. Neutron reflectivity studies of electric field driven structural transformations of surfactants. *Appl. Phys. A* S364–S367 (2002).
- Melato, A. I., Mendonça, M. H. & Abrantes, L. M. Effect of the electropolymerisation conditions on the electrochemical, morphological and structural properties of PEDOT films. *J. Solid State Electrochem.* **13**, 417–426 (2009).
- Melato, A. I., Viana, A. S. & Abrantes, L. M. Different steps in the electrosynthesis of poly(3,4-ethylenedioxythiophene) on platinum. *Electrochim. Acta* **54**, 590–597 (2008).
- Melato, A. I., Viana, A. S. & Abrantes, L. M. Influence of the electropolymerisation mode on PEDOT films morphology and redox behaviour — an AFM investigation. *J. Solid State Electrochem.* **14**, 523–530 (2010).
- Nardes, A. M., Kemerink, M., de Kok, M. M., Vinken, E., Maturova, K. & Janssen, R. A. J. Conductivity, work function, and environmental stability of PEDOT:PSS thin films treated with sorbitol. *Org. Electron.* **9**, 727–734 (2008).
- Nelson, A. Co-refinement of multiple contrast neutron/X-ray reflectivity data using MOTOFIT. *J. Appl. Crystallogr.* **39**, 273–276 (2006).
- Niu, L., Kvarnström, C., Fröberg, K. & Ivaska, A. Electrochemically controlled surface morphology and crystallinity in poly(3,4-ethylenedioxythiophene) films. *Synth. Met.* **122**, 425–429 (2001).
- Norrman, K., Ghanbari-Siahkali, A. & Larsen, N. B. Studies of spin-coated polymer films. *Annu. Rep. Prog. Chem. Sect. C* **101**, 174 (2005).
- Ocampo, C., Oliver, R., Armelin, E., Alemán, C. & Estrany, F. Electrochemical synthesis of poly(3,4-ethylenedioxythiophene) on steel electrodes: properties and characterization. *J. Polym. Res.* **13**, 193–200 (2005).
- Osswald, S., Yushin, G., Mochalin, V., Kucheyev, S. O. & Gogotsi, Y. Control of sp<sup>2</sup>/sp<sup>3</sup> carbon ratio and surface chemistry of nanodiamond powders by selective oxidation in air. *J. Am. Chem. Soc.* **128**, 11635–42 (2006).
- Otero, T. F. & De Larreta, E. Electrochemical control of the morphology, adherence, appearance and growth of polypyrrole films. *Synth. Met.* **26**, 79–88 (1988).

- Patra, S., Barai, K. & Munichandraiah, N. Scanning electron microscopy studies of PEDOT prepared by various electrochemical routes. *Synth. Met.* **158**, 430–435 (2008).
- Penfold, J. *et al.* Recent advances in the study of chemical surfaces and interfaces by specular neutron reflection. *J. Chem. Soc. Faraday Trans.* **93**, 3899–3917 (1997).
- Pigani, L., Heras, A., Colina, Á., Seeber, R. & López-Palacios, J. Electropolymerisation of 3,4-ethylenedioxythiophene in aqueous solutions. *Electrochem. Commun.* **6**, 1192–1198 (2004).
- Randriamahazaka, H., Bonnotte, T., Noël, V., Martin, P., Ghilane, J., Asaka, K. & Lacroix, J.-C. Medium effects on the nucleation and growth mechanisms during the redox switching dynamics of conducting polymers: case of poly(3,4-ethylenedioxythiophene). *J. Phys. Chem. B* **115**, 205–16 (2011).
- Richardson, R. M., Swann, M. J., Hillman, A. R. & Roser, S. J. In situ neutron reflectivity studies of electroactive films. *Faraday Discuss.* **94**, 295–306 (1992).
- Sadki, S., Schottland, P., Brodie, N. & Sabouraud, G. The mechanisms of pyrrole electropolymerization. *Chem. Soc. Rev.* **29**, 283–293 (2000).
- Sakmeche, N., Aeiyaeh, S., Aaron, J., Jouini, M., Lacroix, J. C. & Lacaze, P.-C. Improvement of the electrosynthesis and physicochemical properties of poly(3,4-ethylenedioxythiophene) using a sodium dodecyl sulfate micellar aqueous medium. *Langmuir* **15**, 2566–2574 (1999).
- Samba, R., Fuchsberger, K., Matyichyn, I., Epple, S., Kiesel, L., Stett, A., Schuhmann, W. & Stelzle, M. Application of PEDOT-CNT microelectrodes for neurotransmitter sensing. *Electroanalysis* **26**, 548–555 (2014).
- Sangian, D., Zheng, W. & Spinks, G. M. Optimization of the sequential polymerization synthesis method for polypyrrole films. *Synth. Met.* **189**, 53–56 (2014).
- Scanning Probe Microscopy Training Notebook - Version 3.0.* (Veeco Metrology Group, Digital Instruments, 2000).
- Schwan, J., Ulrich, S., Batori, V., Ehrhardt, H. & Silva, S. R. P. Raman spectroscopy on amorphous carbon films. *J. Appl. Phys.* **80**, 440 (1996).
- Sears, V. F. Neutron scattering lengths and cross sections. *Neutron News* **3**, 26–37 (1992).
- Shimoda, S. & Smela, E. The effect of pH on polymerization and volume change in PPy(DBS). *Electrochim. Acta* **44**, 219–238 (1998).
- Sivia, D. S. *Elementary Scattering Theory For X-ray and Neutron Users.* (Oxford University Press, 2011).

- Snook, G. A., Kao, P. & Best, A. S. Conducting-polymer-based supercapacitor devices and electrodes. *J. Power Sources* **196**, 1–12 (2011).
- Sönmez, G. & Saraç, A. S. Structural study of pyrrole-EDOT copolymers on carbon fiber micro-electrodes. *Synth. Met.* **135-136**, 459–460 (2003).
- Tamburri, E., Guglielmotti, V., Matassa, R., Orlanducci, S., Gay, S., Reina, G., Terranova, M. L., Passeri, D. & Rossi, M. Detonation nanodiamonds tailor the structural order of PEDOT chains in conductive coating layers of hybrid nanoparticles. *J. Mater. Chem. C* **2**, 3703 (2014).
- Tamburri, E., Orlanducci, S., Guglielmotti, V., Reina, G., Rossi, M. & Terranova, M. L. Engineering detonation nanodiamond – Polyaniline composites by electrochemical routes: Structural features and functional characterizations. *Polymer (Guildf)*. **52**, 5001–5008 (2011).
- Tewari, A., Kokil, A., Ravichandran, S., Nagarajan, S., Bouldin, R., Samuelson, L. A., Nagarajan, R. & Kumar, J. Soybean peroxidase catalyzed enzymatic synthesis of pyrrole/EDOT copolymers. *Macromol. Chem. Phys.* **211**, 1610–1617 (2010).
- Thombare, J. V., Rath, M. C., Han, S. H. & Fulari, V. J. The influence of monomer concentration on the optical properties of electrochemically synthesized polypyrrole thin films. *J. Semicond.* **34**, 1674–4926 (2013).
- Todorov, T. N. Carbon nanotubes as long ballistic conductors. **393**, 240–242 (1998).
- Tronin, A., Chen, C.-H., Gupta, S., Worcester, D., Lauter, V., Strzalka, J., Kuzmenko, I. & Blasie, J. K. Structural changes in single membranes in response to an applied transmembrane electric potential revealed by time-resolved neutron/X-ray interferometry. *Chem. Phys.* **422**, 283–289 (2013).
- Veder, J.-P., De Marco, R., Clarke, G., Chester, R., Nelson, A., Prince, K., Pretsch, E. & Bakker, E. Elimination of undesirable water layers in solid-contact polymeric ion-selective electrodes. *Anal. Chem.* **80**, 6731–40 (2008).
- Veder, J.-P., De Marco, R., Clarke, G., Jiang, S. P., Prince, K., Pretsch, E. & Bakker, E. Water uptake in the hydrophilic poly(3,4-ethylenedioxythiophene):poly(styrene sulfonate) solid-contact of all-solid-state polymeric ion-selective electrodes. *Analyst* **136**, 3252–8 (2011).
- Veder, J.-P., De Marco, R., Patel, K., Si, P., Grygolowicz-Pawlak, E., James, M., Alam, M. T., Sohail, M., Lee, J., Pretsch, E. & Bakker, E. Evidence for a surface confined ion-to-electron transduction reaction in solid-contact ion-selective electrodes based on poly(3-octylthiophene). *Anal. Chem.* **85**, 10495–502 (2013).
- Veder, J.-P., Patel, K., Sohail, M., Jiang, S. P., James, M. & De Marco, R. An electrochemical impedance spectroscopy/neutron reflectometry study of water uptake in the poly(3,4-ethylenedioxythiophene):poly(styrene sulfonate)/polymethyl methacrylate-polydecyl methacrylate copolymer solid-contact ion-selective electrode. *Electroanalysis* **24**, 140–145 (2012).

- Vernitskaya, T. V & Efimov, O. N. Polypyrrole: a conducting polymer; its synthesis, properties and applications. *Russ. Chem. Rev.* **66**, 443 – 457 (1997).
- Villarreal, I., Morales, E., Otero, T. F. & Acosta, J. L. Electropolymerization kinetics of pyrrole in aqueous solution on graphite felt electrodes. *Synth. Met.* **123**, 487–492 (2001).
- Wagner, K., Pringle, J. M., Hall, S. B., Forsyth, M., MacFarlane, D. R. & Officer, D. L. Investigation of the electropolymerisation of EDOT in ionic liquids. *Synth. Met.* **153**, 257–260 (2005).
- Wang, Y. Research progress on a novel conductive polymer–poly(3,4-ethylenedioxythiophene) (PEDOT). *J. Phys. Conf. Ser.* **152**, 012023 (2009).
- Welch, J. O., Li, P., Chaudhary, A., Edgington, R. & Jackman, R. B. The influence of surface functionalisation on the electrical properties and thermal stability of nanodiamonds. *J. Appl. Phys.* **116**, 133705 (2014).
- Wilson, R., Cubitt, R., Glidle, A., Hillman, A. R., Saville, P. M. & Vos, J. G. A neutron reflectivity study of [Os(bipy)<sub>2</sub>(PVP)IOCl]<sup>+</sup> polymer film modified electrodes: effect of redox state and counter ion. *Electrochim. Acta* **44**, 3533–3548 (1999).
- Xia, Y. & Ouyang, J. PEDOT-PSS films with significantly enhanced conductivities induced by preferential solvation with cosolvents and their application in polymer photovoltaic cells. *J. Mater. Chem.* **21**, 4927–4936 (2011).
- Xiao, Y., Ye, X., He, L. & Che, J. New carbon nanotube-conducting polymer composite electrodes for drug delivery applications. *Polym. Int.* **61**, 190–196 (2012).
- Xu, G., Li, B., Cui, X. T., Ling, L. & Luo, X. Electrodeposited conducting polymer PEDOT doped with pure carbon nanotubes for the detection of dopamine in the presence of ascorbic acid. *Sensors Actuators B Chem.* **188**, 405–410 (2013).
- Zamlynny, V., Burgess, I., Szymanski, G., Lipkowski, J., Majewski, J., Smith, G., Satija, S. & Ivkov, R. Electrochemical and neutron reflectivity studies of spontaneously formed amphiphilic surfactant bilayers at the gold-solution interface. *Langmuir* **16**, 9861–9870 (2000).
- Zang, J. B., Wang, Y. H., Zhao, S. Z., Bian, L. Y. & Lu, J. Electrochemical properties of nanodiamond powder electrodes. *Diam. Relat. Mater.* **16**, 16–20 (2007).
- Zang, J., Wang, Y., Bian, L., Zhang, J., Meng, F., Zhao, Y., Ren, S. & Qu, X. Surface modification and electrochemical behaviour of undoped nanodiamonds. *Electrochim. Acta* **72**, 68–73 (2012).
- Zhong, Q., Inniss, D., Kjoller, K. & Elings, V. B. Fractured polymer / silica fiber surface studied by tapping mode atomic force microscopy. *Surf. Sci. Lett.* **290**, L688–L692 (1993).

Zhou, M. & Heinze, J. Electropolymerization of pyrrole and electrochemical study of polypyrrole: I . Evidence for structural diversity of polypyrrole. *Electrochim. Acta* **44**, 1733–1748 (1999).